Design and Analysis of Signal Processing Circuits for Molecular Communication

Bi, Dadi

Awarding institution:
King's College London

Design and Analysis of Signal Processing Circuits for Molecular Communication

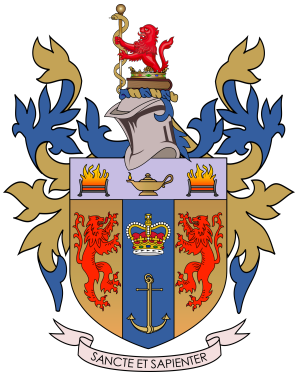

Dadi Bi

Supervisor: Dr. Yansha Deng
Dr. Ali Salehi-Reyhani

Department of Engineering
King's College London

This dissertation is submitted for the degree of
Doctor of Philosophy

July 2022

Declaration

I hereby declare that I am the author of this dissertation and it contains nothing which is the outcome of work done in collaboration with others, except as specified in the text and Acknowledgements. Chapters 3-6 are based on my work performed under the supervision of Dr. Yansha Deng. For all chapters and the corresponding papers, I conducted the literature surveys on relevant topics, formulated the system models, performed the analyses, implemented the simulations, and wrote the manuscripts. My supervisor contributed by providing insightful discussions on the technical aspects of the papers, and revisions and feedback on the manuscripts. I further state that the contents of this dissertation have not been submitted in whole or in part for consideration for any other degree or qualification at King's College London or any other university. This dissertation contains fewer than 100,000 words including all words included within tables, footnotes, and table and figure legends, as prescribed by the Research Degrees Examination Board.

Dadi Bi
July 2022

Acknowledgements

I am deeply grateful for the guidance and support of my supervisors, Dr. Yansha Deng and Dr. Ali Salehi-Reyhani. I am thankful to Yansha for offering me a chance to pursue my Ph.D. at King's College London, for introducing me to the molecular communication field, for her valuable advice and insightful discussions, and for her continuous support of my academic career. I also would like to thank Dr. Ali Salehi-Reyhani for hosting me at Imperial College London and for providing me with the lab space, equipment, and instructions for the microfluidic testbed.

I would like to greatly thank the members of my doctoral committee, Prof. Lie-Liang Yang and Dr. Michael Barros, for their time, their feedback, and their interest in my work.

I am deeply thankful to Prof. Robert Schober, Dr. Adam Noel, and Apostolos Almpanis for the collaboration on the molecular communication survey paper. It has been a great experience for me to work with these excellent researchers and learn from their meticulous attitude toward research. I am also indebted to Dr. Vivien Walter, who trained me to perform chemical experiments and implement the microfluidic testbed. I much appreciate not only his sharing of chemistry knowledge but also his patience to teach me, a rookie, how to use various equipment.

I would like to express my gratitude to current and past members of the Intelligent Connectivity Lab: Dr. Nan Jiang, Dr. Yan Liu, Shengzhi Yang, Fenghe Hu, Liyana Burhanuddin, Hui Zhou, Xiaonan Liu, and Rinrada Jadsadaphongphaibool. Thanks for the various ways of support and help, and I cannot forget the enjoyable time that we spent together conquering spectacular coast paths and exploring types of cuisines. I also acknowledge the warm friendship of Yuan Liao, Lina Wu, and Yibing Wang, who made my stay at Orchard Lisle House a pleasure, especially during the Covid-19 pandemic. In addition, I am particularly indebted to Yan Wang for her elegant presence and for her accompanying during my Ph.D. journey.

Last but not least, my sincerest gratitude goes to my grandma, dad, and mom. Without their constant support and encouragement over the past few years, it would be impossible for me to complete my study.

Abstract

Molecular communication (MC) engineering is inspired by the use of chemical signals as information carriers in cell biology. The biological nature of chemical signaling makes MC a promising methodology for interdisciplinary applications requiring communication between cells and other microscale devices, e.g., smart drug delivery and intelligent surveillance against chemical attacks. The design of communication systems capable of processing and exchanging information through molecules and chemical processes is a rapidly growing interdisciplinary field, which holds the promise to unleash the potential of MC for interdisciplinary applications. While MC theory has had major developments in recent years, more practical aspects in designing components capable of MC functionalities remain less explored. Therefore, the main focus of this dissertation is on the design and analysis of signal processing circuits for MC. In particular, this dissertation presents the design and analysis of two chemical-reactions-based microfluidic circuits with binary concentration shift keying (BCSK) and quadruple CSK (QCSK) modulation-demodulation functions and a genetic circuit with controllable pulse generation function.

First, the basic characteristics of fluids in microfluidic channels are first analyzed. These include the derivations of the concentration and velocity changes for microfluidic devices with combining and separation channels. Then, a five-level architecture is developed for digital microfluidic circuits along with an introduction to the designs of microfluidic digital AND, NAND, OR, NOR, XOR, and XNOR gates.

Second, the design of a chemical-reactions-based microfluidic BCSK transceiver is proposed. Based on the newly derived spatial-temporal concentration distributions, the modulated and demodulated signals are mathematically characterized. Moreover, the BCSK transmitter is further optimized in terms of the microfluidic channel length and the restricted time gap between two consecutive input bits.

Third, the design of a chemical-reactions-based microfluidic QCSK transceiver is presented based on the proposed microfluidic logic gates. The proposed microfluidic circuits are theoretically described by deriving the impulse response of advection-

diffusion channels, and a general mathematical framework is developed which can be used to analyze other new and more complicated circuits.

Fourth, the design of a genetic circuit with a pulse generation function is proposed. The proposed circuit is consisted of three engineered minimal cells which contain the minimal and sufficient number of molecular components and display Boolean logic functions. The behavior of synthetic minimal cells and cell-to-cell propagation channels are mathematically modeled, which reveals the impact of cell spatial configurations and cell regulatory networks on the peak amplitude of generated pulses.

Table of contents

List of figures

List of tables

Nomenclature

Greek Symbols

α_n	The roots of $J_1(\frac{\alpha_n}{\sqrt{D}}r_b)$
Δ	The discriminant of an equation
δ	A variable to numerically find $t_{Y_i}^{\max}$
$\delta(\cdot)$	Kronecker delta function
ϵ	A variable to numerically find L_2
γ_{YFP}	YFP degradation rate
λ	An arbitrary constant
μ	The mean of a Gaussian distribution
Φ	Quantum yield
σ	The standard deviation of a Gaussian distribution
τ	A variable to numerically find $t_{Y_i}^{A}$
θ_{A}	A coefficient that accounts for changes in expression of an activator *InvF*
θ_{Ch}	A coefficient that accounts for changes in expression of a chaperone protein *SicA*
ε	Molar absorptivity
ξ	A variable that describes the relationship between the maximum concentration of species Y at Reaction III channel inlet and the maximum concentration of a generated pulse
ζ	A variable to calculate the maximum concentration of a pulse

ζ_D	The impacts of upstream promoter on downstream promoter
ζ_U	The impacts of downstream promoter on upstream promoter
γ	Degradation rate of the protein controlled by promoter BAD
π	$\simeq 3.14\ldots$

Other Symbols

$*$	Convolution operator
lg	Logarithm (base 10)
ln	Natural logarithm (base e)
$\mathbb{1}_{\{\cdot\}}$	Indicator function that represents the value 1 if the statement is true, and zero otherwise
$\mathcal{A}[\cdot]$	An operator that describes the output concentration of O in a reaction channel containing $S_i + Amp \rightarrow S_i + O$
$\mathcal{F}[\cdot]$	An operator that represents a combination of operators $\mathcal{R}[\cdot]$ and $\mathcal{A}[\cdot]$
$\mathcal{G}[\cdot]$	An operator that describes the output concentration of S_k in a reaction channel containing $S_i + S_j \rightarrow S_k$
$\mathcal{L}^{-1}$	Inverse Laplace Transform
$\mathcal{R}[\cdot]$	An operator that describes the output concentration of S_i in a reaction channel containing $S_i + S_j \rightarrow S_k$
$\mathcal{S}_{\mathrm{RX}}$	The area of an observing region
$\mathcal{T}[\cdot]$	An operator that describes the output of an advection-diffusion channel with length L_T
∇	Nabla operator
$\mathrm{gfp}_i^{\max}$	The fluorescence produced from generic promoter i at maximum induction
$\tilde{\mathcal{S}}_{\mathrm{TX}}$	Molecule releasing surface
$\tilde{\mathcal{S}}_{\mathrm{RX}}$	Adsorbing surface

$\tilde{\mathcal{V}}_{\mathrm{TX}}$ Molecule releasing space

a Maximum transcription rate

b Protein production rate

b_{YFP} YFP production rate

$C_i^{\max}$ The maximum concentration of protein produced from generic promoter i at steady state

$H(x,t)$ The impulse response of a straight advection-diffusion channel

I_0 Incident light intensity

I_i^{SS} The steady state fluorescent intensity controlled by generic promoter i

$I_v(r)$ Modified Bessel functions of the first kind of order v

$J_v(r)$ Bessel functions of the first kind of order v

J_{Adv} Advection flux

J_{Diff} Diffusion flux

k The efficiency of the spectrometer at transferring light

K_1 A constant defined for Shea-Ackers Formalism

k_1 Adsorption rate

K_D Dissociation constant

k_d AHL degradation rate

k_f Rate constant

$K_v(r)$ Modified Bessel functions of the second kind of order v

k_{-1} Desorption rate

L Path length

l Hill coefficient

$N_{\mathrm{RX}}(t)$ Number of molecules observed by the receiver at time t

N_{TX} Number of molecules released by a transmitter

$p(r,t)$ The probability density function of a molecule released by the transmitter with respect to r at time t

P_i The probability of promoter i being in open complex state

$Q(\cdot)$ Q-function

r Radial distance

r_1 Inner radius of an annulus

r_2 Outer radius of an annulus

r_b The distance between a releasing point and the cell culture boundary edge

S_i Generic molecule species

$u(t)$ Heaviside step function

$Y_v(r)$ Bessel functions of the second kind of order v

$\lfloor \cdot \rfloor$ Floor function

∇^2 Laplace operator

Acronyms / Abbreviations

1D One Dimensional

3D Three Dimensional

3OC6 *N*-(β-Ketocaproyl)-L-homoserine lactone

E. Coli *Escherichia coli*

a. u. Arbitrary Unit

AHL Acyl-homoserine lactones

Ara Arabinose

ASK Amplitude Shift Keying

aTc Anhydrotetracycline

AWGN Additive White Gaussian Noise

BC Boundary Condition

BCSK Binary Concentration Shift Keying

BFSK Binary Frequency Shift Keying

CDF Cumulative Distribution Function

CFD Computational Fluid Dynamics

CGG Concentration Gradient Generator

CIR Channel Impulse Response

CRN Chemical Reaction Network

CSK Concentration Shift Keying

ER Endoplasmic Reticulum

EYFP Enhanced YFP

FFL Feed Forward Loop

FSK Frequency Shift Keying

HCN Hydrodynamic Controlled Microfluidic Network

I1-FFL Incoherent Type 1 FFL

IC Initial Condition

IPTG Isopropyl β-D-1-thiogalactopyranoside

ISI Inter Symbol Interference

KCL Kirchhoff's Current Law

KVL Kirchhoff's Voltage Law

LDPC Low-Density Parity-Check

LOC Lab-on-a-chip

MC Molecular Communication

MIMO Multiple-input Multiple-output

MoSK Molecular Shift Keying

MS Mass Spectrometry

NO Nitric Oxide

ODE Ordinary Differential Equation

OOK On-Off Keying

PDE Partial Differential Equation

Pe Péclet Number

QCSK Quadruple Concentration Shift Keying

QS Quorum Sensing

Re Reynolds Number

RFP Red Fluorescent Protein

RNAP RNA Polymerase

RSK Reaction Shift Keying

SPC Single Parity-Check

TF Transcription Factor

XNOR Exclusive NOR

XOR Exclusive OR

YFP Yellow Fluorescent Protein

Chapter 1

Introduction

1.1 What is Molecular Communication?

The communication engineering community has never stopped on the road of pioneering innovative applications to shorten the time needed for communication and expand the space and place of human interactions. The core of these applications is how information is delivered in a medium. Although most applications employ electromagnetic phenomena for communication, this is insufficient to enable nanonetworks (i.e., the interconnection of nano-machines) and bio/nano-applications, e.g., smart drug delivery and intelligent surveillance against chemical attacks. One reason is that components of macroscale transceivers are difficult to operate efficiently and miniaturize to nano/micrometer-scale [1], i.e., to the scale of living cells.

To find an efficient and reliable communication paradigm at the nano/microscale, we can learn a lesson from how cells communicate with each other in nature. Like human beings, cells have their own "social activities" and are in constant communication with each other. One way they achieve communication is by continuously sensing, receiving, and interpreting extracellular signaling molecules, and then coordinating their behaviors in response. A representative example is the neurotransmitter transmission between presynaptic neuron and postsynaptic neuron, which is shown in Fig. 1.1. In this scenario, the presynaptic neuron and postsynaptic neuron act as a transmitter and receiver, respectively. Upon the arrival of an action potential, the neurotransmitters are released by the presynaptic neuron from vesicles at the outer membrane. The released neurotransmitters diffuse over the synaptic cleft and are capable of activating the receptors distributed on the membrane of the postsynaptic neuron. The reception of neurotransmitters by the receptors triggers the opening of ion channels, which leads to an influx of ions to the postsynaptic neuron and finally an action potential

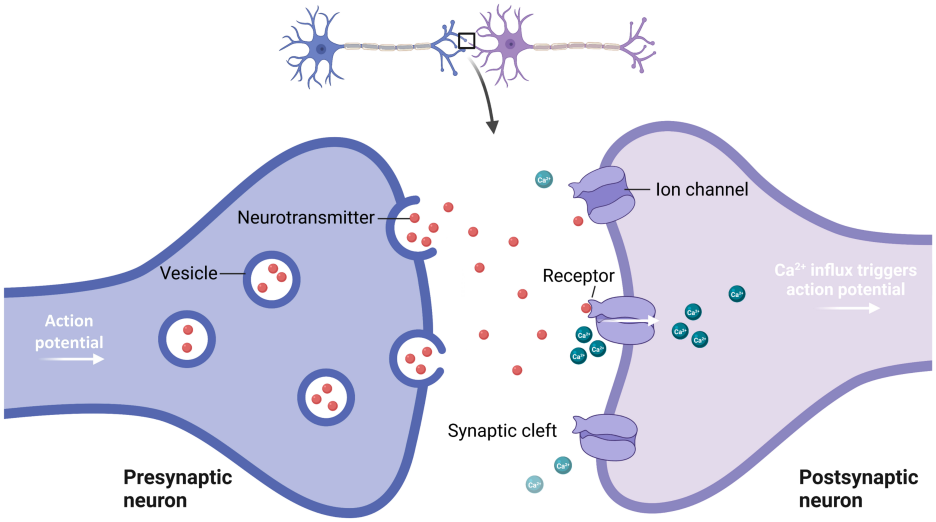

Fig. 1.1 The neuron communication system.

[2, Ch. 11]. The above form of information exchange has motivated the proposal of biologically-inspired *molecular communication* (MC), which employs *chemical signals* to exchange information [1, 3]. Unlike classical communication methods, MC is inherently energy-efficient and robust in physiological environments.

To provide a language for communication engineers to study and interface with MC systems, the aforementioned neural communication system can be interpreted by a five-level communication hierarchy. As shown in Fig. 1.2a, the communication hierarchy is comprised of five levels: 1) **Physical Signal Propagation**; 2) **Physical and Chemical Signal Interaction**; 3) **Signal-Data Interface**; 4) **Local Data Abstraction**; and 5) **Application** [4]. By applying the communication hierarchy to the neuron communication scenario in Fig. 1.2b, the levels of the hierarchy are detailed as follows:

1. **Physical Signal Propagation**: the lowest level includes how molecules are transported between communicating devices[1], e.g., via diffusion, fluid flow, or contact-based means. This level is *not* defined within devices themselves, but directly connects devices that are communicating.[2]

[1] A communication device can act as a transmitter, a receiver, and even a transceiver. In this dissertation, the communication device can be an artificial microfluidic circuit and an engineered minimal cell.

[2] Although Level 1 is not defined within devices themselves for this five-level communication hierarchy, physical signal propagation can occur inside a communication device, e.g., the molecule propagation inside a microfluidic circuit.

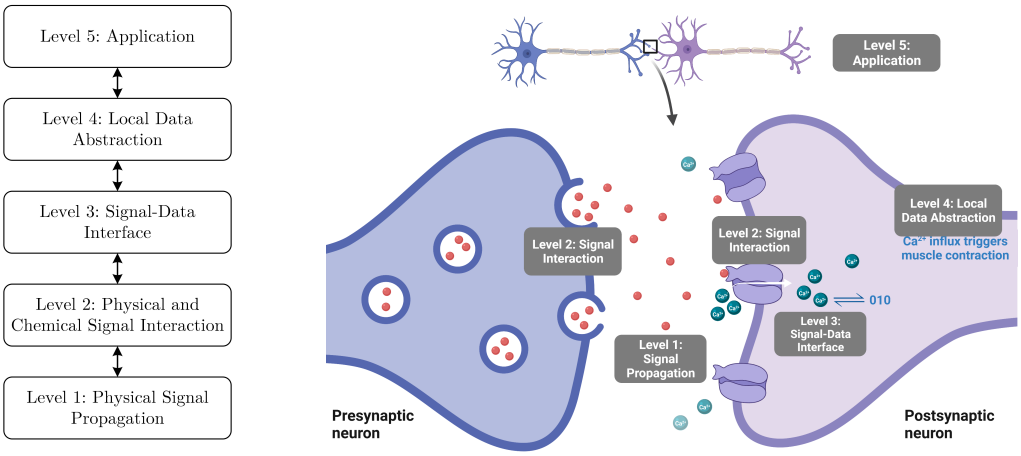

(a) (b)

Fig. 1.2 The application of a five-level communication hierarchy to the neuron communication system.

2. **Physical and Chemical Signal Interaction**: this level deals with how the physical signal is generated at a transmitting device and sampled at a receiving device, e.g., the release of neurotransmitters at the presynaptic neuron and their reception by neurotransmitter receptors at the postsynaptic neuron in Fig. 1.2b. This also includes the biochemical signaling pathways that process molecular signals.

3. **Signal-Data Interface**: this level focuses on how physical signals are mathematically quantified, observed, and controlled. This includes the conversion of data between its mathematical representation and its physical form.

4. **Local Data Abstraction**: this level is concerned about the physical meaning (i.e., the induced action) of quantified data at a local device. Examples of the action of quantified data can include the firing of a neuron in Fig. 1.2b and the initiation of a gene expression to produce a particular protein or the secretion of a useful metabolite. This level includes the information-theoretic limits of molecular signals, and it also includes encoding and decoding in communication networks.

5. **Application**: the top-level behavior is relying on communication. This could be entirely within a biological context, e.g., differentiation of cells in a multicellular

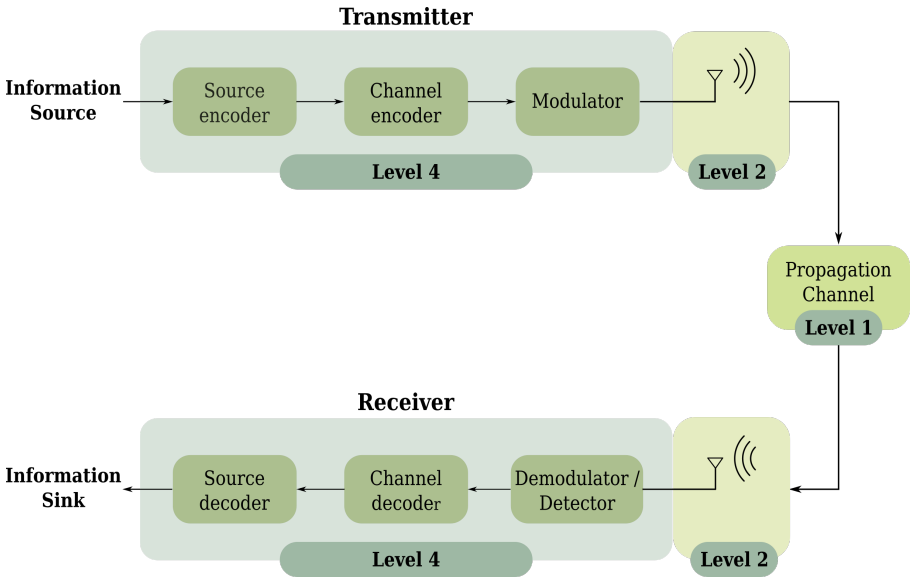

Fig. 1.3 The application of a five-level communication hierarchy to the block diagram of a conventional communication system.

organism or symbiosis between different species, or within a mixed synthetic and biological context, e.g., disease detection by medical sensors.

To emphasize the similarities and differences between an MC system and a conventional communication system, the communication hierarchy in Fig. 1.2a is also applied to a conventional communication system [5]. As shown in Fig. 1.3, Level 1 is mapped to the propagation of electromagnetic waves, and Level 2 is mapped to electromagnetic wave emission and reception via antennas. Although the signal-data interface of Level 3 is not shown in Fig. 1.3, there is still a mapping of this level between these two communication systems, where the interface between chemical molecules and information data is analogous to the interface between electromagnetic waves and the data they represent. Level 4 can be mapped to data manipulation (e.g., modulation-demodulation and encoding-decoding) inside a conventional communication transceiver, and the whole communication system can support an application for Level 5.

1.2 Molecular Communication Development

The basic concept and architecture of MC were initially proposed and described to the communications research community in 2005 [6, 7]. After empirical work aimed to

validate the feasibility of MC [8], this novel field has been primarily engaged with and developed by the theoretical communications research community [9].

Significant progress has been made over the last decade with a flourish of activity to understand the biophysical characteristics of molecule propagation using tools and mechanisms from communication engineering. The focus of channel modeling research has spanned from basic Brownian motion [10] to molecular transport with fluid flow [11] and active propagation that relies on energy sources, such as molecular motors [12] and bacterial chemotaxis [13]. The interactions between information molecules and the receiver have been extensively studied for passive reception [14] and full absorption [15], and recent works have modeled receiver-side reaction kinetics more precisely, e.g., reversible adsorption [16] and ligand-binding [17]. While many works have been based on transmission using simple on-off keying (OOK) modulation [18], more sophisticated modulation and coding schemes have been developed for molecular transmission with higher data rates and improved communication reliability [19, 20]. Accompanying MC system design has been information-theoretical research to quantify the fundamental limits of molecular signaling, i.e., the communication capacity [3].

The biological nature of chemical signaling makes MC a promising methodology for interdisciplinary applications requiring communication between cells and other microscale devices, such as disease diagnosis, drug delivery, and health monitoring. With the ultimate goal of enabling these practical and paradigm-shifting applications, the MC community has sought exploitation in cross-disciplinary research. For example, for disease diagnosis, evaluating the capacity of the brain to encode and retrieve memories could reveal the dysfunction and loss of synaptic communication due to Alzheimer's and other neurodegenerative diseases [21]. For drug delivery, MC theory has been applied to characterize the transport of drug particles in blood vessels with the aim to optimize the drug injection rate while reducing its side effects [22]. For health monitoring, MC could coordinate the movement of intra-body nanoscale sensors to collect health data, which could be further transmitted to external devices via micro-to-macro interfaces for real-time monitoring [23, 24].

In addition to theoretical research, experimental research on MC has sought to validate theoretical models and provide pathways toward applications, both at the macroscale and microscale. For macroscale experiments, alcohol molecules were first employed to demonstrate the feasibility of transmitting a text message using chemical signaling in an open diffusion space [25]. To improve the data rate, this testbed has been extended to multiple-input multiple-output (MIMO) systems [26]. Meanwhile, in-vessel MC testbeds with [27–29] or without a flow [30, 31] were also built to investigate

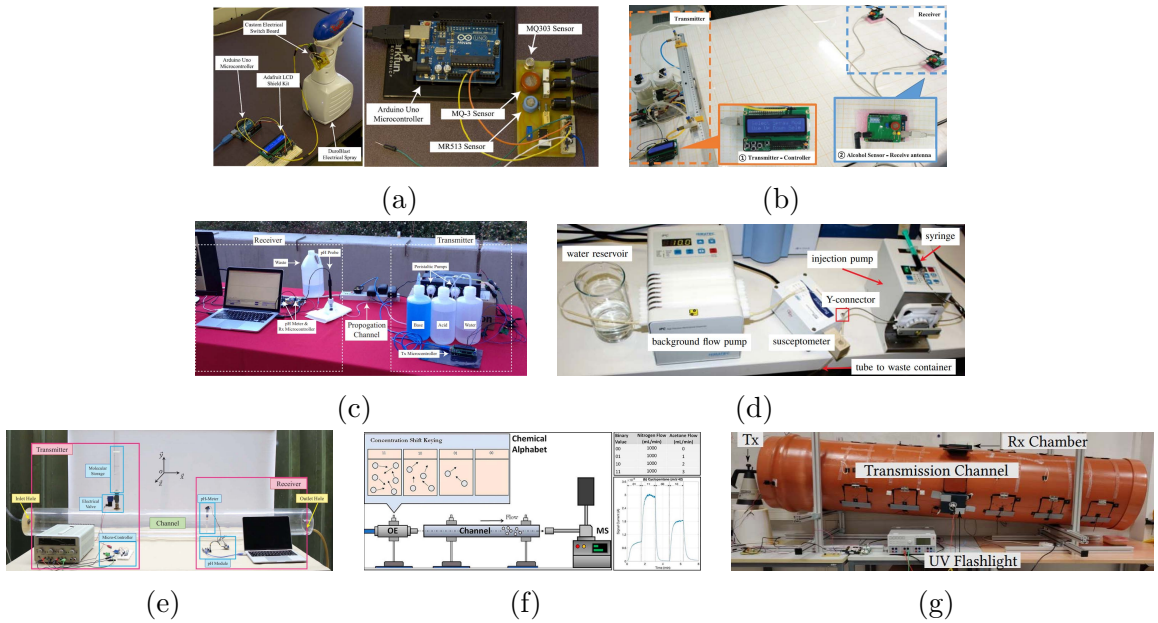

(a) (b) (c) (d) (e) (f) (g)

Fig. 1.4 The macroscale MC testbeds developed in (a) [25], (b) [26], (c) [27], (d) [28], (e) [29], (f) [30], (g) [31].

the possibility of delivering information using acid/base, magnetic nanoparticles, odor molecules, and fluorescein, where improved mathematical models have been proposed to account for discrepancies between theory and experimental results. A graphical summary of the macroscale testbeds is provided in Fig. 1.4.

For microscale MC testbeds, in [32], the genetically engineered *Escherichia coli* (*E. coli*) bacteria, housed in a chamber inside a microfluidic device, serves as an MC receiver using fluorescence detection upon the receipt of signaling molecules. A similar experimental setup was also used in [33, 34]. In [33], a nanoscale microfluidic MC receiver based on graphene field-effect transistor biosensors was fabricated, which is capable of detecting single-stranded DNA molecules flowing through a microfluidic channel; in [34], engineered bacterial with AND logic gate and an electrochemical sensor chip were located at the two ends of a microfluidic tube, where the electrochemical sensor chip was able to detect the changes in protons produced by the engineered bacterial population. The Boolean logic molecular calculation was also investigated in [35], where Boolean logic AND and OR gates were realized through manipulation of the threshold of Ca^{2+} ion flows between astrocyte cells. In addition, the existing microscale MC testbeds have demonstrated how to use macroscale instruments to control microscale systems. Examples include the microscale modulator that transduced external optical signals to a release of protons [36] and the controlled *in vivo* information transfer by applying electrical signals onto the nervous system of common earthworms

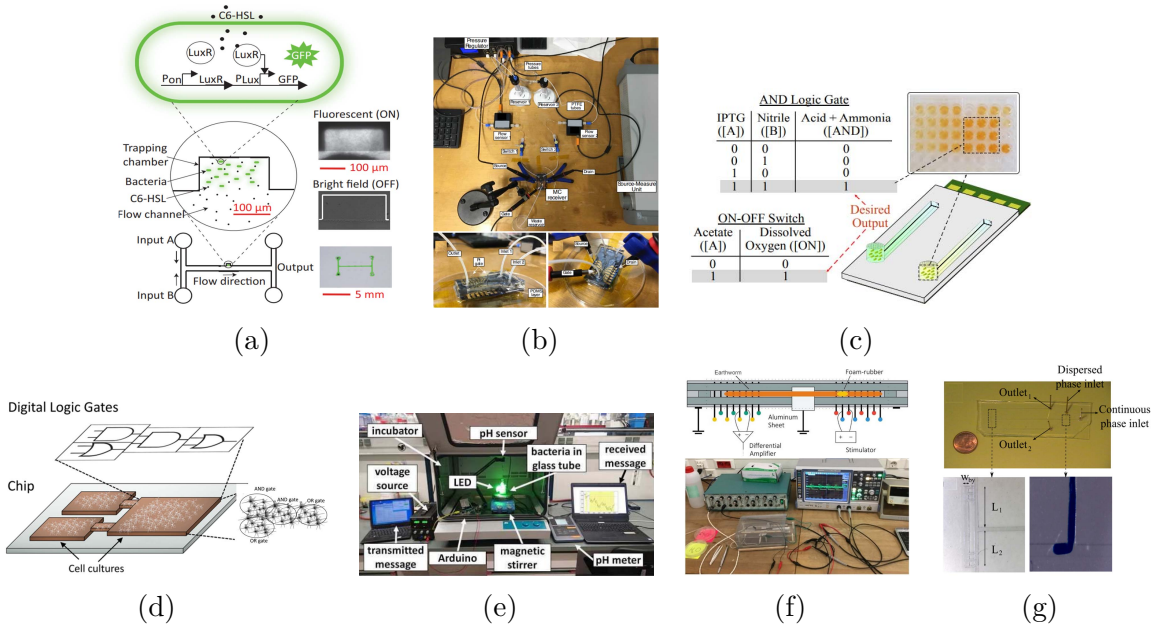

Fig. 1.5 The microscale MC testbeds developed in (a) [32], (b) [33], (c) [34], (d) [35], (e) [36], (f) [37], (g) [38].

[37]. Moreover, the information can also be delivered in droplet-based microfluidic systems. The authors of [38] proposed a hydrodynamic controlled microfluidic network (HCN) and demonstrated how to realize a pure hydrodynamic microfluidic switching function, where the successful routing of payload droplets was achieved by designing the geometry of microfluidic circuits. A graphical summary of the microscale testbeds is provided in Fig. 1.5.

Table 1.1 Summary of MC surveys in terms of their focused topics.

Focus	General Advancements	Propagation Channel Characterization	Modulation Techniques	Communication Capacity	Physical Transceiver Design
Reference	[1, 9, 39]	[40, 41]	[42]	[43]	[44, 45]
Focus	Genetic Circuits	DNA Storage	MC Interface	Medical Applications	MC Hierarchy
Reference	[46]	[47]	[48, 49]	[21, 50–53]	[4]

Over the past ten years, there have been several comprehensive MC surveys to report the progress that has been made. The existing MC surveys are classified into different categories based on their focus in Table 1.1 and their contents are briefly summarized in terms of the communication hierarchy in Table 1.2. For more details of the progress, the readers can refer to these surveys accordingly.

Table 1.2 Summary of MC Surveys in terms of the communication hierarchy in Fig. 1.2a.

Reference	[1]	[9]	[41]	[39]	[51]	[21]	[52]	[50]	[47]	[40]	[43]	[44]	[24]	[46]	[48]	[49]	[45]	[42]	[4]
Year	2008	2012	2013	2016	2016	2016	2017	2017	2018	2019	2019	2019	2019	2019	2019	2019	2020	2020	2021
Level 1: Physical Signal Propagation	✓	✓	✓	✓		✓	✓	✓		✓	✓	✓	✓						✓
Level 2: Device Interface	✓			✓			✓	✓		✓	✓	✓					✓		✓
Level 3: Physical/Data Interface			✓	✓	✓		✓	✓	✓		✓	✓		✓	✓	✓	✓	✓	✓
Level 4: Local Data		✓	✓	✓				✓	✓		✓	✓							✓
Level 5: Application	✓	✓		✓	✓	✓	✓	✓				✓	✓				✓		✓

1.3 Motivation

This dissertation mainly focuses on Level 4, i.e., **Local Data Abstraction**, of the communication hierarchy for MC. The **Local Data Abstraction** level is the interface between the mathematical quantification of physical signals and how the information in these signals is manifested and manipulated within an individual communication device. In other words, this level concerns how an MC transmitter encodes information into a quantifiable form and then modulates it into a physical signal, and how an MC receiver demodulates a received chemical signal to recover the transmitted information. From the review of MC testbeds in Section 1.2, it is clear that most MC testbeds highly rely on electrical devices to manipulate information. For example, the transmitted bit sequence was modulated over the concentration of signaling molecules via the on/off of an electronic spray [25] and air tank [26, 30] controlled by microcontroller boards and laptops. Their high dependency on electrical signals/devices can hardly fulfill the biocompatible and non-invasive requirements of biomedical applications, such as disease diagnosis and drug delivery [54]. Meanwhile, the size of electronic devices can hardly meet the requirement of intra-body healthcare applications promised by MC, where fully MC functional devices are expected to be miniaturized into microscale/nanoscale [44]. This demonstrates that a hindrance to translating MC research results to practical applications is the lack of nano/micro-devices able to process chemical concentration signals, rather than electrical signals, in the biochemical environment. Hence, how to process information flow over molecular concentrations is a very interesting target for MC research. There has been some research that focuses on using chemical reactions and synthetic biology to achieve digital and analog circuits and how these circuits can be used to realize communication functionalities, including modulation-demodulation and encoding-decoding, in an engineered cell biology system. In the following, these signal processing circuits are briefly reviewed to motivate the development of new MC circuits proposed in this dissertation.

In general, biochemical signal processing functions can be realized in two fashions: 1) chemical circuits [55] based on chemical reaction networks (CRNs), and 2) genetic circuits [56] in engineered living cells. In chemical circuits, a set of chemical reactions is designed for a desired chemical response, whereas in genetic circuits, a gene regulatory network based on synthetic biology is designed to achieve the desired function. Considering the scalability of digital design and the discreteness of molecules, it is natural to start by designing circuits to process digital signals that switch rapidly from a distinct low state representing bit-0 to a high state representing bit-1. However, biological systems do not always operate with *reliable* "1" and "0" signals; instead, many signals are processed probabilistically and show a graded analog response from low to high level [57]. In addition, motivated by the fact that biological systems based on analog computation can be more efficient compared with those based on digital computation [57, 58], analog circuit design also receives attention from biologists and engineers.

1.3.1 Digital & Analog Circuits via Chemical Reactions

Many types of digital circuits have already been designed and realized via chemical reactions, demonstrating their capabilities to process molecular concentrations. Designing digital logic functions has also attracted increasing research attention. Combinational gates, including the AND, OR, NOR, and Exclusive OR (XOR) gate, were designed in [59] based on a bistable mechanism. For a single bit, the HIGH and LOW states are indicated by the presence of two different molecular species. The designed gates were mapped into DNA strand-displacement reactions and validated by generating their chemical kinetics. The authors of [60] also used the bistable mechanism, where five general and circuit-free methods were proposed to synthesize arbitrary combinational logic gates.

An architecture of analog circuits to compute polynomial functions of inputs was proposed in [61], where the circuits were built on the basis of analog addition, subtraction, and multiplication gates via DNA strand displacement reactions. Relying on the help of the Taylor Series and Newton Iteration approximations, these analog circuits can also compute non-polynomial functions, such as the logarithm. However, an accurate logarithm computation over a wide range of inputs requires a large number of reactions, due to the high-order power series approximation. In [62], the authors presented a method to accurately compute the logarithm with tunable parameters while maintaining low circuit complexity. In [63], a systematic approach to converting linear electric circuits into chemical reactions with the same functions was presented. The principle of the approach is that both electric circuits and chemical circuits can

be described by ordinary differential equations (ODEs), no matter what quantities the ODEs represent (e.g., voltages or concentrations). Based on this, an electric high-pass filter circuit was realized by a set of chemical reactions.

1.3.2 Digital & Analog Circuits via Synthetic Biology

A fundamental objective of synthetic biology is to control and engineer biochemical signaling pathways to build biological entities that are capable of carrying out desired computing tasks. The single input logic gates were synthesized to carry out simple computations, and these include the BUFFER gate [64] and the NOT gate [65], which are directly inspired by mechanisms of gene expression induced by activators and repressors, respectively. To expand the information processing ability, multi-input logic gates, including a 2/6-input AND gate [65, 66], 2/3/4-input NAND gate [67, 68], and 4/5-input OR gate [68], were also designed. The authors of [65] further optimized their designed multi-input logic gates with modularity (i.e., having exchangeable inputs and outputs to increase the reusability) and orthogonality (i.e., no crosstalk within the host cell to increase robustness and stability). For instance, the proposed 2-input AND gate in [65] can not only be rewired to different input sensors to drive various cellular responses but can also show the same functionality in different types of cells. It is noted that multiple logic gates can be combined to realize much more complicated cellular tasks, such as the multicellular biocomputing [64] and the edge detection algorithm [69].

Many synthetic analog circuits have also been proposed. One example is the wide-dynamic-range, positive-logarithm circuit [70], which consists of a positive-feedback component and a "shunt" component, demonstrating an $\ln(1+m)$ input-output transfer characteristic for a scaled input concentration m. A comprehensive review of 17 different analog circuits is provided in [71]. An intuitive way to understand the design of analog circuits is to interpret the synthetic process as tuning the behavior or response curve of a biological component. In particular, the Hill function that describes gene expression and regulation provides a semi-empirical approach to capturing the desired response curves [72]. For example, in [73], the parameters of the Hill function were optimized to tune the relationship between the temporal change of the output protein and the input transcription factor as close as possible to a hyperbolic tangent and a logarithmic function.

Integrating analog circuits with digital circuits is a strategy to achieve more complicated computations. A digitally controlled logarithm circuit was designed in [70], where a positive or negative logarithm circuit is connected to a digital switch.

This combined circuit achieves a positive or negative logarithm function in the presence of the input inducer, whereas it shuts OFF in the absence of the inducer.

1.3.3 Communication Functionality Realizations

Modulation and Demodulation Functionalities

Chemical circuits have been applied to implement modulation schemes, such as frequency shift keying (FSK), molecular shift keying (MoSK), and reaction shift keying (RSK). The realization of binary FSK (BFSK) demodulation was investigated in [74]. With two symbols encoded with different frequencies, the BFSK receiver consisted of two branches of enzymatic reaction circuits, which is analogous to the design of an electric BFSK decoder. The parameters of the two branches were carefully selected according to the transmitted symbols so that each symbol could only trigger one branch. For MoSK, the receiver architecture was presented in [75], where chemical reactions were exploited to determine if the sampled number of bounded signaling molecules exceeded a predefined level. For RSK, different chemical reactions were exploited for modulating transmission information into different signaling molecule emission patterns [76]. To demodulate RSK signals, the authors in [76] investigated two types of ligand-receptor-based chemical circuits and demonstrated the positive impact of feedback regulation on symbol error rate reduction. The amount of information transferred by chemical-reactions-based transceivers was quantified in [77], where optimal transmitter circuits that maximize the mutual information of the whole communication link were derived for four types of receiver circuits (i.e., ligand binding, degradation, catalytic, and regulation reactions).

An engineered bacteria-based biotransceiver architecture with modulation and demodulation functionalities was proposed in [78]. In this architecture, the transmitter employed a modulator to realize M-ary amplitude modulation, and was capable of generating a transmitted signal via a transmission filter; the receiver first processed a received signal via the receiver filter with the low-pass filtering characteristic to reduce noise and then used the demodulator to decode transmitted bit sequences.

Coding and Decoding Functionalities

Classic coding schemes have been studied for MC to improve the reliability of communication links. A uniform molecular low-density parity-check (LDPC) decoder to retrieve transmitted information from received signals was designed in [79] with chemical reactions. To execute the belief-propagation algorithm, a chemical oscillator

was introduced to schedule the iterative message passing and trigger corresponding computations in each phase. The proposed LDPC decoder design is flexible and can deal with arbitrary code lengths, code rates, and node degrees.

A transceiver design with single parity-check (SPC) encoding and decoding functionalities was developed in [73] using both chemical circuits and genetic circuits. The proposed transmitter is able to generate a parity check bit and modulate the corresponding codeword with concentration shift keying (CSK), and the proposed receiver acts as a soft analog decoder that calculates the a-posteriori log-likelihood ratio of received noisy signals to retrieve transmitted bits. During the aforementioned processes, chemical reactions are used to realize degradation, subtraction, and storage, while engineered gene expression processes are employed to implement some complicated operations, such as amplification, the hyperbolic tangent function, and the logarithm function.

1.4 Contributions

From the description of the existing circuits review, although the digital and analog circuits realized either by chemical reactions or synthetic biology provide the communication community with novel tools for processing chemical signals, the design of MC circuits with communication functions has been less explored. Therefore, this dissertation focuses on the design and analysis of signal processing circuits to realize communication functionalities for MC. In particular, this dissertation presents the integration of chemical reactions and microfluidic devices to develop chemical-reactions-based microfluidic circuits. A microfluidic device processes and manipulates small amounts of fluids using channels in dimensions of tens to hundreds of micrometers (i.e., 10^{-9}∼10^{-18} liters), providing the benefits including rapid analysis, high performance, design flexibility, and reagent economy [80]. As discussed in Section 1.2, previous studies have demonstrated the utility of microfluidic devices for microscale experimental platforms to flexibly manipulate and control molecular transport to realize MC functionalities [32–34, 38], which proves their potential as a tool that offers unprecedented solutions for practical application, e.g., biosensing and therapeutics [4]. Thus, we apply and regulate chemical reactions in different regions of a microfluidic device and provide the design and analysis of chemical-reactions-based microfluidic circuits with binary CSK (BCSK) and quadruple CSK (QCSK) functions. In addition, this dissertation also presents the design and analysis of a multicellular system with a controllable pulse

generation function. The specific contributions of this dissertation are summarized as follows:

- **Chemical-Reactions-based Microfluidic BCSK Realization:** The microfluidic circuits with BCSK modulation and demodulation functions are proposed. For the BCSK transmitter, the modulation is achieved via three chemical reactions that are inspired by the incoherent type 1 feed-forward loop. For the BCSK receiver, the demodulation is realized via two chemical reactions, i.e., a thresholding reaction and an amplifying reaction. The dynamics of molecular species in microfluidic channels, i.e., the spatial-temporal concentration distribution, are mathematically modeled and derived. Based on this, a reaction channel length optimization framework is provided to guide how to tune the maximum concentration of a transmitted pulse. To ensure a continuous transmission of non-distorted pulses, the restriction on the time gap between two consecutive input signals is also derived.

- **Chemical-Reactions-based Microfluidic QCSK Realization:** To facilitate digital microfluidic circuit design, a five-level architecture to describe a microfluidic circuit is proposed. The microfluidic designs of AND, NAND, OR, NOR, XOR, and Exclusive NOR (XNOR) logic gates are presented and then employed to achieve QCSK modulation and demodulation. To characterize the proposed microfluidic circuits, a novel mathematical framework is developed. This framework is scalable with the increase in the number of microfluidic circuits and thus can be applied to analyze other new and more complicated microfluidic circuits.

- **Genetic Circuit with Controllable Pulse Generation:** A new pulse generation system is proposed based on three engineered cells with different digital logic processing capabilities. The design of the proposed multicellular system adopts the divide-and-conquer strategy, i.e., packaging signal processing modules into different cells and wiring them together via intercellular signaling pathways, which can achieve stability, programmability, and ultimately computational complexity at the cell consortium level. Unlike the genetic circuits proposed in the MC field, all the species and the gene interactions of the proposed system are explicitly specified in the synthetic biology domain, which realizes the communication engineering design via synthetic biology tools. The Shea-Ackers formalism is adopted to model the individual behavior of each cell. The response of the intercellular

signaling propagation channel that supports cell-to-cell communication is also derived.

1.5 Outline of the Dissertation

This dissertation is organized into seven chapters, namely the introduction, a chapter reviewing some fundamentals of MC systems, a chapter deriving the basic fluid characterizations and proposing a circuit architecture for microfluidic systems, three technical contribution chapters, a conclusion chapter, and four appendices. In the following, we briefly outline the contents of the chapters and appendices and provide a graphical summary of the chapters in Fig. 1.6 on page 42.

Chapter 2 - Fundamentals of MC Systems: In this chapter, the basics and preliminaries of MC systems are introduced. In particular, the release, propagation, and reception of signaling molecules are mathematically described, which lays the theoretical foundation for subsequent chapters. Furthermore, various modulation schemes are briefly introduced.

Chapter 3 - Preliminaries of Chemical-Reactions-based Microfluidic Circuits: In this chapter, the basic characteristics of fluids in microfluidic channels are first presented. In particular, the velocity profile of microfluidics and its impact on concentration distribution are discussed. Subsequently, the concentration and velocity changes for microchannel networks are derived. Furthermore, this chapter presents a novel five-level architecture for microfluidic circuits with an introduction of some new microfluidic logic gate designs, which provide a tool for the subsequent QCSK transceiver design.

Chapter 4 - Chemical-Reactions-based Microfluidic BCSK Realization: In this chapter, a microfluidic BCSK transmitter design is first presented, which is capable of generating predefined pulse-shaped molecular concentrations upon rectangular triggering signals. A further microfluidic BCSK receiver is designed to demodulate a received signal to a rectangular output signal. To reveal design insights, the theoretical signal responses for the proposed BCSK transceiver are derived, which further facilitates the BCSK transmitter design optimization. Finally, numerical results are reported and conclusions are drawn.

Chapter 5 - Chemical-Reactions-based Microfluidic QCSK Realization: In this chapter, the designs of the microfluidic transmitter and receiver with QCSK modulation and demodulation functionalities are proposed. First, the AND gate design proposed in Chapter 3 is optimized and then applied to both the QCSK transmitter and receiver. Moreover, this chapter also establishes a novel mathematical framework to theoretically

characterize the proposed microfluidic circuits. Finally, numerical results are reported and conclusions are drawn.

Chapter 7 - Genetic Circuit with Controllable Pulse Generation: In this chapter, a synthetic biology system capable of generating a pulse-shaped signal is proposed. As the proposed system packages the pulse generation function into different minimal cells and wires them with intercellular signaling, the designs of these synthetic minimal cells are first introduced. To quantitatively describe the generated pulse, the individual behavior of each minimal cell is modeled using Shea-Ackers formalism and the intercellular signaling channel is derived. Finally, numerical results are reported and conclusions are drawn.

Chapter 8 - Conclusions and Future Research Topics: This chapter provides a summary of the main contributions and findings of this dissertation. Then, future research topics and some open problems are identified.

Appendix A: This appendix contains proofs of the theorems given in Chapter 4.

Appendix B: This appendix contains proofs of one theorem and one lemma given in Chapter 5.

Appendix C: This appendix contains proofs of the lemmas and one corollary given in Chapter 6.

Appendix D: This appendix summarizes the biological terms that appear throughout the dissertation.

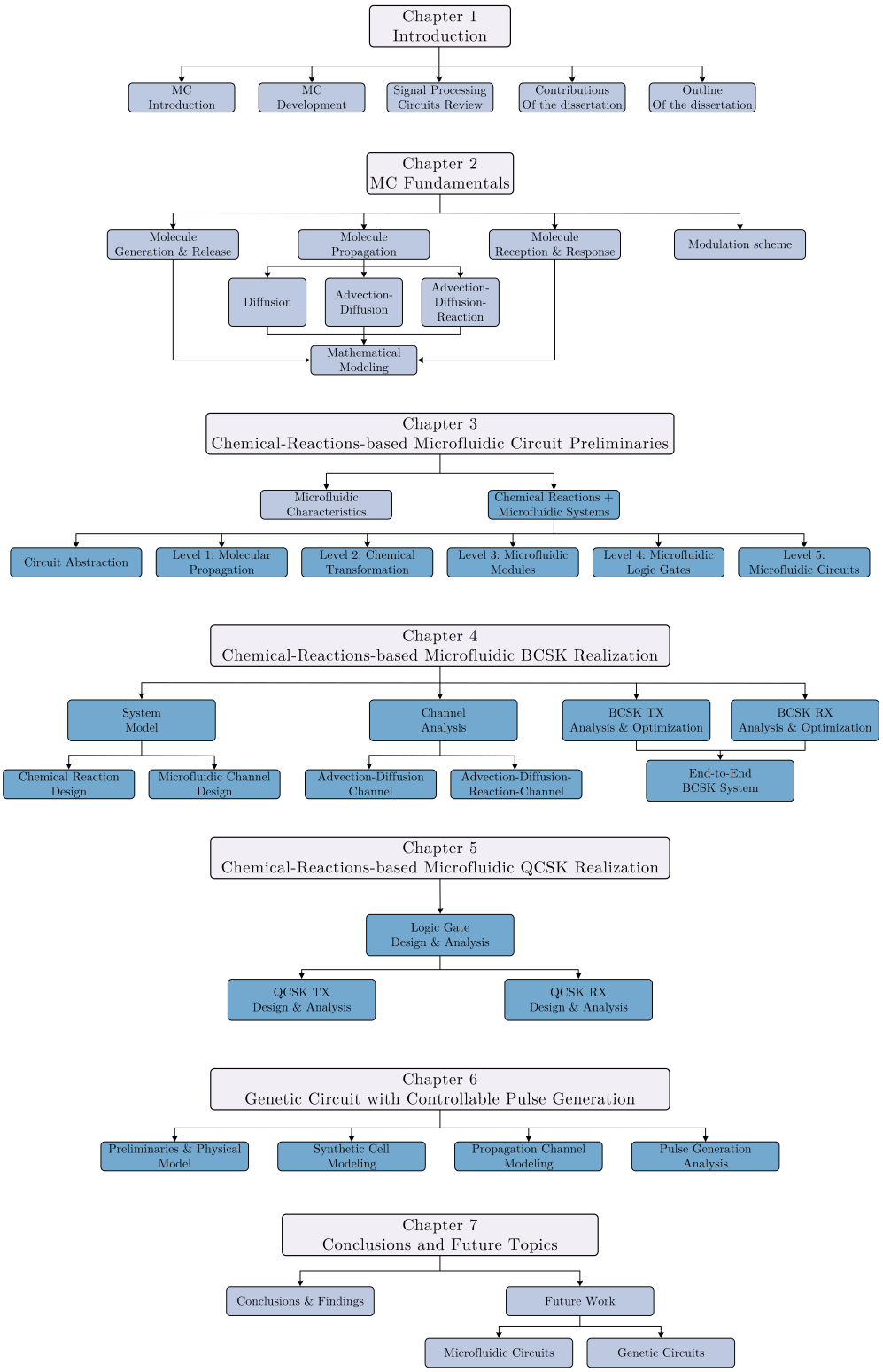

Fig. 1.6 Organization and contents of chapters of this dissertation. The blocks with the blue-colored backgrounds are the main contributions of the dissertation.

Chapter 2

Fundamentals of MC Systems

From the neuron communication example shown in Fig. 1.1, it is clear that the physical mechanisms of an MC system include: 1) molecule release (e.g., neurotransmitter release at presynaptic neuron), 2) molecule propagation (e.g., neurotransmitter diffusion over synaptic cleft), and 3) molecule reception (e.g., neurotransmitter reception at postsynaptic neuron). This chapter further describes these three processes. In particular, the molecule propagation processes presented in this chapter are all diffusion-based phenomena because they are prevalent at the microscale and they have received significant attention within the MC engineering community. Furthermore, this chapter includes the underlying partial differential equation (PDE) descriptions for diffusion-based propagation, which integrate with the initial conditions (ICs) and boundary conditions (BCs) imposed by molecule release, propagation, and reception to determine the corresponding channel response, see Fig. 2.1. These mathematical descriptions lay the theoretical analysis foundation for subsequent chapters. In addition, some modulation schemes are also discussed.

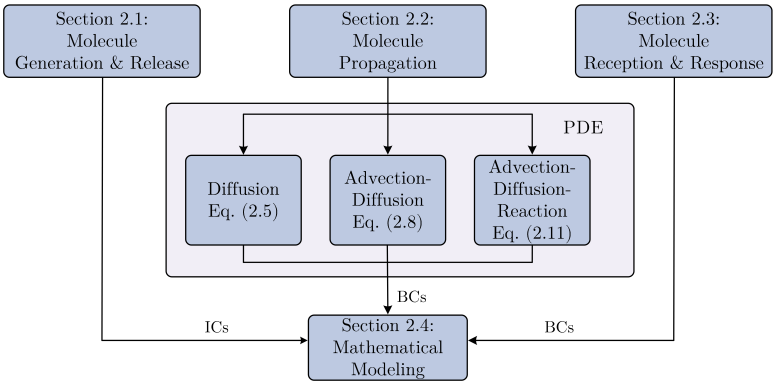

Fig. 2.1 Overview of the modeling of an MC system.

2.1 Molecule Generation and Release Management

The transmitter in an MC system needs to be able to generate and release a molecular signal. These molecules may be harvested from within the transmitter or its surrounding environment, or synthesized from its constituent components. If the molecules do not need to be released as soon as they are ready, then the transmitter also needs a mechanism for storing the molecules until they are needed. For example, Ca^{2+} ions stored in the endoplasmic reticulum (ER) are released via Ca^{2+} gates to restore the cytosolic ion concentration when it is depleted [81].

A common technique for storing molecules within eukaryotic cells, either for transportation or until the stored molecules are needed, is within vesicles. Vesicles are usually spherical or near-spherical shapes that are composed of a lipid bilayer. Thus, they can securely hold many types of molecules, e.g., proteins, neurotransmitters, or even invading bacteria. Vesicles can vary in size from about 50 nm (synaptic vesicles) to several microns in diameter [82], and even smaller vesicles can contain many thousands of molecules. To empty their contents, vesicles merge with another bilayer (such as a cell's plasma membrane) and release their molecules onto the other side of the other bilayer (e.g., outside the cell as shown in Fig. 1.2b) via exocytosis. Thus, molecules can be directly released from an intracellular vesicle into the extracellular space, which can occur very quickly; synaptic vesicles released by neurons can empty their contents within about a millisecond or less [83].

While many transport vesicles are produced at a cell's Golgi apparatus, processes that rely on rapid and precise vesicle release can fabricate them locally [2, Ch. 13]. For example, synaptic vesicles are produced locally from budding at the plasma membrane to help ensure a steady supply. No matter where they are produced, vesicles are generally too large to efficiently move by diffusion alone. So, they are carried along cytoskeletal fibers by motor proteins. Proteins that "coat" the outside of a vesicle are used to identify its intended destination so that it can bind to a suitable molecular motor. For example, a vesicle could be intended for an endosome instead of the plasma membrane. Additional surface proteins are used to control both vesicle docking and fusion once it has reached its target.

A key advantage of using vesicles is the precise regulation that is provided for molecule release, since particular proteins need to be available and in the correct state for a vesicle to be transported, docked, and fused with the destination membrane. However, vesicles in the constitutive exocytosis pathway are used for immediate uncontrolled release of their contents when fusing with the plasma membrane [2, Ch. 13]. These provide materials to grow a plasma membrane, but can also carry proteins for secretion

Table 2.1 Summary of Physical Signal Propagation.

Propagation Mechanism	Example	Speed	Reference
Diffusion-Based Propagation	Calcium ions	Diffusion coefficient: $7 - 12 \times 10^{-11}$ m^2/s	[87]
	Pheromones	Diffusion coefficient: $0.1 - 1.06 \times 10^{-9}$ m^2/s	[88]
	lac repressor protein	Diffusion coefficient: $10^{-14} - 5 \times 10^{-12}$ m^2/s	[89]
Advection-Diffusion -Based Propagation	Human skin capillary	Mean velocity: $3.5^{-4} - 9.5 \times 10^{-4}$m/s	[90]
Advection-Diffusion -Reaction-Based Propagation	Antibody-antigen interaction	Diffusion coefficient: $\approx 10^{-10}$ m^2/s	[91]

to outside the cell. In this pathway, proteins can be secreted as fast as they are produced; the only delay is in transport. In other cases, released molecules can bypass vesicle pathways entirely if they are able to directly pass through the plasma membrane [2, Ch. 11]. This is true for small uncharged or weakly polar molecules, e.g., nitric oxide, or molecules that have dedicated transmembrane channels, e.g., the common ions sodium, potassium, and calcium.

As noted, MC models typically treat molecule generation and release as instantaneous processes, or at least as steps that take negligible time relative to molecule propagation across the channel of interest [40, 44]. Exceptions include [84, 85], which have modeled transmitter molecule release with chemical reaction kinetics. The authors of [86] modeled the impact of vesicle preparation and release on the information capacity in a chemical neuronal synapse.

2.2 Physical Signal Propagation

A fundamental characteristic of any communication network is how information propagates between the devices. In this section, the diffusion-based means is discussed and mathematically described. A summary of the propagation mechanisms, including representative molecules for each mechanism, is provided in Table 2.1.

2.2.1 Diffusion-Based Propagation

Diffusion refers to the random walk, namely Brownian motion, of molecules in a medium arising from the molecules' thermal energy [92]. It is a simple and efficient movement

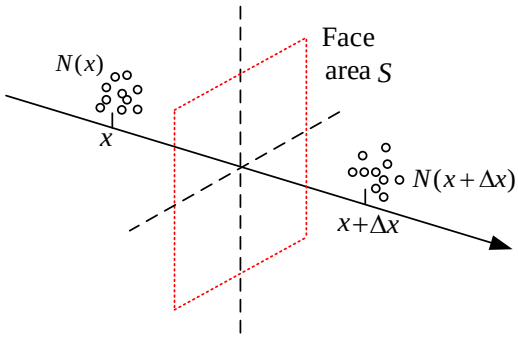

Fig. 2.2 A macroscopic one dimensional (1D) random walk model where the small circles represent molecules and move along the x-axis. The dotted red square is in the plane that is orthogonal to the x-axis.

paradigm without a need for infrastructure or external energy sources. Therefore, there are many examples found in nature, including calcium signaling among cells [93], pheromonal communication among animals [94], and propagation of DNA binding molecules over a DNA segment [95].

The mathematics of Brownian motion are often modeled using Fick's laws of diffusion. As a conceptual example, it is useful to describe Fick's first law of diffusion from first principles using the macroscopic approach presented in [95, Ch. 2]. Let us consider the simplified case shown in Fig. 2.2, where molecules move one step at a time along only one axis with a displacement step Δx and a time step ΔT. It is assumed that each molecule walks independently and the probabilities of moving forward and backward are both 1/2. Let $N(x)$ denote the number of molecules at position x and time t. During the time interval $[t, t+\Delta T]$, we expect that half of the molecules at x will move to $x+\Delta x$ and traverse the normal face that is orthogonal to the axis and located at $(x+\Delta x)/2$. At the same time, it is expected that half of the molecules at $x+\Delta x$ will cross the face in the opposite direction. Hence, the net *expected* number of molecules coming to $x+\Delta x$ will be $\frac{1}{2}[N(x)-N(x+\Delta x)]$. Dividing by the face area S and time step ΔT, the net flux J_{Diff} crossing the face by diffusion is

$$J_{\text{Diff}}\Big|_{\text{1D}} = -\frac{1}{2\Delta T}\frac{[N(x+\Delta x)-N(x)]}{S}. \tag{2.1}$$

If we further multiply the right-hand side of (2.1) by $\Delta x^2/\Delta x^2$, then it becomes

$$\begin{aligned} J_{\text{Diff}}\Big|_{\text{1D}} &= -\frac{1}{\Delta x}\frac{\Delta x^2}{2\Delta T}\frac{[N(x+\Delta x)-N(x)]}{S\Delta x} \\ &= -\frac{1}{\Delta x}\frac{\Delta x^2}{2\Delta T}[C(x+\Delta x)-C(x)], \end{aligned} \tag{2.2}$$

where $C(x+\Delta x) = N(x+\Delta x)/(S\Delta x)$ and $C(x) = N(x)/(S\Delta x)$ are the molecular concentrations at locations $x+\Delta x$ and x, respectively. By considering $\Delta x \to 0$ and defining the *diffusion coefficient* $D = \Delta x^2/(2\Delta T)$, we arrive at Fick's first law in 1D sapce [95, eq. (2.1)], i.e.,

$$J_{\text{Diff}}\Big|_{\text{1D}} = -D\frac{\partial C(x,t)}{\partial x}. \tag{2.3}$$

Correspondingly, Fick's first law in three-dimensional (3D) space is

$$J_{\text{Diff}}\Big|_{\text{3D}} = -D\nabla C(\mathbf{d},t), \tag{2.4}$$

where ∇ is the Nabla operator and vector $\mathbf{d} = [x, y, z]$ specifies the molecule position.

Fick's first law describes the relationship between the diffusion flux and the concentration gradient. The value of the diffusion coefficient D determines how fast a certain type of molecule moves. In general, D is dependent upon the environment (e.g., temperature, viscosity) as well as the molecule size and shape. For example, in a given environment, smaller molecules tend to diffuse faster. However, even when a molecule's diffusion coefficient is on the order of $1000\,\mu\text{m}^2/\text{s}$ (a relatively large value), it is estimated that it would take nearly half a millisecond for such a molecule to travel over $1\,\mu$m (the width of a bacterium) [95], demonstrating that diffusion alone is quite a slow process.

The impact of diffusion on concentration change with respect to time can be described by Fick's second law as [95, eq. (2.5)]

$$\frac{\partial C(\mathbf{d},t)}{\partial t} = D\nabla^2 C(\mathbf{d},t), \tag{2.5}$$

where ∇^2 is the Laplace operator. Solutions to (2.5) can be obtained under different initial and boundary conditions, depending on the diffusion environment. We discuss examples of initial and boundary conditions in greater detail in Section 2.4.

2.2.2 Advection-Diffusion-Based Propagation

The diffusion process can be accelerated by introducing additional phenomena. In particular, molecule transport can be assisted by two physical mechanisms: 1) force-induced drift, and 2) advection, i.e., bulk flow. Force-induced drift is caused by applying an external force directly to the particles rather than the fluid containing them. Examples include applying a magnetic field to magnetic nanoparticles, an electrical field to charged particles, and a gravitational force to particles with sufficient

mass [40]. Advection refers to molecule transport assisted by bulk movement of the entire fluid, including the molecules of interest. Examples include endocrine signaling in blood vessels and the manipulation of fluids in microfluidic channels. Here, we focus on advection, and in the following, we present a mathematical framework to approximate molecular transport assisted by advection.

Analogous to diffusion, the advection process also results in a flux of concentration crossing the surface of a given region. It has been shown that the concentration flux caused by advection is simply a concentration shift over time; thus the flux J_{Adv} with *local* velocity $\mathbf{u}$ can be described by [96]

$$J_{\text{Adv}} = \mathbf{u}C. \tag{2.6}$$

The temporal change in concentration is jointly determined by the diffusion flux and the advection flux, and can be expressed as [97, eq. (4.3)]

$$\frac{\partial}{\partial t}\int_V C dV = -\int_S (J_{\text{Diff}} + J_{\text{Adv}}) \cdot \mathbf{n} \mathrm{d}S, \tag{2.7}$$

where V is the volume of a given region with differential element dV, S is the surface of the volume with differential element dS, and $\mathbf{n}$ is a unit outward normal vector. Substituting (2.4) and (2.6) into (2.7), and applying the divergence theorem, we obtain the advection-diffusion equation in differential form as [98]

$$\frac{\partial C(\mathbf{d}, t)}{\partial t} = D\nabla^2 C(\mathbf{d}, t) - \mathbf{u} \cdot \nabla C(\mathbf{d}, t). \tag{2.8}$$

2.2.3 Advection-Diffusion-Reaction-Based Propagation

In addition to the diffusion and advection processes, chemical reactions often occur simultaneously during molecular movement. Examples include the polymerase chain reaction (for synthetically copying DNA [99]) and surface capture [91, 100]. To analyze molecular transport under chemical reactions, we consider the example of a second-order (bimolecular) reaction $S_i + S_j \xrightarrow{k_f} S_k$, where species S_i reacts with species S_j to generate product S_k under the rate constant k_f.[1] If molecular transport is subjected to diffusion and reaction, then the concentration changes of the reactant S_i (analogously

[1]Reactions may proceed in forward or reverse directions, which are characterized by forward and reverse reaction rates, respectively. Within the scope of this dissertation, we assume unbalanced reactions where the forward reaction rate is much greater than the reverse rate.

S_j) and the product S_k can be expressed as

$$\frac{\partial C_{S_i}(\mathbf{d},t)}{\partial t} = D\nabla^2 C_{S_i}(\mathbf{d},t) - k_f C_{S_i}(\mathbf{d},t) C_{S_j}(\mathbf{d},t), \tag{2.9a}$$

$$\frac{\partial C_{S_k}(\mathbf{d},t)}{\partial t} = D\nabla^2 C_{S_k}(\mathbf{d},t) + k_f C_{S_i}(\mathbf{d},t) C_{S_j}(\mathbf{d},t). \tag{2.9b}$$

From (2.9a) and (2.9b), a general diffusion-reaction equation is given by [40]

$$\frac{\partial C_{S_{i/k}}(\mathbf{d},t)}{\partial t} = D\nabla^2 C_{S_{i/k}} + qf[k_f, C_{S_i}(\mathbf{d},t)], \tag{2.10}$$

where $q = -1$ holds for reactants, $q = 1$ holds for products, and $f[\cdot]$ is the reaction term which in general can account for the presence of multiple reactions. Furthermore, if molecular propagation is simultaneously governed by advection, diffusion, and chemical reaction, then the spatial-temporal concentration distribution can be expressed by the following advection-diffusion-reaction equation [40]

$$\frac{\partial C_{S_{i/k}}(\mathbf{d},t)}{\partial t} = D\nabla^2 C_{S_{i/k}}(\mathbf{d},t) - \mathbf{u}\cdot\nabla C_{S_i}(\mathbf{d},t) + qf[k_f, C_{S_i}(\mathbf{d},t)]. \tag{2.11}$$

With certain initial and boundary conditions, the expected time-varying concentration of each type of molecule can be derived. Some analytical solutions of the 1D form of (2.11) can be found in [101].

2.3 Molecule Reception and Responses

The receiver in an MC system needs to be able to detect and respond to a molecular signal. Depending on the type of received molecule and the receiver's sensitivity, some threshold signal quantity may need to be observed in order to stimulate a corresponding response.

2.3.1 Molecule Reception

In cells, extracellular signal molecules generally fall into one of two families: 1) molecules that are small or hydrophobic enough to easily cross the receiver cell membrane, and 2) molecules that are too large or too hydrophilic to cross the receiver cell membrane, as summarized in Table 2.2. The first family of molecules can directly pass the cell membrane to activate intracellular enzymes or bind to intracellular receptor proteins, while the second family of molecules relies on receptors at the surface of the target

Table 2.2 Summary of Reception Mechanism.

Reception Type		Example
Reception Site	Receptor Protein	
Intracellular reception: Molecules can cross cell membrane	Intracellular enzyme	Dissolved gases
	Intracellular receptor	Cortisol, estradiol, testosterone
Surface reception: Molecules cannot cross cell membrane	Ion-channel-coupled receptor	Acetylcholine, glycine, γ-aminobutyric acid, ions
	G-protein-coupled receptor	Neurotransmitters, local mediators, hormones
	Enzyme-coupled receptor	Insulin, nerve growth factor

cell to relay their messages across the cell membrane [2, Ch. 11]. In the MC literature, these two reception paradigms are usually referred to as passive reception and active reception, respectively [3].

Dissolved gases and steroid hormones are representatives of the first family [2, Ch. 15]. Most dissolved gases can cross the plasma membrane and enter the cell interior to directly activate intracellular enzymes. For example, smooth muscle relaxation in a blood vessel wall can be triggered by Nitric Oxide (NO). Unlike molecules that directly activate intracellular enzymes, the detection of steroid hormones (such as cortisol, estradiol, and thyroxine) relies on intracellular receptors. All of these molecules cross the plasma membrane of the target cell and bind to their protein receptors distributed either in the *cytosol* (i.e., the liquid inside the cell) or the nucleus to regulate gene expression.

The vast majority of extracellular signal molecules belong to the second family. They are either too large or hydrophilic to cross the plasma membrane, so their detection requires the use of surface receptor proteins; see Fig. 2.3. According to their biochemical signaling pathways, the surface-binding receptors can be further classified into three classes: ion-channel-coupled receptors, G-protein-coupled receptors, and enzyme-coupled receptors [2, Ch. 15].

- Ion-channel-coupled receptors are prevalent in the nervous system and other electrically excitable cells. This kind of receptor binds with ion molecules and can transduce changes in ion concentrations into changes in membrane potential.
- G-protein-coupled receptors associate with a G protein in the cytosolic domain. Once extracellular signal molecules are bound to G-protein-coupled receptors, these receptors are able to activate membrane-bound, GTP-binding proteins

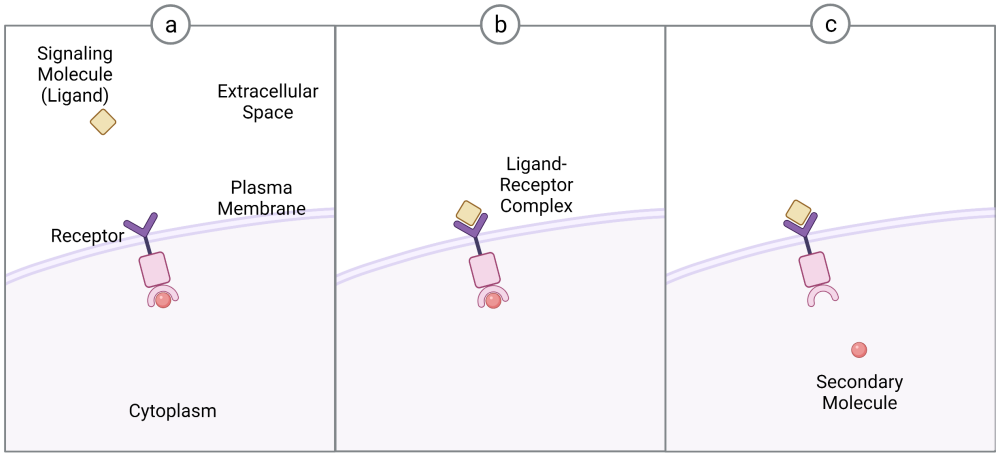

Fig. 2.3 Steps of a generic molecule reception process. (a) There is a receptor embedded in the plasma membrane that separates a cell's cytoplasm from the extracellular space. The receptor can bind to a ligand, which in this case is the signaling molecule of interest. (b) The ligand binds to the receptor to form a ligand-receptor complex. This instigates a conformational change in the receptor. (c) The conformational change leads to a response, e.g., the release of an internal secondary signaling molecule as shown.

(G proteins), which then turn on or off an enzyme or ion channel on the same membrane and finally alter a cell's behavior [102, 103]. Examples of this type of reception include the transduction of a heartbeat slowdown signal for heart muscle cells, a glycogen breakdown signal for the liver, and a contraction signal for smooth muscle cells. A recent review of G-proteins can be found in [104].

- The cytoplasmic domain of enzyme-coupled receptors either acts on an enzyme itself or associates with another protein to form an enzyme once signaling molecules bind to the outer surface of the plasma membrane. Enzyme-coupled receptors play a significant role in the response to the growth factor molecules that regulate cell growth, proliferation, differentiation, and survival.

2.3.2 Reception Responses

There is a broad diversity in how biochemical receptors respond to molecular signals, and even receptors sensitive to the same kind of signaling molecule can behave differently in different cells [2, Ch. 15]. For example, responses to acetylcholine include decreasing the firing of action potentials, stimulating muscle contraction, and stimulating saliva production. Another example is calcium signaling. The same stimulus can trigger a

Ca^{2+} wave across one cell, local calcium oscillations in another cell, or cause only a localized increase in the concentration in yet another cell [105]. The different responses are due to the ability of Ca^{2+} to bind to a large variety of different proteins. Thus, the same signal activates different signaling pathways depending on the cell type and the available proteins.

The diversity in biochemical responses means that a given type of receptor (or a collection of coupled receptors along a pathway) has several distinguishing properties [2, Ch. 15]. The *timing* of responses can vary by many orders of magnitude, from milliseconds for muscle control and other synaptic responses [106, 107], to seconds for bacteria using chemotaxis to respond to chemical gradient changes [95], to hours or even days for changes in the behavior or fate of a cell (e.g., gene regulation, differentiation, or cell death). Correspondingly, the *persistence* of a response could be very brief (as is usually needed in synapses) or even permanent. *Sensitivity* to a signal can be controlled by the number of receptors present or by the strength of a secondary signal created by an activated receptor. Similarly, a biochemical system's *dynamic range* specifies its responsiveness over a range of molecular signal strengths. More complex responses can be achieved using biochemical *signal processing*, e.g., applying feedback to implement switches and oscillators. Some responses are controlled by the *integration* of multiple molecular signals, which we can study with a mathematical understanding of local data abstraction. Conversely, a single molecular signal can *coordinate multiple responses* simultaneously within the same cell, e.g., to stimulate both growth and cell division.

2.4 Mathematical Modeling of Emission, Propagation, and Reception

The release and reception processes can be mathematically modeled by defining ICs and BCs for the propagation equations, such as those discussed for diffusion in Section 2.2. In this way, the spatial-temporal concentration distribution can be obtained by solving the PDEs that describe propagation channels with ICs and BCs. In other words, the release strategy, propagation channel, and reception mechanism jointly determine the channel response and the observed signal. The recent survey [40] summarized channel impulse responses (CIRs) under different models for the transmitter, physical channel, and receiver, where the CIR was formally defined as the *probability of observation* of one output molecule at the receiver when one molecule is impulsively released at a transmitter. It is noted that although the CIR definition implies the impulsive release of signaling molecules, the transmitter geometry, and molecular generation method

Table 2.3 Comparison of Diffusion-based Propagation Mechanisms.

Release Strategy		Propagation Environment			Reception Mechanism		Channel Response
TX	IC	Boundary	Equation	BC	RX Type	BC	
Point	IC_1	Unbounded	Eq. (3)	BC_2	N/A	N/A	[95, Eq. (2.8)]
					Spherical fully absorbing	BC_4	[15, Eq. (22)]
					Reversible absorbing	BC_3	[16, Eq. (8)]
		Spherical bounded		BC_1	Spherical fully absorbing	BC_4	[108, Eq. (13)]
		Rectangular bounded			Fully absorbing walls	BC_4	[109, Eq. (19)]
		Rectangular/Circular bounded		BC_1, BC_2	N/A	N/A	[110, Eq. (14.4.4), (14.13.7)]
		Unbounded	Eq. (6)	BC_1			[111, Eq. (18)]
		Cylindrical bounded					[112, Eq. (11)]
		Unbounded	Eq. (12)	BC_2	Reversible absorbing	BC_3	[17, Eq. (23)]
					Passive receiver		[14, Eq. (9)]
					Partially absorbing	BC_3	[113, Eq. (16), (17), (29), (30)]
			Eq. (13)		N/A	N/A	[114, Eq. (8)]
Volume	IC_2	Unbounded	Eq. (3)	BC_1	Passive & active receiver	BC_4	[115, Eq. (12)]

still affect the CIR. Unlike [40], here the focus is on the mathematical formulation of specific (mostly ideal) conditions so that the ICs and BCs can be mapped to the discussions in Sections 2.1 and 2.3. With these conditions, a brief summary of some known channel responses is provided in Table 2.3.

2.4.1 ICs on Release Strategies

As stated earlier, the simplest scenario is that N_{TX} molecules are released from a point in an impulsive manner at time t_0, so the IC can be expressed as

$$\mathrm{IC}_1 : C(\mathbf{d}, t_0) = N_{\mathrm{TX}} \delta(\mathbf{d} - \mathbf{d}_{\mathrm{TX}}), \tag{2.12}$$

where $\delta(\cdot)$ is the Kronecker delta function and $\mathbf{d}_{\mathrm{TX}}$ is the location of the release point.

Although the point transmitter has been widely used in MC research, it is quite idealized. Another idealized transmitter is the volume transmitter, which occupies physical space and its surface does not impede molecular movement. Signaling molecules are released from a releasing space $\tilde{\mathcal{V}}_{\mathrm{TX}}$ or a releasing surface $\tilde{\mathcal{S}}_{\mathrm{TX}}$ of the volume transmitter. Therefore, a volume transmitter can be regarded as a superposition of many point transmitters that are located at different positions, and the corresponding IC can be expressed by extending (2.12) as follows:

$$\mathrm{IC}_2 : \int_{\mathbf{d}_{\mathrm{TX}} \in \tilde{\mathcal{V}}_{\mathrm{TX}}} N_{\mathrm{TX}} \delta(\mathbf{d} - \mathbf{d}_{\mathrm{TX}}) \mathrm{d}V \text{ or } \int_{\mathbf{d}_{\mathrm{TX}} \in \tilde{\mathcal{S}}_{\mathrm{TX}}} N_{\mathrm{TX}} \delta(\mathbf{d} - \mathbf{d}_{\mathrm{TX}}) \mathrm{d}S, \tag{2.13}$$

where $\mathbf{d}_{\mathrm{TX}}$ is a location within the releasing volume $\tilde{\mathcal{V}}_{\mathrm{TX}}$ or on the releasing surface $\tilde{\mathcal{S}}_{\mathrm{TX}}$. We note that (2.13) can also describe the molecule release from an ion-channel-based transmitter if it has many open ion channels [40].

2.4.2 BCs on Propagation Channels

An unbounded environment is a common assumption to simplify the derivation of the channel response. However, in practice, the molecular propagation medium is often much more complex. Molecular propagation can be constrained by various boundaries, such as the tunnel-like structure of a blood vessel, the oval shape of liver cells, and the rectangular geometry of plant cells. A bounded medium can provide molecules with the guided transmission, limits dispersion, and can have beneficial effects for long-range communication. The boundaries of a constrained medium are often assumed to be reflective, and the corresponding BC is given as

$$\mathrm{BC}_1 : \left.\frac{\partial C(\mathbf{d},t)}{\partial d_i}\right|_{d_i=d_b} = 0, \tag{2.14}$$

where $d_i \in [x, y, z]$ is an element of the position vector $\mathbf{d}$ and d_b is the position of the propagation boundary along direction d_i.

In addition, for both unbounded and bounded environments, the concentration at locations sufficiently far away from the releasing source is usually assumed to be zero, which can be mathematically described as

$$\mathrm{BC}_2 : C(\|\mathbf{d}\| \to \infty, t) = 0. \tag{2.15}$$

2.4.3 BCs on Reception Mechanisms

As stated earlier, the two conventional paradigms for molecule reception in the MC literature are active and passive, where molecules do and do not participate in chemical reactions at the receiver, respectively. If a receiver is passive, then molecules are transparently observed by the receiver without disturbing their propagation. If the receiver is active, then the molecules are usually detected by surface receptors via absorption. However, if molecules can be *adsorbed* (i.e., "stick" to the surface) instead of just be *absorbed* (i.e., removed from the surface), then it is also possible that the receiver is capable of desorbing the molecules that were previously adsorbed. This type of receiver can be called a reversible adsorption receiver and examples include the reception of hormones and neurotransmitters [116]. The corresponding BC is given as [117]

$$\mathrm{BC}_3 : D\left.\frac{\partial C(\mathbf{d},t)}{\partial \mathbf{d}}\right|_{\mathbf{d}\in\tilde{\mathcal{S}}_{\mathrm{RX}}} = k_1 C(\mathbf{d} \in \tilde{\mathcal{S}}_{\mathrm{RX}}, t) - k_{-1} C_a(t). \tag{2.16}$$

where k_1 is the adsorption rate, k_{-1} is the desorption rate, $\tilde{\mathcal{S}}_{\mathrm{RX}}$ is the adsorbing surface of the receiver, and $C_a(t)$ is the average adsorbed concentration on the receiver surface at time t. We note that BC_3 in (2.16) is a general formulation and can be reduced to relevant special cases as follows. When $k_1 \to \infty$ and $k_{-1} = 0$, i.e., every collision leads to *absorption* and there can be no desorption, then the receiver becomes a fully absorbing receiver, and BC_3 in (2.16) reduces to [15]

$$\mathrm{BC}_4 : C(\mathbf{d} \in \tilde{\mathcal{S}}_{\mathrm{RX}}, t) = 0. \tag{2.17}$$

When k_1 is a non-zero finite constant and $k_{-1} = 0$, then the receiver becomes a partially absorbing receiver [16].

We note that the aforementioned ICs and BCs are very general, and one type of IC or BC can be represented in various forms. The reason for this is that the different models can be expressed in terms of different coordinate systems, e.g., Cartesian coordinates, cylindrical coordinates, and spherical coordinates, as appropriate for a given MC environment. For example, cylindrical coordinates are preferred in scenarios that have some rotational symmetry about the longitudinal axis, such as a circular duct channel.

2.5 Modulation Schemes

In MC systems, there are various ways to encode information into physical signals, i.e., modulation. The most widely used scheme is CSK which employs varying concentration levels (or molecule numbers) to encode information. For the BCSK case, an MC transmitter releases a certain number of molecules to send a bit-0, and a higher number of molecules to send a bit-1. When zero molecules are released to send a bit-0, then BCSK is also known as OOK. Clearly, the CSK modulation is analogous to the amplitude shift keying (ASK) modulation in wireless communication systems. The modulation can also be achieved by exploiting the type of chemical molecules, and this technique is named as MoSK. In addition, information can be encoded into the release time of molecules. A graphical summary of the above modulation schemes is provided in Fig. 2.4 on the next page. For more information on modulation, the readers can refer to [42].

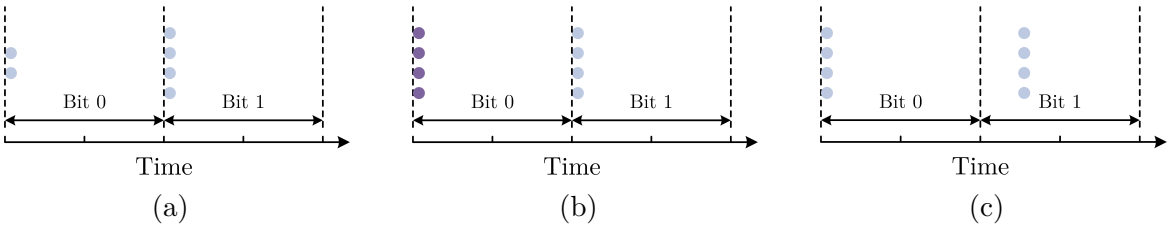

Fig. 2.4 An illustration of (a) concentration shift keying, (b) molecular type shift keying, and (c) release time shift keying.

Chapter 3

Preliminaries of Chemical-Reactions-based Microfluidic Circuits

From the description of the advection phenomenon in Chapter 2.2, it is clear that the flow properties, such as the velocity $\mathbf{u}$, have a significant impact on the distribution of molecule concentration. Motivated by this, Chapter 3 first presents the basic characteristics of fluid flow at the microscale, especially in microfluidic channels. The reason to study microfluidic channels is that they provide microscale experimental platforms to flexibly manipulate and control molecular transport to realize MC functionalities with high performance and reagent economy [32, 38]. Specifically, this chapter starts with the Navier-Stokes equation, which governs the motion of fluids. Then, two dimensionless numbers are discussed to classify and characterize the transport behavior of fluids. Moreover, the hydraulic circuit analysis is introduced. This analysis helps the derivation of the concentration and velocity changes for microfluidic devices with combining channels and separation channels, which are not fully investigated in the existing literature. A graphical summary of the contents is provided in Fig. 3.1. The new results are presented as lemmas in order to distinguish them from the known results in fluid dynamics. The results provided in this chapter serve as the foundation for the analysis in the following chapters. Subsequently, this chapter draws attention to the integration of chemical reactions and microfluidic systems to propose chemical-reactions-based microfluidic circuits [118]. In particular, a novel five-level architecture is proposed for digital microfluidic circuit design. Moreover, six types of microfluidic logic gates, including AND, NAND, OR, NOR, XOR, and XNOR gates, are

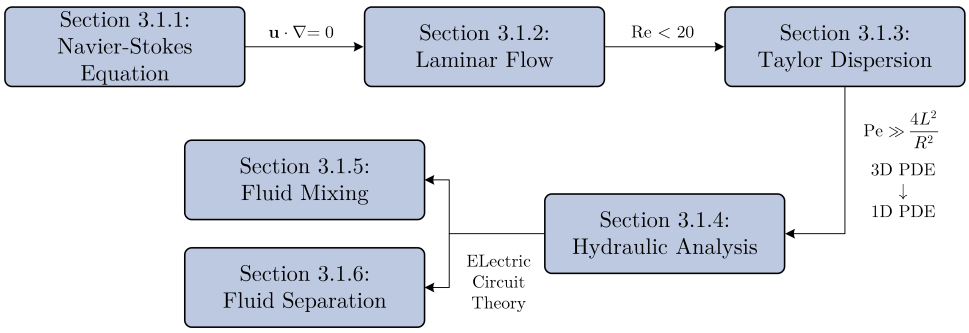

Fig. 3.1 Overview of the fluid characteristic discussion.

also provided. The proposed design principle builds a basis for the QCSK transceiver design which will be discussed in Chapter 5.

3.1 Characteristics of Microfluidics

Miniaturized instrumentation has attracted great interest over the past three decades due to its high performance, design flexibility, and reagent economy. Motivated by these advantages, researchers have started to fabricate lab-on-a-chip (LOC) systems by scaling down standard laboratory setups by a factor of 1000 or more from the decimeter scale to $100\mu m$ microscopic scale [98]. As a core technology of LOC systems, microfluidic technology deals with the manipulation of fluids in channels with dimensions of tens of micrometers [119]. With the reduction of size, the interplay between different forces and the relative dominance of these forces becomes different in microfluidic devices compared with macro devices. The *scaling law* reveals this feature and expresses the variation of physical quantities with the size l of a given system or object when other quantities (e.g., time, pressure, and temperature) are constant. For example, the basic scaling law for the ratio of *surface forces*, such as pressure force and viscosity force, to *volume forces*, such as gravitational force and inertia force, can be expressed as [98, eq. (1.1)]

$$\frac{\text{surface forces}}{\text{volume forces}} \propto \frac{l^2}{l^3} = l^{-1} \to \infty \ (l \to 0). \tag{3.1}$$

The above equation reveals that when scaling down to the microscale, the volume forces, which are very important in our daily life, become much less important. Instead, the surface forces will play a dominant role in microfluidic devices.

3.1.1 Navier-Stokes Equation

In general, the Navier-Stokes equation is used to formulate the motion of fluid flow as [98, eq. (2.30b)]

$$\rho\left[\frac{\partial \mathbf{u}}{\partial t} + (\mathbf{u}\cdot\nabla)\mathbf{u}\right] = -\nabla p + \eta\nabla^2\mathbf{u} + \mathbf{F}, \tag{3.2}$$

where ρ is the density of the flow, $\mathbf{u}$ is the velocity field, p is the pressure force, η is the viscosity of the fluid, and $\mathbf{F}$ is the body force applied to the fluid. Although (3.2) cannot be solved analytically in the general case due to the non-linear term $(\mathbf{u}\cdot\nabla)\mathbf{u}$, it is still possible to obtain solutions by making some assumptions.

3.1.2 Laminar Flow

To eliminate the non-linear convective term in (3.2), an assumption can be made that the fluid velocity and the velocity gradients are orthogonal. As such, the flow is *laminar*, and regular streamline flow patterns can be experimentally observed; otherwise, the flow is *turbulent*, and a single stable flow pattern cannot be observed in practice. The Reynolds number (Re) determines whether the flow is in the laminar regime or the turbulent regime, which is defined as [98, eq. (2.39)]

$$\mathrm{Re} = \frac{\rho u_{\mathrm{eff}} d}{\eta}, \tag{3.3}$$

where u_{eff} is the average velocity and d is the characteristic length scale. For flows in a pipe or tube, the characteristic length scale d becomes the hydraulic diameter of the pipe [11, eq. (3)].

In the laminar regime, the Reynolds number is normally less than 2300. In contrast, in the turbulent regime, the Reynolds number is larger than 2300. For microscale channels (whether synthetic or blood vessels), the Reynolds number is frequently less than 20; thus, laminar flows are often assumed [120]. For example, it has been demonstrated that most blood vessels (except the aorta with $\mathrm{Re} \in [1200, 4500]$) are laminar [121, 122]. Based on this, the authors of [22] derived a time-varying drug delivery concentration profile based on the advection-diffusion equation in (2.8). This work provided an initial understanding of drug propagation and laid the foundation to establish advanced therapeutic methods.

A typical example of laminar flow is Poiseuille flow, where a pressure drop exists between the inlet and outlet of a microfluidic channel. If the flow only moves along the x direction, the channel cross-section is invariant and circular, and neglected body

force, then the solution of (3.2) can be expressed as [98, eq. (3.42a)]

$$u_x(r) = \frac{\Delta P}{4\eta L}(R^2 - r^2), \tag{3.4}$$

where ΔP is the pressure drop, L is the channel length, R is the radius of the cross-section, and r is the radial location. In particular, the Poiseuille flow is also called Hagen–Poiseuille flow, which refers specifically to pressure-driven flow through a tube of circular cross-section. Eq. (3.4) indicates that the velocity follows a parabolic distribution, such that the flow velocity increases from the boundary towards the center of the channel. The velocity distributions for other cross-section shapes can be found in [98, Ch. 3].

3.1.3 Taylor Dispersion

The parabolic velocity profile of laminar flow has a huge impact on the interaction between diffusion and advection. The Péclet number (Pe) compares the relative dominance of advection versus diffusion and is defined as [98, eq. (5.53)]

$$\mathrm{Pe} = \frac{u_{\mathrm{eff}} L}{D}. \tag{3.5}$$

For $\mathrm{Pe} = 0$, the molecular movement is purely diffusive; for $\mathrm{Pe} \to \infty$, the movement becomes a pure bulk flow process.

The Péclet number is useful to predict the molecular distribution under Taylor dispersion, which describes how axial advection and radial diffusion jointly affect molecular transport in pressure-driven bulk flow [98]. Specifically, as shown in Fig. 3.2, a homogeneous band of solute is injected at $x = 0$ to travel through a cylindrical microchannel with radius R. A very short time after injection, the solute molecules are stretched into a parabolic plug by the flow having the velocity profile in (3.4). Subsequently, two concentration gradients are established at the front and back ends of the solute plug. Due to these gradients, there is a net migration of solute molecules at the front end from the high concentration area (i.e., the channel center) to the low concentration area (i.e., the channel boundary). On the contrary, there is a net migration of molecules at the back end from the channel boundary to the area around the channel center. We use $R^2/(4D)$ to characterize the expected diffusion time along the radial direction, and use L/u_{eff} to represent the time of molecule transport at average fluid velocity u_{eff} over distance L. If $R^2/(4D) \gg L/u_{\mathrm{eff}}$ (i.e., $\mathrm{Pe} \gg 4L^2/R^2$), then the cross-sectional diffusion cannot be ignored and fully counteracts the parabolic plug,

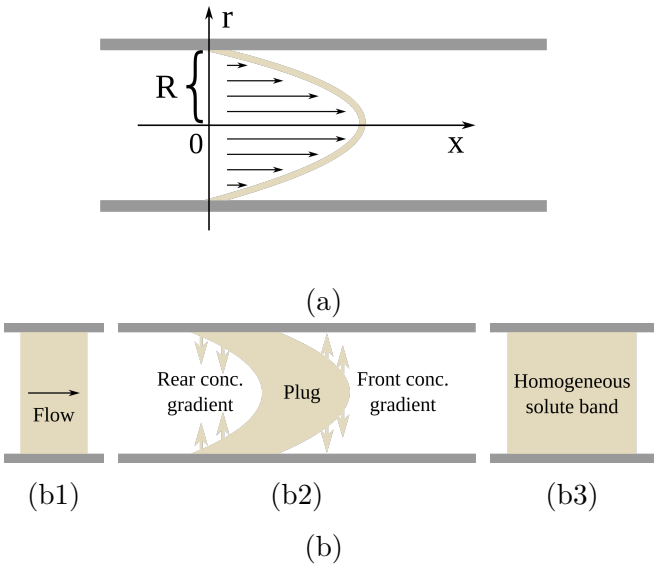

Fig. 3.2 The schematic of Taylor dispersion in Poiseuille flow. (a) In a microfluidic channel, the velocity increases from the boundaries inwards, following the parabolic distribution in (3.4) (R: cross-section radius, r: radial location, x: direction of flow). (b) Taylor dispersion progression inside a microfluidic channel: (b1) A homogeneous solute band is injected into the channel. (b2) After injection, the solute band is stretched into a parabolic plug due to the parabolic velocity distribution. Then, the concentration gradients established at the front and back ends, cause the net motion of solute molecules to counteract the parabolic plug. (b3) Finally, the molecules are uniformly distributed over the cross-section.

which leads to a uniform distribution of the solute over the cross-section [112, 123]. Thus, in this case, the 1D advection-diffusion equation with a modified diffusion coefficient can be used to approximate the 3D Poiseuille flow.

3.1.4 Hydraulic Circuit Analysis

Recall that the velocity distribution of Hagen–Poiseuille flow has been derived in (3.4). By integrating (3.4) over the cross-section surface, the volumetric flow rate Q can be calculated as

$$\begin{aligned} Q &= \int_{\mathcal{S}} u_x(r)\mathrm{d}S \\ &= \frac{\pi R^4}{8\eta}\Delta P. \end{aligned} \tag{3.6}$$

If the *hydraulic resistance* R_{h} is defined as

$$R_{\mathrm{h}} = \frac{8\eta}{\pi R^4}, \tag{3.7}$$

eq. (3.6) can be rewritten as

$$\Delta P = R_{\mathrm{h}} Q. \tag{3.8}$$

The above relation is the famous *Hagen–Poiseuille law*, which describes the hydraulic behavior of pressure-driven flow through a circular channel and is approximately correct for long channels [97].

With the laminar, viscous, and incompressible flow assumption, there is a well-known analogy between Hagen-Poiseuille law and Ohm's law ($\Delta V = R_{\mathrm{e}} I$), where the pressure drop ΔP, the flow rate Q, and the hydraulic resistance R_{h} in hydraulic circuits are analogous to the voltage drop ΔV, the electric current I, and the electric resistance R_{e} in electric circuits, respectively. On the one hand, this analogy enables a sound engineering estimate of steady-state pressure drop, flow rate, and hydraulic resistance of a 1D long and straight microchannel, and is still effective even for channels with non-circular cross-sections that are neither perfectly straight nor infinite in extent. On the other hand, this analogy enables the application of electric circuit theory, such as *Kirchhoff's Current Law* (KCL) and *Kirchhoff's Voltage Law* (KVL), to microchannel network analysis [124].

In the following subsections, the hydraulic circuit analysis is adopted to derive the concentration and velocity changes for microchannel networks. Moreover, considering that the rectangular-shaped cross-section is a common geometry in MC literature [33, 38, 125], the rectangular-shaped cross-section with width w and height h is assumed for all the proposed microfluidic circuits in this dissertation. As such, the average velocity u_{eff} can be expressed in terms of volumetric flow rate Q and cross-sectional area as [124, eq. (5)]

$$u_{\mathrm{eff}} = \frac{Q}{wh}. \tag{3.9}$$

3.1.5 Fluid Mixing at Combining Connections

In a microfluidic circuit, fluids flowing in different channels can mix to a single flow at a combining connection, and we name this behavior as fluid mixing for simplicity.

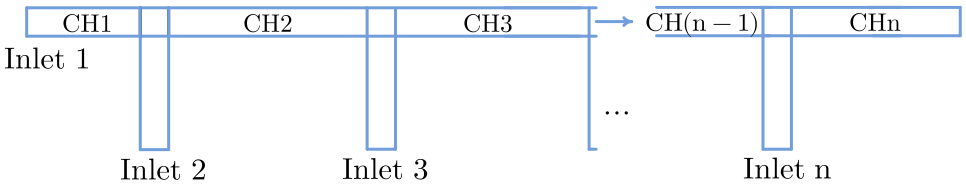

Fig. 3.3 A microfluidic device for fluid mixing analysis.

Concentration Change

Let us consider a general microfluidic device with n inlets and n combining channels as shown in Fig. 3.3. We assume that a solution containing species S_i $(1 \leq i \leq n)$ is constantly injected into Inlet i with concentration $C_{S_{i_0}}$, average velocity u_{eff_i}, and volumetric flow rate Q_i. According to the analogy between Hagen-Poiseuille law and Ohm's law and based on KCL, the volumetric flow rate in the nth combining channel $Q^{\text{CH}n}$ is the summation of coming flow rates, such that

$$\begin{cases} Q^{\text{CH1}} = Q_1, \\ Q^{\text{CH2}} = Q^{\text{CH1}} + Q_2 = \sum\limits_{i=1}^{2} Q_i, \\ \qquad \cdots\cdots, \\ Q^{\text{CH}n} = Q^{\text{CH}(n-1)} + Q_n = \sum\limits_{i=1}^{n} Q_i. \end{cases} \tag{3.10}$$

Therefore, the mixed concentrations of species S_1 and S_2 in the second combining channel are [124]

$$\begin{cases} C_{S_1}^{\text{CH2}} &= \frac{Q_1}{Q_1+Q_2} C_{S_{1_0}}, \\ C_{S_2}^{\text{CH2}} &= \frac{Q_2}{Q_1+Q_2} C_{S_{2_0}}. \end{cases} \tag{3.11}$$

Then, when $n \geq 3$, the mixed concentrations of species S_1, S_2, $\cdots$, S_n in the nth combining channel become

$$\begin{cases} C_{S_1}^{\text{CH}n} = \frac{Q^{\text{CH}(n-1)}}{Q^{\text{CH}(n-1)}+Q_n} C_{S_1}^{\text{CH}(n-1)} = \frac{\sum\limits_{i=1}^{n-1} Q_i}{\sum\limits_{i=1}^{n} Q_i} C_{S_1}^{\text{CH}(n-1)}, \\ C_{S_2}^{\text{CH}n} = \frac{Q^{\text{CH}(n-1)}}{Q^{\text{CH}(n-1)}+Q_n} C_{S_2}^{\text{CH}(n-1)} = \frac{\sum\limits_{i=1}^{n-1} Q_i}{\sum\limits_{i=1}^{n} Q_i} C_{S_2}^{\text{CH}(n-1)}, \\ \qquad\qquad \cdots\cdots \qquad\qquad , \\ C_{S_n}^{\text{CH}n} = \frac{Q_n}{Q^{\text{CH}(n-1)}+Q_n} C_{S_{n_0}} = \frac{Q_n}{\sum\limits_{i=1}^{n} Q_i} C_{S_{n_0}}. \end{cases} \tag{3.12}$$

Lemma 1. *For the fluid mixing from n inlets to one combining channel, the mixed concentration of species S_i $(1 \leq i \leq n)$ can be derived as*

$$C_{S_i}^{\mathrm{CH}n} = \frac{Q_i}{\sum_{i=1}^{n} Q_i} C_{S_{i_0}}, \tag{3.13}$$

where Q_i and $C_{S_{i_0}}$ are the volumetric flow rate and the species concentration injected into Inlet i. If all the species are injected with volumetric flow rate Q (i.e., $Q_1 = \cdots = Q_n = Q$), species S_i will be diluted to $1/n$ of its injected concentration in the nth combining channel, that is

$$C_{S_i}^{\mathrm{CH}n} = \frac{1}{n} C_{S_{i_0}}. \tag{3.14}$$

Proof. The last line of (3.12) can be reduced to (3.13) using (3.11) and other equations in (3.12). □

Remark 1. *From* (3.14)*, we can conclude that a higher volume of injected fluids can lead to a decrease of the output concentration of each species.*

Velocity Change

Injecting fluids into a combining channel influences not only the species concentration but also the flow velocity.

Lemma 2. *For the fluid mixing from n inlets to one combining channel, the flow rate in the nth combining channel can be expressed in terms of average velocity and channel geometry as*

$$\begin{aligned} Q^{\mathrm{CH}n} &= Q^{\mathrm{CH}n-1} + Q_n \\ \Rightarrow w^{\mathrm{CH}n} h^{\mathrm{CH}n} u_{\mathrm{eff}}^{\mathrm{CH}n} &= w^{\mathrm{CH}(n-1)} h^{\mathrm{CH}(n-1)} u_{\mathrm{eff}}^{\mathrm{CH}(n-1)} + w_n h_n u_{\mathrm{eff}_n}, \end{aligned} \tag{3.15}$$

where u_{eff_n}, w_n, and h_n are the average velocity, the width, and the height of Inlet n, and $u_{\mathrm{eff}}^{\mathrm{CH}n}$, $w^{\mathrm{CH}n}$, and $h^{\mathrm{CH}n}$ are the average velocity, the width, and the height of the nth combining channel, respectively. If all inlets and combining channels share the same geometry and the same average velocity u_{eff}, the average velocity in the nth combining channel becomes

$$u_{\mathrm{eff}}^{\mathrm{CH}n} = n u_{\mathrm{eff}}. \tag{3.16}$$

Proof. Based on KCL and (3.9), we can obtain (3.15). □

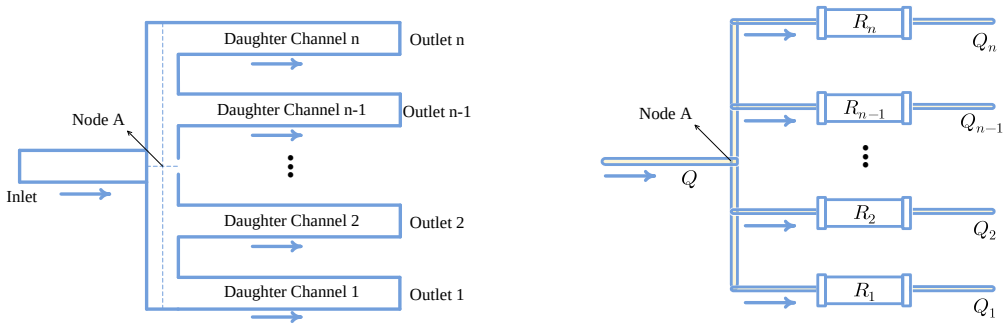

(a) A microfluidic device (b) Hydraulic circuit analog

Fig. 3.4 A microfluidic device for fluid separation analysis.

Remark 2. *It is revealed in* (3.16) *that a higher volume of injected fluids can lead to an increase of the average velocity.*

3.1.6 Fluid Separation at Bifurcation Connections

In a microfluidic circuit, a single flow can be separated into different flow streams at a bifurcation connection, and we name this behavior as fluid separation for simplicity. Let us consider a microfluidic device with one inlet and n outlets as shown in Fig. 3.4a, where a single flow is separated into n streams traveling over n daughter channels. Assuming that the solution containing species S_1 is injected with concentration $C_{S_{1_0}}$ and average velocity u_{eff}, the concentration at each outlet is the same as $C_{S_{1_0}}$, because species S_1 is not diluted by other species. However, the average velocity in each outlet varies for different geometry of its daughter channel. To derive the outlet velocities, we establish the hydraulic circuit model in Fig. 3.4b. Analogous to current division in electric circuits, the relationship between the volumetric flow rate Q_i $(1 \leq i \leq n)$ and the supplied volumetric flow rate Q can be described by [124, eq. (18)]

$$Q_i = \frac{R_{\text{h}_{\text{eq}}}}{R_{\text{h}_i}} Q \tag{3.17}$$

where R_{h_i} is the hydraulic resistance of the ith daughter channel and $R_{\text{h}_{\text{eq}}}$ is the equivalent resistance of all daughter channels. Let us denote L_{D_i} as the length from the crosspoint Node A in Fig. 3.4b to outlet i, and w_i and h_i as the geometry width and height of the ith daughter channel, R_{h_i} [124, eq. (10)] and $R_{\text{h}_{\text{eq}}}$ [124, eq. (13)] can be calculated as

$$R_{\text{h}_i} = \frac{12\eta L_{D_i}}{w_i h_i^3 \left[1 - \sum\limits_{i=1,3,5,\cdots}^{\infty} \frac{192 h_i}{w_i \pi^5 i^5} \tanh_i\left(\frac{i\pi w_i}{2h_i}\right)\right]}, \tag{3.18}$$

$$R_{\mathrm{h_{eq}}} = \frac{1}{1/R_1 + 1/R_2 + \cdots + 1/R_n}. \tag{3.19}$$

Lemma 3. *For the fluid separation from one inlet to n outlets, the average velocity* u_{eff_i} *in the ith outlet can be derived as*

$$u_{\mathrm{eff}_i} = \frac{R_{\mathrm{h_{eq}}}}{R_{\mathrm{h_i}}} \frac{wh}{w_i h_i} u_{\mathrm{eff}}, \tag{3.20}$$

where w and h are the width and the height of the injection channel, w_i *and* h_i *are the width and the height of the ith daughter channel,* R_{h_i} *and* $R_{h_{eq}}$ *are given in* (3.18) *and* (3.19)*, respectively. If all daughter channels share the same geometry (i.e.,* $w_1 h_1 = \cdots = w_n h_n = wh$ *and* $L_{D_1} = \cdots = L_{D_n}$*), eq.* (3.20) *can be reduced to*

$$u_{\mathrm{eff}_i} = \frac{1}{n} u_{\mathrm{eff}}. \tag{3.21}$$

Proof. Substituting (3.9) into (3.17), we can obtain (3.20). When all daughter channels share the same geometry, $R_{\mathrm{h}_i} = nR_{\mathrm{h_{eq}}}$ and thus (3.20) can be reduced to (3.21). □

Remark 3. *It is indicated from* (3.21) *that fluid separation results in a reduction of average velocity by n times.*

3.2 Chemical-Reactions-based Microfluidic Circuits

The CRNs can integrate with microfluidic systems to construct chemical-reactions-based microfluidic circuits. As discussed in Chapter 1.4, chemical-reactions-based microfluidic circuits not only are endowed with the advantages of rapid analysis and low reagent costs due to size reduction but can also benefit from an additional space level of chemical control through applying and regulating reactions in different regions of a microfluidic device.

3.2.1 Microfluidic Processing System Abstraction

As discussed in Chapter 1.3, the digital circuit design has received attention owing to the scalability of digital circuits and the discreteness of molecules. In effect, digital signals are ideal for reliable state transitions and signal integration, and are useful for decision-making circuits [126]. Motivated by these facts, in this section, the ability of chemical-reactions-based microfluidic circuits to process digital chemical signals is exploited. Specially, in order to facilitate microfluidic circuit design, a five-level

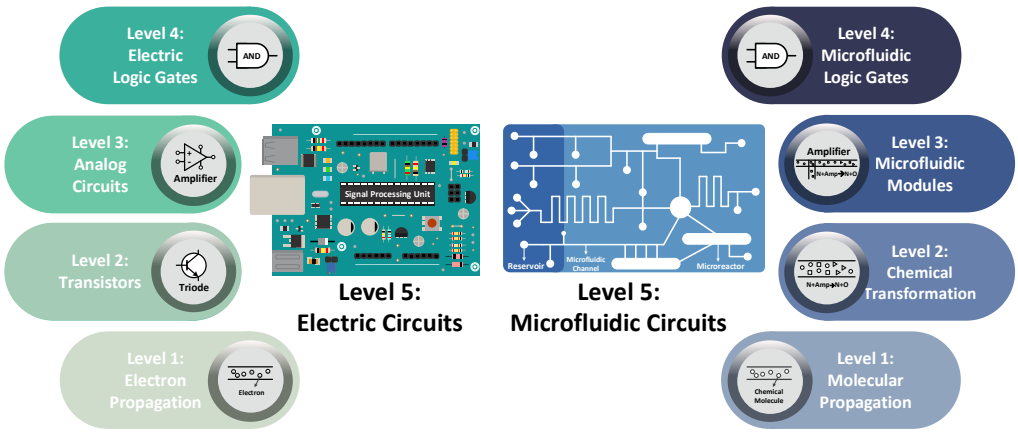

Fig. 3.5 The illustration of levels of abstraction for an electronic processing system and a microfluidic processing system along with typical building components at each level.

abstraction of a microfluidic processing system is proposed and shown in Fig. 3.5. The levels of abstraction are as follows:

- **Level 1: Molecular Propagation** – the movement of chemical molecules in microfluidic channels.
- **Level 2: Chemical Transformation** – the interaction between different molecular species, i.e., the chemical reactions that support various signal processing functions.
- **Level 3: Microfluidic Modules** – the basic modules performing simple arithmetic calculations, such as addition, subtraction, and amplification operations.
- **Level 4: Microfluidic Logic Gates** – the digital logic gates that are selected and assembled from the microfluidic modules designed for Level 3. Although the microfluidic modules at Level 3 process a continuous range of concentrations, an appropriate combination of them can lead to digital signal operations.
- **Level 5: Microfluidic Circuits** – the top level is the microfluidic circuit itself, which is built from the logic gates designed for Level 4 and can perform a specific signal processing function, such as modulation-demodulation and encoding-decoding for MC.

As shown in Fig. 3.5, the proposed levels of microfluidic processing systems can be mapped to those of electronic processing systems [127] level-by-level. The main differences between these two types of systems lie in Levels 1 and 2. In electronic processing systems, Level 1 focuses on the propagation of electrons, which can be

described by quantum mechanics and Maxwell's equations. By contrast, Level 1 in microfluidic processing systems is based on the movement of chemical particles, which is often analyzed by fluid mechanics. The Level 2 of electronic processing systems is composed of transistors (e.g., diode and triode), whereas that of microfluidic processing systems is based on chemical reactions for signal transformation. The Levels 3–5 in microfluidic processing systems have similar functions as electronic processing systems, but they are realized differently via either electronic components or microfluidic components. In the following, the components at Levels 1 and 2 are presented, and the utilization of these components to support the construction of the microfluidic modules at Level 3 will be provided. In addition, this section will also present the basic designs of some microfluidic logic gates at Level 4. For Level 5, the microfluidic circuits with QCSK modulation and demodulation functions are a concrete example of the application of the proposed five-level architecture, which will be discussed in Chapter 5.

3.2.2 Level 1: Molecular Propagation

In Level 1, the movement of chemical molecules is bounded by channel geometry, and its dispersion is governed by diffusion and advection. A channel without reactions refers to an *advection-diffusion channel*. According to the channel shape, we consider three types of geometry: Y junction, T junction, and straight advection-diffusion channel as shown in Fig. 3.6. The Y and T junctions are two exchangeable merging channels with two inlets and one outlet, and they can facilitate the mixing of different species injected through two inlets. The straight advection-diffusion channels only provide a pathway for chemical molecules.

3.2.3 Level 2: Chemical Transformation

In Level 2, chemical reactions are introduced into advection-diffusion channels. The channels with chemical reactions are named as *advection-diffusion-reaction channels* and are filled with grey-gradient color as shown in Fig. 3.6. In this dissertation, two types of chemical reactions are considered:

- Type I: $S_i + S_j \rightarrow S_k$,
- Type II: $S_i + Amp \rightarrow S_i + O$.

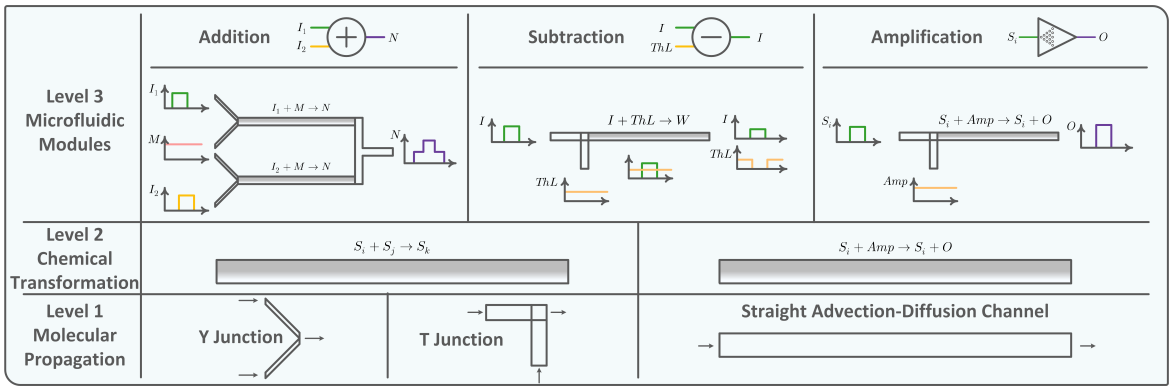

Fig. 3.6 The components at Levels 1 and 2, and their construction to the addition, subtraction, and amplification modules for Level 3.

Some examples of the two types of reactions along with the Level 4 circuit realizations are discussed in Chapter 7.2.1. By introducing chemical reactions, microfluidic circuits are endowed with signal processing capabilities.

3.2.4 Level 3: Microfluidic Modules

By combining the components at Levels 1 and 2, we can construct the *Addition*, *Subtraction*, and *Amplification* modules in Level 3. As illustrated in Fig. 3.6, each module contains one or two chemical reactions. In the following, we reveal the signal transformation nature of the reactions at Level 2 and discuss the mechanism of each module.

Addition Module

The addition module calculates the total concentration of two different molecular species and is achieved by converting them to the same molecular species. As shown in the addition module of Fig. 3.6, it is composed of two Y junctions, two reaction channels, and advection-diffusion channels. The inputs of an addition module are three chemical signals that contain species I_1, M, and I_2, respectively. The output is the chemical signal with species N. In reaction channels, molecular species I_1 and I_2 are transformed to species N in terms of reactions $I_1 + M \rightarrow N$ and $I_2 + M \rightarrow N$. Due to the one-to-one stoichiometric relationship between reactants and product, the concentration of generated species N is equal to the consumed concentration of species I_1 (or I_2). Moreover, the stoichiometric relationship also reveals that the amount of transformed species of I_1 (or I_2) depends on the concentration of species M. To ensure a complete conversion of species I_1 and I_2 to species N, the concentration of species

M needs to be greater than or at least equal to the concentration of species I_1 (or I_2). Meanwhile, it is likely that reactions $I_1 + M \rightarrow N$ and $I_2 + M \rightarrow N$ have different reaction speeds, and thus one reaction needs a longer reaction channel to achieve a full conversion of input molecules to species N than the other. In this case, the channels containing the above reactions should be long enough to ensure that both reactions are complete at the reaction channel outlet. Otherwise, the output will be incorrect. After chemical reactions, the species N generated in two reaction channels converge at advection-diffusion channels to generate the final output.

Subtraction Module

The subtraction module calculates the concentration difference between two molecular species. To perform such an operation, the module relies on the depletion of one species by the other species. As shown in the subtraction module of Fig. 3.6, it is consisted of a T junction and a reaction channel with species I and ThL as the inputs and the remaining species I as the output. In the reaction channel, the input species I is consumed by species ThL according to reaction $I + ThL \rightarrow W$, where species W represents a waste species whose concentration we do not keep track of. The module output, i.e., the concentration of remaining species I, is determined by the concentration of species ThL. Under the condition that the concentration of species ThL is greater than the concentration of species I, species I will be fully depleted. As a result, the concentration of species I will be set as zero due to the one-to-one stoichiometric relationship between species I and species ThL and the non-negative property of concentration. In this context, we name the reaction $I + ThL \rightarrow W$ as a thresholding reaction. In the subtraction module context, the Type I reaction, i.e., $S_i + S_j \rightarrow S_k$, is also named as a thresholding reaction.

Amplification Module

The amplification module generates a chemical signal whose width and amplitude are determined by two input signals. As shown in the amplification module of Fig. 3.6, it uses the same geometry structure as the subtraction module but with a different reaction $S_i + Amp \rightarrow S_i + O$ [128]. In the presence of species S_i, species S_i acts as a catalyst to enable the conversion of the other input species Amp to the output species O; if species S_i is absent, species O will not be produced. In this way, species S_i determines the time period when the output species O is generated, whereas reactant Amp influences the concentration of species O. The higher the concentration of species Amp, the higher the concentration of species O, which allows for a flexible adjustment

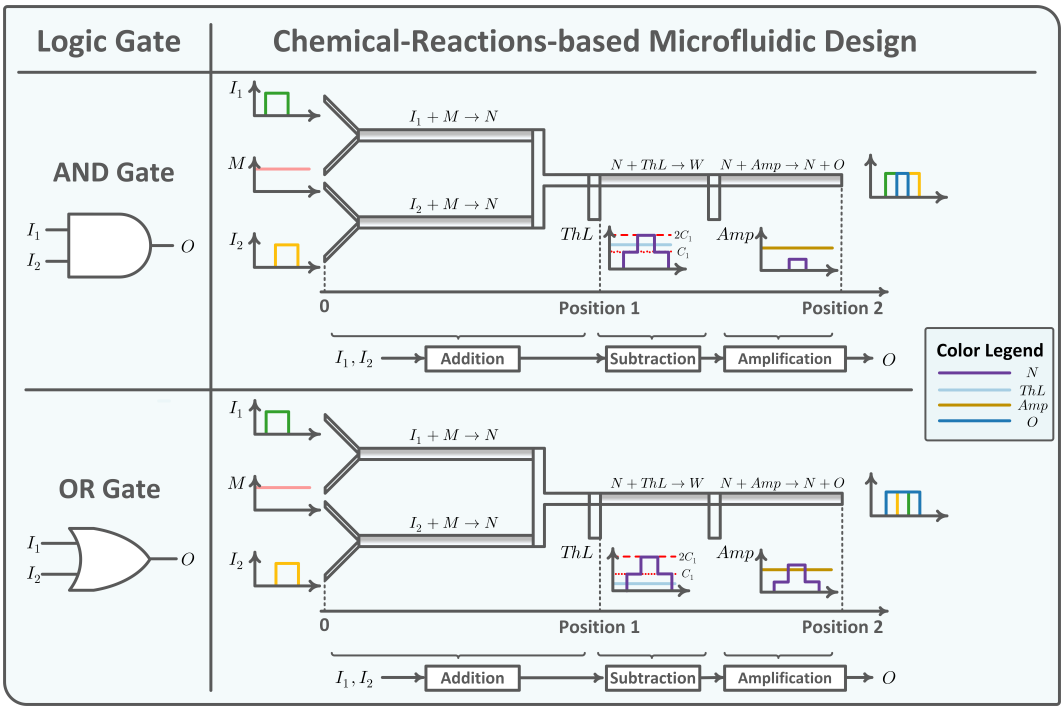

Fig. 3.7 The chemical-reactions-based microfluidic AND gate and OR gate.

of the output concentration of species O. In this context, we name the reaction $S_i + Amp \rightarrow S_i + O$ as an amplifying reaction. In addition, it is also expected that the concentration waveform of species O varies with the concentration waveform of species Amp. For the purpose of implementing digital processing, species Amp should be constantly injected so that the concentration of species O keeps a steady level during the presence of species S_i.

3.2.5 Level 4: Microfluidic Logic Gates

Flowing fluids in microfluidic channels allows for an easy serial processing operation, which endows microfluidic circuits with the feature of integrating different functional modules to build the microfluidic logic gates at Level 4. In particular, the addition, subtraction, and amplification modules designed for Level 3 are applied to construct the AND, NAND, OR, NOR, XOR, and XNOR gates. Throughout this dissertation, the HIGH state (bit-1) and the LOW state (bit-0) are represented by non-zero concentrations and zero concentrations, respectively.

AND and NAND Gates

We first design the AND gate as shown in Fig. 3.7, which is consisted of the addition, subtraction, and amplification modules at Level 3. The AND gate takes input signals I_1 and I_2 and produces a HIGH state for output species O only when both inputs are HIGH. The addition module first converts species I_1 and I_2 to an intermediate species N assisted by species M. According to the combination of input species I_1 and I_2, the species N concentration C_N at Position 1 has a ladder-shaped distribution (the purple line in the subtraction module in Fig. 3.7) with three typical values:

- $C_N = 0$ when both input species are LOW,
- $C_N = C_1$ when only one input species is HIGH (the red dot line in Fig. 3.7),
- $C_N = 2C_1$ when both input species are HIGH (the red dash line in Fig. 3.7).

To achieve an AND function, the concentration of species N in the amplification module is required to span over the time period where both species I_1 and I_2 are HIGH. With this goal in mind, the species N generated by the addition module flows into a subtraction module and undergoes a depletion by species ThL that is continuously supplied through the first T junction. Note that the concentration of species ThL at Position 1, i.e., C_{ThL}, must satisfy $C_1 < C_{ThL} < 2C_1$ so that the concentration of remaining species N is larger than zero only when both inputs are HIGH. Once the remaining species N arrives at the amplification module, the reaction $N + Amp \rightarrow N + O$ is activated, which induces the conversion of species Amp to the output species O. By doing so, we complete the AND logic operation in the molecular domain. Note that the AND gate can be converted to a NAND gate with the addition of a subtraction module.

OR and NOR Gates

The OR gate can be designed using a similar geometry structure as the AND gate, as shown in Fig. 3.7. Different from the AND gate, an OR gate generates a HIGH state for output species O when one or both input species I_1 and I_2 are HIGH. The only difference in design parameters between AND gate and OR gate is the injected concentration of species ThL at the subtraction module. In theory, the concentration of species N at Position 1 should be zero when both species I_1 and I_2 are LOW. However, this value is likely to be slightly larger than zero in practice. To mitigate this fluctuation, the output species N generated by the addition module is required to

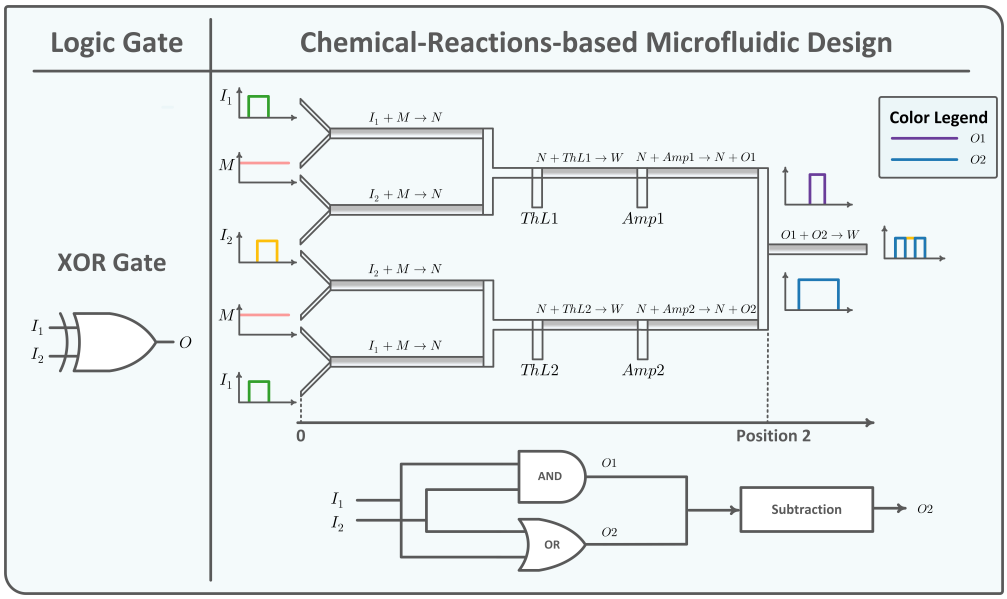

Fig. 3.8 The chemical-reactions-based microfluidic XOR gate.

be further processed by a subtraction module in which the concentration of species ThL at Position 1 (i.e., C_{ThL}) should be larger than the fluctuation level and smaller than C_1 (i.e., the concentration of species N at Position 1 when only one input is HIGH). When either one input is HIGH or both inputs are HIGH, the remaining concentrations of species N after reaction $N + ThL \rightarrow W$ have two different values, and an amplification module is used to ensure that these two values can lead to a generation of the same amount of output species O. Analogous to the transformation of an AND gate to a NAND gate, the OR gate can be converted to a NOR gate with a cascade of a subtraction module.

XOR and XNOR Gates

The XOR gate is designed based on an AND gate, an OR gate, and a subtraction module. As shown in Fig. 3.8, the input signals I_1 and I_2 first flow into the AND and OR gates that operate parallelly to generate species $O1$ and $O2$ at Position 2, respectively. Then, the generated species $O1$ and $O2$ enter a subtraction module to activate reaction $O1 + O2 \rightarrow W$. In this reaction, species $O1$ is completely depleted by species $O2$ so that the remaining concentration of specie $O2$ only shows a HIGH state when either input species I_1 or I_2 is HIGH, thus achieving the XOR operation. Similar to the NAND and NOR gates, the XOR gate can be converted to an XNOR gate with a cascade of a subtraction module.

3.3 Conclusion

In this chapter, the characteristics of flows in microfluidic channels are discussed, and the chemical-reactions-based microfluidic circuits are introduced. Compared to the flow at the macroscale, the flow at the microscale usually shows a laminar property. The parabolic velocity profile of laminar flows has a significant impact on molecular transport, and the interplay between diffusion and advection can be evaluated by the Péclet number. The analogy between Hagen-Poiseuille law and Ohm's law allows for the derivation of the concentration and velocity changes for microfluidic devices with combining channels and separation channels. Then, chemical-reactions-based microfluidic circuits are proposed. The properties of electric circuits are further exploited to propose a similar five-level architecture for microfluidic circuits. The components at each level are briefly introduced and most importantly six microfluidic logic gates are presented. In conclusion, this chapter provides the design and analysis basis for the following chapters.

Chapter 4

Chemical-Reactions-based Microfluidic BCSK Realization

4.1 Introduction

As discussed in Chapter 1.3, performing signal processing functions over chemical signals can be achieved by chemical circuits and genetic circuits. While genetic circuits offer biocompatibility, non-invasiveness, and miniaturization, they still currently face challenges, e.g., slow speed and unreliability. Motivated by these facts, this chapter focuses on the design and analysis of novel chemical circuits for rapid prototyping and testing communication systems based on chemical reactions, which lead to direct translation to potential genetic circuits to be engineered in biological cells. Considering the advantages brought by the integration of chemical reactions and microfluidic systems, a chemical-reactions-based microfluidic MC transmitter design was proposed in [129]. The proposed MC transmitter is capable of generating a molecular concentration pulse upon a rectangular signal, thus realizing the BCSK modulation function. Although the theoretical analysis in [129] captured the effect of channel parameters on transmitted signals, a further optimization design is not investigated. In addition, it is also unclear how to realize BCSK demodulation, i.e., the receiver design.

The objective of this chapter is to study the realization of BCSK modulation and demodulation functions via chemical-reactions-based microfluidic circuits [130]. Different from [129], an optimized BCSK transmitter design and a novel microfluidic BCSK receiver design are proposed. The optimized MC transmitter modulates rectangular digital inputs to pulse-shaped signals, which is analogous to ASK modulation in wireless communication. Instead of directly emitting the digital inputs, the maximum concentrations of the modulated pulses can be tuned according to the proposed optimization

framework. This framework brings an opportunity to transmit multiple symbols using different maximum concentration levels, which may improve the data rate. The proposed microfluidic BCSK receiver demodulates a received pulse to a rectangular-shaped signal that has a steep transition between minimum and maximum concentrations. The digital characteristic of rectangular-shaped digital signals allows the receiver to further incorporate Boolean computations to generate customized behaviors [131]. The main contributions of this chapter are listed as follows:

- We first optimize the microfluidic BCSK transmitter design proposed in [129]. We present a reaction channel length optimization framework to guide how to tune the maximum concentration of a generated pulse. We also analyze the restricted time gap between two consecutive input signals to ensure a continuous transmission of non-distorted pulses.

- We then propose a microfluidic BCSK receiver design capable of demodulating a received signal to a rectangular output signal. This demodulation is realized via two chemical reactions, where a thresholding reaction is proposed to first deplete the received signal below the threshold, and an amplifying reaction converts the residual received signal into a digital output.

- Unlike [32], we address a new challenge in mathematically modeling the dynamics of molecular species in microfluidic channels by deriving the channel response of straight advection-diffusion-reaction channels. Although only rectangular and Gaussian concentration profiles are considered for channel input, the presented methodology can be used for any other concentration profiles. Importantly, the analytical results are validated via the simulations performed in COMSOL Multiphysics finite element solver.

The proposed BCSK transmitter and receiver design not only constitute a simple end-to-end MC system but also bring new opportunities for certain applications. For example, the transmitter design can act as a concentration gradient generator (CGG) to investigate the role of concentration gradients in cell development, inflammation, and wound healing [132], while the receiver design can be attached to field-deployable biosensors to detect chemical and biological threats [119].

The rest of this chapter is organized as follows. In Chapter 4.2, we present the microfluidic transmitter and receiver design in terms of chemical reactions and microfluidic components. In Chapter 4.3, we analyze advection-diffusion channels and advection-diffusion-reaction channels. In Chapters 4.4 and 4.5, we not only present

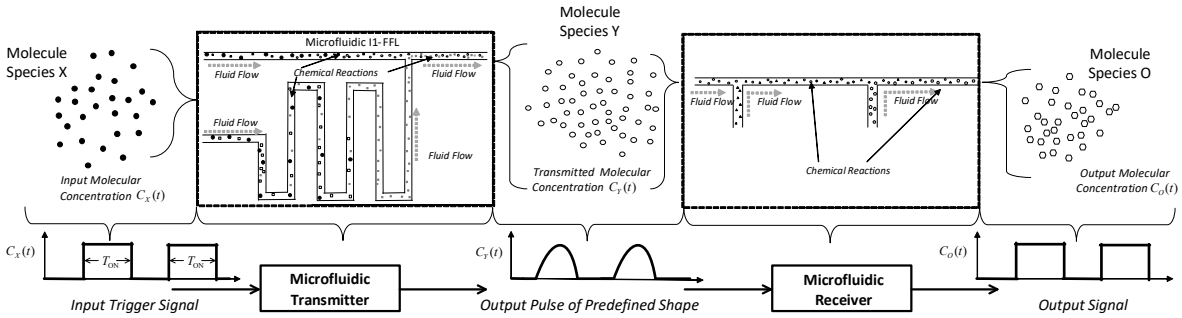

Fig. 4.1 Overall scheme of the proposed BCSK transmitter and receiver.

the design and analysis of the proposed microfluidic BCSK transmitter and receiver, but also provide numerical simulation results performed in COMSOL Multiphysics. In Chapter 4.6, we combine the microfluidic transmitter with the receiver to show a basic end-to-end MC system. Finally, Chapter 4.7 concludes this chapter.

4.2 System Model

The overall scheme of the proposed BCSK transmitter and receiver is shown in Fig. 4.1. At the microfluidic BCSK transmitter, a high digital rectangular input molecular signal composed of the molecular species X in a fluid with concentration $C_X(t)$ enters the microfluidic transmitter that upon a variation in $C_X(t)$ produces an output molecular signal composed of molecular species Y with concentration $C_Y(t)$ by following a predefined pulse shape. After advection-diffusion of the emitted pulse $C_Y(t)$, a microfluidic receiver is designed to demodulate the received pulse to a rectangular output signal using species O with concentration $C_O(t)$. Here, both the pulse shape and the demodulated signal shape are dependent on the values of parameters in the microfluidic device implementation. As the fluids flow through microfluidic device channels, a series of chemical reactions occur to generate the molecules of species Y and species O, which guarantee successful pulse modulation and signal demodulation. In the following, we first introduce these chemical reactions at the transmitter side and the receiver side and then describe the microfluidic components of the transmitter and receiver.

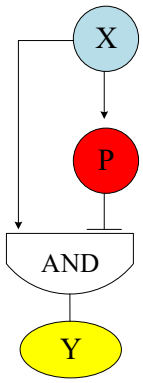

Fig. 4.2 The I1-FFL network motif.

4.2.1 Chemical Reaction Design

Chemical Reaction Design for Microfluidic BCSK Transmitter

Gene regulatory networks are sets of interconnected biochemical processes in a biological cell [133], where DNA genes are linked together by activation and repression mechanisms of certain biological macromolecules that regulate their expressions into proteins. Each DNA gene contains coding sequences and regulatory sequences which are sites the proteins (transcription factor) can bind and control the rate of the gene expression, either by increasing (activation) or decreasing (repression) the rate of protein synthesis. The gene expression is discussed in greater detail in Chapter 6.2.1. In gene regulatory networks, genes are interconnected such that the proteins produced by one or more genes regulate the expression of one or more genes, which results in complex protein expression dynamics.

Gene regulatory networks can be abstracted with nodes representing the genes, interconnected by directed edges that correspond to the control of a gene (edge destination) expression by a transcription factor (TF) encoded by another gene (edge source). Network motifs are patterns of nodes and directed edges that occur more frequently in natural gene transcription networks than randomized networks [134]. The feed-forward loop (FFL) is a family of network motifs among all three-node patterns frequently observed in nature [134, 135]. In the structure of FFL, the TF protein X regulates the genes expressing other two proteins, namely, P and Y, where P is also a TF that regulates the gene expressing protein Y. Depending on the types of these regulations, either activation or repression, there are 8 different FFLs [136].

Among all the FFLs found in nature, the incoherent type 1 FFL (I1-FFL) results in pulse-like dynamics of its output Y [135]. As shown in Fig. 4.2, an input gene expresses the protein X, which is a TF for the genes expressing Y and P. In the

presence of X, the expressions of the genes encoding protein Y and protein P are activated, resulting in the building up of the concentrations of protein Y and protein P, respectively. In its turn, the protein P is another TF that works as a repressor for the gene encoding protein Y. The AND input to the gene that encodes Y corresponds to a situation where this gene is activated when TF X binds to the regulatory sequence, but it is inactivated whenever TF P binds to the same sequence independently from the presence of X. In this way, protein X initializes the rapid expression of the gene encoding protein Y first, and after a delay, enough P accumulates and represses the production of protein Y, whose concentration will continuously decrease because of natural degradation. This generates a pulse shape for the concentration of protein Y as a function of the time. One example of I1-FFL is the galactose system of *E. coli* [137].

In this chapter, we take inspiration from the I1-FFL to design a BCSK transmitter in molecular domain, and explore the realization of I1-FFL via mass-action chemical reactions. To execute the same functionality of an I1-FFL with a CRN, we define three chemical reactions as follows:

$$\text{Reaction I} : X + S_y \rightarrow Y, \tag{4.1}$$

$$\text{Reaction II} : X + S_p \rightarrow P, \tag{4.2}$$

$$\text{and} \quad \text{Reaction III} : Y + P \rightarrow Z, \tag{4.3}$$

where these reactions involve the input molecular species X, the molecular species S_p and S_y, the intermediate product molecular species P, and the output molecular species Y. Note that these reactions all belong to the Type I reaction introduced to **Level 2 Chemical Transformation** for the five-level architecture proposed in Chapter 3.2.

In the I1-FFL gene regulation network, the protein X first activates the gene expressing the protein Y, and only when P accumulates sufficiently, it suppresses the expression of the protein Y, generating the aforementioned pulse-like concentration signal. Here, the molecular species X, S_p, and S_y are only injected at $t = 0$, and the chemical reactions in (4.1), (4.2), and (4.3) happen simultaneously with a much quicker speed under well-stirred environment than that of the I1-FFL gene regulation network dynamics, which may not result in the pulse-like output signal Y when these three reactions have the same reaction rate and are in the same space. One way to cope with it is to apply and regulate reactions in different regions of a microfluidic device to control the occurring sequence of these reactions. Thus, we propose a microfluidic

BCSK transmitter containing the reactions (4.1), (4.2), and (4.3) to realize the same functionality of I1-FFL as in the gene regulation network in Fig. 4.3, which a pulse-like output is triggered by the rectangular input representing bit-1 transmission.

Chemical Reaction Design for Microfluidic BCSK Receiver

According to the demodulation requirement of traditional communication systems, we aim to design a microfluidic BCSK receiver capable of demodulating the received pulse to a rectangular signal. To do so, we design the chemical reactions as follows:

$$\text{Reaction IV} : Y + ThL \rightarrow Waste, \tag{4.4}$$

$$\text{and} \quad \text{Reaction V} : Y + Amp \rightarrow Y + O, \tag{4.5}$$

where these reactions involve the input molecular species Y, the molecular species ThL and Amp, intermediate product molecular species $Waste$, and the output molecular species O. Once the species Y arrives at the receiver, the Reaction IV is immediately activated, resulting in a depletion of species Y that is below the concentration of species ThL. Then, any remaining Y catalyzes the conversion of species Amp into the output species O. Obviously, output species O will only be produced when the concentration of Y is greater than the concentration of ThL, so we regard the concentration of ThL as a threshold and name Reaction IV as the thresholding reaction. Reaction V refers to an amplifying reaction. Indeed, Reaction IV and Reaction V can be regarded as a realization of the Subtraction module and Amplification module (see Chapter 3.2), respectively. Similar to the chemical reactions at the transmitter, the sequence of Reaction IV and Reaction V is controlled by the microfluidic receiver geometry design, which will be presented next.

We note that Reaction V is necessary and we detect species O instead of species Y. The reasons are as follows. First, the concentration of remaining species Y may not reach the minimum detectable level of a detector. With Reaction V, the output can satisfy a detector's sensitivity by adjusting the concentration of injected species Amp. Second, Reaction V is performed to generate the output to be a rectangular digital signal, which can allow the receiver to link post-Boolean computational modules [131]. One example is to perform an AND operation for multiple outputs to further enhance biosensors' specificity [65].

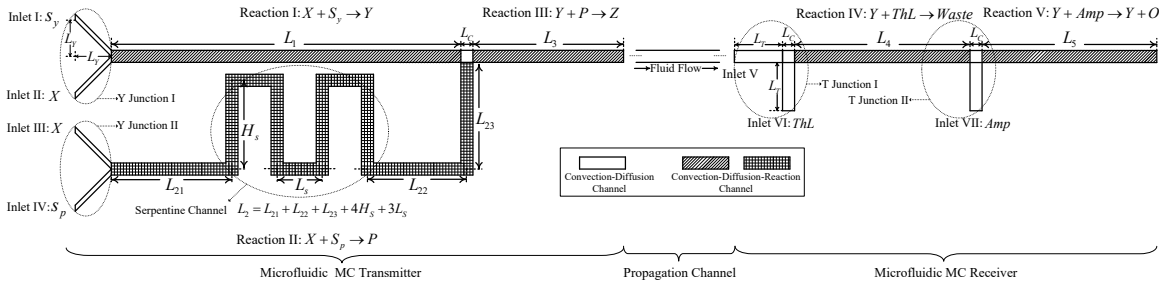

Fig. 4.3 Novel Design of the microfluidic MC transmitter and receiver.

4.2.2 Microfluidic Channel Design

In this subsection, we describe each component of the proposed microfluidic BCSK transmitter and receiver in Fig. 4.3. As discussed in Chapter 3.2, according to whether a microfluidic channel contains chemical reactions, we classify microfluidic components as advection-diffusion channel and advection-diffusion-reaction channel.

Advection-Diffusion Channel

- **Y Junction at the microfluidic transmitter:** The reactions between reactants require mixing to occur in a short distance, which can be facilitated by advection-diffusion in Y junctions. A Y junction is configured by one outlet and two inlets, i.e., Y junction I and Y junction II in Fig. 4.3, where the outlet width is doubled compared with each inlet width, and the angle between the main channel and the first inlet starting anticlockwise from the main channel is 145^o. The fluid flow containing input reactant X with concentration $C^{\mathrm{II}}_{X_0}(t)$ and $C^{\mathrm{III}}_{X_0}(t)$ is injected into Inlet II and Inlet III using syringe pumps, which can be described by a rectangular pulse signal, as in Fig. 4.1, with the value of the width being equal to the length of injection time T_{ON}, whereas the reactant S_y with concentration $C^{\mathrm{I}}_{S_{y0}}$ and reactant S_p with concentration $C^{\mathrm{IV}}_{S_{p0}}$ are continuously injected into Inlet I and Inlet IV, respectively. By doing so, the flows from Inlet I and Inlet IV can flush the microfluidic device continuously without influencing Reaction III in (4.3).

- **T Junction at the microfluidic receiver:** T junctions are chosen at the receiver equipping with the same functionality as Y junctions. A T Junction has one outlet and two inlets, i.e., T junction I and T junction II in Fig. 4.3, where the angle between the second inlet starting anticlockwise from the first inlet is 90^o, and one inlet of T junction II is merged into an advection-diffusion-reaction channel. After propagation, the transmitted molecules from the microfluidic transmitter

propagate to enter the receiver, and the reactant ThL with concentration $C^{\mathrm{VI}}_{ThL_0}$ and Amp with concentration $C^{\mathrm{VII}}_{Amp_0}$ are continuously injected into Inlet VI and Inlet VII, respectively.

- **Straight Advection-Diffusion Channel:** This channel is used to connect the transmitter with the receiver and provides a propagation pathway for a generated pulse.

Advection-Diffusion-Reaction Channel

For simplicity, in the following, we refer to the channel in which Reaction i happens as the Reaction i channel.

- **Transmitter**

  Straight Reaction I Channel: The outflow of Y junction I passes through the Reaction I channel with length L_1 to realize the Reaction I in (4.1) to generate the output signal Y.

  Serpentine Reaction II Channel: The outflow of Y junction II passes through the Reaction II channel to generate P according to the Reaction II in (4.2). To realize the pulse-shaped concentration of emitted signal Y, the Reaction II channel is designed to be longer than the Reaction I channel, with the result of delaying the contact between species P and Y, and therefore delaying the Reaction III. Furthermore, a serpentine channel is designed and replaces a straight reaction channel to delay the arrival of species P in a compact space within the microfluidic transmitter. The width and height of the serpentine channel are denoted as L_s and H_s, respectively. The design in Fig. 4.3 is conventionally denoted as containing 2 delay lines, due to its two bent tubes with height H_s in the serpentine channel. The equivalent straight channel length of this serpentine channel is denoted as L_2 and can be calculated as $L_2 = L_{21}+L_{22}+L_{23}+4H_s+3L_s$.

  Straight Reaction III Channel: Once P arrives at the Reaction III channel with length L_3, Reaction III in (4.3) occurs to decrease the output signal Y.

- **Receiver**

  Straight Reaction IV Channel: The outflow of T junction I flows through the Reaction IV channel with length L_4 to deplete Y below the concentration of species ThL according to Reaction IV in (4.4).

Straight Reaction V Channel: When the remaining Y arrives at the Reaction V channel with length L_5, Reaction V in (4.5) is activated to convert the species Amp into output species O.

4.3 Basic Microfluidic Channel Analysis

In this section, we use a 1D model to approximate and derive analytical expressions for advection-diffusion channels and advection-diffusion-reaction channels. Numerical results are also provided to verify the theoretical analysis.

4.3.1 Advection-Diffusion Channels

For advection-diffusion channels, the spatial-temporal concentration distribution can be described by the 3D advection-diffusion equation given in (2.8). In this dissertation, the main assumption used is that the flow inside the microfluidic channel is laminar and falls into the dispersion regime (see Chapter 3.1.3). Therefore, the interaction between cross-sectional diffusion and advection can lead to a uniform molecule distribution along the cross-section, such that (2.8) can be reduced to a 1D advection-diffusion equation as [112]

$$\frac{\partial C(x,t)}{\partial t} = D_{\text{eff}} \frac{\partial^2 C(x,t)}{\partial x^2} - u_{\text{eff}} \frac{\partial C(x,t)}{\partial x}, \tag{4.6}$$

where u_{eff} is the average velocity of the laminar flow and D_{eff} is the Taylor-Aris effective diffusion coefficient. When the cross-section is rectangular-shaped, D_{eff} can be calculated as [125, eq. (3)]

$$D_{\text{eff}} = \left[1 + \frac{8.5 u_{\text{eff}}^2 h^2 w^2}{210 D^2 (h^2 + 2.4hw + w^2)}\right] D, \tag{4.7}$$

where h is the cross-section height, w is the cross-section width, and D is the molecular diffusion coefficient. It is clear that D_{eff} captures the geometry of 3D channels.

4.3.2 Advection-Diffusion-Reaction Channels

For advection-diffusion-reaction channels, the spatial-temporal concentration distribution can be described by the 3D advection-diffusion-reaction equation given in (2.11). Similar to the simplification of the 3D advection-diffusion equation, eq. (2.11) can also be reduced to a 1D form. Let us assume that reaction $S_i + S_j \to S_k$ occurs inside an advection-diffusion-reaction channel. Thus, the spatial-temporal concentration

distribution of species S_i and S_k can be described as

$$\frac{\partial C_{S_i}(x,t)}{\partial t} = D_{\text{eff}}\frac{\partial^2 C_{S_i}(x,t)}{\partial x^2} - u_{\text{eff}}\frac{\partial C_{S_i}(x,t)}{\partial x} - k_f C_{S_i}(x,t)C_{S_j}(x,t), \tag{4.8}$$

$$\frac{\partial C_{S_k}(x,t)}{\partial t} = D_{\text{eff}}\frac{\partial^2 C_{S_k}(x,t)}{\partial x^2} - u_{\text{eff}}\frac{\partial C_{S_k}(x,t)}{\partial x} + k_f C_{S_i}(x,t)C_{S_j}(x,t), \tag{4.9}$$

where k_f is the rate constant. Assuming species S_j with concentration $C_{S_{j_0}}$ is continuously injected at the inlet of the channel at $x = 0$ and $t = 0$ with velocity u_{eff}, we solve the above advection-diffusion-reaction equations in the following two theorems, when species S_i is injected with rectangular and Gaussian concentration profiles as they are considered as the inputs of transmitter and receiver later.

Theorem 1. *With species S_i following a rectangular concentration distribution*

$$C_{S_{i0}}(t) = C_{S_{i0}}[u(t) - u(t - T_{\text{ON}})] \tag{4.10}$$

being injected at the inlet of a straight microfluidic channel at $x = 0$ and $t = 0$ using velocity u_{eff}, the concentration distributions of S_i and S_k are derived as

$$C_{S_i}(x,t) = \begin{cases} g(x,t), & 0 \le t \le T_{\text{ON}} \\ g(x,t) - g(x,t - T_{\text{ON}}), & t > T_{\text{ON}}, \end{cases} \tag{4.11}$$

and

$$C_{S_k}(x,t) = \begin{cases} h(x,t) - g(x,t), & 0 \le t \le T_{\text{ON}} \\ [h(x,t) - g(x,t)] - [h(x,t - T_{\text{ON}}) - g(x,t - T_{\text{ON}})], & t > T_{\text{ON}}, \end{cases} \tag{4.12}$$

where $u(t)$ is the Heaviside step function,

$$h(x,t) = \frac{C_0}{2}\Big[\text{erfc}\Big(\frac{x - u_{\text{eff}}t}{2\sqrt{D_{\text{eff}}t}}\Big) + e^{\frac{u_{\text{eff}}x}{D_{\text{eff}}}}\text{erfc}\Big(\frac{x + u_{\text{eff}}t}{2\sqrt{D_{\text{eff}}t}}\Big)\Big], \tag{4.13}$$

$$g(x,t) = \frac{C_0}{2}\left\{\exp\left[\frac{(u_{\text{eff}} - \alpha)\,x}{2D_{\text{eff}}}\right]\text{erfc}\left[\frac{x - \alpha t}{2\sqrt{D_{\text{eff}}t}}\right] + \exp\left[\frac{(u_{\text{eff}} + \alpha)\,x}{2D_{\text{eff}}}\right]\text{erfc}\left[\frac{x + \alpha t}{2\sqrt{D_{\text{eff}}t}}\right]\right\}, \tag{4.14}$$

with $C_0 = \min\left\{C_{S_{i0}}, C_{S_{j0}}\right\}$ and $\alpha = \sqrt{u_{\text{eff}}^2 + 4kC_0D_{\text{eff}}}$.

Proof. Please refer to Appendix A.1. □

Theorem 2. *With species S_i following a Gaussian concentration distribution*

$$C_{S_{i0}}(t) = \frac{C_{S_{i0}}}{\sqrt{2\pi\sigma^2}} e^{-\frac{(t-\mu)^2}{2\sigma^2}} \tag{4.15}$$

being injected at the inlet of a straight microfluidic channel at $x = 0$ and $t = 0$ using velocity u_{eff} and $C_{S_{j_0}} < \max\{C_{S_{i0}}(t)\}$, the concentration distribution of S_i can be derived as

$$C_{S_i}(x,t) = C_{S_i}^{\text{Method1}}(x,t) = \begin{cases} C_{S_{i0}}(t - \frac{x}{u_{\text{eff}}}) - C_{S_{j_0}}, & t_1 + \frac{x}{u_{\text{eff}}} \le t \le t_2 + \frac{x}{u_{\text{eff}}}, \\ 0, & \textit{otherwise.} \end{cases} \tag{4.16}$$

$$\textit{or } C_{S_i}(x,t) = C_{S_i}^{\text{Method2}}(x,t) = \frac{1}{2\pi}\int_0^\infty \Big[e^{-j\omega t}\overline{\widetilde{C_{S_i}^{\text{Method2}}}(x,\omega)} + e^{j\omega t}\widetilde{C_{S_i}^{\text{Method2}}}(x,\omega)\Big]\mathrm{d}\omega, \tag{4.17}$$

where

$$\widetilde{C_{S_i}^{\text{Method2}}}(x,s) = l(s)e^{\frac{u_{\text{eff}} - \sqrt{u_{\text{eff}}^2 + 4D_{\text{eff}}s}}{2D_{\text{eff}}}x}, \tag{4.18}$$

$$l(s) = C_{S_{i0}}e^{-s\mu + \frac{(\sigma s)^2}{2}}\Big[Q(\frac{t_1 + \sigma^2 s - \mu}{\sigma}) - Q(\frac{t_2 + \sigma^2 s - \mu}{\sigma})\Big] - \frac{C_{S_{j0}}}{s}(e^{-st_1} - e^{-st_2}), \tag{4.19}$$

$$t_1 = \mu - \sqrt{-2\sigma^2 \ln \frac{C_{S_{j_0}}\sqrt{2\pi\sigma^2}}{C_{S_{i0}}}}, \tag{4.20}$$

$$\textit{and } t_2 = \mu + \sqrt{-2\sigma^2 \ln \frac{C_{S_{j_0}}\sqrt{2\pi\sigma^2}}{C_{S_{i0}}}}. \tag{4.21}$$

Proof. Please refer to Appendix A.2. □

The derivation $C_{S_i}^{\text{Method2}}(x,t)$ can be easily computed using Matlab. Importantly, eqs. (4.11), (4.16), and (4.17) reduce to solutions of an advection-diffusion equation when $C_{S_{j_0}} = 0$.

In Figs. 4.4 and 4.5, we plot the analytical concentrations of species S_k in **Theorem 1**, species S_i in **Theorem 2** at a channel outlet and their simulation results using COMSOL Multiphysics. COMSOL Multiphysics is a type of computational fluid dynamics (CFD) simulator and can simulate flows in the *most accurate* way close to

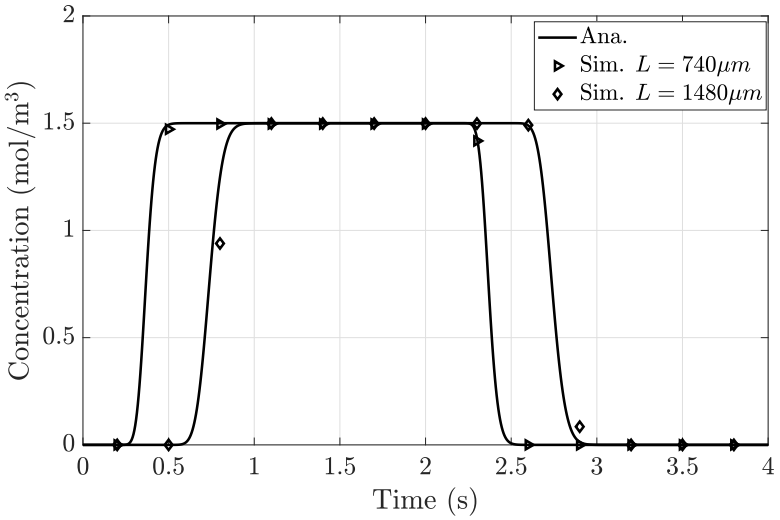

Fig. 4.4 The concentration of species S_k in **Theorem 1** with different channel length L.

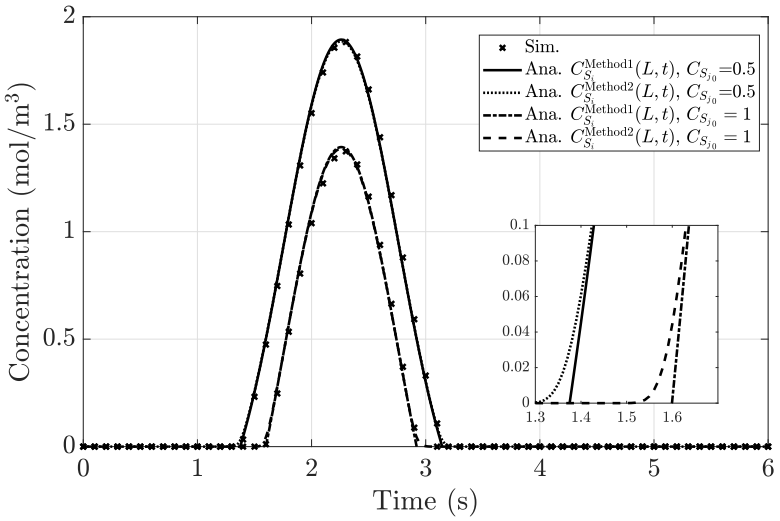

Fig. 4.5 The concentration of species S_i in **Theorem 2** with $L = 540\mu$m and different $C_{S_{j_0}}$.

physics [138]. In addition, we use "Ana." and "Sim." to abbreviate "Analytical" and "Simulation", respectively, and these notations are also used throughout the rest of this chapter.

We set the parameters: $C_{S_{i0}} = C_{S_{j_0}} = 1.5\text{mol/m}^3$ in **Theorem 1**, $C_{S_{i0}} = 3\text{mol/m}^3$ in **Theorem 2**, $\mu = 2$, $\sigma^2 = 0.25$, $D = 10^{-8}\text{m}^2/\text{s}$, $k_f = 400\text{m}^3/(\text{mol}\cdot\text{s})$, $T_{\text{ON}} = 2\text{s}$. The simulation points are plotted using the outlet of a straight microfluidic channel

with rectangular-shaped cross section, $h = 10\mu$m and $w = 20\mu$m, where species S_i and S_j are both injected with the same velocity $u_{\text{eff}} = 0.2$cm/s. In Fig. 4.4, it clearly demonstrates a close match between the analytical curves and the simulation points with different channel lengths L. In Fig. 4.5, we observe that both methods can capture the concentration variation of residual S_i after reaction $S_i + S_j \rightarrow S_k$. When C_{S_i} approaches zero, the curve using the second method is smoother than that using the first method due to the consideration of the diffusion effect.

4.4 BCSK Transmitter Analysis and Design Optimization

In this section, we first analyze the Y Junction and three reaction channels, and then we provide the microfluidic transmitter design in terms of the optimal design of the Reaction II channel length and the restricted time gap between two consecutive input bits, which enable us to control the maximum concentration of a generated pulse and ensure a continuous transmission of non-distorted pulses, respectively.

4.4.1 Microfluidic MC Transmitter Analysis

Y Junction

The fluid flows containing input reactant X with concentration

$$C_{X_0}^{\text{II}}(t) = C_{X_0}^{\text{II}}[u(t) - u(t - T_{\text{ON}})] \tag{4.22}$$

$$\text{and } C_{X_0}^{\text{III}}(t) = C_{X_0}^{\text{III}}[u(t) - u(t - T_{\text{ON}})] \tag{4.23}$$

are injected into Inlet II and Inlet III using syringe pumps. The reactant S_y with concentration $C_{S_{y_0}}^{\text{I}}$ and reactant S_p with concentration $C_{S_{p_0}}^{\text{VI}}$ are continuously injected into Inlet I and Inlet IV, respectively. We let the inlets of a Y Junction as the location origin ($x = 0$) and let the time that species are injected at Y Junction inlets as the time origin ($t = 0$). For Y Junction I, the outlet concentration of species X can be expressed using (4.11) in **Theorem 1** with $C_{S_{j_0}} = 0$ and a substitution of $C_{X_0}^{\text{II}}$ for $C_{S_{i_0}}$. However, the complicated form of (4.11) will make the Reaction I channel intractable since the outlet concentration of species X at Y Junction I is an initial condition for the advection-diffusion-reaction equation describing the Reaction I channel. Taking into account that the Y Junction length is shorter than the Reaction I channel length, for simplicity, we assume the outlet concentration of species X is only a time shift of

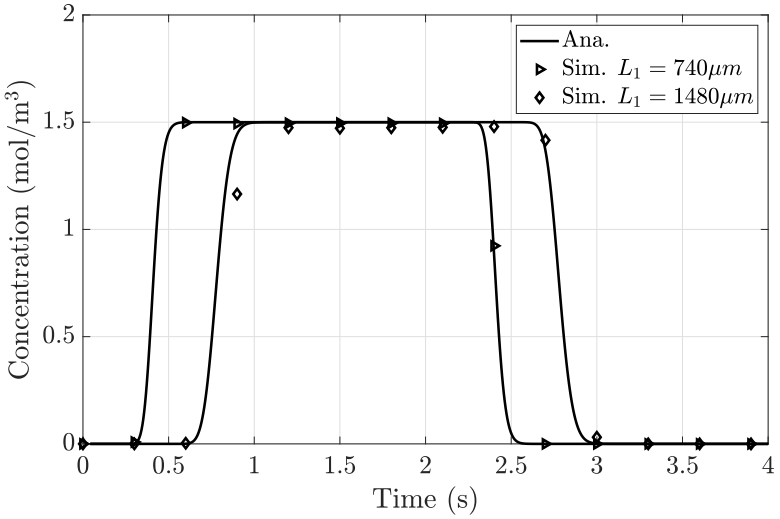

Fig. 4.6 The concentration of species Y at Reaction I channel outlet.

its injected concentration due to the traveling of Y Junction I, that is

$$C_X(L_Y, t) = C^{\mathrm{II}}_{X_0}[u(t - t_{\mathrm{Y}}) - u(t - T_{\mathrm{ON}} - t_{\mathrm{Y}})], \tag{4.24}$$

where $t_{\mathrm{Y}} = \frac{\sqrt{2}L_Y}{u_{\mathrm{eff}}}$ is the travelling time of a Y Junction (L_Y is marked in Fig. 4.3). Apparently, the above analysis can also be applied to Y junction II.

Straight Reaction I Channel

The outflow of Y junction I enters the Reaction I channel to activate Reaction I in (4.1). The simultaneous flush of independent X and S_y leads to a concentration dilution, which can be treated as diluting species X using S_y or diluting species S_y using X. According to the analysis of fluid mixing in **Lemma** 1, the concentrations of species X and S_y at the inlet of Reaction I channel become $\frac{1}{2}C_X(L_Y, t)$ and $\frac{1}{2}C^{\mathrm{I}}_{S_{y_0}}$, respectively. Based on this, the outlet concentration of species Y can be expressed using (4.12) in **Theorem 1** by substituting $C_{S_{i0}}$ and $C_{S_{j0}}$ with $C^{\mathrm{II}}_{X_0}$ and $C^{\mathrm{I}}_{S_{y_0}}$, that is

$$C_Y(L_Y + L_1, t) = \frac{1}{2}C_{S_k}(L_1, t - t_{\mathrm{Y}}), \tag{4.25}$$

where L_1 is the length of the Reaction I channel.

Fig. 4.6 plots the concentration of species Y at the outlet of Reaction I channel with Y Junction I. We set the parameters: $C^{\mathrm{II}}_{X_0} = C^{\mathrm{I}}_{S_{y_0}} = 3\mathrm{mol/m}^3$, $D = 10^{-8}\mathrm{m}^2/\mathrm{s}$, $k_f = 400\mathrm{m}^3/(\mathrm{mol{\cdot}s})$, $T_{\mathrm{ON}} = 2\mathrm{s}$, $u_{\mathrm{eff}} = 0.2\mathrm{cm/s}$, $L_Y = 60\mu\mathrm{m}$, $h = 10\mu\mathrm{m}$, and $w = 10\mu\mathrm{m}$.

It is evident that the simulation points are in agreement with the theoretical analysis in (4.25) under different L_1, which validates the analysis of the straight Reaction I channel.

Serpentine Reaction II Channel

The analysis of the straight Reaction I channel can also be applied to the serpentine Reaction II channel, which yields

$$C_P(L_Y + L_1, t) = \frac{1}{2} C_{S_k}(L_2, t - t_{\mathrm{Y}}), \tag{4.26}$$

where L_2 is the length of the Reaction II channel. The application of Reaction I channel analysis to the Reaction II channel can be explained by the following reasons: 1) although turning corners in the serpentine channel usually cause different laminar flows propagating different distances, we can approximate outlet concentrations of the serpentine channel as those of a straight channel with equivalent length when fluids are in low Reynolds number with very small side length tube, and 2) the form of the advection-diffusion-reaction equation and its initial boundary conditions still hold with only a substitution of $C_P(x,t)$, $C^{\mathrm{IV}}_{S_{p_0}}$, and $C^{\mathrm{III}}_{X_0}$ for $C_Y(x,t)$, $C^{\mathrm{I}}_{S_{y_0}}$, and $C^{\mathrm{II}}_{X_0}$, respectively.

Straight Reaction III Channel

The generated species Y and P mix with each other at a conjunction with length L_C and leads to a concentration dilution before flowing to the Reaction III channel. Therefore, at the inlet of straight Reaction III channel, the concentrations of species Y and P are

$$C_Y(L_Y + L_1 + L_C, t) = \frac{1}{4} C_{S_k}(L_1, t - t_{\mathrm{Y}} - t_{\mathrm{C}}), \tag{4.27}$$

$$\text{and } C_P(L_Y + L_1 + L_C, t) = \frac{1}{4} C_{S_k}(L_2, t - t_{\mathrm{Y}} - t_{\mathrm{C}}), \tag{4.28}$$

where $t_{\mathrm{C}} = \frac{L_C}{2u_{\mathrm{eff}}}$ is the travelling time of the conjunction. When both species Y and P appear in the Reaction III channel, Reaction III in (4.3) is activated, and the corresponding advection-diffusion-reaction equations can be constructed as (4.8) and (4.9). Unfortunately, it is foreseeable that deriving the spatial-temporal concentration distribution of species Y, exactly the concentration distribution of the generated pulse, is intractable, since the initial condition with the form of C_{S_k} in (4.12) is mathematically not solvable in closed-form. However, it is possible to obtain the

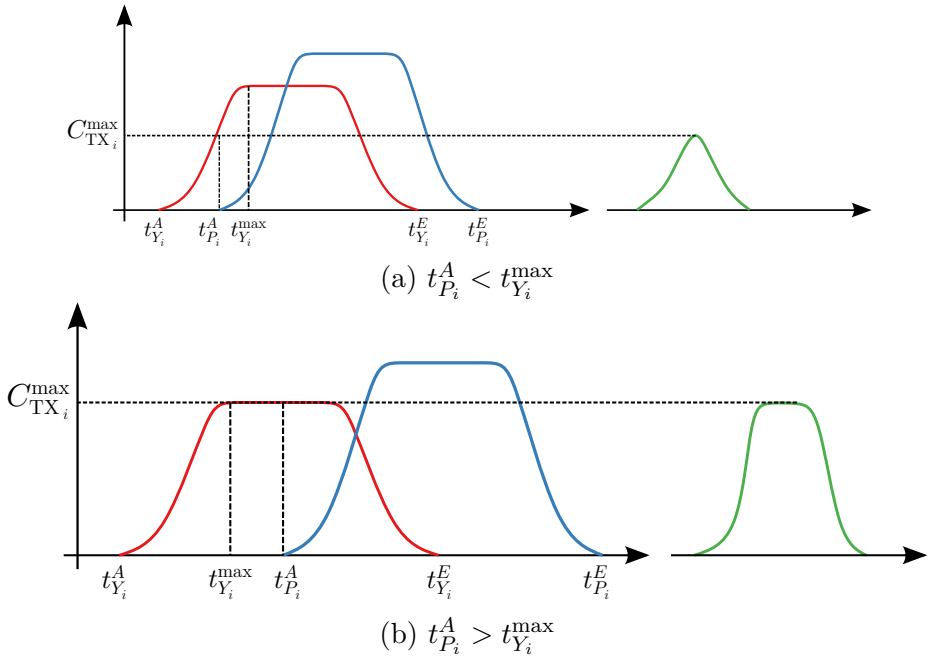

(a) $t^A_{P_i} < t^{\max}_{Y_i}$

(b) $t^A_{P_i} > t^{\max}_{Y_i}$

Fig. 4.7 The generated pulses (green curve) with different arriving times of species P at Reaction III channel.

maximum concentration of the generated pulse, which will be presented in the next subsection.

4.4.2 Microfluidic MC Transmitter Design Optimization

Optimal Design of the Reaction II Channel Length

As stated earlier, although the advection-diffusion-reaction equation describing the Reaction III channel cannot be theoretically solved, the maximum concentration of a generated pulse can be obtained. Let $C^{\max}_{\mathrm{TX}_i}$ denote the maximum concentration of the transmitted pulse generated by the ith input bit. In fact, there are many factors affecting $C^{\max}_{\mathrm{TX}_i}$, such as the rate constant k_f and reaction channel lengths L_1, L_2, and L_3. However, if we assume that the rate constant k_f and reaction channel lengths collectively ensure that reactants are fully converted into a product in each reaction, the Reaction II channel length L_2 will be the only parameter affecting $C^{\max}_{\mathrm{TX}_i}$.

At the transmitter, the design of channel length $L_2 > L_1$ allows species Y to first enter the Reaction III channel with a result of the concentration increase of a generated pulse. By contrast, the late arrival of species P prevents this increase, and leads to a decrease in the generated pulse, as Y will be immediately depleted by P as soon as P appears in the Reaction III channel (shown in Fig. 4.7). Let us denote the arriving

and leaving time of species Y at Reaction III channel inlet as $t_{Y_i}^A$ and $t_{Y_i}^E$ for the ith input bit, and the time that species Y reaches its maximum concentration at Reaction III channel inlet as $t_{Y_i}^{\max}$. Similarly, for the ith input bit, the arriving and leaving time of species P at Reaction III channel inlet are $t_{P_i}^A$ and $t_{P_i}^E$, respectively. There are two situations that lead to different $C_{\mathrm{TX}_i}^{\max}$.

- If $t_{P_i}^A < t_{Y_i}^{\max}$, the generated pulse will be consumed by P before reaching $\max\{C_Y(L_Y + L_1 + L_C, t)\}$, causing $C_{\mathrm{TX}_i}^{\max} < \max\{C_Y(L_Y + L_1 + L_C, t)\}$. See Fig. 4.7a.
- If $t_{P_i}^A > t_{Y_i}^{\max}$, the generated pulse will reach $\max\{C_Y(L_Y + L_1 + L_C, t)\}$, where the reaction between Y and P only influences the tail shape of the generated pulse. See Fig. 4.7b.

Therefore, we conclude that $C_{\mathrm{TX}_i}^{\max} = \xi C_Y(L_Y + L_1 + L_C, t)$ with $\xi \in [0, 1]$. Meanwhile, the arriving time of species P is determined by the length of Reaction II channel L_2. As such, we can flexibly control $C_{\mathrm{TX}_i}^{\max}$ by choosing different L_2. Based on this, we propose a step-by-step L_2 optimization flow as follows:

Initialization: Given L_1, ξ, and initial concentrations $C_{S_{y_0}}^{\mathrm{I}}$, $C_{X_0}^{\mathrm{II}}$, $C_{X_0}^{\mathrm{III}}$, and $C_{S_{p_0}}^{\mathrm{IV}}$.

Step 1: Search for the time $t_{Y_i}^{\max}$ that satisfies

$$0 \leq \frac{\mathrm{d}C_Y(L_Y + L_1 + L_C, t)}{\mathrm{d}t} \leq \delta,\ t \leq t_{Y_i}^{\max}, \tag{4.29}$$

$$-\delta \leq \frac{\mathrm{d}C_Y(L_Y + L_1 + L_C, t)}{\mathrm{d}t} \leq 0,\ t > t_{Y_i}^{\max}, \tag{4.30}$$

where $C_Y(L_Y + L_1 + L_C, t)$ is given in (4.27). We introduce a variable δ to numerically find $t_{Y_i}^{\max}$, as it is difficult to analytically solve $\frac{\mathrm{d}C_Y(L_Y+L_1+L_C,t)}{\mathrm{d}t} = 0$.

Step 2: Calculate the maximum concentration of a generated pulse that $C_{\mathrm{TX}_i}^{\max} = \xi C_Y(L_Y + L_1 + L_C, t_{Y_i}^{\max})$.

Step 3: Calculate the time $t_{\mathrm{TX}_i}^{\max}$ to satisfy $C_Y(L_Y + L_1 + L_C, t_{\mathrm{TX}_i}^{\max}) = C_{\mathrm{TX}_i}^{\max}$.

Step 4: Calculate the Reaction II channel length L_2 via

$$C_P(L_Y + L_1 + L_C, t_{\mathrm{TX}_i}^{\max}) \geq \epsilon,\ x \leq L_2, \tag{4.31}$$

$$C_P(L_Y + L_1 + L_C, t_{\mathrm{TX}_i}^{\max}) < \epsilon,\ x > L_2, \tag{4.32}$$

where $C_P(L_Y + L_1 + L_C, t)$ is given in (4.28). Similar to δ, ϵ is introduced here to numerically find L_2.

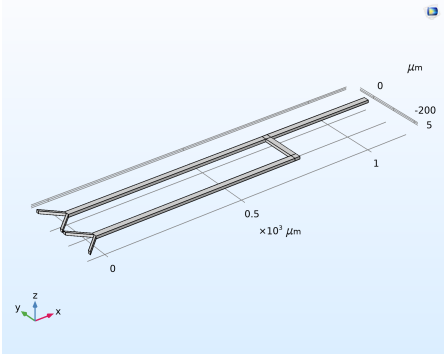

(a) 0 delay line, $\xi = 1/3$

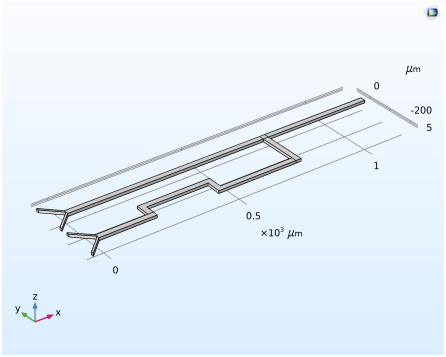

(b) 1 delay line, $\xi = 2/3$

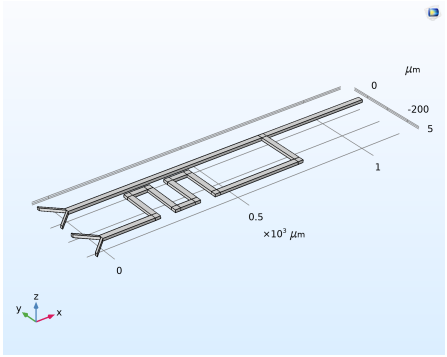

(c) 2 delay lines, $\xi = 1$

Fig. 4.8 The COMSOL implementation of the optimized microfluidic transmitter with different numbers of delay lines.

To examine the proposed L_2 optimization flow, we implement three designs with different numbers of delay lines in COMSOL to achieve different $C_{\mathrm{TX}_i}^{\max}$. The implementation is shown in Fig. 4.8 and geometric parameters are listed in Table 4.1 and Table 4.2. Unless otherwise noted, the length unit is μm. Other parameters are set as follows: $C_{S_{y_0}}^{\mathrm{I}} = C_{X_0}^{\mathrm{II}} = 3\mathrm{mol/m^3}$, $C_{X_0}^{\mathrm{III}} = C_{S_{p_0}}^{\mathrm{IV}} = 4\mathrm{mol/m^3}$, $D = 10^{-8}\mathrm{m^2/s}$, $k_f = 400\mathrm{m^3/(mol{\cdot}s)}$, $T_{\mathrm{ON}} = 2\mathrm{s}$, $u_{\mathrm{eff}} = 0.2\mathrm{cm/s}$. Here, we modify $\max\{C_Y(L_Y + L_1 + L_C, t)\}$ from 0.75 to 0.7498. From the results shown in Fig. 4.6, when $L_1 = 740\mu\mathrm{m}$, $C_Y(L_Y + L_1, t)$ rapidly reaches 1.4995 at 0.55s and then increases very slowly to the maximum concentration 1.5 at 0.9511s. It takes 0.4s to reach the maximum concentration from 1.4995, while the concentration increase is less than 0.001. In order to generate a pulse that both two sides of the maximum concentration showing a distinct increase or decrease, we modify $\max\{C_Y(L_Y + L_1, t)\}$ and $t_{Y_i}^{\max}$ as 1.4995 and 0.55s, respectively, thus $\max\{C_Y(L_Y + L_1 + L_C, t)\} = \frac{1}{2}\max\{C_Y(L_Y + L_1, t)\} = 0.7498$.

In Fig. 4.9, we plot the concentrations of generated pulses for implementations in Fig. 4.8. As expected, the output pulses are generated successfully during T_{ON},

Table 4.1 The parameters of the proposed microfluidic transmitter.

Channel	Length	Width	Height
Y Junction	$L_Y = 60$	10	10
Conjunction	$L_C = 20$	20	10
Reaction I Channel	$L_1 = 740$	20	10
Reaction III Channel	$L_3 = 400$	20	10

Table 4.2 The parameters of serpentine Reaction II channel in Fig. 4.8.

Channel	L_2	L_{21}	L_{22}	L_{23}	L_s	H_s	ξ	δ	ϵ
0 delay line	887	/	/	137	/	/	1/3	0.13	10^{-1}
1 delay line	1019	200	300	157	250	56	2/3	0.13	3×10^{-2}
2 delay lines	1516	200	325	177	75	147.25	1	0.13	10^{-3}

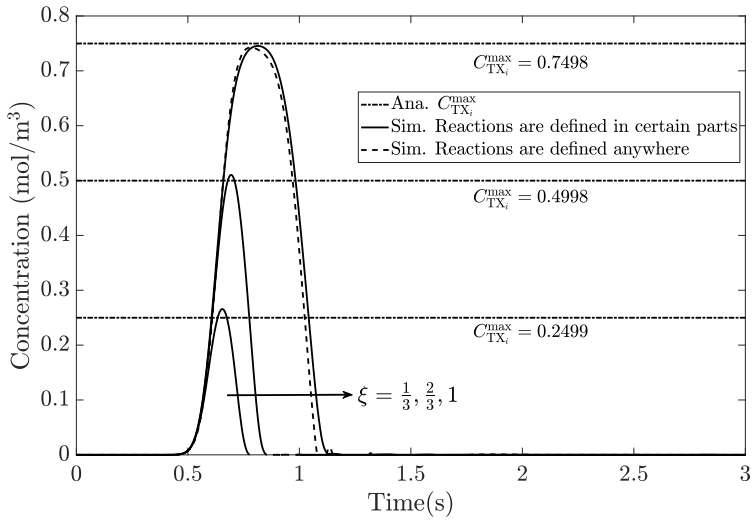

Fig. 4.9 The concentrations of generated pulses for different transmitter implementations.

demonstrating a successful BCSK modulation. Moreover, we can observe that all the maximum concentrations of pulses reach their corresponding analytical values (black dash-dot lines). It is also seen that the longer the Reaction II channel is, the wider the generated pulse, because of the longer time given to reach a higher maximum concentration. However, we remark that there is a trade-off between the maximum concentration and the pulse width, as a wider generated pulse is more likely to cause inter-symbol interference (ISI). These observations reveal the dependency of the maximum concentration of a generated pulse on the Reaction II channel length L_2, show how the predefined shaping of the pulse can be controlled, and highlight the

importance of deriving theoretical signal responses in the design stage. Since different concentration levels can represent various symbols, the results also demonstrate the capability of optimization flow in implementing higher-order CSK to enhance data rate. In addition, the black dash line represents the simulation results that the three chemical reactions in (4.1)-(4.3) are defined in all channels in Fig. 4.8(c). We can see that the transmitter output is almost the same as the results that reactions are defined in certain parts. The reason is that the selected channel lengths, mean velocity, and rate constant can jointly allow for completing reactions fast enough before leaving defined regions.

Optimal Design of the Restricted Time Gap

The design that the Reaction II channel is longer than the Reaction I channel ($L_2 > L_1$) is also likely to cause distorted pulses if the time gap ΔT between two consecutive input bits is not chosen appropriately. Assuming that species Y generated by the $(i+1)$th input bit arrives earlier than the leaving time of species P generated by the ith input bit at Reaction III channel inlet, Y will be immediately consumed according to Reaction III when they simultaneously enter Reaction III channel so that the maximum concentration of the generated pulse for the $(i+1)$th input bit is distorted and smaller than $C_{\mathrm{TX}_i}^{\max}$. To prevent this, the time gap ΔT should be restricted.

Recall that the arriving and leaving time of species Y at Reaction III channel inlet are denoted as $t_{Y_i}^A$ and $t_{Y_i}^E$ for the ith input bit, and corresponding the arriving and leaving time of species P are denoted as $t_{P_i}^A$ and $t_{P_i}^E$. As shown in Fig. 4.10, species Y generated by the $(i+1)$th input bit can appear earlier (i.e., $t_{P_i}^E > t_{Y_{i+1}}^A$) or later (i.e., $t_{P_i}^E < t_{Y_{i+1}}^A$) than species P generated by the ith input bit via adjusting ΔT. In Case I, the earlier arriving of Y makes itself react with the tail of P, thus breaking the principle that Y should increase to $C_{\mathrm{TX}_i}^{\max}$ and then drop to zero. To avoid this, ΔT needs to satisfy

$$\Delta T \geq t_{P_i}^E - t_{Y_i}^A, \tag{4.33}$$

where $t_{Y_i}^A$ and $t_{P_i}^E$ can be numerically solved by

$$C_Y(L_Y + L_1 + L_C, t) \leq \tau,\ t \leq t_{Y_i}^A,\ C_Y(L_Y + L_1 + L_C, t) > \tau,\ t > t_{Y_i}^A; \tag{4.34}$$

$$C_P(L_Y + L_1 + L_C, t) \geq \tau,\ t \leq t_{P_i}^E,\ C_P(L_Y + L_1 + L_C, t) < \tau,\ t > t_{P_i}^E. \tag{4.35}$$

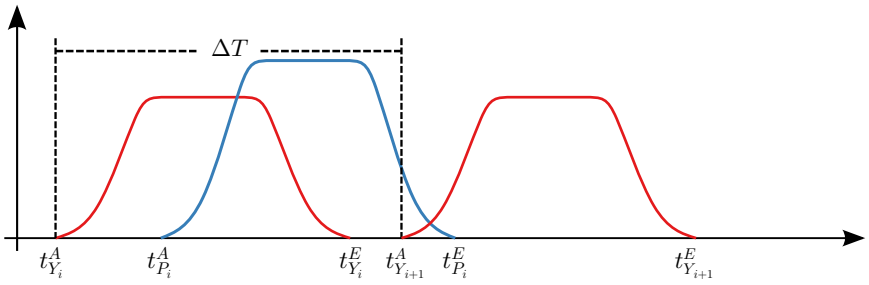

(a) Case I: $t^E_{P_i} > t^A_{Y_{i+1}}$

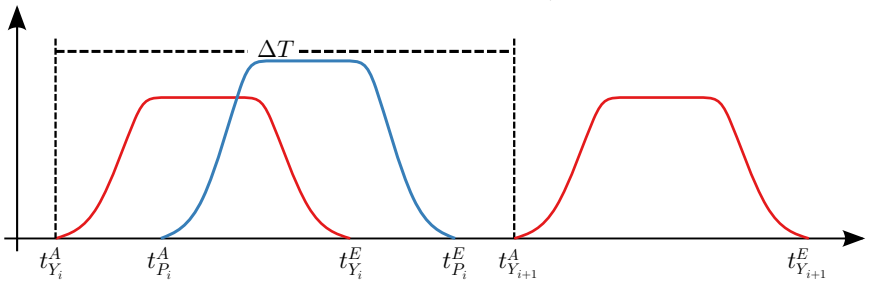

(b) Case II: $t^E_{P_i} < t^A_{Y_{i+1}}$

Fig. 4.10 Two cases of the arriving and leaving of species Y and P at Reaction III channel.

Here, τ is a small variable to find $t^A_{Y_i}$ and $t^E_{P_i}$ that $C_Y(L_Y + L_1 + L_C, t^A_{Y_i}) = 0$ and $C_P(L_Y + L_1 + L_C, t^E_{P_i}) = 0$, respectively.

In Fig. 4.11, we plot the concentrations of species Y and P at the Reaction III channel inlet and the generated pulses with different ΔT. We use the parameters for Fig. 4.8c (i.e., 2 delay lines) and $\tau = 10^{-3}$. We numerically solve (4.34), (4.35) and obtain $\Delta T \geq 2.75$s. Fig. 4.11c shows that the second pulse is distorted compared to the first pulse. With $\Delta T = 2.3$s, the species Y generated by the 2nd input bit is first consumed by the tail of P generated by the 1st input bit and then by species P generated by the 2nd input bit. On the contrary, Fig. 4.11d illustrates a generation of two non-distorted and identical-shaped pulses with a satisfied ΔT.

4.5 BCSK Receiver Analysis and Design Optimization

In this section, we analyze the T Junction and two reaction channels and then provide some guidelines on how to design a microfluidic MC receiver.

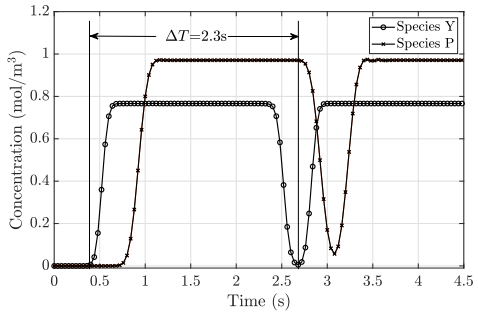

(a) The durations of two consecutive input bits are $[0.1, 2.1]$ and $[2.4, 4.4]$, $\Delta T = 2.3$s.

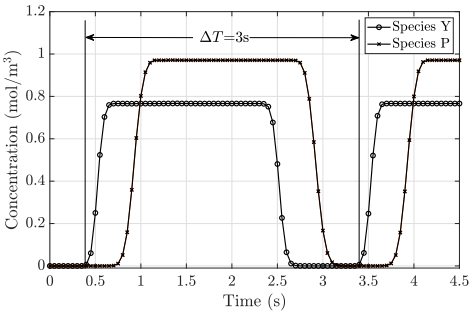

(b) The durations of two consecutive input bits are $[0.1, 2.1]$ and $[3.1, 5.1]$, $\Delta T = 3.0$s.

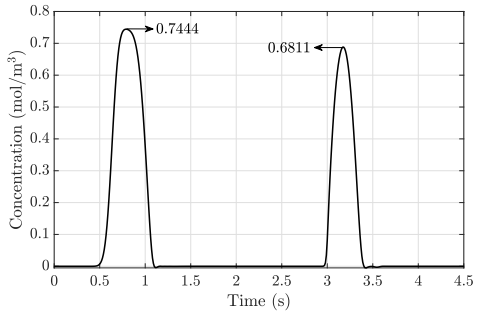

(c) The generated pulses of (a).

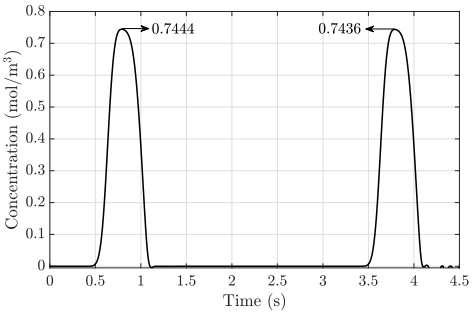

(d) The generated pulses of (b).

Fig. 4.11 The concentrations of species Y and P at Reaction III channel inlet and their generated pulses with different ΔT.

4.5.1 Microfluidic MC Receiver Analysis

T Junction

After propagation, the transmitted molecules Y finally enter the receiver through Inlet V (see Fig. 4.3). Here, we set the location of Inlet V as the position origin and the time that species Y flows into Inlet V as the time origin. Since the transmitted pulse cannot be theoretically derived, we use a Gaussian concentration distribution with mean μ and variance σ^2 to represent the received pulse, which is

$$C_{Y_0}(t) = \frac{C_{Y_0}^{\mathrm{V}}}{\sqrt{2\pi\sigma^2}} e^{-\frac{(t-\mu)^2}{2\sigma^2}}. \tag{4.36}$$

The motivation for using a Gaussian signal as the receiver input is that it can reveal the dispersion effect of molecule diffusion (i.e., Taylor dispersion) on transmitted signals, thus representing the distortion of transmitted signals occurring in the propagation channel between a transmitter and a receiver. For more details on Taylor dispersion, we refer readers to Chapter 3.1.3. Although a Gaussian concentration profile is considered,

the methodology for deriving **Theorem 2** and analyzing the receiver performance can also deal with other concentration profiles.

As the length of one T junction branch L_T is much shorter than that of the following reaction channel, and no reaction happens in a T junction, we further assume the concentration of species Y at the T junction I outlet as

$$C_Y(L_T + L_C, t) = \frac{1}{2} C_{Y_0}(t - t_{\mathrm{T}}), \tag{4.37}$$

where the coefficient $\frac{1}{2}$ describes the dilution of species Y by species ThL according to (3.14) in **Lemma 1**, and t_{T} is the travelling time over T junction I. Based on (3.16) in **Lemma 2**, the fluxes from Inlet V and Inlet VI double the averaged velocity in the conjunction of T junction I. Thus, t_{T} can be calculated as

$$t_{\mathrm{T}} = \frac{L_T}{u_{\mathrm{eff}}} + \frac{L_C}{2u_{\mathrm{eff}}}, \tag{4.38}$$

where u_{eff} is the average injection velocity at Inlet V and Inlet VI, and L_T and L_C have been labeled in Fig. 4.3. Assuming that species ThL is continuously injected into Inlet VI with concentration $C^{\mathrm{VI}}_{ThL_0}$, the outlet concentration of species ThL can be expressed as

$$C_{ThL}(L_T + L_C, t) = \frac{1}{2} C^{\mathrm{VI}}_{ThL_0},\ t \geq t_{\mathrm{T}}. \tag{4.39}$$

Straight Reaction IV Channel

The outflow of T junction I enters the Reaction IV channel with length L_4 to proceed Reaction IV (the thresholding reaction) in (4.4), where the portion of species Y, whose concentration is below $\frac{1}{2} C^{\mathrm{IV}}_{ThL_0}$, is depleted by reactant ThL. With (4.37) and (4.39), the concentration of species Y at Reaction IV channel outlet can be expressed using (4.16) or (4.17) in **Theorem 2** by substituting $C_{S_{i_0}}$ and $C_{S_{j_0}}$ with $C^{\mathrm{V}}_{Y_0}$ and $C^{\mathrm{VI}}_{ThL_0}$, which yields

$$C_Y(L_T + L_C + L_4, t) = \frac{1}{2} C^{\mathrm{Method1}}_{S_i}(L_4, t - t_{\mathrm{T}}) \ \text{ or } \ \frac{1}{2} C^{\mathrm{Method2}}_{S_i}(L_4, t - t_{\mathrm{T}}). \tag{4.40}$$

Straight Reaction V Channel

After Reaction IV, the remaining species Y flows into the Reaction V channel and catalyzes the conversion of species Amp into output species O, where Amp is continuously infused with constant concentration $C^{\mathrm{VII}}_{Amp_0}$ into Inlet VII. As a catalyst, species

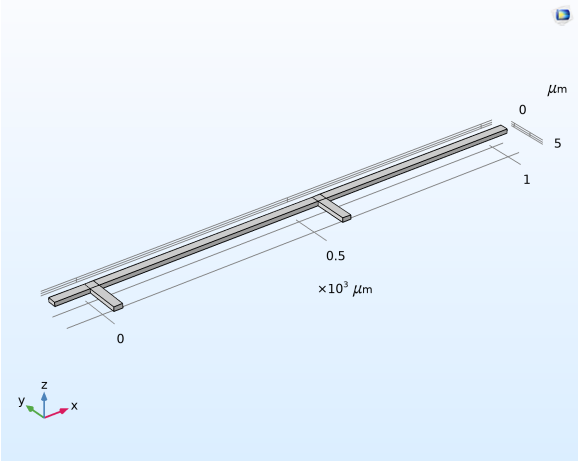

Fig. 4.12 The COMSOL implementation of the proposed microfluidic receiver design.

Table 4.3 The parameters of the proposed microfluidic receiver.

Channel	Length	Width	Height
T Junction	$L_T = 80$	20	10
Conjunction	$L_C = 20$	20	10
Reaction IV Channel	$L_4 = 520$	20	10
Reaction V Channel	$L_5 = 470$	20	10

Y does not react with species Amp, and the produced quantity of species O equals the reacting concentration of Amp according to their stoichiometric relation. Considering the dilution at T junction II, the reacting concentration of Amp is diluted to one-third of its injected concentration by flows injected at Inlet V and Inlet VI. Based on this and ignoring the diffusion effect in the Reaction V channel, the demodulated signal containing species O can be expressed as

$$C_O(t) = \begin{cases} \frac{1}{3}C_{Amp_0}^{\mathrm{VII}}, & C_Y(L_T + 2L_C + L_4 + L_5, t - \frac{L_C+L_5}{3v_{\mathrm{eff}}}) \geq 0 \\ 0, & \text{otherwise,} \end{cases} \tag{4.41}$$

where $C_Y(x,t)$ can be expressed using $C_{S_i}^{\mathrm{Method1}}$ or $C_{S_i}^{\mathrm{Method2}}$ given in **Theorem 2**. Note that without the broadening effect of diffusion [96], the width of (4.41) is exactly a lower bound of the rectangular width.

Simulation Results

To examine the microfluidic receiver analysis, we implement the receiver design in COMSOL (shown in Fig. 4.12) with geometric parameters listed in Table 4.3. We set

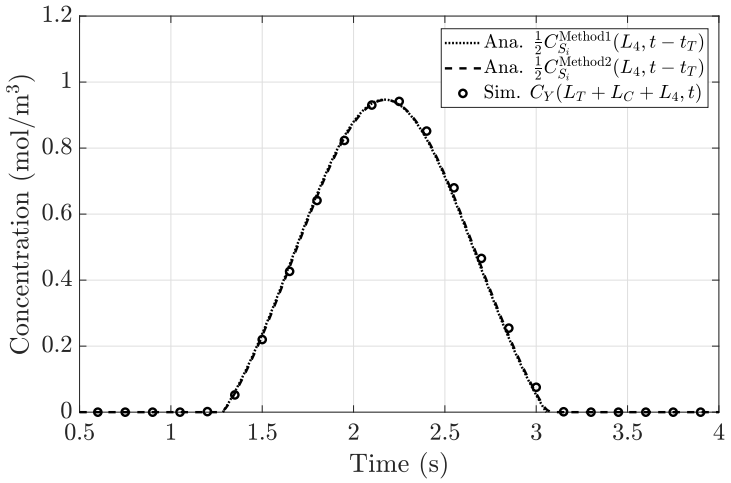

Fig. 4.13 The concentration of species Y at Reaction IV channel outlet.

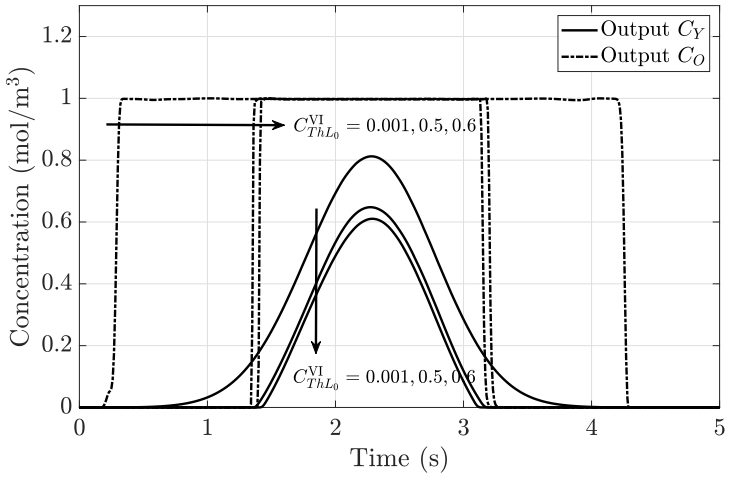

Fig. 4.14 The concentrations of species Y and O at Reaction V channel outlet with different $C_{ThL_0}^{\text{VI}}$, where the concentration of species O is normalized to 1mol/m^3.

the parameters: $C_{Y_0}^{\text{V}} = 3\text{mol/m}^3$, $\mu = 2$, $\sigma^2 = 0.25$, $k_f = 400\text{m}^3/(\text{mol·s})$, $D = 10^{-8}\text{m}^2/\text{s}$, and $u_{\text{eff}} = 0.2\text{cm/s}$.

Fig. 4.13 compares the concentration of species Y at Reaction IV channel outlet with the two expressions in (4.40). We observe that the two expressions can capture the simulation results, which further demonstrates the correctness of **Theorem 2**. Fig. 4.14 demonstrates the significant role of $C_{ThL_0}^{\text{VI}}$ on the width of the demodulated signal $C_O(t)$. As $C_{ThL_0}^{\text{VI}}$ increases, the width of the demodulated signal decreases. If $C_{ThL_0}^{\text{VI}} > \max\{C_{Y_0}(t)\}$, we expect that there is no residual Y in Reaction V channel, so that species O cannot be produced. Fig. 4.15 plots the concentrations of species O at

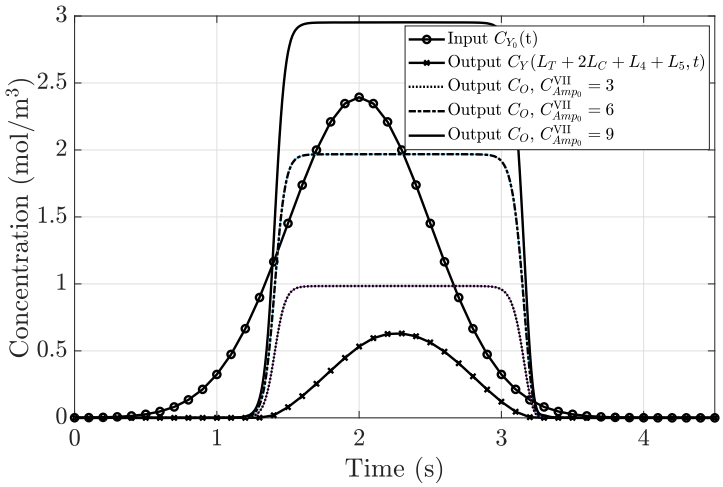

Fig. 4.15 The outlet concentrations of species O at Reaction V channel with different $C^{\mathrm{VII}}_{Amp_0}$.

Reaction V channel outlet with different $C^{\mathrm{VII}}_{Amp_0}$. As expected, the outlet concentration of species O varies with $C^{\mathrm{VII}}_{Amp_0}$ and approximately equals $\frac{1}{3}C^{\mathrm{VII}}_{Amp_0}$, which not only validates the derivation (3.14) in **Lemma 1** but also reveals the possibility to reach any level C_O via adjusting $C^{\mathrm{VII}}_{Amp_0}$.

4.5.2 Microfluidic MC Receiver Design Optimization

Based on the simulation results in Fig. 4.14 and 4.15, we conclude two receiver design guidelines. First, the results in Fig. 4.14 reveal that the width of demodulated signals is dependent on $C^{\mathrm{VI}}_{ThL_0}$, and $C^{\mathrm{VI}}_{ThL_0}$ cannot exceed the maximum concentration of a received pulse. This guideline in turn highlights the necessity and importance of studying the maximum concentration control of a generated pulse in Chapter 4.4.2. Second, the results in Fig. 4.15 present the relation between $C^{\mathrm{VII}}_{Amp_0}$ and C_O, which follows $C_O = \frac{1}{3}C^{\mathrm{VII}}_{Amp_0}$. This insight is helpful for concentration detection. If concentration is detected through fluorescence, the relation $C_O = \frac{1}{3}C^{\mathrm{VII}}_{Amp_0}$ enables us to determine how much $C^{\mathrm{VII}}_{Amp_0}$ should be injected to ensure fluorescent species O to be captured by a microscopy.

4.6 End-to-End BCSK System Implementation

In this section, we combine the microfluidic transmitter with the receiver to form a basic end-to-end BCSK system as proposed in Fig. 4.3, where the transmitter and

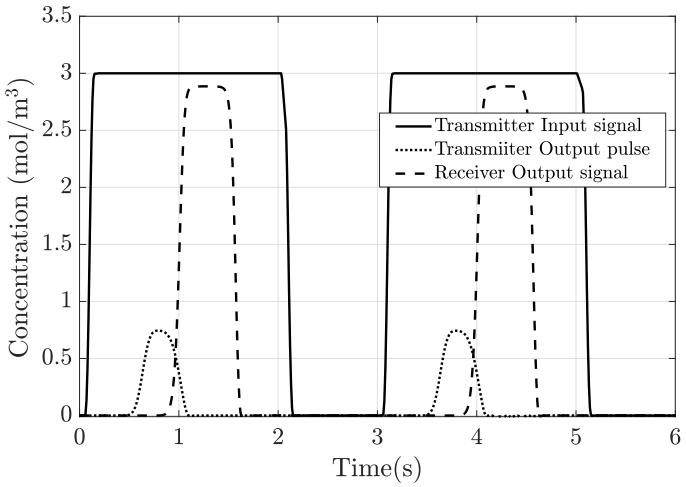

Fig. 4.16 The transmitter input signals, transmitter output pulses, and receiver output signals for the basic end-to-end MC implementation.

the receiver share the same design parameters as implementations in Fig. 4.11b and Fig. 4.12, and the propagation channel is a straight advection-diffusion channel with length 1000μm. Considering the reacting concentration of species *Amp* is diluted to one-fourth of its injected concentration $C^{\mathrm{VII}}_{Amp_0}$ by flows from Y Junction I outlet, Y Junction II outlet, and Inlet VI, we set $C^{\mathrm{VII}}_{Amp_0} = 12\mathrm{mol/m}^3$ for the purpose of restoring the output concentration level to input concentration of species X injected at Inlet II ($C^{\mathrm{II}}_{X_0} = 3\mathrm{mol/m}^3$).

Fig. 4.16 plots the transmitter input signals, transmitter output pulses, and receiver output signals. It is clear that two consecutive rectangular signals are successfully transmitted with a data rate 2bits/6s=$\frac{1}{3}$bit/s. This data rate would be increased or decreased in practical applications depending on the selected molecule types. Moreover, we observe that although the concentrations of transmitter output pulses are much lower than concentrations of transmitter input signals due to two dilutions that occurred at Y Junction output and the conjunction between Reaction I/II channel and Reaction III channel, the concentrations of receiver output signals can be approximately restored to the same concentration level of input signals via adjusting $C^{\mathrm{VII}}_{Amp_0}$.

4.7 Conclusion

In this chapter, we presented an optimized BCSK transmitter design. Specifically, we proposed a reaction channel length optimization framework to control the maximum concentration of an output pulse at the transmitter, and then derived a time gap

constraint between two consecutive input bits to ensure a continuous transmission of non-distorted and identical-shaped pulses upon consecutive digital inputs. We then proposed a microfluidic BCSK receiver design based on a thresholding reaction and an amplifying reaction to demodulate a received signal into a rectangular output signal. Both the proposed designs were based on microfluidic systems with standard and reproducible components, and these microfluidic components were analytically characterized to reveal the dependence of generated pulses and demodulated signals on design parameters. Finally, we implemented an end-to-end microfluidic BCSK system by connecting the transmitter with the receiver, and simulation results performed in COMSOL Multiphysics demonstrated successful pulse generation and signal demodulation, thus the effectiveness of the proposed designs.

Chapter 5

Chemical-Reactions-based Microfluidic QCSK Realization

5.1 Introduction

The objective of this chapter is to further explore how chemical-reactions-based microfluidic circuits can be utilized to achieve MC functions. In Chapter 4, although a chemical-reactions-based microfluidic BCSK transceiver design has been presented, there are some interesting problems that are still needed to be considered. First, the proposed reaction channel length optimization framework demonstrates the possibility of using different channel lengths to achieve higher-order CSK, but it is unclear how to change channel length on the fly. Second, the mathematical framework presented in Chapter 4 only focuses on a *single* channel but failed to provide the closed-form expressions of transmitted pulses and demodulated signals. In other words, this mathematical framework is not scalable with the increase in the number of microfluidic circuits, which highlights the challenge of theoretically characterizing microfluidic circuits. Furthermore, for the five-level microfluidic circuit architecture and the digital logic gates proposed in Chapter 3, it is worthwhile to seek what signal processing functions can be built for the top level through combinations of the logic gates proposed at a lower level (see Fig. 3.5).

Motivated by the above, this chapter aims to employ microfluidic logic gates to achieve QCSK modulation-demodulation function and establish a mathematical framework to analyze any microfluidic MC circuit [139, 140]. The main contributions of this chapter are as follows:

- We first optimize the chemical-reactions-based microfluidic AND gate design proposed in Chapter 3, based on which, we design the microfluidic transmitter and receiver with QCSK modulation and demodulation functionalities, showing how logic computations can process molecular concentrations and realize communication functionalities. The QCSK transceiver design presents a specific example of how digital electronics theory and the five-level microfluidic circuit architecture can facilitate microfluidic circuit design, which serves as a foundation for utilizing simple microfluidic logic gates to achieve more complex MC functions.

- We develop a novel mathematical framework to characterize the proposed microfluidic circuits, which can be applied to analyze other new and more complicated microfluidic circuits. We first derive the impulse response of a straight advection-diffusion channel. Based on this, we derive the spatial-temporal concentration distribution of an advection-diffusion-reaction channel with two types of reactions.

- To evaluate the proposed microfluidic designs, we identify four elementary microfluidic blocks of the basic AND gate, and define five corresponding operators to represent the output concentration distribution of each elementary block. Relying on these, we derive not only the output concentration distribution of the proposed AND gate, but also the output distributions for the designed QCSK transmitter and receiver. The functionalities of our proposed microfluidic designs and the corresponding theoretical results are validated via simulations performed in COMSOL Multiphysics finite element solver.

The remainder of this chapter is organized as follows. In Chapter 5.2, a mathematical framework to theoretically characterize the optimized AND gate is established. In Chapter 5.3, the designs and analyses of the QCSK transmitter and receiver are proposed. Numerical results in Chapter 5.4 validate the proposed microfluidic designs and their theoretical analyses. Finally, Chapter 5.5 concludes the chapter.

5.2 Optimized AND Logic Gate Design and Analysis

In this section, we first optimize the microfluidic AND logic gate proposed in Chapter 3 and then propose a new mathematical framework for microfluidic circuits.

The optimized AND gate design is presented in Fig. 5.1. To distinguish between advection-diffusion channels and advection-diffusion-reaction channels, the latter is

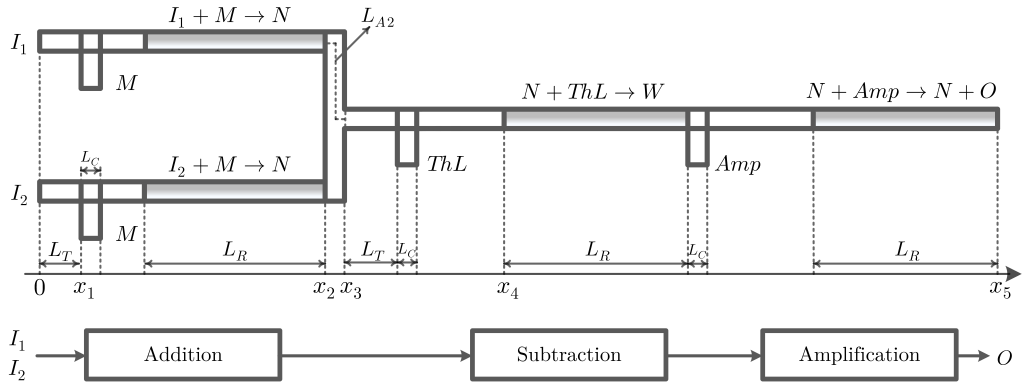

Fig. 5.1 The optimized chemical-reactions-based microfluidic AND logic gate.

filled with grey-gradient color. Compared to the AND gate design shown in Fig. 3.7, on the one hand, some extra advection-diffusion channels are introduced before advection-diffusion-reaction channels to act as buffer channels, which allow reactants to be well mixed with each other; on the other hand, the Y junctions are replaced by T junctions to simplify the following analysis. As can be seen from Fig. 5.1, the optimized AND gate design is still consisted of the addition, subtraction, and amplification modules proposed for Level 3 of the five-level microfluidic circuit architecture (see Figs. 3.5 and 3.6). Specifically, the addition module first converts two input species I_1 and I_2 to an intermediate species N. Recall that we use non-zero concentrations to represent the HIGH state (bit-1), and zero concentration to represent the LOW state (bit-0); thus, the state of species N will be HIGH if either I_1 or I_2 is HIGH. Then, species N flows into a subtraction module with reaction $N + ThL \rightarrow W$ and undergoes a depletion by species ThL. By injecting a certain amount of species ThL, the remaining concentration of species N can be larger than zero only when both input species I_1 and I_2 are HIGH. Finally, the remaining species N catalyzes the conversion of species Amp to output species O in an amplification module via reaction $N + Amp \rightarrow N + O$, and the concentration of species O can be adjusted to a desired level based on the injected concentration of species Amp.

To derive the output concentration of the designed AND gate, we first need to study the molecule concentration distribution in a single channel. For a 3D straight microfluidic channel, under the assumption that molecule transport falls into the dispersion regime, molecules will be uniformly distributed across the cross-section.

Thus, the 3D advection-diffusion-reaction equation in (2.11) can be reduced to

$$\frac{\partial C_{S_i}(x,t)}{\partial t} = D_{\text{eff}}\frac{\partial^2 C_{S_i}(x,t)}{\partial x^2} - u_{\text{eff}}\frac{\partial C_{S_i}(x,t)}{\partial x} + qf[k_f, C_{S_i}(x,t)], \tag{5.1}$$

where the calculation of *Taylor-Aris* effective diffusion coefficient D_{eff} has been given in (4.7). In addition, when $k_f = 0$, eq. (5.1) reduces to the 1D advection-diffusion equation in (4.6).

In the following, we first derive the impulse response of an advection-diffusion channel in Chapter 5.2.1. Based on the impulse response, we then study the molecule concentration of a reaction channel. In particular, we study the reaction channel with Type I reaction, i.e., $S_i + S_j \rightarrow S_k$, in Chapter 5.2.2 and the reaction channel with Type II reaction, i.e., $S_i + Amp \rightarrow S_i + O$, in Chapter 5.2.3. Furthermore, relying on the fluid mixing and separation analysis in Chapters 3.1.5 and 3.1.6, we define and model four elementary blocks (Chapter 5.2.4) in order to simplify the theoretical characterizations of the AND gate in Chapter 5.2.5 and the more complicated microfluidic circuits proposed in Chapter 5.3.

5.2.1 Advection-Diffusion Channel

Without chemical reactions, the concentration distribution of species S_i can be expressed using the 1D advection-diffusion equation given in (4.6), which is

$$\text{Eq. (4.6)}: \ \frac{\partial C_{S_i}(x,t)}{\partial t} = D_{\text{eff}}\frac{\partial^2 C_{S_i}(x,t)}{\partial x^2} - u_{\text{eff}}\frac{\partial C_{S_i}(x,t)}{\partial x}.$$

Although the above PDE has been studied in **Theorem 1** for input signals with a rectangular concentration profile, the complex expression of the solution in (A.13) does not allow the cascaded channels to be mathematically solvable in closed-form. This shortcoming motivates us to derive the impulse response of a microfluidic channel so that the output of a microfluidic circuit can be written as the convolution of an input and a cascade of the impulse response of each channel. We solve the impulse response in the following theorem.

Theorem 3. *The impulse response of a straight advection-diffusion channel is derived as*

$$H(x,t) = \frac{1}{2\pi}\int_0^\infty [e^{-j\omega t}\overline{\widetilde{C_{S_i}}(x,\omega)} + e^{j\omega t}\widetilde{C_{S_i}}(x,\omega)]\mathrm{d}\omega, \tag{5.2}$$

where

$$\widetilde{C_{S_i}}(x,\omega) = \exp\left[\frac{u_{\text{eff}}x}{2D_{\text{eff}}} - \sqrt{\frac{x^2(u_{\text{eff}}^2 + 4j\omega D_{\text{eff}})}{4D_{\text{eff}}^2}}\right] \tag{5.3}$$

and $\overline{\widetilde{C_{S_i}}(x,\omega)}$ *is the complex conjugate of* $\widetilde{C_{S_i}}(x,\omega)$.

Proof. Please refer to Appendix B.1. □

From **Theorem 3**, the concentration of species S_i can be expressed as

$$C_{S_i}(x,t) = C_{S_{i_0}}(t) * H(x,t), \tag{5.4}$$

where $C_{S_{i_0}}(t)$ is the input concentration of species S_i at channel inlet and "$*$" denotes the convolution operator.

5.2.2 Reaction Channel with Type I Reaction

When a microfluidic channel contains a reaction $S_i + S_j \to S_k$, the spatial-temporal concentration distributions of reactant and product can be expressed by (4.8) and (4.9), which are

$$\text{Eq. (4.8)}: \ \frac{\partial C_{S_i}(x,t)}{\partial t} = D_{\text{eff}}\frac{\partial^2 C_{S_i}(x,t)}{\partial x^2} - u_{\text{eff}}\frac{\partial C_{S_i}(x,t)}{\partial x} - k_f C_{S_i}(x,t)C_{S_j}(x,t),$$

$$\text{Eq. (4.9)}: \ \frac{\partial C_{S_k}(x,t)}{\partial t} = D_{\text{eff}}\frac{\partial^2 C_{S_k}(x,t)}{\partial x^2} - u_{\text{eff}}\frac{\partial C_{S_k}(x,t)}{\partial x} + k_f C_{S_i}(x,t)C_{S_j}(x,t).$$

Compared with the advection-diffusion equation in (4.6), the newly introduced reaction term is fully coupled with the advection and diffusion process, which complicates the resolution of (4.8) and (4.9). A strategy to tackle this coupling is to apply the "operator splitting" method. It first divides an original differential equation into several sub-equations, which are solved separately to give their individual solutions. Then, the solutions for sub-equations are combined to form a solution for the original equation [141]. The derived impulse response of an advection-diffusion channel in **Theorem 3** motivates us to separate an advection-diffusion-reaction equation into a reaction term and an advection-diffusion term. This separation can be achieved via 1) assuming the reactants are added into a virtual reactor, and the unconsumed reactants and generated product flow into an advection-diffusion channel as soon as the reaction stops; and 2) treating the solution of the reaction term as the initial input for the advection-diffusion part.

With species S_i and S_j continuously flowing into a channel, we regard that S_i and S_j are continuously added into a virtual reactor, where the continuous reactant supply is a superposition of reactant addition with constants at different times. To solve the reaction part, we consider the following two scenarios:

- **Scenario 1**: species S_i and S_j are only added at $t = 0$ with concentration $C_{S_{i_0}}$ and $C_{S_{j_0}}$;
- **Scenario 2**: species S_i and S_j are added continuously with concentration $C_{S_{i_0}}(t)$ and $C_{S_{j_0}}(t)$.

We first derive the concentration changes of reactants and product for **Scenario 1**, which will then be applied to **Scenario 2** to derive the solutions of the separated reaction term.

Scenario 1

Let $c(t)$ denote the consumed concentration of reactant S_i or S_j during the reaction. Note that $c(t)$ can also represent the concentration of product species S_k due to a one-to-one stoichiometric relation between reactants and product. The remaining concentrations of species S_i and S_j can be expressed as

$$C_{S_i}(t) = C_{S_{i_0}} - c(t), \tag{5.5a}$$

$$C_{S_j}(t) = C_{S_{j_0}} - c(t). \tag{5.5b}$$

Then, the reaction equation can be expressed as [142, eq. (9.13)]

$$\frac{\mathrm{d}[C_{S_{i_0}} - c(t)]}{\mathrm{d}t} = -k_f[C_{S_{i_0}} - c(t)][C_{S_{j_0}} - c(t)]. \tag{5.6}$$

After rearrangement, eq. (5.6) becomes

$$\frac{\mathrm{d}c(t)}{[C_{S_{i_0}} - c(t)][C_{S_{j_0}} - c(t)]} = k_f \mathrm{d}t. \tag{5.7}$$

By taking the integral of the two sides of (5.7), we yield

$$c(t) = \begin{cases} \frac{C_{S_{i_0}} C_{S_{j_0}} \exp\left[(C_{S_{j_0}} - C_{S_{i_0}})k_f t\right] - C_{S_{i_0}} C_{S_{j_0}}}{C_{S_{j_0}} \exp\left[(C_{S_{j_0}} - C_{S_{i_0}})k_f t\right] - C_{S_{i_0}}}, & C_{S_{i_0}} \leq C_{S_{j_0}}, \\ \frac{C_{S_{i_0}} C_{S_{j_0}} \exp\left[(C_{S_{i_0}} - C_{S_{j_0}})k_f t\right] - C_{S_{i_0}} C_{S_{j_0}}}{C_{S_{i_0}} \exp\left[(C_{S_{i_0}} - C_{S_{j_0}})k_f t\right] - C_{S_{j_0}}}, & C_{S_{i_0}} \geq C_{S_{j_0}}. \end{cases} \tag{5.8}$$

Remark 4. *It can be observed from* (5.8) *that* $c(t)$ *is proportional to the rate constant* k_f*. The higher the rate constant is, the faster a reactant is consumed and decreased to zero.*

Lemma 4. *For reaction* $S_i + S_j \to S_k$*, when reaction rate* $k_f \to \infty$*, the consumed concentration* $c(t)$ *of reactant can be derived as*

$$\lim_{k\to\infty} c(t) = \varphi(C_{S_{i_0}}, C_{S_{j_0}}), \tag{5.9}$$

where $C_{S_{i_0}}$ *and* $C_{S_{j_0}}$ *are the initial concentrations of species* S_i *and* S_j*, and* $\varphi(\cdot,\cdot)$ *is defined as*

$$\varphi(x, y) = \min\{x, y\}. \tag{5.10}$$

Proof. With $k_f \to \infty$, eq. (5.8) can be easily reduced to (5.9). □

Scenario 2

Now, we consider the continuous injection of species S_i and S_j with concentrations $C_{S_{i_0}}(t)$ and $C_{S_{j_0}}(t)$. **Scenario 2** can be regarded as a superposition of **Scenario 1** in time domain. To apply the analysis of **Scenario 1**, we first discretize the reaction process into many time intervals with step Δt. Thus, the added concentration of species S_i can be denoted as $C^n_{S_i,a} = C_{S_{i_0}}(n\Delta t)$ $(n \geq 0)$, where the subscript a refers to addition.[1] We also denote $C^n_{S_{i_0}}$ and $C^n_{S_i,r}$ as the initial and the remaining concentrations of S_i at $t = n\Delta t$, respectively. The same notations are also applied to species S_j.

We propose **Algorithm 1** to numerically calculate the remaining concentrations of S_i and S_j for reaction $S_i + S_j \to S_k$. **Algorithm 1** describes that for any time interval $[n\Delta t, (n+1)\Delta t]$, the consumed concentration can be calculated according to (5.8), but with different initial concentrations $C^n_{S_{i_0}}$. The difference in the initial concentration is due to the fact that the initial concentration at any time interval is influenced not only by the newly added concentration, but also by the incompletely consumed concentration that was added in previous intervals. For instance, the initial concentration $C^1_{S_{i_0}}$ for the time interval $[\Delta t, 2\Delta t]$ is the sum of the newly added concentration $C^1_{S_i,a}$ and the remaining concentration $C^1_{S_i,r}$ that added at $t = 0$.

The value of the rate constant k_f influences the approximation accuracy. The smaller the k_f is, the larger volume of reactants remain. The unconsumed reactants accumulate in the reactor and would participate in the reaction in the following time interval, which introduces a correlation between different time intervals. By contrast,

[1] Throughout this chapter, the superscript for concentration C does not represent a mathematical operation.

Algorithm 1: The Calculation of Remaining Concentrations of Species S_i and S_j

Input: The input concentrations $C_{S_{i_0}}(t)$ and $C_{S_{j_0}}(t)$. The calculation time interval $[0, T]$. The time step Δt.

1 Initialization of $C^0_{S_{i_0}}{=}C^0_{S_i,a}$ and $C^0_{S_{j_0}}{=}C^0_{S_j,a}$.

2 **for** $n \leftarrow 1, \lfloor T/\Delta t \rfloor$ **do**

3 Calculate the consumed concentration c^{n-1} during $[(n-1)\Delta t, n\Delta t]$ according to (5.8) by interchanging $C_{S_{i_0}} \rightarrow C^{n-1}_{S_{i_0}}$ and $C_{S_{j_0}} \rightarrow C^{n-1}_{S_{j_0}}$.

4 Update the remaining concentration $C^n_{S_i,r}{=}C^{n-1}_{S_{i_0}}{-}c^{n-1}$ and $C^n_{S_j,r}{=}C^{n-1}_{S_{j_0}}{-}c^{n-1}$.

5 Update the initial concentration $C^n_{S_{i_0}}{=}C^n_{S_i,r}{+}C^n_{S_i,a}$ and $C^n_{S_{j_0}}{=}C^n_{S_j,r}{+}C^n_{S_j,a}$ for $[n\Delta t, (n+1)\Delta t]$.

6 **end**

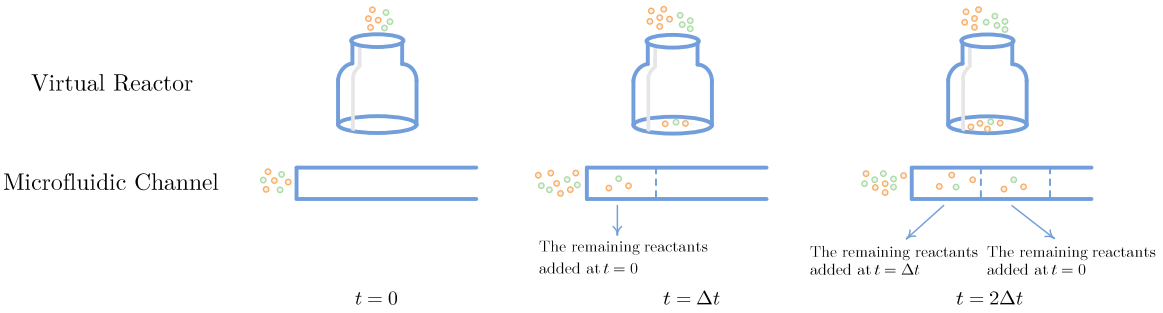

Fig. 5.2 Illustration of reaction $S_i + S_j \rightarrow S_k$ in a bottle-shaped virtual reactor and a microfluidic channel. The two reactants are marked with different colors.

this correlation does not exist in practical scenarios. As shown in Fig. 5.2, for time interval $[\Delta t, 2\Delta t]$, the flowing fluid carries remaining reactants added at $t = 0$ and $t = \Delta t$ forward, preventing them from interacting with each other. Therefore, in the virtual reactor, we should make rate constant approach infinity to ensure that reaction is always complete inside any time interval, thus eliminating the correlation[2]. With $\Delta t \rightarrow 0$, the remaining concentrations of S_i and S_j calculated in **Algorithm 1** reduce to

$$C_{S_i,r}(t) = C_{S_{i_0}}(t) - \varphi[C_{S_{i_0}}(t), C_{S_{j_0}}(t)], \tag{5.11a}$$

$$C_{S_j,r}(t) = C_{S_{j_0}}(t) - \varphi[C_{S_{i_0}}(t), C_{S_{j_0}}(t)], \tag{5.11b}$$

[2]In order to eliminate the correlation between different time intervals, the assumption $k_f \rightarrow \infty$ is only made in **Algorithm 1**. In practice, k_f cannot be infinity and k_f should be selected to ensure that a reaction is complete inside a given microfluidic channel. Otherwise, there will be a disagreement between our theoretical analysis and the simulation results.

where $\varphi(\cdot,\cdot)$ is given in (5.10).

We derive the output concentrations of species S_i, S_j, and S_k in the following lemma.

Lemma 5. *For a straight reaction channel with reaction $S_i + S_j \rightarrow S_k$, the output concentrations of species S_i, S_j, and S_k can be derived as*

$$C_{S_i}(x,t) = C_{S_i,r}(t) * H(x,t), \tag{5.12a}$$

$$C_{S_j}(x,t) = C_{S_j,r}(t) * H(x,t), \tag{5.12b}$$

$$C_{S_k}(x,t) = \varphi[C_{S_{i_0}}(t), C_{S_{j_0}}(t)] * H(x,t), \tag{5.12c}$$

where $C_{S_i,r}(t)$, $C_{S_j,r}(t)$, $H(x,t)$, and $\varphi(\cdot,\cdot)$ are given in (5.11a), (5.11b), (5.2), *and* (5.10), *respectively.*

Proof. Please refer to Appendix B.2. □

5.2.3 Reaction Channel with Type II Reaction

Lemma 6. *For a straight reaction channel with amplifying reaction $S_i + Amp \rightarrow S_i + O$, the output concentration of species O can be derived as*

$$C_O(x,t) = \left[C_{Amp_0}(t) \cdot \mathbb{1}_{\{C_{S_{i_0}}(t)>0\}}\right] * H(x,t), \tag{5.13}$$

where $C_{Amp_0}(t) = C_{Amp_0}u(t)$ and $C_{S_{i_0}}(t)$ are the injected concentrations of species Amp and S_i, $u(t)$ is the Heaviside step function, $\mathbb{1}_{\{\cdot\}}$ is the indicator function that represents the value 1 if the statement is true, and zero otherwise.

Proof. To analyze a straight microfluidic channel with amplifying reaction $S_i + Amp \rightarrow S_i + O$, we also separate it into a reaction term and an advection-diffusion term. For the reaction term, as species O is only produced in the presence of S_i and the concentration of species O equals the injected concentration of species Amp [128], the reaction solution can be expressed as $C_{Amp_0}(t) \cdot \mathbb{1}_{\{C_{S_{i_0}}(t)>0\}}$. Taking the reaction solution as the initial input for an advection-diffusion channel, we derive the concentration of product O in (5.13). □

5.2.4 Elementary Blocks

Relying on the analyses of fluid mixing in **Lemma 1** and **Lemma 2**, advection-diffusion channel in **Theorem 3**, and advection-diffusion-reaction channel in **Lemma 5 and 6**,

Table 5.1 Four elementary blocks.

Operator	Elementary Block	Operator Output
$\mathcal{T}[C_{S_{i_0}}(t), n]$ Eq. (5.14)	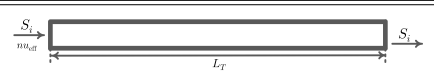	$C_{S_i}(t)$: The output of a advection-diffusion channel with length L_T.
$\mathcal{G}[C_{S_{i_0}}(t), C_{S_{j_0}}(t), n]$ Eq. (5.16)	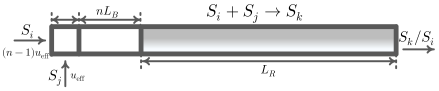	$C_{S_k}(t)$: The concentration of product S_k with $S_i + S_j \to S_k$.
$\mathcal{R}[C_{S_{i_0}}(t), C_{S_{j_0}}(t), n]$ Eq. (5.17)		$C_{S_i}(t)$: The remaining concentration of S_i with $S_i + S_j \to S_k$.
$\mathcal{A}[C_{S_{i_0}}(t), C_{Amp_0}(t), n]$ Eq. (5.18)	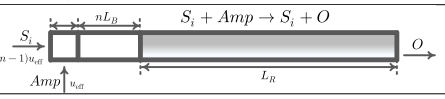	$C_O(t)$: The concentration of product O with $S_i + Amp \to S_i + O$.
$\mathcal{F}[C_{S_{i_0}}(t), C_{S_{j_0}}(t), C_{Amp_0}(t), n]$ Eq. (5.19)	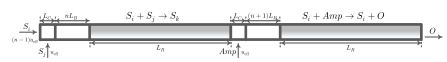	$C_O(t)$: The concentration of product O with $S_i + S_j \to S_k$ and $S_i + Amp \to S_i + O$.

we focus on the analysis of four elementary blocks of the designed AND gate (Fig. 5.1) in Table 5.1. Meanwhile, to simplify the output expression of a microfluidic circuit, we also define five typical operators for the four elementary blocks. As shown in Table 5.1, the operator $\mathcal{T}[\cdot]$ represents the output of an advection-diffusion channel with length L_T, and can be expressed as

$$\mathcal{T}[C_{S_{i_0}}(t), n] \triangleq C_{S_{i_0}}(t) * H_n(L_T, t), \tag{5.14}$$

where the subscript n of H_n indicates that the average velocity in the channel is nu_{eff}.

For the block with thresholding reaction $S_i + S_j \to S_k$, solutions containing species S_i and S_j are injected to a channel with length L_C from two inlets. The initial concentrations of species S_i and S_j are $C_{S_{i_0}}(t)$ and $C_{S_{j_0}}(t)$, and the injection speeds of species S_i and S_j are $(n-1)u_{\text{eff}}$ and u_{eff}. The combining of two solutions will result in a concentration dilution, and the diluted concentrations of S_i and S_j are $(n-1)C_{S_{i_0}}(t)/n$ and $C_{S_{j_0}}(t)/n$ following (3.13) in **Lemma 1**, respectively. Meanwhile, the average velocity will increase to nu_{eff} following (3.16) in **Lemma 2**. Then, species will flow to a buffer channel before the advection-diffusion-reaction channel filled with grey-gradient color.[3] The buffer channel allows reactants to be well mixed before a reaction, and the reactant mixing along the radial direction only relies on diffusion. The minimum buffer length L_B can be estimated as

$$L_B = \frac{w^2 + h^2}{D} u_{\text{eff}}. \tag{5.15}$$

[3]In practice, by cooling the buffer channel while heating the corresponding reaction channel, it would allow us to keep the buffer channel thermally isolated from the reaction channel, which ensures that pre-mixed reactants do not react until they reach the reaction channel [143].

The term $\frac{w^2+h^2}{D}$ quantifies the time required for molecules to be transported over distance $\sqrt{w^2+h^2}$ along the radial direction to achieve a fully diffusional mixing, and (5.15) represents how far molecules have traveled along the axial direction by advection.

We define operator $\mathcal{G}[\cdot]$ to describe the concentration of product S_k, and according to (5.12c), operator $\mathcal{G}[\cdot]$ can be expressed as

$$\mathcal{G}[C_{S_{i_0}}(t), C_{S_{j_0}}(t), n] \triangleq \varphi[(n-1)C_{S_{i_0}}(t)/n, C_{S_{j_0}}(t)/n] * H_n(nL_B + L_C, t) * H_n(L_R, t). \tag{5.16}$$

For the same reaction, we define operator $\mathcal{R}[\cdot]$ to characterize the residual concentration of S_i. According to (5.12a), operator $\mathcal{R}[\cdot]$ can be expressed as

$$\begin{aligned}\mathcal{R}[C_{S_{i_0}}(t), C_{S_{j_0}}(t), n] \triangleq &\Big[(n-1)C_{S_{i_0}}(t)/n - \varphi[(n-1)C_{S_{i_0}}(t)/n, C_{S_{j_0}}(t)/n]\Big] \\ &* H_n(nL_B + L_C, t) * H_n(L_R, t).\end{aligned} \tag{5.17}$$

For the amplifying reaction $S_i + Amp \rightarrow S_i + O$, operator $\mathcal{A}[\cdot]$ describes the concentration of product O, and can be expressed using **Lemma 6** as

$$\begin{aligned}\mathcal{A}[C_{S_{i_0}}(t), C_{Amp_0}(t), n] \triangleq &\Big[[C_{Amp_0}(t)/n * H_n(nL_B + L_C, t)] \\ &\cdot \mathbb{1}_{\{[((n-1)C_{S_{i_0}}(t)/n) * H_n(nL_B+L_C,t)]>0\}}\Big] * H_n(L_R, t).\end{aligned} \tag{5.18}$$

As seen in the AND gate design in Fig. 5.1, a threshold reaction is cascaded with an amplifying reaction; thus, we define operator $\mathcal{F}[\cdot]$ as a combination of operators $\mathcal{R}[\cdot]$ and $\mathcal{A}[\cdot]$, which represents the concentration of product O with $S_i + S_j \rightarrow S_k$ and $S_i + Amp \rightarrow S_i + O$ as

$$\mathcal{F}[C_{S_{i_0}}(t), C_{S_{j_0}}(t), C_{Amp_0}(t), n] \triangleq \mathcal{A}\Big[\mathcal{R}[C_{S_{i_0}}(t), C_{S_{j_0}}(t), n], C_{Amp_0}(t), n+1\Big]. \tag{5.19}$$

5.2.5 AND Logic Gate Analysis

We denote the initial concentrations of input species I_1 and I_2 as $C_{I_{1_0}}(t)$ and $C_{I_{2_0}}(t)$. Remind that we use non-zero concentrations to represent the HIGH state (bit-1), and zero concentrations to represent the LOW state (bit-0). Therefore, at any time t, $C_{I_{1_0}}(t)$ and $C_{I_{2_0}}(t)$ are either greater than or equal to 0. Species M, ThL, and Amp are injected continuously; thus, their initial concentrations follow $C_{M_0}(t) = C_{M_0}u(t)$, $C_{ThL_0}(t) = C_{ThL_0}u(t)$, and $C_{Amp_0}(t) = C_{Amp_0}u(t)$. For simplicity, all reactants are injected using the same average velocity u_{eff}.

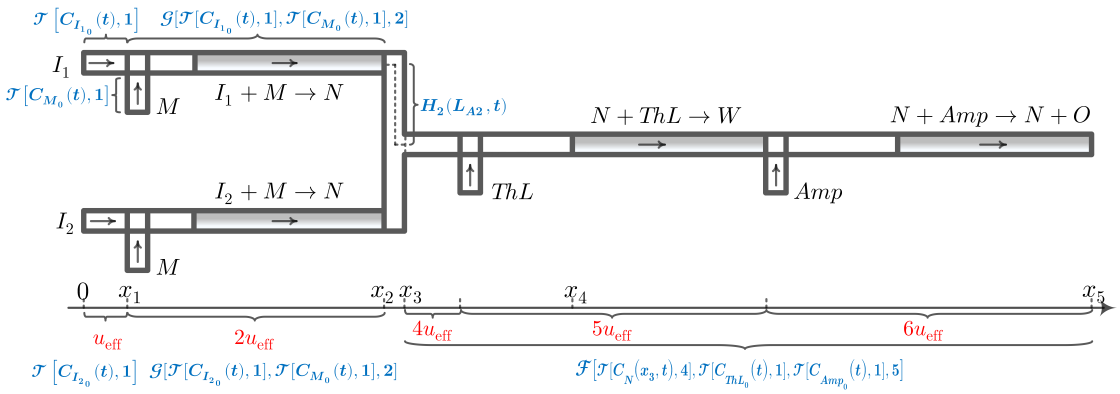

Fig. 5.3 An illustration of the theoretical characterization of our proposed AND gate design in Fig. 5.1 using the four elementary blocks and five operators in Table 5.1.

Theorem 4. *The concentration of product species O in the designed AND gate in Fig. 5.1 can be derived as*

$$C_O(x_5, t) = \mathcal{F}\Big\{\mathcal{T}[C_N(x_3, t), 4], \mathcal{T}[C_{ThL_0}(t), 1], \mathcal{T}[C_{Amp_0}(t), 1], 5\Big\}, \tag{5.20}$$

where

$$\begin{aligned} C_N(x_3, t) =& \frac{1}{2}\Big\{\mathcal{G}\Big[\mathcal{T}[C_{I_{1_0}}(t), 1], \mathcal{T}[C_{M_0}(t), 1], 2\Big] \\ &+ \mathcal{G}\Big[\mathcal{T}[C_{I_{2_0}}(t), 1], \mathcal{T}[C_{M_0}(t), 1], 2\Big]\Big\} * H_2(L_{A2}, t). \end{aligned} \tag{5.21}$$

In (5.20) *and* (5.21)*, operators $\mathcal{T}[\cdot]$, $\mathcal{G}[\cdot]$, $\mathcal{F}[\cdot]$ are defined in Table 5.1, L_{A2} is the traveling distance of the laminar located at the center channel from x_2 to x_3 in Fig. 5.1.*

Proof. To facilitate the understanding of the derivation, we illustrate the flow velocity changes using red font and the mathematical descriptions of some elementary blocks in Fig. 5.3. At position $x = x_1$, the concentrations of species I_1 and I_2 can be expressed as $\mathcal{T}[C_{I_{1_0}}(t), 1]$ and $\mathcal{T}[C_{I_{2_0}}(t), 1]$, respectively. Then, species I_1 (or I_2) and M flow into the second elementary block defined in Table 5.1, and the output product species N can be described using operator $\mathcal{G}[\cdot]$, that is: $\mathcal{G}\Big[\mathcal{T}[C_{I_{1_0}/I_{2_0}}(t), 1], \mathcal{T}[C_{M_0}(t), 1], 2\Big]$. The species N separately generated by inputs I_1 and I_2 merge with each other at position $x = x_3$. The concentration of species N at $x = x_3$ can be derived as (5.21), where the coefficient $1/2$ explains the dilution of species N generated in the upper branch by the flow in the lower branch, or vice versa. Finally, species N travels over an advection-diffusion channel and enters the elementary block $\mathcal{F}[\cdot]$ consisting of reactions $N + ThL \to W$ and $N + Amp \to N + O$ to produce the gate output O. According to

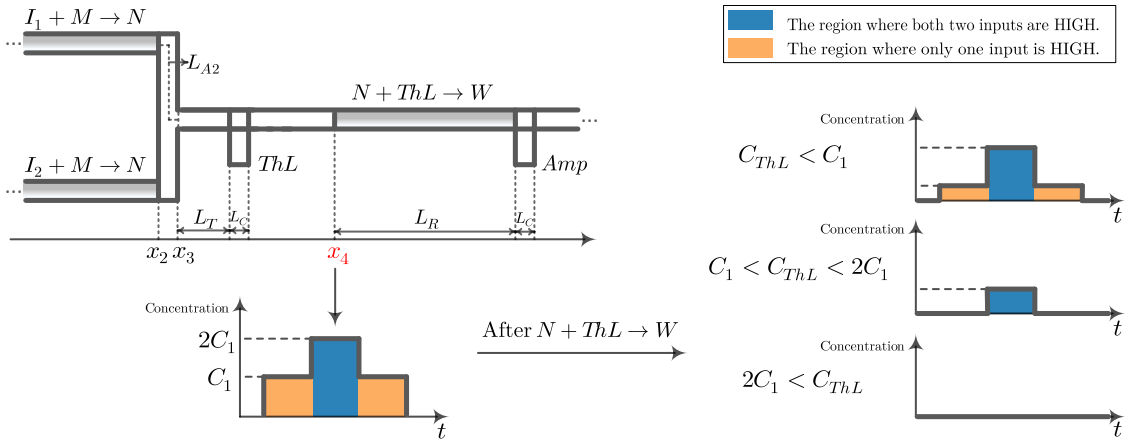

Fig. 5.4 The concentration of species N before and after the reaction $N + ThL \to W$ in the designed AND gate.

the definition of $\mathcal{F}[\cdot]$ in (5.19), the concentration of species O at location $x = x_5$ can be derived as (5.20). □

For the thresholding reaction $N + ThL \to W$ in Fig. 5.3, C_{ThL_0} directly determines the gate function. We derive the constraint for C_{ThL_0} in the following lemma.

Lemma 7. *To ensure that the designed microfluidic circuit exhibits AND logic behavior, the concentration of species ThL needs to satisfy*

$$C_{\text{Con}} < C_{ThL_0} < 2C_{\text{Con}}, \tag{5.22}$$

where

$$C_{\text{Con}} = \frac{\lim\limits_{t\to\infty} 2\mathcal{G}\Big\{\mathcal{T}[C_0 u(t), 1], \mathcal{T}[C_{M_0} u(t), 1], 2\Big\} * q(t)}{\lim\limits_{t\to\infty} \mathcal{T}[u(t), 1] * H_5(5L_B + L_C, t)}. \tag{5.23}$$

In (5.23), C_0 *is the HIGH concentration of input species* I_1 *and* I_2, C_{M_0} *is the HIGH concentration of species* M, $q(t) = H_2(L_{A2}, t) * H_4(L_T, t) * H_5(5L_B + L_C, t)$, $H(x, t)$ *is the impulse response derived in* (5.2), *and* $\mathcal{T}[\cdot]$ *and* $\mathcal{G}[\cdot]$ *are defined in* (5.14) *and* (5.16), *respectively.*

Proof. Let C_1 and C_{ThL} denote the steady-state concentrations of species N and ThL at location $x = x_4$, respectively. Fig. 5.4 plots the concentration of species N before and after reaction $N + ThL \to W$. When only one input is HIGH, the steady-state

concentration C_1 can be expressed as

$$C_1 = \lim_{t\to\infty} \frac{4}{5} \cdot \frac{1}{2} \cdot \mathcal{G}\Big\{\mathcal{T}[C_0 u(t), 1], \mathcal{T}[C_{M_0} u(t), 1], 2\Big\} * q(t), \tag{5.24}$$

where the coefficient 4/5 explains the dilution of species N by species ThL. When both inputs are HIGH, the steady-state concentration becomes $2C_1$. For species ThL, its steady-state concentration C_{ThL} at $x = x_4$ can be expressed as

$$C_{ThL} = \lim_{t\to\infty} \frac{1}{5} \mathcal{T}[C_{ThL_0} u(t), 1] * H_5(5L_B + L_C, t), \tag{5.25}$$

where the coefficient 1/5 explains the dilution of species ThL by the flow coming from location x_3. As shown in Fig. 5.4, the blue region represents that both two inputs are HIGH, and the yellow region represents that only one input is HIGH. The relationship between C_1 and C_{ThL} has three cases:

- $C_{ThL} < C_1$: After the reaction, the remaining concentration of species N contains the region where one or both the inputs are HIGH.
- $C_1 < C_{ThL} < 2C_1$: After the reaction, the remaining concentration of species N only contains the region where both two inputs are HIGH.
- $2C_1 < C_{ThL}$: After the reaction, species N is completely depleted.

Therefore, to capture the region where both the inputs are HIGH, the concentration of species ThL needs to satisfy the condition $C_1 < C_{ThL} < 2C_1$. Combined with (5.24) and (5.25), we can obtain (5.22) and (5.23). □

5.3 Microfluidic QCSK Transmitter and Receiver

In this section, we present the microfluidic designs to show how logic computations can process molecular concentration so as to achieve QCSK modulation and demodulation. Meanwhile, we also theoretically characterize the output concentration distributions of the proposed QCSK transmitter and receiver. In the end, we discuss the synchronization of molecular species in microfluidic circuits.

I_2	I_1	$O4$	$O3$	$O2$	$O1$
0	0	0	0	0	1
0	1	0	0	1	0
1	0	0	1	0	0
1	1	1	0	0	0

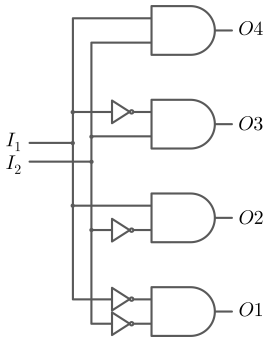

Fig. 5.5 The truth table and implementation of an electric 2:4 decoder.

5.3.1 QCSK Transmitter

QCSK Transmitter Design

QCSK modulation represents two digital inputs as four concentration levels of an output signal, which is analogous to the ASK modulation in wireless communication [144]. A challenge of implementing a QCSK MC transmitter is how to control the output concentration via four different input combinations (i.e., "00", "01", "10", and "11"). We solve this challenge by borrowing the mechanism of an electric 2:4 decoder. In electric circuits, a 2:4 decoder, which has 2 inputs and 4 outputs, selects exactly one of its outputs according to the input combination. Fig. 5.5 presents the truth table and an implementation of the electric 2:4 decoder, where four AND gates receive the HIGH or the LOW of inputs I_1 and I_2.

Inspired by the electric 2:4 decoder, we propose a chemical-reactions-based microfluidic 2:4 decoder (with a combiner) to realize QCSK modulation as shown in Fig. 5.6. The proposed microfluidic device is made up of four microfluidic units corresponding to four different concentration outputs. For ease of reference, these four units are named as Unit 4, Unit 3, Unit 2, and Unit 1 from top to bottom. Analogous to the electric 2:4 decoder in Fig. 5.5, the AND gate in each unit takes either I_1 and I_2 or their complementary species P_1 and P_2 as its inputs. Species P_1 and P_2 are supplied continuously with a HIGH state so that after reactions $I_1 + P_1 \rightarrow W_1$ and $I_2 + P_2 \rightarrow W_2$, the remaining concentrations of species P_1 and P_2, i.e., $C_{P_1/P_2}(x_1, t)$, can represent the complementary states of species I_1 and I_2, thus achieving the NOT gate. Unlike an electric 2:4 decoder that an identical voltage level is produced no matter which unit is selected, the proposed chemical 2:4 decoder will output different concentration levels. As each unit output $C^i_O(t)$ is influenced by $C^i_{Amp_0}$ through an amplifying reaction, the concentration variation of transmitted signals is represented via different concentrations of injected species Amp as $C^i_{Amp_0}(t) = C^i_{Amp_0} u(t)$

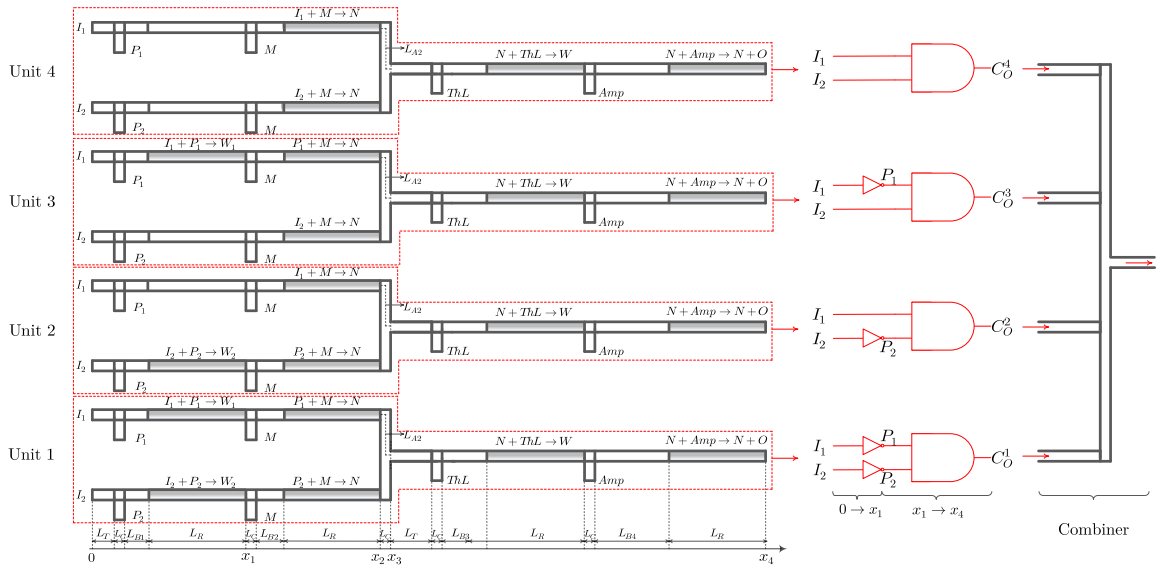

Fig. 5.6 The chemical-reactions-based microfluidic 2:4 decoder.

$(1 \leq i \leq 4)$ for different units. Here, we set $C^4_{Amp_0} > C^3_{Amp_0} > C^2_{Amp_0} > C^1_{Amp_0}$ to ensure $\max\{C^4_O(t)\} > \max\{C^3_O(t)\} > \max\{C^2_O(t)\} > \max\{C^1_O(t)\}$. The combiner acts as a transmitter-channel interface and merely combines the four outputs $C^i_O(t)$. We highlight that it does not have an impact on the QCSK modulation function. Thus, for simplicity, we will not consider it in the following analysis, which also brings flexibility to test each unit of our proposed design.

QCSK Transmitter Analysis

The objective of the following analysis is to derive the transmitter output $C^i_O(t)$ of the design in Fig. 5.6. We first derive the inputs of an AND gate, i.e., the concentrations of I_1, I_2, P_1, and P_2 at location $x = x_1$. When input species I_1 and I_2 directly flow into an AND gate, their concentrations can be expressed as

$$C_{I_1/I_2}(x_1, t) = \Big[\mathcal{T}[C_{I_{1_0}/I_{2_0}}(t), 1] * H_2(L_C + L_{B1} + L_R, t)\Big]/2, \tag{5.26}$$

where $C_{I_{1_0}/I_{2_0}}(t)$ is the concentration of input species I_1 or I_2, operator $\mathcal{T}[\cdot]$ is defined in Table 5.1, the coefficient $1/2$ explains the dilution of species I_1 by species P_1 (or I_2 by P_2). When the complementary species P_1 and P_2 flow into an AND gate, their concentrations can be expressed as

$$C_{P_1/P_2}(x_1, t) = \mathcal{R}\Big\{\mathcal{T}[C_{P_{1_0}/P_{2_0}}(t), 1], \mathcal{T}[C_{I_{1_0}/I_{2_0}}(t), 1], 2\Big\}, \tag{5.27}$$

where $C_{P_{1_0}/P_{2_0}}(t)$ is the input concentration of species P_1 or P_2, and operator $\mathcal{R}[\cdot]$ is defined in Table 5.1.

With the derived AND gate inputs $C_{I_1/I_2}(x_1,t)$ in (5.26) and $C_{P_1/P_2}(x_1,t)$ in (5.27), the transmitter output $C_O^i(t)$ can be expressed using **Theorem 4** by interchanging the parameters in (5.20) via:

- $\mathcal{T}[C_N(x_3,t),4] \rightarrow \mathcal{T}[C_N(x_3,t),6]$,
- $C_{Amp_0}(t) \rightarrow C_{Amp_0}^i(t)$,
- $n=5 \rightarrow n=7$;

and by interchanging the parameters in (5.21) via:

- $\mathcal{T}[C_{I_{1_0}}(t),1] \rightarrow C_{I_1/I_2}(x_1,t)$ if an AND gate input is I_1/I_2, $\mathcal{T}[C_{I_{1_0}}(t),1] \rightarrow C_{P_1/P_2}(x_1,t)$ if an AND gate input is P_1/P_2,
- $n=2 \rightarrow n=3$,
- $H_2(L_{A2},t) \rightarrow H_3(L_{A2},t)$.

5.3.2 QCSK Receiver

QCSK Receiver Design

From the communication perspective, the QCSK microfluidic receiver is required to distinguish different concentration levels from different input combinations to achieve demodulation. In this chapter, we consider a Gaussian signal $C_O^i(t)$ as the input for the receiver, which can be expressed as

$$C_O^i(t) = \frac{C_{O_0}^i}{\sqrt{2\pi\sigma^2}} e^{-\frac{(t-\mu)^2}{2\sigma^2}} \quad (1 \leq i \leq 4), \tag{5.28}$$

where the superscript i indicates the four concentration levels of QCSK, μ is the mean, and σ is the standard deviation. For simplicity, we use $C_O(t)$ to denote the general receiver input. To focus on the fundamental principle and mechanism of our proposed QCSK transceiver, we leave the analysis of the propagation channel between transmitter and receiver for our future work. We also denote $C_{Y_1}(t)$ and $C_{Y_2}(t)$ as the final demodulated concentration signals, which correspond to the transmitter concentration inputs $C_{I_{1_0}}(t)$ and $C_{I_{2_0}}(t)$, respectively.

To detect four concentration levels, we first design three detection units in Fig. 5.7 to serve as a front-end processing module for the QCSK receiver. Each detection

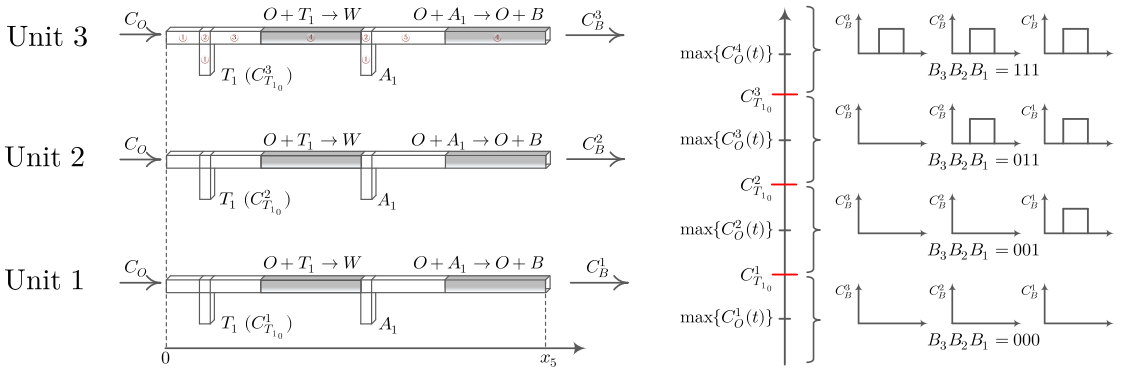

Fig. 5.7 Three detection units [130] serve as a front-end processing module. Each channel is labeled with a channel number to denote channel length as L_{number}. By setting $\max\{C_O^i(t)\} < C^i_{T_{1_0}} < \max\{C_O^{i+1}(t)\}$, the front-end processing module can distinguish four concentration regions.

Table 5.2 The relation between the receiver input $C_O(t)$, front-end module output binary signal B, and receiver output binary signal Y.

$\max\{C_O(t)\}$	B_3	B_2	B_1	Y_2	Y_1
$[0, C^1_{T1_0}]$	0	0	0	0	0
$[C^1_{T1_0}, C^2_{T1_0}]$	0	0	1	0	1
$[C^2_{T1_0}, C^3_{T1_0}]$	0	1	1	1	0
$[C^3_{T1_0}, \infty)$	1	1	1	1	1

unit follows the receiver design proposed in Chapter 4 (see Fig. 4.3) and is capable of generating a rectangular signal if the maximum concentration of a received signal exceeds a predefined threshold. As shown in Fig. 5.7, the only difference among the three detection units is the injected concentration $C^i_{T_{1_0}}(t) = C^i_{T_{1_0}} u(t)$ $(1 \le i \le 3)$ of thresholding reactant T_1. By setting $\max\{C_O^i(t)\} < C^i_{T_{1_0}} < \max\{C_O^{i+1}(t)\}$, the concentration region of $C_O(t)$ can be identified for three-bit binary signals $B_3B_2B_1$ as shown in Fig. 5.7. For instance, if $\max\{C_O(t)\} > C^3_{T_{1_0}}$, all detection units will produce a HIGH state with $B_3B_2B_1 = 111$.

The three detection units in Fig. 5.7 can only demodulate $C_O(t)$ to three concentration signals $C_B^3(t)$, $C_B^2(t)$, and $C_B^1(t)$ instead of $C_{Y_2}(t)$ and $C_{Y_1}(t)$, which means extra signal processing units are required. Consider the output of front-end module $C_B(t)$ exhibits a rectangular concentration profile and its digital characteristic is ideal to perform logic computations [65], this motivates us to design logic circuits to transform $C_B^i(t)$ to desired outputs $C_{Y_2}(t)$ and $C_{Y_1}(t)$. To inspire the design for this signal transformation, we present the relation between the binary signal B_i $(1 \le i \le 3)$ and the binary signal Y_j $(j = 1, 2)$ in the truth table of Table 5.2. Based on Table 5.2, we

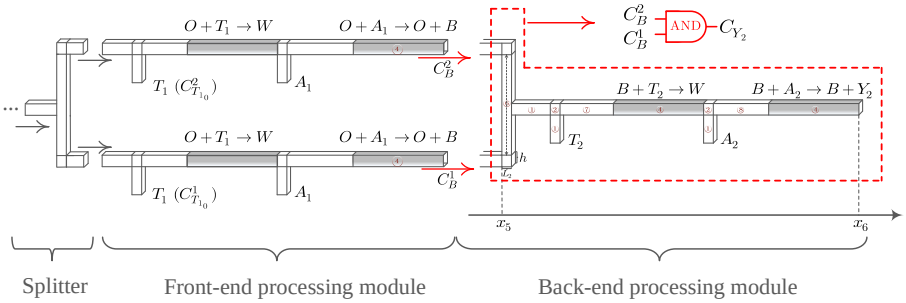

(a) Microfluidic channels to calculate C_{Y_2}

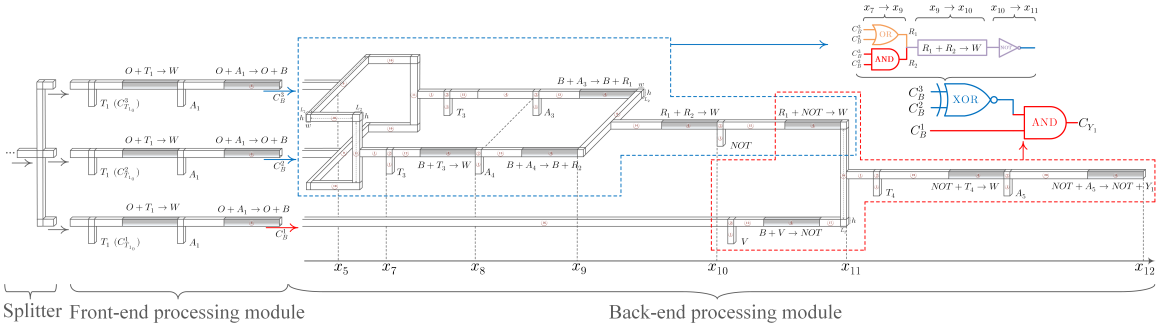

(b) Microfluidic channels to calculate C_{Y_1}

Fig. 5.8 The microfluidic QCSK receiver design. Each channel is labeled with a channel number to denote channel length as L_{number}.

express the Boolean equations [127] for Y_2 and Y_1 as

$$Y_2 = \bar{B}_3 B_2 B_1 + B_3 B_2 B_1 = B_2 B_1, \tag{5.29}$$

$$\text{and} \quad Y_1 = \bar{B}_3 \bar{B}_2 B_1 + B_3 B_2 B_1 = B_1 (B_3 \odot B_2), \tag{5.30}$$

where $\bar{B}_3$ is the complementary form of B_3, $B_2 B_1$ represents the AND operation of B_2 and B_1, and $\odot$ is the XNOR operation. Inspired by (5.29) and (5.30), we connect the front-end module with an AND gate to compute $C_{Y_2}(t)$ as shown in Fig 5.8a, as well as an XNOR gate and an AND gate to calculate $C_{Y_1}(t)$ as shown in Fig. 5.8b.

Fig. 5.8 also includes the splitter that acts as a channel-receiver interface. This interface only has an impact on the velocities of flows entering the front-end processing module, which can be revealed by (3.20) in **Lemma 3**. Since the design principle of the QCSK receiver and the mechanisms of all the involved digital gates are independent of the flow velocities, we will not consider the channel-receiver interface in the following analysis.

QCSK Receiver Analysis

To theoretically characterize receiver outputs $C_{Y_2}(t)$ and $C_{Y_1}(t)$, we denote $C_{[\cdot]_0}(t)$ as the concentration of any injected species $[\cdot]$, and L_i as the length of the microfluidic channel with number i. Moreover, we assume that the injection velocity of any flow is u_{eff}. In the following, we first derive the front-end processing output $C_B^i(t)$ in Fig. 5.7, and then derive the QCSK receiver outputs $C_{Y_2}(t)$ and $C_{Y_1}(t)$ in Fig. 5.8. In addition, the **location** and **channel number** are in bold in the following so that readers can easily follow our derivation.

$C_B^i(t)$ Derivation: As shown in Fig. 5.7, each detection unit in the front-end processing module consists of a thresholding reaction $O + T_1 \rightarrow W$ and an amplifying reaction $O + A_1 \rightarrow O + B$. The output of a detection unit can be expressed using the operator $\mathcal{F}[\cdot]$ defined in Table 5.1 as

$$C_B^i(x_5, t) = \mathcal{F}\Big\{\mathcal{T}[C_O(t), 1], \mathcal{T}[C^i_{T_{1_0}}(t), 1], \mathcal{T}[C_{A_{1_0}}(t), 1], 2\Big\}, \tag{5.31}$$

where $C_O(t)$ is the receiver input concentration.

$C_{Y_2}(t)$ Derivation: As shown in in Fig. 5.8a, $C_B^2(t)$ and $C_B^1(t)$ flow into an AND gate to produce $C_{Y_2}(t)$. At $\boldsymbol{x = x_6}$, $C_{Y_2}(t)$ can be derived as

$$\begin{aligned} C_{Y_2}(x_6, t) = \mathcal{F}\Big\{\mathcal{T}[\frac{1}{2}\sum_{j=1}^{2} C_B^j(x_5, t) * H_3(\frac{2L_2 + L_6 + h}{2}, t), 6] \\ \mathcal{T}[C_{T_{2_0}}(t), 1], \mathcal{T}[C_{A_{2_0}}(t), 1], 7\Big\}, \end{aligned} \tag{5.32}$$

where $1/2$ represents the dilution of $C_B^1(x_5, t)$ by $C_B^2(x_5, t)$ and vice versa, $H_n(x, t)$ is given in **Theorem 3** with n indicating that the average velocity is nv_{eff}, and the operator $\mathcal{T}[\cdot]$ is defined in Table 5.1.

$C_{Y_1}(t)$ Derivation: As shown in Fig. 5.8b, an XNOR gate and an AND gate are linked to the front-end processing module to produce $C_{Y_1}(t)$.

- **XNOR Gate Analysis**: Relying on the fluid separation analysis in **Lemma 3**, at $\boldsymbol{x = x_5}$, $C_B^j(x_5, t)$ $(j = 2, 3)$ is equally separated from channel **9** to channels **10** due to the symmetrical microfluidic design from $\boldsymbol{x_5}$ to $\boldsymbol{x_9}$ in Fig. 5.8b, resulting in a velocity reduction from $3u_{\text{eff}}$ in channel **4** [4] with $O + A_1 \rightarrow O + B$ to $1.5u_{\text{eff}}$ in channels **10**. In channels **11**, the confluence of $C_B^3(x_5, t)$ and $C_B^2(x_5, t)$ occurs, and then is diluted by species T_3 injected at $\boldsymbol{x_7}$. Subsequently, the outer fluid

[4]Since there are three inlets in each unit of the front-end processing module and a flow at each inlet is injected with u_{eff}, the average velocity in channel **4** is $3u_{\text{eff}}$.

performs reaction $B + T_3 \rightarrow W$ to capture the region where both $C_B^3(x_5, t)$ and $C_B^2(x_5, t)$ are HIGH as the second case in Fig. 5.4, while the inner fluid flows forward without reaction $B + T_3 \rightarrow W$. After reactions $B + A_3 \rightarrow B + R_1$ and $B + A_4 \rightarrow B + R_2$, the concentrations of products R_1 and R_2 at $\boldsymbol{x = x_9}$ can be expressed as

$$C_{R_1}(x_9, t) = \mathcal{A}\Big\{\underbrace{\mathcal{T}[\frac{1}{2}\sum_{j=2}^{3} C_B^j(x_5, t) * H_{1.5}(\frac{3L_2 + L_9 + 2L_{10} + L_{11} + h + 2w}{2}, t), 3]}_{C_B^{\text{Inner}}(x_7, t)} * \frac{3}{4} H_4(L_2 + L_{12} + L_4, t), \mathcal{T}[C_{A_{3_0}}(t), 1], 5\Big\}, \tag{5.33}$$

and

$$C_{R_2}(x_9, t) = \mathcal{F}\Big\{\underbrace{\mathcal{T}[\frac{1}{2}\sum_{j=2}^{3} C_B^j(x_5, t) * H_{1.5}(\frac{3L_2 + L_9 + 2L_{10} + L_{11} + h + 2w}{2}, t), 3]}_{C_B^{\text{Outer}}(x_7, t)}, \mathcal{T}[C_{T_{3_0}}(t), 1], \mathcal{T}[C_{A_{4_0}}(t), 1], 4\Big\}, \tag{5.34}$$

where the superscript "Inner" and "Outer" represent the outer and inter fluids from $\boldsymbol{x_7}$ to $\boldsymbol{x_9}$, and 3/4 in (5.33) represents the dilution of species B by species T_3.

After reaction $R_1 + R_2 \rightarrow W$, the remaining species R_1 at $\boldsymbol{x = x_{10}}$ will be HIGH when either $C_B^3(x_5, t)$ or $C_B^2(x_5, t)$ is HIGH, thus achieving an XOR gate[5]. Relying on (5.12a) in **Lemma 5**, the remaining concentration of species R_1 is

[5]As the inner fluid does not perform any reaction from x_7 to x_8, after reaction $B + A_3 \rightarrow B + R_1$, species R_1 is HIGH when one or both $C_B^3(x_5, t)$ and $C_B^2(x_5, t)$ are HIGH, thus achieving an OR gate. Note that this OR gate design is slightly different from the OR gate design introduced in Fig. 3.7 of Chapter 3.2.5. In Fig. 3.7, we considered a reaction $N + ThL \rightarrow W$ for the subtraction module between the addition and amplification modules. The motivation of $N + ThL \rightarrow W$ is to mitigate the fluctuations of N when both inputs are Low (i.e., the concentrations of N should be zero). Since the PDEs describing molecule propagation are deterministic, the noise effects are not captured. Therefore, we omit the subtraction module for the OR gate in Fig. 5.8. By contrast, with reaction $B + T_3 \rightarrow W$, after reaction $B + A_4 \rightarrow B + R_2$, species R_2 is HIGH only when both $C_B^3(x_5, t)$ and $C_B^2(x_5, t)$ are HIGH, thus achieving an AND gate. Therefore, the XOR gate is consisted of an OR gate, an AND gate, and a thresholding reaction $R_1 + R_2 \rightarrow W$ as shown in Fig. 5.8b, which is the same as the XOR gate design proposed in Fig. 3.8 of Chapter 3.2.5.

derived as

$$\begin{aligned} C_{R_1}(x_{10},t) =& \frac{1}{2}\Big\{C_{R_1}(x_9,t) - \varphi[C_{R_1}(x_9,t), C_{R_2}(x_9,t)]\Big\} \\ & * H_5(\frac{L_2+L_9+2w}{2},t) * H_{10}(L_{14},t) * H_{10}(L_4,t), \end{aligned} \tag{5.35}$$

where $\varphi[\cdot,\cdot]$ is given in (5.10). The cascaded reaction $R_1 + NOT \to W$ functions as a NOT gate similar to the reaction $I_1 + P_1 \to W$ in the QCSK transmitter in Fig. 5.6 in order to achieve the XNOR gate. At $\boldsymbol{x} = \boldsymbol{x_{11}}$, the concentration of NOT can be expressed using the operator $\mathcal{R}[\cdot]$ defined in Table 5.1 as

$$\begin{aligned} C^{2\&3}_{NOT}(x_{11},t) =& \mathcal{R}\Big\{\mathcal{T}[C_{NOT_0}(t),1], C_{R_1}(x_{10},t), 11\Big\} \\ & * H_{11}(\frac{2L_2+L_{18}+h}{2},t), \end{aligned} \tag{5.36}$$

where the superscript 2&3 represents the species NOT generated by $C^2_B(x_5,t)$ and $C^3_B(x_5,t)$.

- **AND Gate Analysis**: The calculation of receiver output $C_{Y_1}(t)$ also needs $C^1_B(x_5,t)$. To perform the AND gate, the product species B (indicated by the red arrow) should be converted to molecular type NOT via $B + V \to NOT$. At $\boldsymbol{x} = \boldsymbol{x_{11}}$, the concentration of species NOT generated by $C^1_B(x_5,t)$ can be expressed using operator $\mathcal{G}[\cdot]$ defined in Table 5.1 as

$$\begin{aligned} C^1_{NOT}(x_{11},t) =& \mathcal{G}\Big\{C^1_B(x_5,t) * H_3(L_{16},t), \mathcal{T}[C_{V_0}(t),1], 4\Big\} \\ & * H_4(\frac{2L_2+2L_{17}+L_{18}+h}{2},t). \end{aligned} \tag{5.37}$$

Finally, we can derive the QCSK receiver output $C_{Y_1}(x_{12},t)$ as

$$\begin{aligned} C_{Y_1}(x_{12},t) = \mathcal{F}\Big\{\mathcal{T}[&\frac{4}{15}C^1_{NOT}(x_{11},t) + \frac{11}{15}C^{2\&3}_{NOT}(x_{11},t), 15], \\ & \mathcal{T}[C_{T_{4_0}}(t),1], \mathcal{T}[C_{A_{5_0}}(t),1], 16\Big\}, \end{aligned} \tag{5.38}$$

where 4/15 represents the dilution of $C^1_{NOT}(x_{11},t)$ by $C^{2\&3}_{NOT}(x_{11},t)$, while 11/15 represents the dilution of $C^{2\&3}_{NOT}(x_{11},t)$ by $C^1_{NOT}(x_{11},t)$.

5.3.3 Microfluidic Circuit Synchronization

There are mainly two synchronization cases that need to be taken into account: 1) species synchronization at the inlets of microfluidic circuits and 2) species synchronization inside microfluidic circuits. The first case refers to the simultaneous injection of different species to microfluidic circuits. In practice, we can deal with this synchronization issue by grouping syringe pumps with a microcontroller board (e.g., Arduino) and sending the release signal to syringe pumps at the same time. For the second case, one example is the synchronization of the two intermediate inputs $C^1_{NOT}(x_{11}, t)$ and $C^{2\&3}_{NOT}(x_{11}, t))$ of the AND gate used in Fig. 5.8b. As these two intermediate signals are generated by the same received signal, the synchronization of $C^1_{NOT}(x_{11}, t)$ and $C^{2\&3}_{NOT}(x_{11}, t)$ requires that they must arrive at $\boldsymbol{x_{11}}$ simultaneously; otherwise, the AND gate is unable to produce a correct logic gate and thus the receiver fails to decode the received signal. To prevent this issue, the inputs $C_O(t)$ of three detection units should have the same traveling time from the front-end module to position $\boldsymbol{x_{11}}$ in Fig. 5.8b. Based on the fact that the advection effect is merely a shift of the molecular profile in time with average velocity and without any change of shape [96], the design should satisfy the following requirement

$$\sum_{i\in\mathcal{I}} L_i/u_i = \sum_{j\in\mathcal{J}} L_j/u_j, \tag{5.39}$$

where $\mathcal{I}$ is the set of the microfluidic channels used to generate $C^{2\&3}_{NOT}(x_{11}, t)$, $\mathcal{J}$ is the set of the microfluidic channels used to generate $C^1_{NOT}(x_{11}, t)$, and L_i and u_i are the channel length and the corresponding flow velocity of a microfluidic channel with label i.

5.4 Performance Evaluation

In this section, we implement our proposed microfluidic AND gate, QCSK transmitter, and QCSK receiver design in Fig. 5.1, Fig. 5.6, and Fig. 5.8 using COMSOL Multiphysics, which are then used to validate our corresponding theoretical analysis. The impulse response $H(x, t)$ given in **Theorem 3** is computed in Matlab using *quadgk*. As *quadgk* is only an approximation of $H(x, t)$, the computed results may fluctuate around their steady values. If a computed value is slightly larger than steady value 0, it can induce an instant change on the output value of the indicator function in (5.13) from 0 to 1, which would further lead to a generation of output signals in

undesired regions after an amplifying reaction. To avoid this phenomenon, we modify the statement of an indicator function $C_{S_{i_0}}(t) > 0$ as $C_{S_{i_0}}(t) > \frac{1}{10}\max\{C_{S_{i_0}}(t)\}$. By doing so, the width of a rectangular output is expected to be smaller than that of the corresponding simulation result. In COMSOL simulations, unless otherwise stated, we set $u_{\text{eff}} = 0.1\text{cm/s}$, $D_{\text{eff}} = 10^{-8}\text{m}^2/\text{s}$, $w = 20\mu\text{m}$, $h = 10\mu\text{m}$, $k_f = 400\text{m}^3/(\text{mol}\cdot\text{s})$. Considering these values and water as a solvent, the value of the Reynolds number is roughly 3, which is less than 2000 so the laminar flow assumption is valid. Furthermore, we use "Ana." and "Sim." to abbreviate "Analytical" and "Simulation" in all figures.

5.4.1 The Impact of Rate Constant

To remove the coupling between advection-diffusion and reaction, we applied the operator splitting method with the assumption $k_f \to \infty$ in **Algorithm 1** to theoretically characterize the cascade of reaction channels. In practice, the rate constant k_f cannot be infinite and k_f should be selected to ensure that a reaction is complete inside a given microfluidic channel. Before showing the results of AND gate and QCSK transceiver, we first investigate the impact of the rate constant on the accuracy of operator splitting and determine the value of the rate constant for other simulations. In particular, a straight microfluidic channel with reaction $S_1 + S_2 \to S_3$ is implemented in COMSOL. Species S_1 and S_2 are injected into the channel with initial concentrations $C_{S_{1_0}} = 3[u(t-1) - u(t-3)]$ and $C_{S_{2_0}} = 2[u(t-1) - u(t-3)]$, respectively. The channel length is $250\mu\text{m}$, and the average velocity of the fluid containing S_1 and S_2 is 2cm/s.

In Fig. 5.9, we plot the simulation results of output concentrations of species S_1, S_2, and S_3 obtained from COMSOL and their analytical results using (5.12a)-(5.12c). As shown in Fig. 5.9, when the rate constant is relatively low (e.g., $k_f = 50$ and 100), the theoretical analysis is not in agreement with the simulation results. The reason for this mismatch is that the reaction is not completed, which is demonstrated by the remaining species S_2 in Figs. 5.9a and b. When $k_f = 400$, the remaining concentration of S_2 is zero (i.e., the reaction is complete), and the theoretical characterization can well predict the channel outputs. The above observations are consistent with the discussions in Chapter 5.2.2, where we state that theoretical analysis can match simulation results only when reactions are complete. With a longer reaction channel (i.e., $500\mu\text{m}$) and a lower velocity (i.e., 0.1cm/s), $k_f = 400$ can ensure all reactions are complete and will be used in the remaining simulations.

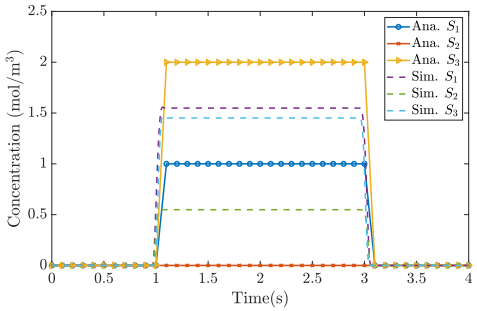

(a) $k_f = 50$

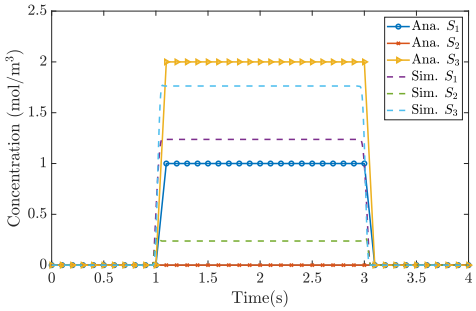

(b) $k_f = 100$

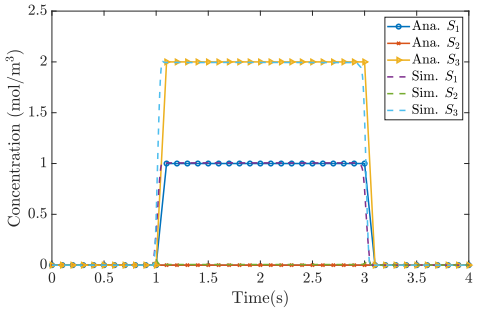

(c) $k_f = 400$

Fig. 5.9 The output concentrations of species S_1, S_2, and S_3 with different rate constant k_f.

5.4.2 AND Logic Gate

Fig. 5.10 presents the COMSOL simulation results of the AND logic gate design depicted in Fig. 5.1. We set the parameters: $C_{I_{1_0}}(t) = 8[u(t-1) - u(t-3)]$, $C_{I_{2_0}}(t) = 8[u(t-2) - u(t-4)]$, $C_{M_0}(t) = 8u(t)$, $C_{Amp_0}(t) = 12u(t)$, $L_T = 80\mu$m, $L_C = 20\mu$m, $L_R = 500\mu$m, $L_{A2} = 120\mu$m. In order to examine the impact of the injected concentration of species ThL on the gate behavior, we consider three cases: $C_{ThL_0}(t) = 5u(t)$, $C_{ThL_0}(t) = 10u(t)$, $C_{ThL_0}(t) = 20u(t)$, which correspond to the cases $C_{ThL} < C_1$, $C_1 < C_{ThL} < 2C_1$, and $C_{ThL} < 2C_1$ in Fig. 5.4, respectively.

Fig. 5.10a plots the concentrations of species N and ThL before reaction $N+ThL \rightarrow W$ in Fig. 5.1. We observe that the simulated concentration points agree with the analytical concentration curves, thus demonstrating the correctness of our analysis of advection-diffusion in **Theorem 3** and advection-diffusion-reaction channels in **Lemma 5**. For the three different injected concentrations, species ThL is nearly diluted to one-fifth of its injected concentration due to that species ThL entering the microfluidic device via the fifth inlet, which validates the concentration analysis for fluid mixing in **Lemma 1**. Moreover, we also plot the concentration constraint C_{Con} in (5.23) for

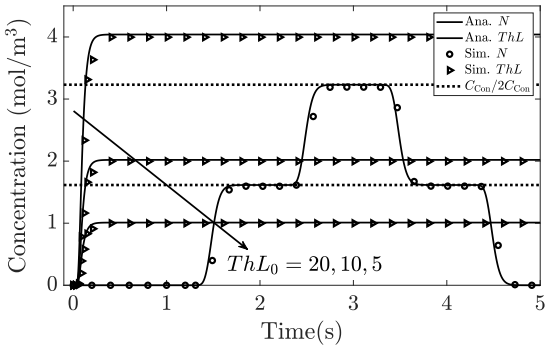

(a) The concentration of species N and ThL at $x = x_4$.

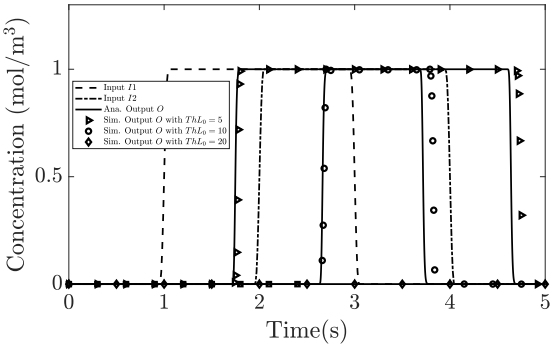

(b) The normalized concentrations of input species I_1, I_2, and output species O.

Fig. 5.10 The evaluation of an AND logic gate.

species ThL using black dash lines. For the curves with $C_{ThL_0}(t) = 5u(t)$ and $20u(t)$, these values do not satisfy the concentration constraint in **Lemma 7**; as expected, the microfluidic device fails to achieve the AND function, which is demonstrated in Fig. 5.10b. Fig. 5.10b plots the normalized inputs and the final output product O in (5.20). Only for $C_{ThL_0}(t) = 10u(t)$, the width of species O equals the width where both input species I_1 and I_2 are HIGH, demonstrating the desired behavior of an AND gate. Furthermore, due to the modification of the indicator function set, we can see the width of (5.20) is smaller than that of the simulation results.

5.4.3 QCSK Transmitter

Fig. 5.11 plots the outputs of the proposed microfluidic QCSK transmitter design in Fig. 5.6 and their analytical values $C_O^i(t)$ in Chapter 5.3.1. Species I_1 and I_2 are injected with either $12[u(t-1) - u(t-3)]$ representing bit-1 or $0u(t)$ representing bit-0.

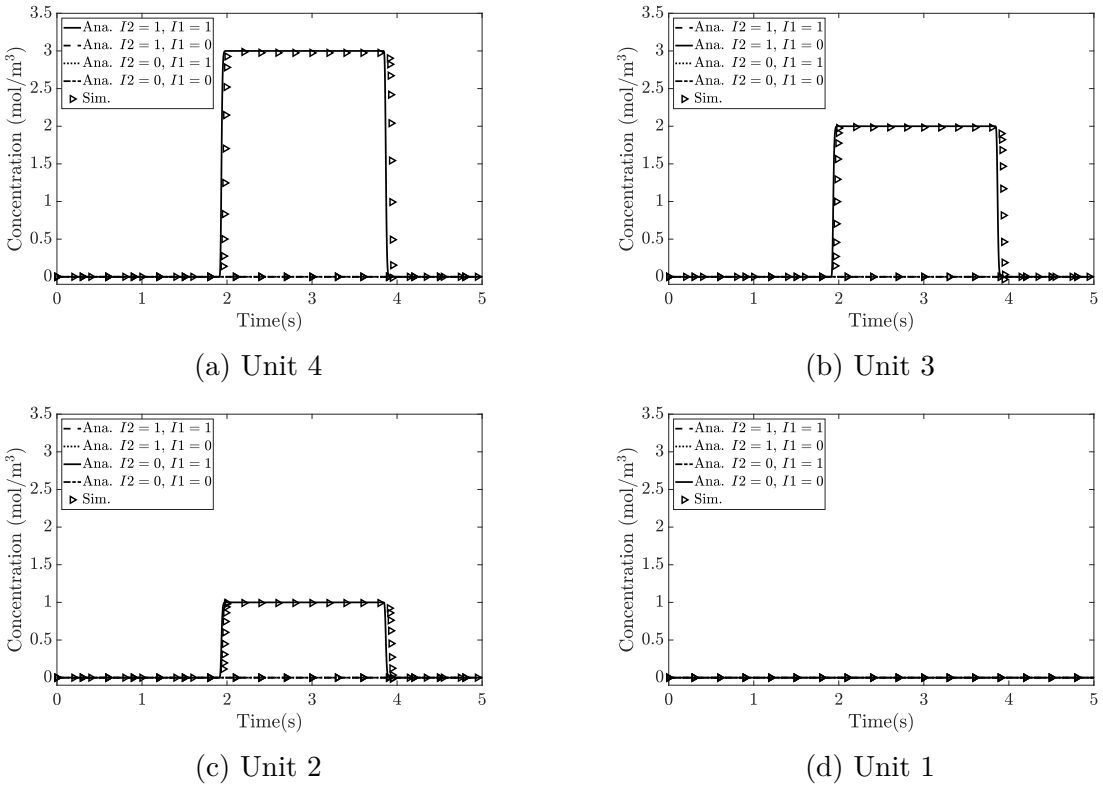

(a) Unit 4

(b) Unit 3

(c) Unit 2

(d) Unit 1

Fig. 5.11 The output concentrations of the proposed microfluidic QCSK transmitter.

For other molecular types, their injected concentrations are set as: $C_{P_{1_0}}(t) = C_{P_{2_0}}(t) = 12[u(t-1) - u(t-3)]$, $C_{M_0}(t) = 12u(t)$, $C_{ThL_0}(t) = 16u(t)$, $C^4_{Amp_0}(t) = 24u(t)$, $C^3_{Amp_0}(t) = 16u(t)$, $C^2_{Amp_0}(t) = 8u(t)$, and $C^1_{Amp_0}(t) = 0$. The buffer channels are configured with $L_{B1} = 100\mu$m, $L_{B2} = 150\mu$m, $L_{B3} = 350\mu$m, and $L_{B4} = 400\mu$m.

As shown in Fig. 5.11, for any input combination, only one unit outputs a HIGH signal except in the case where both I_1 and I_2 are LOW due to $C^1_{Amp_0}(t) = 0$. In addition, for each unit, it is selected under a specific input combination (e.g., Unit 4 is only selected when both input species I_1 and I_2 are HIGH) so that the outputs for the other three input combinations are all in a LOW state and the corresponding curves are completely overlapped. Moreover, the analytical curves always capture the simulation points, which again demonstrates the effectiveness of our theoretical analysis $C^i_O(t)$ in Chapter 5.3.1. As species *Amp* is supplied with different injected concentrations for each unit, we see that the selected unit reaches different concentration levels, proving that the proposed microfluidic QCSK transmitter successfully modulates input bits to the concentration level of output species O.

5.4.4 QCSK Receiver

To evaluate the proposed QCSK receiver design in Fig. 5.8, we consider Gaussian signals $C_O(t)$ with four peak amplitudes as the receiver input: $C^1_{O_0} = 0$, $C^2_{O_0} = 0.85$, $C^3_{O_0} = 1.7$, and $C^4_{O_0} = 2.55$, with the mean $\mu = 2$ and standard deviation $\sigma = 0.34$. Accordingly, to distinguish these four concentration levels, the concentration of species T_1 for three units in Fig. 5.7 is set as: $C^3_{T_{1_0}}(t) = 2.2u(t)$, $C^2_{T_{1_0}}(t) = 1.2u(t)$, and $C^1_{T_{1_0}}(t) = 0.8u(t)$. Other parameters and the geometry are summarized in Table 5.3 and 5.4.

Table 5.3 The parameters of the QCSK receiver in Fig. 5.8.

Molecular Type	Concentration (mol/m^3)	Molecular Type	Concentration (mol/m^3)
A_1	$9u(t)$	T_2	$14u(t)$
A_2	$24u(t)$	T_3	$7u(t)$
A_3	$20u(t)$	T_4	$32u(t)$
A_4	$20u(t)$	NOT	$22u(t)$
A_5	$51u(t)$	V	$28u(t)$

Table 5.4 The geometry of the QCSK receiver in Fig. 5.8.

Channel Number	Length (μm)	Channel Number	Length (μm)
1	80	11	180
2	20	12	200
3	100	13	250
4	500	14	500
5	150	15	550
6	220	16	1911
7	350	17	50
8	400	18	320
9	210	19	750
10	200	20	800

Fig. 5.12 plots the outputs of the proposed QCSK receiver design in Fig. 5.8 and the corresponding analytical results of $C_{Y_2}(t)$ in (5.32) and $C_{Y_1}(t)$ in (5.38). Moreover, Fig. 5.12 also provides the corresponding heat maps of the concentrations of Y_2 and Y_1 at 3s and 3.7s, respectively. First, we can see that although simulation curves are not in precise agreement with analytical curves, the close match can still confirm the correctness of the mathematical characterization of $C_{Y_2}(t)$ and $C_{Y_1}(t)$. Second, we observe that the width difference between analytical and simulation curves for C_{Y_1} is larger than that for C_{Y_2}. This is because the modification of the statement of an indicator function results in the width difference in each amplifying reaction, and the more amplifying reactions are utilized to compute C_{Y_1} in Fig. 5.8b, the bigger

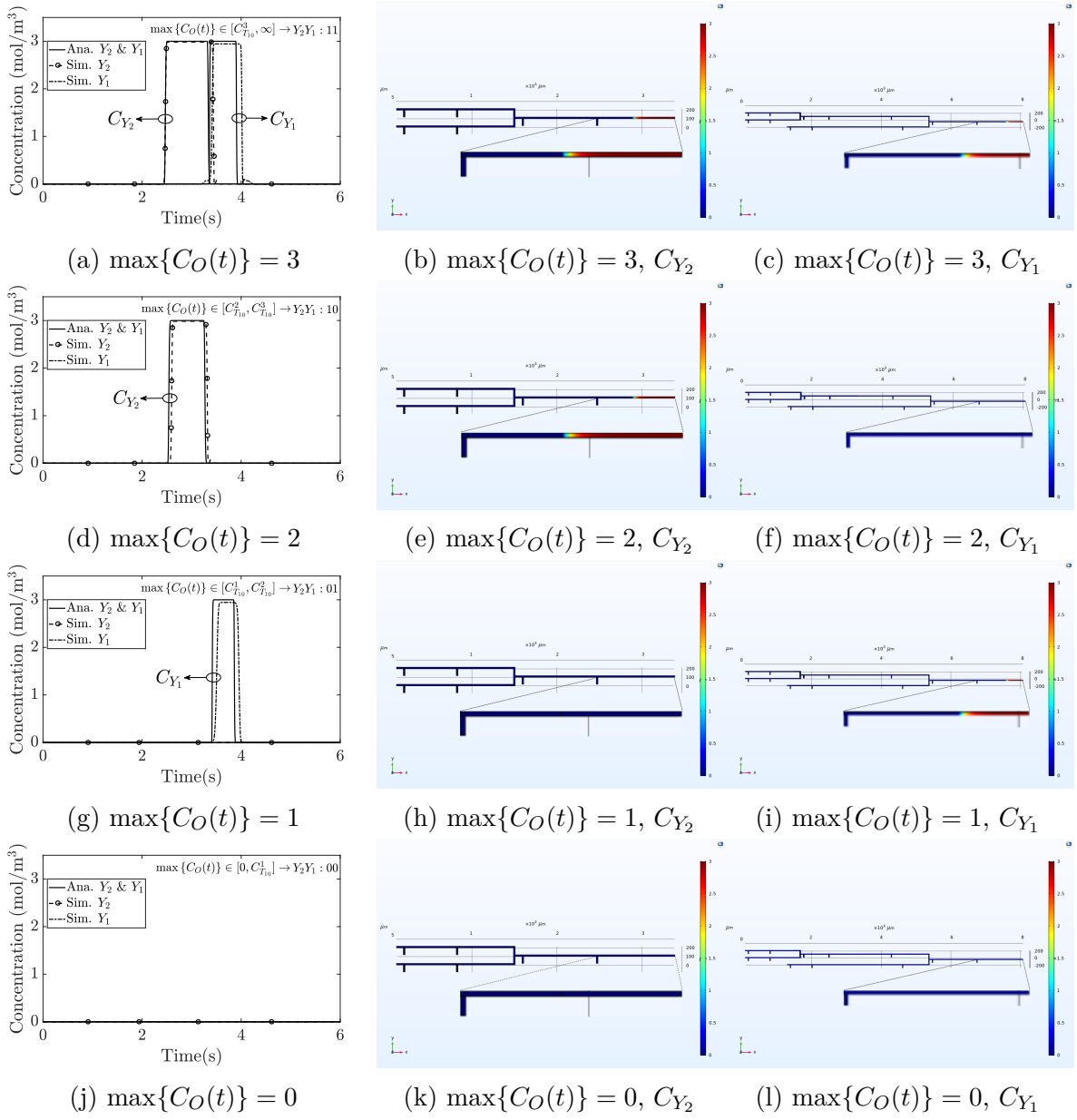

(a) $\max\{C_O(t)\} = 3$ (b) $\max\{C_O(t)\} = 3$, C_{Y_2} (c) $\max\{C_O(t)\} = 3$, C_{Y_1}

(d) $\max\{C_O(t)\} = 2$ (e) $\max\{C_O(t)\} = 2$, C_{Y_2} (f) $\max\{C_O(t)\} = 2$, C_{Y_1}

(g) $\max\{C_O(t)\} = 1$ (h) $\max\{C_O(t)\} = 1$, C_{Y_2} (i) $\max\{C_O(t)\} = 1$, C_{Y_1}

(j) $\max\{C_O(t)\} = 0$ (k) $\max\{C_O(t)\} = 0$, C_{Y_2} (l) $\max\{C_O(t)\} = 0$, C_{Y_1}

Fig. 5.12 The output concentrations of the proposed microfluidic QCSK receiver and the heat maps for receiver outputs C_{Y_2} and C_{Y_1}.

the width difference is. Third, we see that the proposed receiver design can well demodulate the received signal $C_O(t)$ to two outputs C_{Y_2} and C_{Y_1}. Recall that we use non-zero concentrations to represent the HIGH state (bit-1), and zero concentrations to represent the LOW state (bit-0). We also observe that the relationship between the maximum concentration of the receiver input $\max\{C_O(t)\}$, the concentration of

species T_1, and binary signals Y_2 and Y_1 is consistent with the truth table of Table 5.2, which demonstrates the effectiveness of our proposed design.

5.5 Conclusion

In this chapter, we considered the realization of QCSK modulation and demodulation functionalities for MC using chemical-reactions-based microfluidic circuits. We first presented an optimized AND gate design and then showed how to utilize logic computations to achieve QCSK modulation and demodulation functions. To theoretically characterize a microfluidic circuit, we established a general mathematical framework that is scalable with the increase of circuit scale and can be used to analyze other new and more complicated circuits. We derived the output concentration distributions of the AND gate, QCSK transmitter, and receiver designs. Simulation results obtained from COMSOL Multiphysics showed all the proposed microfluidic circuits responded appropriately to input signals and closely matched our derived analytical results.

Chapter 6

Genetic Circuit with Controllable Pulse Generation

6.1 Introduction

Genetic circuits execute desired signal operations by embedding synthetic gene networks in living cells. Specifically, synthetic gene networks rely on the interactions of different genes, where the expression product of one gene acts as a TF to regulate the expressions of others [136]. In the genetic circuit literature, it is common to explicitly specify the synthetic gene networks and their hosted environment, where the programmed functions of living cells are often verified by experimental data. By contrast, chemical circuits are often described by high-level languages and generic species (e.g., species A, B, C), and their behavior is simulated by mass action kinetics. Therefore, it is still unclear what molecules can achieve these chemical circuits in real biological scenarios. Thus, genetic circuits demonstrate the credibility of their direct implementation in practical biological applications compared to chemical circuits.

For genetic circuits, complex biological signal processing functions can be engineered in a single cell or multiple cells connected by signaling pathways. Current efforts of programming large-scale genetic circuits in a single cell have met with much frustration because it is often resource-taxing and error-prone [145]. Only a limited number of functionalities can be achieved with a few circuits in one cell due to the confined volume of a cell [146, 147]. By contrast, the multicellular approach provides an opportunity to break the aforementioned bottlenecks by dividing complex signal processing functions into different cells with simple functions and "wiring" them together via diffusive signaling molecules [148], which can achieve stability, programmability, and ultimately computational complexity at the cell consortium level [149]. Importantly, the partition

of desired functionalities into simple parts that reside in individual cells allows them to be added, removed, or replaced simply by changing the spatial arrangement of the cells with flexibility.

For the multicellular approach, it is essential to establish intercellular signaling (i.e., cell-to-cell communication) for multiple cells to facilitate the division of tasks and achieve community-level functions. One means of this communication is by bacterial quorum sensing (QS) systems [150]. QS systems rely on the exchange of small extracellular autoinducers, which enables cell-to-cell communication among bacteria. In this way, the propagation of autoinducers is analogous to the electronic wires that coordinate a large number of computational units in an electronic device.

There have been significant research efforts to explore the possibility of wiring multiple cells to carry out desired coordinated behavior in cell communities. The most representative example is the combination of single cells with simple logic processing capability to construct more complex signal processing functions, such as the full-adder computation [151]. The pulse behavior is a prevalent pattern in a natural environment with examples including bacterial flagellar development [152] and feed-forward motif [136]. Building and studying synthetic networks that exhibit similar behavior can be helpful for an improved understanding of the principles and kinetics behind such a spatial-temporal pattern in gene expression [153], which could further provide opportunities to achieve signal processing functionalities by exploiting the key characteristics of a pulse, such as the pulse intensity and duration. Although the pulse behavior can be achieved in a single cell, the realization of this function through a multicellular approach can reveal the impact of individual cells on the system performance and provide insights into devising more complex signal processing functions. Motivated by these, the objective of this chapter is to utilize simple digital logic circuits to generate a pulse in a controlled manner [154, 155]. The main contributions of this chapter are as follows:

- We propose a new pulse generation system based on three engineered minimal *E. Coli* cells with different digital logic processing capabilities. Most importantly, unlike the genetic circuits proposed in [73, 78], all the species and the gene interactions of the proposed system are explicitly specified in the synthetic biology domain, which realizes the communication engineering design via synthetic biology tools.

- We adopt the Shea-Ackers formalism to model the individual behavior of each synthetic minimal cell and derive the response of the intercellular signaling

propagation channel that supports cell-to-cell communication. To support cell-to-cell communication, we derive the closed-form response of the intercellular signaling molecules, which is usually numerically analyzed in biology papers. This analytical framework not only leads to the mathematical characterization of the generated pulse, but also provides a basis for examining effective cell-to-cell communication. Importantly, this analytical model can be easily applied to analyze other multi-cell genetic systems.

- We simulate the behavior of our proposed system and evaluate the pulse generation in terms of cell spatial configuration and cell input promoters. The simulation results demonstrate that it is able to control the peak amplitude of a pulse by arranging cells in different spatial configurations. By quantifying the output of an engineered cell via fluorescent protein, we also show that an engineered digital logic gate with a larger ratio of maximum fluorescence to minimum fluorescence and a higher maximum fluorescence intensity can result in a higher peak amplitude of a pulse.

The rest of this chapter is organized as follows. In Section 6.2, we provide the preliminaries of genetic circuits and introduce the proposed pulse generation system. Sections 6.3 to 6.5 sequentially detail the mathematical modeling of each synthetic minimal cell and the propagation channel of autoinducers. In Section 6.6, we detail the mechanism of pulse generation. In Section 6.7, we present and discuss the simulation results. We conclude this chapter in Section 6.8.

6.2 Genetic Circuit Preliminaries and Physical Model

In this section, we first briefly introduce the composition of a genetic circuit. This includes the basic gene expression process and its mathematical characterization, which provide the preliminaries to understand the theoretical analysis of the proposed system in the following sections. In particular, we use Shea-Ackers formalism [156] to model the stochastic behavior of gene expression. This is because that the Shea-Ackers formalism has a relatively straightforward relationship to the stochastic representations of gene expression models and clearly reveals the impact of different transcription states on gene expression compared to the traditional Hill function kinetics [157]. In addition, the Shea-Ackers formalism has been experimentally validated for a variety of gene networks [158]. Finally, we describe the system model that is capable of generating a pulse-shaped signal.

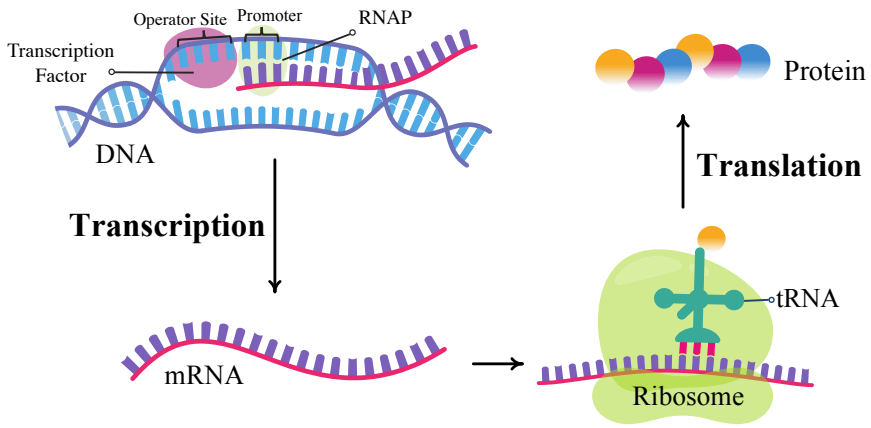

Fig. 6.1 Overview of the gene expression process.

6.2.1 Gene Expression

The synthetic regulatory networks of a genetic circuit are composed of a cascade of gene expression processes. As shown in Fig. 6.1, the protein expression of a gene (i.e., a stretch of DNA) goes through the fundamental processes of transcription and translation. The gene transcription begins when the enzyme RNA polymerase (RNAP) recognizes and binds to the promoter region which can be found at the beginning of a gene. With the RNAP binding to the promoter sequence, RNAP unwinds the DNA at the starting point and begins to synthesize a strand of mRNA. Through translation, mRNA is then translated by a ribosome into protein molecules with the help of tRNA. In this mechanism, the promoter occupancy by RNAP accounts for the basal expression rate of a gene, but this rate can be further regulated by the binding of TFs to operator sites that are near the promoter region. The TFs can act as activators/repressors to enhance/preclude the binding ability of RNAP to promoters to control the targeted gene expression rate.

6.2.2 Shea-Ackers Formalism

The aforementioned gene expression process can be modeled by Shea-Ackers formalism [156, 159]. Based on the fact that the probability of promoter occupancy by RNAP is simply proportional to the level of expression of a given gene, the Shea-Ackers formalism estimates the probabilities for different transcription states (i.e., whether the promoter is occupied by RNAP and the operator is occupied by TFs) from which an overall transcription rate can be derived. The Shea-Ackers formalism holds based on the assumption that all chemical reactions on the regulatory region (promoter and

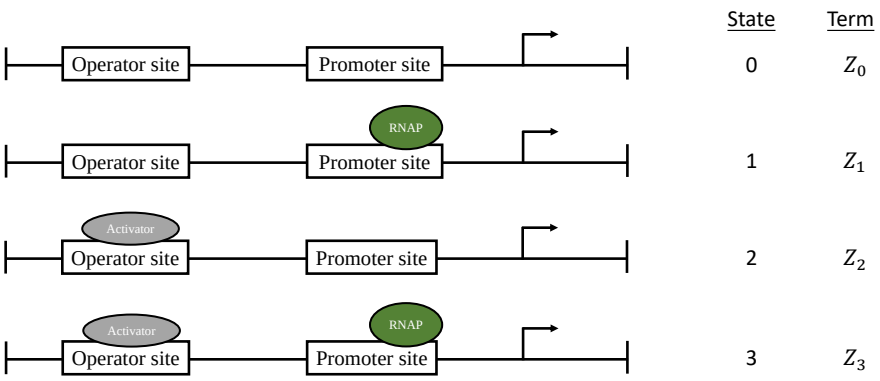

Fig. 6.2 Schematic of the various states of a promoter. The bent arrow indicates areas where transcription starts.

operator sites) equilibrate on a much faster time scale than transcription [158], and it can be well applied when synthetic regulatory networks are engineered in bacterial (e.g., *E. coli*) and eukaryotic cells. For instance, the typical binding/unbinding time of TFs and RNAP is on the order of milliseconds for bacteria to seconds for eukaryotes, while the transcription time is on the order of minutes [136].

To illustrate the mechanism of Shea-Ackers formalism, we provide a simple example in Fig. 6.2 to analyze the transcription probability, i.e., the probability that a promoter is occupied by RNAP in the presence of an activator. As shown in Fig. 6.2, there are four transcription states:

- State 0 with weight Z_0: neither the operator site or promoter is unoccupied;
- State 1 with weight Z_1: only the promoter is occupied by RNAP;
- State 2 with weight Z_2: only the operator site is occupied by an activator;
- State 3 with weight Z_3: both of the regions are occupied.

We also note that each state is associated with a weight Z_i, which is a product of the binding affinity of a site and a cooperative factor describing the interaction between a pair of proteins (TFs or RNAP) bound to two sites [160, eq. (M4)]. Finally, the probability of promoter occupancy can be constructed as the ratio of the sum of the statistical weights for the occupied promoter to the sum of all the statistical weights, which is

$$P = \frac{Z_1 + Z_3}{Z_0 + Z_1 + Z_2 + Z_3}. \tag{6.1}$$

Compared to Hill function kinetics, the weight terms in the Shea-Ackers formalism can be easily changed by altering the promoter region which enables the models based on Shea-Ackers to be tested experimentally [157].

6.2.3 Physical Model

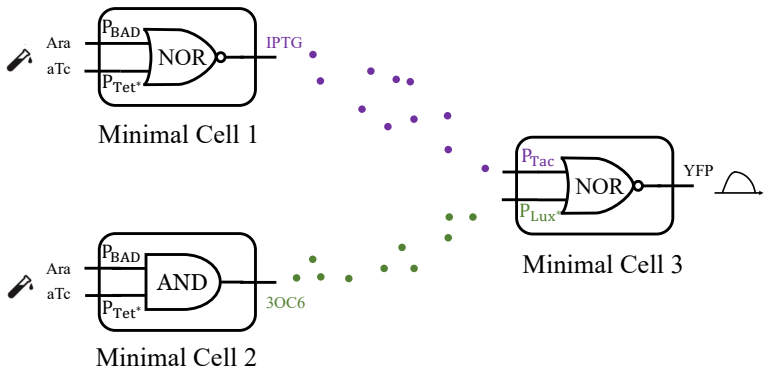

Fig. 6.3 Overall scheme of the proposed pulse generation system. Promoters BAD and Tet* (* represents a mutant) are induced by Ara and aTc, respectively. Molecules IPTG (purple circles) and 3OC6 (green circles) are used to connect Minimal Cell 1 with Minimal Cell 3 and Minimal Cell 2 with Minimal Cell 3. The cognate promoters of IPTG and 3OC6 are Tac and Lux*, respectively.

The proposed synthetic pulse generation system is shown in Fig. 6.3, where the whole system is consisted of three engineered minimal cells, and each of them takes two promoters as its input to perform a specific logic operation. With the absence of Arabinose (Ara) and Anhydrotetracycline (aTc) molecules, the NOR operation of Minimal Cell 1 is switched on to produce Isopropyl β-D-1-thiogalactopyranoside (IPTG) molecules which represent a logic 1 state, while the AND operation of Minimal Cell 2 is switched off. On the contrary, upon the addition of Ara and aTc molecules into the cell culture, the NOR operation of Minimal Cell 1 is switched off, while the AND operation of Minimal Cell 2 is switched on to produce N-(β-Ketocaproyl)-L-homoserine lactone (3OC6) molecules which represent a logic 1 state. The released IPTG and 3OC6 molecules diffuse in the environment along with a natural degradation and a portion of them can arrive at Minimal Cell 3. As long as the concentration of arrived IPTG or 3OC6 molecules exceeds the logic thresholds of the two promoters of Minimal Cell 3, the activity of the Minimal Cell 3 NOR gate will change from a HIGH state to a LOW state and finally prevents the accumulation of yellow fluorescent protein (YFP), which is an output indicator of the system. Thus, adjusting the propagation distance

between Minimal Cell 1 and Minimal Cell 3 and the distance between Minimal Cell 2 and Minimal Cell 3 allows us to control the maximum fluorescent intensity of YFP. In this chapter, we focus on investigating the impact of different distances between Minimal Cell 2 and Minimal Cell 3 on the generated pulse and leave other cases for future work.

6.3 Construction and Modeling of Minimal Cells 1 and 2

This section details the synthetic regulatory networks of Minimal Cells 1 and 2, and the corresponding mathematical characterizations are also derived based on the Shea-Ackers formalism introduced in Section 6.2.2. In this way, we quantify the concentrations of released IPTG at Minimal Cell 1 and 3OC6 at Minimal Cell 2, which will be used for the propagation channel analysis in Section 6.4.

6.3.1 NOR Gate of Minimal Cell 1

The NOR gate demonstrates a NOT-OR behavior and generates a logic 1 output when both inputs are logic 0. For Minimal Cell 1, we borrow the NOR gate design from [64], where the gene expression product of two tandem promoters acts as a repressor that inactivates an output promoter. As the expression of a repressor by tandem promoters is common in genomes, this NOR gate design represents a fundamental unit of biological computation. As shown in Fig. 6.4, promoters BAD and Tet* with the same orientation are selected as the tandem promoters that perform an OR operation, and the promoter CI repressed by protein CI serves as a NOT gate. The LacI sequence is controlled by promoter CI and is responsible for generating molecule IPTG that connects Minimal Cells 1 and 3 in Fig. 6.3. In the following, we first present the modeling of a single promoter and then show how to use it to mathematically characterize the NOR gate design in Fig. 6.4.

Single Promoter Modeling

Take the promoter BAD for example, in the following we will show the mathematical characterizations of i) the inducer binding to TF, ii) the TF binding to DNA, and iii) the expressed protein quantity of gene expression. Ara is the inducer for promoter BAD and it first binds to its cognate TF, which can be modeled by [161, eq. (1)] at

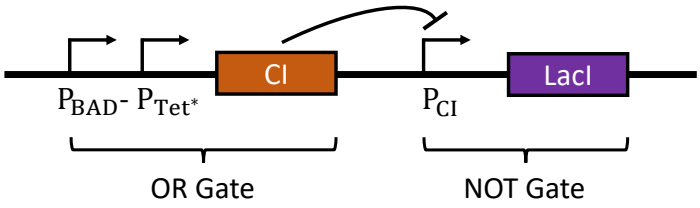

Fig. 6.4 The genetic NOR gate of Minimal Cell 1, where the bent arrow indicates areas where transcription starts, the rectangle represents the DNA sequences that are read during translation to create proteins, and the $\perp$ symbol denotes the repression of promoter CI by protein CI. For the tandem promoters BAD and Tet*, BAD can be considered as the upstream promoter, while Tet* can be considered as the downstream promoter.

equilibrium as

$$f_{TL} = \frac{C_{\text{Ara}}^l}{K_D^l + C_{\text{Ara}}^l}, \tag{6.2}$$

where f_{TL} is the fraction of TF bound to inducer, C_{Ara} is the concentration of inducer, K_D is the dissociation constant, and l is the Hill coefficient. With mass conservation, the fraction of TF without inducer bound is

$$f_T = 1 - f_{TL}. \tag{6.3}$$

The binding of TF to promoter BAD is modeled according to the Shea-Ackers formalism introduced in (6.1). Fig. 6.5 plots the transcription states of promoter BAD with binding sites O1, O2, and I1-I2. Recall that gene transcription begins with the binding of RNAP to the promoter region, we know that state 1 (i.e., RNAP alone) and state 2 (i.e., RNAP with AraC-Ara complex) can result in the expression of a gene; thus the probability of promoter BAD being in the open complex state (i.e., ready for the start of transcription) is

$$P_{\text{BAD}} = \frac{K_1 + K_2 f_{TL}}{1 + K_1 + K_2 f_{TL} + K_3 f_T}, \tag{6.4}$$

where K_1, K_2, and K_3 are constant coefficients defined for different binding states, and their values will be given in Section 6.7.

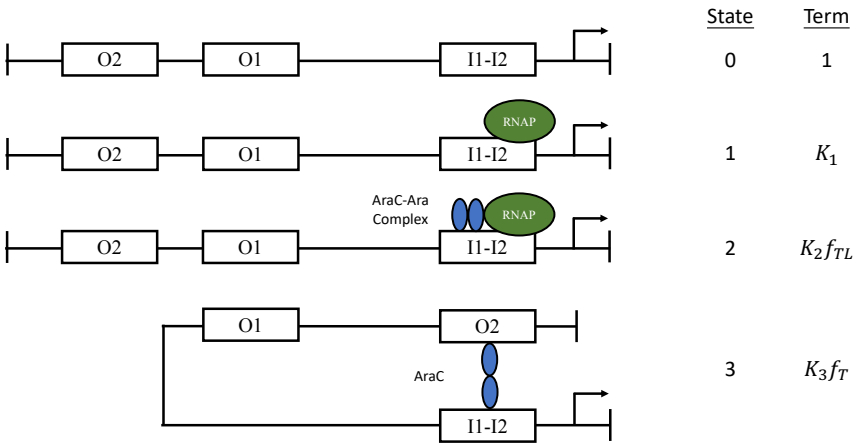

Fig. 6.5 The transcription states of the promoter BAD. Some transcription states are ignored as they are assumed to be infrequently occurred [161]. The term values of states (≥ 1) are normalized by the value of state 0 so that the state 0 value is 1. It is noted that K_1, K_2, and K_3 vary from promoter to promoter and these parameters are even likely to have different units.

For the protein controlled by promoter BAD, its production can be modeled as [161, eq. (7)]

$$\frac{\mathrm{d}C_{\mathrm{BAD}}}{\mathrm{d}t} = abP_{\mathrm{BAD}} - \gamma C_{\mathrm{BAD}}, \tag{6.5}$$

where a is the maximum transcription rate, b is the protein production rate, P_{BAD} is given in (6.4), and γ is the degradation rate. The differential equation in (6.5) can be converted to a more practical non-differential expression by simply considering the steady state condition [73]. As such, the steady-state concentration of protein $C_{\mathrm{BAD}}^{\mathrm{SS}}$ is expressed as

$$C_{\mathrm{BAD}}^{\mathrm{SS}} = (ab/\gamma) \cdot P_{\mathrm{BAD}} = C_{\mathrm{BAD}}^{\max} \cdot P_{\mathrm{BAD}}, \tag{6.6}$$

where we denote $(ab/\gamma) = C_{\mathrm{BAD}}^{\max}$ to represent the maximum concentration of protein produced from promoter BAD at a steady state.

In practice, fluorescent protein is usually chosen as the gene expression product since it is easier to estimate the protein concentration by measuring the fluorescent intensity via fluorescence spectroscopy. As such, we can express the steady state fluorescent intensity $I_{\mathrm{BAD}}^{\mathrm{SS}}$ by replacing (6.6) with

$$I_{\mathrm{BAD}}^{\mathrm{SS}} = \mathrm{gfp}_{\mathrm{BAD}}^{\max} \cdot P_{\mathrm{BAD}}, \tag{6.7}$$

where $\text{gfp}_{\text{BAD}}^{\max}$ is the fluorescence produced at maximum induction. Substituting (6.2)-(6.4) into (6.7), we can obtain

$$I_{\text{BAD}}^{\text{SS}} = \frac{\text{gfp}_{\text{BAD}}^{\max}[(K_1 + K_2)C_{\text{Ara}}^l + K_1 K_D^l]}{(1 + K_1 + K_2)C_{\text{Ara}}^l + (1 + K_1 + K_3)K_D^l}. \tag{6.8}$$

When $\text{gfp}_{\text{BAD}}^{\max}$ is given, it is essential to establish the relation between fluorescent intensity and concentration. In general, the molecular concentration $C_{\text{BAD}}^{\text{SS}}$ can be retrieved from fluorescent intensity using the following equation [162]

$$C_{\text{BAD}}^{\text{SS}} = \frac{1}{\varepsilon L}\lg\frac{kI_0\Phi}{kI_0\Phi - I_{\text{BAD}}^{\text{SS}}}, \tag{6.9}$$

where ε is the molar absorptivity, L is the path length, k describes the efficiency of the spectrometer at transferring light, I_0 is incident light intensity, and Φ is the quantum yield that is defined as the ratio of the number of photons emitted to the number of photons absorbed. From (6.9), it is clear that the fluorescent intensity $I_{\text{BAD}}^{\text{SS}}$ is dependent on the fluorescent protein type via ε and Φ, and the experimental setup via L, k, and I_0.

NOR Gate Modeling

Based on the above single promoter modeling, we derive the output of the NOR gate of Minimal Cell 1 (see Fig. 6.4) in the following. The input of protein CI in Fig. 6.4 can be expressed by a linear combination of the steady activities of tandem promoters BAD and Tet*, which is

$$I_{\text{BAD-Tet}^*}^{\text{SS}} = \zeta_U I_{\text{BAD}}^{\text{SS}} + \zeta_D I_{\text{Tet}^*}^{\text{SS}}, \tag{6.10}$$

where ζ_U denotes the impacts (e.g., interference) of downstream promoter Tet* on upstream promoter BAD, ζ_D denotes the impacts of upstream promoter BAD on downstream promoter Tet*, and $I_{\text{Tet}^*}^{\text{SS}}$ is the steady activity of promoter Tet*. Fig. 6.6 plots the transcription states of promoter Tet*. Relying on the single promoter modeling for promoter BAD in (6.2)-(6.4), (6.8), $I_{\text{Tet}^*}^{\text{SS}}$ can be derived as

$$I_{\text{Tet}^*}^{\text{SS}} = \frac{\text{gfp}_{\text{Tet}^*}^{\max}[K_1(K_D^l + C_{\text{aTc}}^l)^2]}{(K_D^l + C_{\text{aTc}}^l)[(1 + K_1)(K_D^l + C_{\text{aTc}}^l) + 2K_2K_D^l] + (K_2K_D^l)^2}, \tag{6.11}$$

where C_{aTc} is the concentration of inducer aTc and $\text{gfp}_{\text{Tet}^*}^{\max}$ is the fluorescence produced at maximum induction.

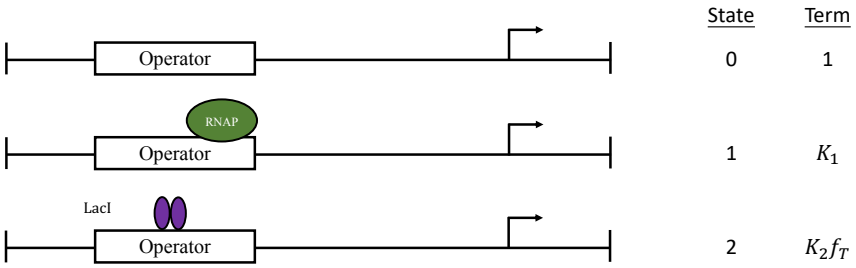

Fig. 6.6 The transcription states of the promoter Tet*.

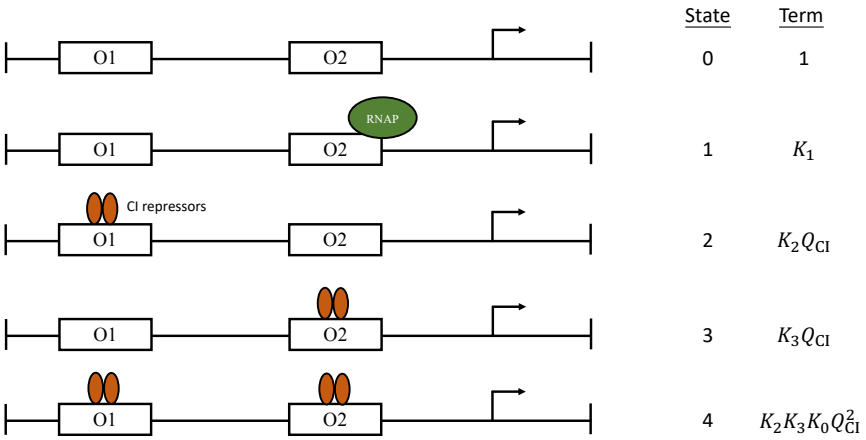

Fig. 6.7 The transcription states of the promoter CI.

As shown in Fig. 6.4, the protein CI further turns off the downstream promoter CI as a repressor to perform the NOT gate. According to transcription states in Fig. 6.7, we can write the probability of promoter CI being in the open complex state as

$$P_{\mathrm{CI}} = \frac{K_1}{1 + K_1 + K_2 Q_{\mathrm{CI}} + K_3 Q_{\mathrm{CI}} + K_2 K_3 K_0 Q_{\mathrm{CI}}^2}, \tag{6.12}$$

where Q_{CI} represents the amount of the generated protein, either expressed in terms of concentration or fluorescent intensity. When the units of parameters K_2 and K_3 are fluorescence related, Q_{CI}=$I^{\mathrm{SS}}_{\mathrm{BAD\text{-}Tet^*}}$. Hence, we derive the fluorescent intensity of the NOR gate output as

$$I^{\text{Cell-1}}_{\mathrm{NOR}} = \frac{\mathrm{gfp}^{\max}_{\mathrm{CI}} K_1}{1 + K_1 + [K_2 + K_3 + K_2 K_3 K_0 (\zeta_U I^{\mathrm{SS}}_{\mathrm{BAD}} + \zeta_D I^{\mathrm{SS}}_{\mathrm{Tet^*}})](\zeta_U I^{\mathrm{SS}}_{\mathrm{BAD}} + \zeta_D I^{\mathrm{SS}}_{\mathrm{Tet^*}})}, \tag{6.13}$$

where $\mathrm{gfp}^{\max}_{\mathrm{CI}}$ is the fluorescence produced at maximum induction for promoter CI, and $I^{\mathrm{SS}}_{\mathrm{BAD}}$ and $I^{\mathrm{SS}}_{\mathrm{Tet^*}}$ are given in (6.8) and (6.11), respectively.

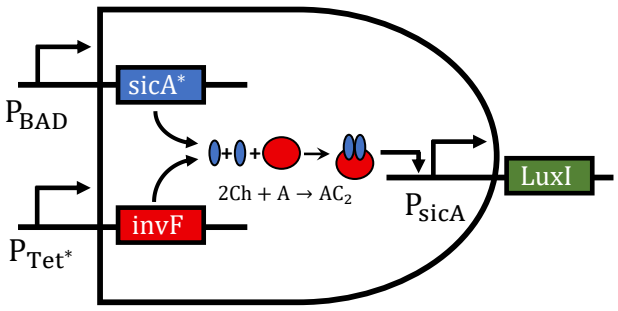

Fig. 6.8 The genetic AND gate of Minimal Cell 2. sicA* is a mutant of sicA.

6.3.2 AND Gate of Minimal Cell 2

The AND gate of Minimal Cell 2 can be implemented by layering multiple NOR gates due to the functional completeness of the NOR gate (i.e., any computational operation can be implemented by layering NOR gates). However, this construction requires orthogonality of the intercellular signaling channels and would complicate the whole system. For the sake of reducing the number of promoters, we borrow the AND gate design proposed in [161], which has been verified by wet lab experiments.

Fig. 6.8 depicts the structure of the AND gate of Minimal Cell 2, where the input promoters are the same as those of the NOR gate of Minimal Cell 1. Unlike that $\mathrm{P_{BAD}} - \mathrm{P_{Tet^*}}$ collectively drives the expression of the protein CI, in the AND gate, these two promoters individually controls the expression of two proteins. In particular, promoter BAD drives the expression of a chaperone protein *SicA* (coding sequence: sicA*), and promoter Tet* drives the expression of an activator *InvF* (coding sequence: invF). According to (6.7), the *total* amounts of the expressed chaperone protein $I^{\mathrm{SS}}_{\mathrm{Ch}_0}$ and activator $I^{\mathrm{SS}}_{\mathrm{A}_0}$ are

$$I^{\mathrm{SS}}_{\mathrm{Ch}_0} = \theta_{\mathrm{Ch}} \cdot \mathrm{gfp}^{\max}_{\mathrm{BAD}} \cdot P_{\mathrm{BAD}} = \theta_{\mathrm{Ch}} \cdot I^{\mathrm{SS}}_{\mathrm{BAD}}, \tag{6.14}$$

$$I^{\mathrm{SS}}_{\mathrm{A}_0} = \theta_{\mathrm{A}} \cdot \mathrm{gfp}^{\max}_{\mathrm{Tet^*}} \cdot P_{\mathrm{Tet^*}} = \theta_{\mathrm{A}} \cdot I^{\mathrm{SS}}_{\mathrm{Tet^*}}, \tag{6.15}$$

where θ_{Ch} and θ_{A} are two coefficients that account for changes in the expression of the genes by various factors, such as different ribosome binding sites (RBSs). $I^{\mathrm{SS}}_{\mathrm{BAD}}$ and $I^{\mathrm{SS}}_{\mathrm{Tet^*}}$ are given in (6.8) and (6.11), respectively.

From Fig. 6.8, two chaperone molecules (denoted by species Ch) can react with one activator molecule (denoted by species A) to generate a SicA—InvF complex (denoted

by species AC_2) following the reaction

$$2\mathrm{Ch} + \mathrm{A} \rightarrow \mathrm{AC}_2. \tag{6.16}$$

After the above reaction, the amount of the *remaining* reactants and product at the equilibrium can be related via the dissociation constant K_{AC} as

$$K_{AC} = \frac{I^{\mathrm{SS}}_{\mathrm{A}}(I^{\mathrm{SS}}_{\mathrm{Ch}})^2}{I^{\mathrm{SS}}_{\mathrm{AC}_2}}. \tag{6.17}$$

Based on the mass balances, we have the following relations:

$$I^{\mathrm{SS}}_{\mathrm{A}_0} = I^{\mathrm{SS}}_{\mathrm{A}} + I^{\mathrm{SS}}_{\mathrm{AC}_2}, \tag{6.18}$$

$$I^{\mathrm{SS}}_{\mathrm{Ch}_0} = I^{\mathrm{SS}}_{\mathrm{Ch}} + 2I^{\mathrm{SS}}_{\mathrm{AC}_2}. \tag{6.19}$$

Substituting (6.14), (6.15), (6.18), and (6.19) into (6.17), the cubic equation for $I^{\mathrm{SS}}_{\mathrm{AC}_2}$ is

$$4(I^{\mathrm{SS}}_{\mathrm{AC}_2})^3 - 4(I^{\mathrm{SS}}_{\mathrm{A}_0} + I^{\mathrm{SS}}_{\mathrm{Ch}_0})(I^{\mathrm{SS}}_{\mathrm{AC}_2})^2 + [4I^{\mathrm{SS}}_{\mathrm{A}_0}I^{\mathrm{SS}}_{\mathrm{Ch}_0} + (I^{\mathrm{SS}}_{\mathrm{Ch}_0})^2 + K_{AC}]I^{\mathrm{SS}}_{\mathrm{AC}_2} - I^{\mathrm{SS}}_{\mathrm{A}_0}(I^{\mathrm{SS}}_{\mathrm{Ch}_0})^2 = 0. \tag{6.20}$$

We derive the amount of SicA-InvF complex $I^{\mathrm{SS}}_{\mathrm{AC}_2}$ in the following lemma.

Lemma 8. *The solution of the cubic equation in* (6.20) *is derived as*

$$I^{\mathrm{SS}}_{\mathrm{AC}_2} = \sqrt[3]{-\frac{q}{2} + \sqrt{(\frac{q}{2})^2 + (\frac{p}{3})^3}} + \sqrt[3]{-\frac{q}{2} - \sqrt{(\frac{q}{2})^2 + (\frac{p}{3})^3}} - \frac{I^{\mathrm{SS}}_{\mathrm{A}_0} + I^{\mathrm{SS}}_{\mathrm{Ch}_0}}{3}, \tag{6.21}$$

where

$$p = [12K_{AC} - (4I^{\mathrm{SS}}_{\mathrm{A}_0} - 2I^{\mathrm{SS}}_{\mathrm{Ch}_0})^2]/48 \tag{6.22}$$

$$\textit{and } q = [-8(I^{\mathrm{SS}}_{\mathrm{A}_0})^3 + 12(I^{\mathrm{SS}}_{\mathrm{A}_0})^2 I^{\mathrm{SS}}_{\mathrm{Ch}_0} - 6I^{\mathrm{SS}}_{\mathrm{A}_0}(I^{\mathrm{SS}}_{\mathrm{Ch}_0})^2 + 9(I^{\mathrm{SS}}_{\mathrm{A}_0} + I^{\mathrm{SS}}_{\mathrm{Ch}_0}) + (I^{\mathrm{SS}}_{\mathrm{Ch}_0})^3]/108. \tag{6.23}$$

Proof. Please refer to Appendix C.1. □

From Fig. 6.8, the inducible promoter of AC_2 (i.e., SicA—InvF complex) is sicA. With the transcription states of the promoter sicA shown in Fig. 6.9, the transcription

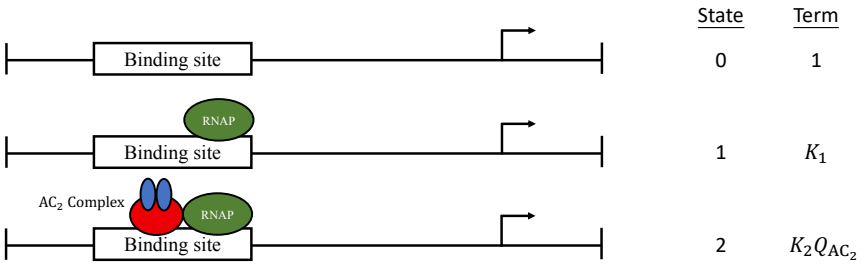

Fig. 6.9 The transcription states of the promoter sicA.

probability of sicA is

$$P_{\text{sicA}} = \frac{K_1 + K_2 Q_{\text{AC}_2}}{1 + K_1 + K_2 Q_{\text{AC}_2}}, \tag{6.24}$$

where Q_{AC_2} represents the amount of the generated protein. Given the maximum fluorescence $\text{gfp}_{\text{sicA}}^{\max}$, we derive the output fluorescent intensity of the AND gate in Minimal Cell 2 as

$$I_{\text{AND}}^{\text{Cell-2}} = \frac{\text{gfp}_{\text{sicA}}^{\max}[K_1 + K_2 I_{\text{AC}_2}^{\text{SS}}]}{1 + K_1 + K_2 I_{\text{AC}_2}^{\text{SS}}}, \tag{6.25}$$

where $I_{\text{AC}_2}^{\text{SS}}$ is defined in (6.21). Until now, we complete the derivation of the outputs of Minimal Cells 1 and 2, which will be used in Section 6.4.

6.4 Propagation Analysis of Signalling Molecules

The communication between Minimal Cells 1/2 and 3 relies on the QS systems, where autoinducers are released by Minimal Cells 1 and 2, and diffuse in the environment along with a natural degradation. In particular, the digital gates are hosted inside *E. Coli* which is a type of gram-negative bacteria and the released autoinducers are referred to as acyl-homoserine lactones (AHL). In this section, we focus on the propagation analysis of AHL. This helps to determine the amount of molecules that arrive at Minimal Cell 3, whose analytical results will be used in Section 6.5. Generally, the spatial-temporal behavior of AHL can be described using a diffusion-reaction PDE. To facilitate the propagation channel analysis, we make the following assumptions:

- All three minimal cells are spotted in a circular culture plate. It is assumed that there is no diffusion along the vertical axis of the plate, thus the diffusion only occurs along the horizontal plane of the culture [163].

- The distance between two minimal cells is much longer than the diameter of the minimal cells, therefore resulting in an approximation of the minimal cells as points at their respective locations. Thus, the presence of the minimal cells does not interfere with the diffusion of AHL molecules [73]. We note that each minimal cell can be regarded as a passive receiver for others because the AHL molecules released by *E. Coli* are small enough to cross the minimal cell membrane (see Chapter 2.3.1). In this sense, all the minimal cells also do not impede the AHL diffusion.

- At steady state, the concentration of AHL is appropriately homogeneous inside and around a minimal cell.

- The culture is homogeneous so that the diffusion coefficient is constant.

Based on the above assumptions, we adopt the polar coordinate system and consider the release point as the origin. Thus, the general diffusion-reaction equation given in (2.10) for Chapter 2.2.3 can be reduced to model the diffusion of AHL, which is

$$\frac{\partial C(r,t)}{\partial t} = D[\frac{1}{r}\frac{\partial}{\partial r}r(\frac{\partial C(r,t)}{\partial r})] - k_d C(r,t), \tag{6.26}$$

where r is the radial distance, D is the diffusion coefficient, k_d is the molecule degradation rate.[1] Similar to [73], we define the steady state output $I_{\text{NOR}}^{\text{Cell-1}}$ in (6.13) of Minimal Cell 1 (or $I_{\text{AND}}^{\text{Cell-2}}$ in (6.25) of Minimal Cell 2) as the initial concentration C_0 for diffusion (C_0 should be retrieved from $I_{\text{NOR}}^{\text{Cell-1}}$ or $I_{\text{AND}}^{\text{Cell-2}}$ via (6.9)), and the time that Minimal Cell 1 or 2 reaches the steady state as the released time (i.e., $t = 0$). Thus, in a polar coordinate system, the initial condition for (6.26) is[2]

$$\text{IC}_7 : C(r,0) = \frac{C_0}{2\pi r}\delta(r). \tag{6.27}$$

At the edge of a culture r_b, the production of AHL is zero, so we can define a Neumann boundary condition as [64, eq. (14)]

$$\text{BC}_6 : J_{\text{Diff}}|_{r=r_b} = 0, \tag{6.28}$$

[1]For simplicity, we use the general variables D and k_d for AHL. The values of the diffusion coefficient and degradation rate for IPTG and 3OC6 (i.e., D_{IPTG}, D_{3OC6}, $k_{d_{\text{IPTG}}}$, and $k_{d_{\text{3OC6}}}$) will be given in Section 6.7.

[2]We note the r and 2π in denominator represent the coordinate conversion from Cartesian coordinate to polar coordinate and the azimuthal symmetry, respectively. Thus, eq. (6.27) is equivalent to $C_0\delta(x)\delta(y)$ in Cartesian coordinate.

where J_{Diff} is the AHL diffusion flux and is defined in (2.1) for Chapter 2.2.1. We solve (6.26) in the following theorem.

Theorem 5. *With the initial condition* (6.27) *and the boundary condition* (6.28)*, the solution of the diffusion-reaction equation in* (6.26) *is derived as*

$$C(r,t) = \frac{C_0}{\pi r_b^2} \sum_{n=0}^{\infty} \frac{J_0(\frac{\alpha_n}{\sqrt{D}} r)}{J_0^2(\frac{\alpha_n}{\sqrt{D}} r_b)} e^{-(\alpha_n^2 + k_d)t}, \tag{6.29}$$

where $J_0(r)$ is the Bessel function of the first kind with order zero and α_n should satisfy $J_1(\frac{\alpha_n}{\sqrt{D}} r_b) = 0$.

Proof. To solve (6.26), we use the separation variable method [164]. Let us assume that the solution of (6.26) has the form $C(r,t) = R(r)T(t)$. Thus, eq. (6.26) can be rewritten as

$$\frac{1}{T(t)} \frac{\mathrm{d}T(t)}{\mathrm{d}t} = \frac{D}{R(r)} [\frac{\mathrm{d}^2 R(r)}{\mathrm{d}r^2} + \frac{1}{r} \frac{\mathrm{d}R(r)}{\mathrm{d}r}] = -(\lambda - k_d), \tag{6.30}$$

where λ is an arbitrary constant. Meanwhile, the BC_6 in (6.28) can be rewritten as

$$T(t) \frac{\mathrm{d}R(r)}{\mathrm{d}r}|_{r=r_b} = 0. \tag{6.31}$$

For any $t > 0$, eq. (6.31) is further reduced to the following BC_6 for r, which is

$$\frac{\mathrm{d}R(r)}{\mathrm{d}r}|_{r=r_b} = 0. \tag{6.32}$$

Relying on the separation variable method, we convert (6.30) into two ODEs as

$$\frac{\mathrm{d}T(t)}{\mathrm{d}t} + \lambda T(t) = 0, \tag{6.33}$$

$$\text{and} \quad r^2 \frac{\mathrm{d}^2 R(r)}{\mathrm{d}r^2} + r \frac{\mathrm{d}R(r)}{\mathrm{d}r} + \frac{(\lambda - k_d) r^2}{D} R(r) = 0. \tag{6.34}$$

In the following, we consider three cases for $\lambda - k_d$, that is: $\lambda - k_d = -\alpha^2 < 0$, $\lambda - k_d = 0$, and $\lambda - k_d = \alpha^2 > 0$.

Case 1: If $\lambda - k_d = -\alpha^2 < 0$, the general solution of ODE in (6.34) is

$$R(r) = c_1 I_0(\frac{\alpha}{\sqrt{D}} r) + c_2 K_0(\frac{\alpha}{\sqrt{D}} r), \tag{6.35}$$

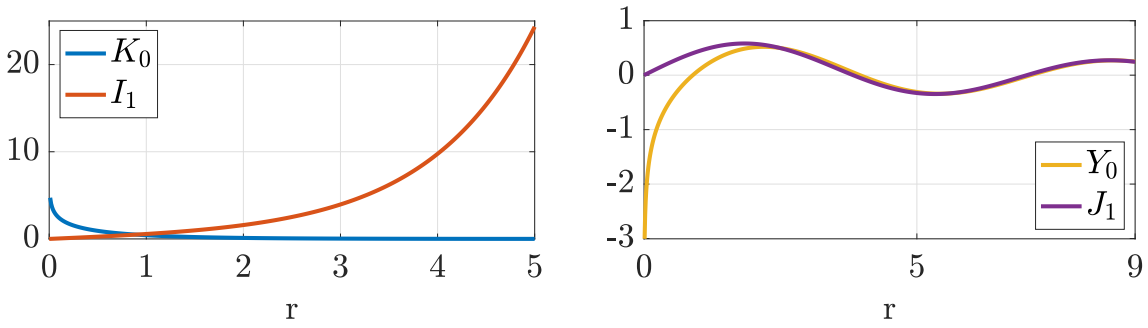

(a) $K_0(r)$ and $I_1(r)$ (b) $Y_0(r)$ and $J_1(r)$

Fig. 6.10 Illustration of some Bessel functions.

where c_1 and c_2 are two free constants, and $I_0(r)$ and $K_0(r)$ are the modified Bessel functions of the first kind and second kind with order zero. In Fig. 6.10a, we note that $K_0(r)$ becomes infinite as r approaches 0 so $K_0(r)$ is excluded from the solution by setting $c_2 = 0$. With the derivation property, we then apply the BC_6 in (6.32) and arrive at

$$\frac{c_1\alpha}{\sqrt{D}} I_1(\frac{\alpha}{\sqrt{D}} r_0) = 0. \tag{6.36}$$

As shown in Fig. 6.10a, the above equation only holds when $\alpha = 0$ but this contradicts the condition of $\lambda - k_d = -\alpha^2 < 0$; thus, the solution for (6.26) does not exist in this case.

Case 2: If $\lambda - k_d = 0$ (i.e., $\lambda = k_d$), the general solution of (6.34) is

$$R(r) = c_3 \ln(r) + c_4, \tag{6.37}$$

where c_3 and c_4 are two free constants. With (6.32), we have $R(r) = c_4$ for (6.34). Moreover, the solution for (6.33) is $c_5 e^{-k_d t}$. Therefore, the general solution of $C(r,t)$ is

$$C(r,t) = R(r)T(t) = A_0 e^{-k_d t}, \tag{6.38}$$

where $A_0 = c_4 c_5$.

Case 3: If $\lambda - k_d = \alpha^2 > 0$, the general solution of (6.34) is

$$R(r) = c_6 J_0(\frac{\alpha}{\sqrt{D}} r) + c_7 Y_0(\frac{\alpha}{\sqrt{D}} r), \tag{6.39}$$

where c_6 and c_7 are two free constants, and $Y_0(r)$ is the Bessel function of the second kind with order zero. Similar to the analysis of $K_0(r)$ in **Case I**, $Y_0(r)$ is also excluded from the solution. With the derivation property and (6.32), we have

$$c_6\frac{\alpha}{\sqrt{D}}J_1(\frac{\alpha}{\sqrt{D}}r)=0 \text{ or } J_1(\frac{\alpha}{\sqrt{D}}r)=0. \tag{6.40}$$

From Fig. 6.10b, we observe that there exists an infinite set of nontrivial coefficients given the oscillatory behavior of $J_1(r)$. We now denote the set of roots (i.e., $J_1(\frac{\alpha}{\sqrt{D}}r_b)=0$) as $\{\alpha_n\}_{n=1}^{\infty}$ with $0<\alpha_1<\cdots<\alpha_\infty$. For the ODE in (6.33), the solution is

$$T_n(t)=c_{8_n}e^{-(\alpha_n^2+k_d)t}, \tag{6.41}$$

where c_{8_n} is a free constant. Then, the solution of (6.28) in **Case 3** becomes

$$C(r,t)=\sum_{n=1}^{\infty}A_nJ_0(\frac{\alpha_n}{\sqrt{D}}r)e^{-(\alpha_n^2+k_d)t}, \tag{6.42}$$

where c_{8_n} in (6.41) becomes a part of A_n which will be determined by the IC_7 in (6.27).

According to the superposition principle [164], we can integrate **Case 2** with **Case 3** and derive

$$C(r,t)=A_0e^{-k_dt}+\sum_{n=1}^{\infty}A_nJ_0(\frac{\alpha_n}{\sqrt{D}}r)e^{-(\alpha_n^2+k_d)t}. \tag{6.43}$$

Due to $J_0(\frac{0}{\sqrt{D}}r)=1$, the term $A_0e^{-k_dt}$ can be rewritten as $A_0J_0(\frac{0}{\sqrt{D}}r)e^{-(0^2+k_d)t}$. Therefore, with $\alpha_0=0$, eq. (6.43) becomes

$$C(r,t)=\sum_{n=0}^{\infty}A_nJ_0(\frac{\alpha_n}{\sqrt{D}}r)e^{-(\alpha_n^2+k_d)t}. \tag{6.44}$$

With the IC_7 in (6.27), the unknown coefficients A_n are determined by operating on both sides of (6.44) by the operator $\int_0^{r_b}rJ_0(\frac{\alpha_m}{\sqrt{D}}r)\mathrm{d}r$ and using the orthogonality relation of Bessel function (i.e., **Lemma 9**) presented after this proof.

With **Lemma** 9, we can obtain A_n as

$$\begin{aligned}A_n\int_0^{r_b}rJ_0^2(\frac{\alpha_n}{\sqrt{D}}r)\mathrm{d}r&=\int_0^{r_b}\frac{C_0}{2\pi r}\delta(r)rJ_0(\frac{\alpha_n}{\sqrt{D}}r)\mathrm{d}r,\\ =>\quad A_n&=\frac{C_0}{\pi r_b^2}\frac{1}{J_0^2(\frac{\alpha_n}{\sqrt{D}}r_b)}.\end{aligned} \tag{6.45}$$

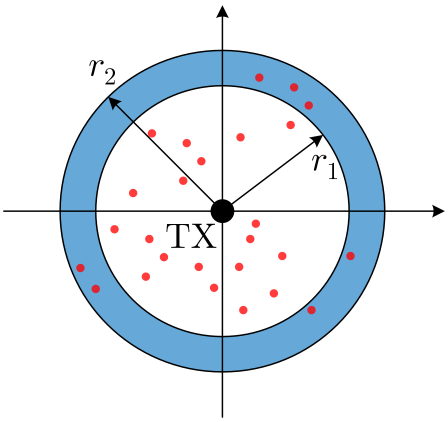

Fig. 6.11 Illustration of an observing region (blue). The red dots are signaling molecules.

Substituting (6.45) into (6.44), we arrive at the solution of the diffusion-reaction equation in (6.29). □

Lemma 9. *The orthogonality property for* $J_0(\frac{\alpha}{\sqrt{D}}r)$ *can be expressed as*

$$\int_0^{r_b} rJ_0(\frac{\alpha_n}{\sqrt{D}}r)J_0(\frac{\alpha_m}{\sqrt{D}}r)\mathrm{d}r = \begin{cases} 0, & \text{for n} \neq \text{m}, \\ \frac{r_b^2}{2}J_0^2(\frac{\alpha_n}{\sqrt{D}}r_b), & \text{for n} = \text{m}. \end{cases} \tag{6.46}$$

Proof. Please refer to Appendix C.2. □

To verify the spatial-temporal concentration distribution in (6.29), we further derive the expected number of molecules for an observing region. Specifically, as shown in Fig. 6.11, we consider an annulus with inner radius r_1 and outer radius r_2 as the observing region. The spatial-temporal concentration distribution can be interpreted as the probability density function (PDF) of a molecule released by a point transmitter when $C_0 = 1$, that is $p(r,t) = C(r,t)\big|_{C_0=1}$. From [40, eqs. (33) and (68)], the expected number of molecules observed at the receiver at time t can be obtained by

$$N_{\mathrm{RX}}(t) = N_{\mathrm{TX}} \int_{r\in\mathcal{S}_{\mathrm{RX}}} p(r,t)\mathrm{d}S, \tag{6.47}$$

where N_{TX} is the number of molecules released by the transmitter at time $t = 0$ and $\mathcal{S}_{\mathrm{RX}}$ is the area of the observing region. We solve (6.47) in the following corollary.

Corollary 1. *Due to the release of* N_{TX} *molecules by the minimal cell at time* $t = 0$*, the expected number of molecules inside an annulus with inner radius* r_1 *and outer*

Table 6.1 The tandem-promoter combinations for the NOR gate of Minimal Cell 3.

Comb 1	Comb 2	Comb 3	Comb 4	Comb 5
Tac Lux	Tac Lux*	Tac Las	Las Lux	Las Lux*

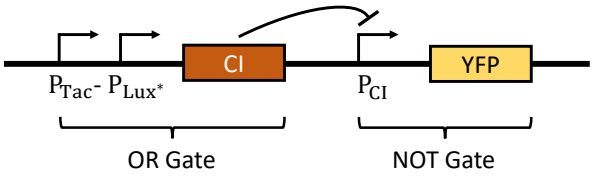

Fig. 6.12 The genetic NOR gate of Minimal Cell 3.

radius r_2 at time t is derived as

$$N_{\mathrm{RX}}(t) = \frac{N_{\mathrm{TX}}}{r_b^2}\left\{\frac{r_2^2 - r_1^2}{2}e^{-k_d t} + \sum_{n=1}^{\infty}\frac{[r_2 J_1(\beta_n r_2) - r_1 J_1(\beta_n r_1)]}{\beta_n J_0^2(\beta_n r_b)}e^{-(\alpha_n^2 + k_d)t}\right\}. \tag{6.48}$$

Proof. Please refer to Appendix C.3. □

6.5 Construction and Modeling of Minimal Cell 3

Based on **Theorem 1** in Section 6.4, we can obtain the concentrations of IPTG and 3OC6 which are the inducers of the input promoters of Minimal Cell 3. The NOR gate of Minimal Cell 3 takes the same structure (i.e., tandem promoters and promoter CI) as that of Minimal Cell 1 but with different input promoters. The motivation is to ensure the orthogonality of the intercellular signaling channels, preventing the inducers of Minimal Cells 1 and 2 (i.e., Ara and aTc) from directly activating Minimal Cell 3. With the promoters provided in [64, 161], four promoters (i.e., promoters Tac, Lux, Lux*, and Las) are still available to be constructed for the NOR gate of Minimal Cell 3. The four promoters can result in five tandem-promoter combinations as summarized in Table 6.1. According to their transfer functions (the simulations see Fig. 6.21 in Section 6.7), we finally choose promoters Tac and Lux* and design the NOR gate as shown in Fig. 6.12.

Followed by the analysis of the tandem promoter in (6.10), the production of the protein CI controlled by promoters Tac and Lux* can be expressed as

$$I^{\mathrm{SS}}_{\text{Tac-Lux}^*} = \zeta_U I^{\mathrm{SS}}_{\mathrm{Tac}} + \zeta_D I^{\mathrm{SS}}_{\mathrm{Lux}^*}, \tag{6.49}$$

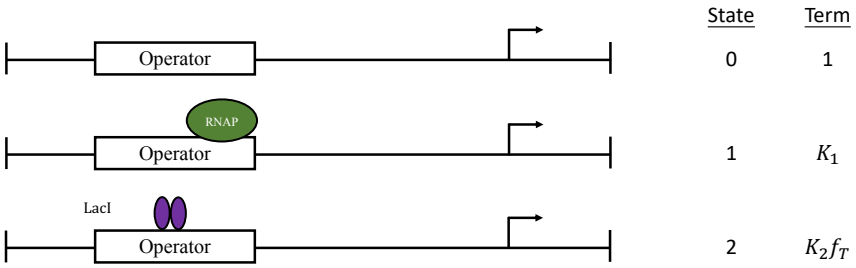

Fig. 6.13 The transcription states of the promoter Tac.

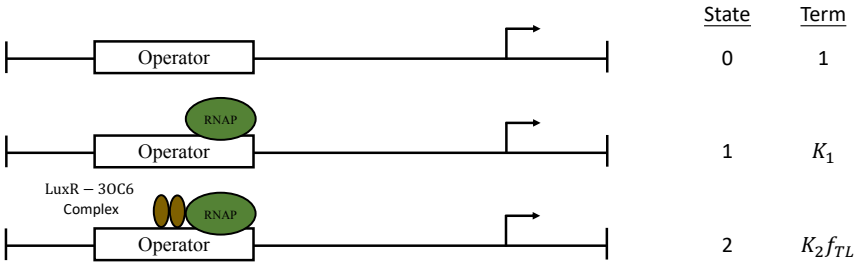

Fig. 6.14 The transcription states of the promoter Lux*.

where $I^{\mathrm{SS}}_{\mathrm{Tac}}$ and $I^{\mathrm{SS}}_{\mathrm{Lux}^*}$ are the steady fluorescent intensities. Given the binding sites of promoter Tac and Lux* in Figs. 6.13 and 6.14, $I^{\mathrm{SS}}_{\mathrm{Tac}}$ and $I^{\mathrm{SS}}_{\mathrm{Lux}^*}$ are calculated as

$$I^{\mathrm{SS}}_{\mathrm{Tac}} = \frac{\mathrm{gfp}^{\max}_{\mathrm{Tac}} K_1 (K_D^l + C^l_{\mathrm{IPTG}})}{(1+K_1)(K_D^l + C^l_{\mathrm{IPTG}}) + K_2 K_D^l} \tag{6.50}$$

$$\text{and} \quad I^{\mathrm{SS}}_{\mathrm{Lux}^*} = \frac{\mathrm{gfp}^{\max}_{\mathrm{Lux}^*} [K_1 (K_D^l + C^l_{\mathrm{3OC6}}) + K_2 C^l_{\mathrm{3OC6}}]}{(1+K_1)(K_D^l + C^l_{\mathrm{3OC6}}) + K_2 C^l_{\mathrm{3OC6}}}, \tag{6.51}$$

where C_{IPTG} and C_{3OC6} are the concentrations of inducers IPTG and 3OC6 that arrive at Minimal Cell 3 and can be determined by (6.29), and $\mathrm{gfp}^{\max}_{\mathrm{Tac}}$ and $\mathrm{gfp}^{\max}_{\mathrm{Lux}^*}$ are the maximum fluorescence.

The expressed protein CI represses the downstream promoter that controls the production of YFP. Here, we consider a continuous model for the fluorescence I_{YFP} of the receiver output, which is expressed by the following differential equation [64, eq. (13)]

$$\frac{\mathrm{d}I_{\mathrm{YFP}}}{\mathrm{d}t} = b_{\mathrm{YFP}} P_{\mathrm{CI}}(C_{\mathrm{IPTG}}, C_{\mathrm{3OC6}}) - \gamma_{\mathrm{YFP}} I_{\mathrm{YFP}}, \tag{6.52}$$

where b_{YFP} is the production rate of YFP, γ_{YFP} is the YFP degradation rate, and $P_{\mathrm{CI}}(C_{\mathrm{IPTG}}, C_{3\mathrm{OC6}})$ is the transcription probability of promoter CI that is the function of the received concentrations C_{IPTG} and $C_{3\mathrm{OC6}}$. Based on (6.12) and (6.49), $P_{\mathrm{CI}}(C_{\mathrm{IPTG}}, C_{3\mathrm{OC6}})$ is expressed as

$$\begin{aligned} &P_{\mathrm{CI}}(C_{\mathrm{IPTG}}, C_{3\mathrm{OC6}}) \\ =&\frac{K_1}{1+K_1+[K_2+K_3+K_2K_3K_0(\zeta_U I^{\mathrm{SS}}_{\mathrm{Tac}}+\zeta_D I^{\mathrm{SS}}_{\mathrm{Lux}^*})](\zeta_U I^{\mathrm{SS}}_{\mathrm{Tac}}+\zeta_D I^{\mathrm{SS}}_{\mathrm{Lux}^*})}, \end{aligned} \tag{6.53}$$

where $I^{\mathrm{SS}}_{\mathrm{Tac}}$ and $I^{\mathrm{SS}}_{\mathrm{Lux}^*}$ are functions of C_{IPTG} (see (6.50)) and $C_{3\mathrm{OC6}}$ (see (6.51)), respectively.

As the initial fluorescent intensity is zero at $t = 0$, the solution of (6.52) can be derived as

$$I_{\mathrm{YFP}}(t) = e^{-\gamma_{\mathrm{YFP}}t}\left[c + b_{\mathrm{YFP}}\int P_{\mathrm{CI}}(C_{\mathrm{IPTG}}, C_{3\mathrm{OC6}})e^{\gamma_{\mathrm{YFP}}t}\mathrm{d}t\right], \tag{6.54}$$

where $c = -b_{\mathrm{YFP}}\int P_{\mathrm{CI}}(C_{\mathrm{IPTG}}, C_{3\mathrm{OC6}})e^{\gamma_{\mathrm{YFP}}t}\mathrm{d}t|_{t=0}$.

6.6 Pulse Generation Analysis

In previous sections, we individually describe the behavior of each synthetic minimal cell and the propagation channel of AHL; in this section, we integrate them together to detail the mechanism of the whole system. According to the system model in Fig. 6.3, without IPTG and 3OC6, the two inputs of Minimal Cell 3 are both logic 0, and Minimal Cell 3 can produce a logic 1 output, which results in an accumulation of YFP. When enough Ara and aTc are added to the environment, the Minimal Cell 2 output is converted from logic 0 to logic 1 with a release of 3OC6. If this logic 1 signal arrives at Minimal Cell 3, the output of Minimal Cell 3 is then changed to logic 0. This state change prevents YFP accumulation and leads to a decrease with the natural YFP degradation.

One important requirement to ensure the pulse generation is the functional connection between Minimal Cells 2 and 3, which means that the arrived 3OC6 molecules from Minimal Cell 2 should span the input threshold of Minimal Cell 3. Unlike electric circuits where the logic level (e.g., voltage value) is identical for all gates, different genetic gates have unique thresholds because they are based on different promoters and

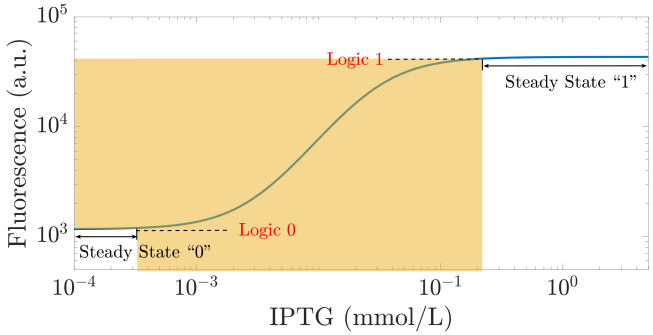

(a) Promoter Tac: Eq. (6.50)

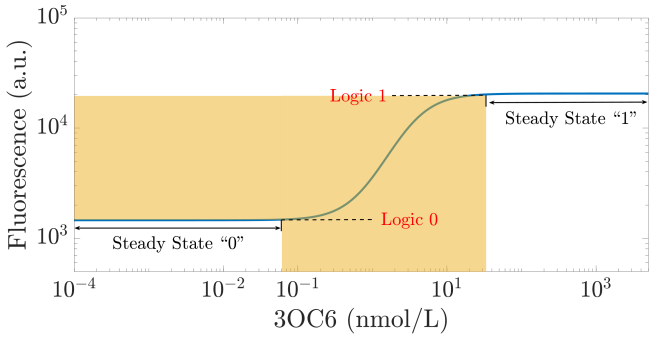

(b) Promoter Lux*: Eq. (6.51)

Fig. 6.15 The transfer functions of the promoters Tac and Lux* of the inducible systems.

have different transfer functions.[3] To illustrate this, we provide the transfer functions of promoters Tac and Lux* in Fig. 6.15, where their different dynamic ranges are highlighted using a yellow block. From Fig. 6.15, it is clear that each promoter has two steady output states (i.e., steady states "1" and "0"), which are interpreted as logic 1 and logic 0, respectively. More importantly, these states are caused by different inducer concentrations. Thus, at Minimal Cell 3, the concentration of 3OC6 must trigger a logic change of promoter Lux* for pulse generation.

With the functional connection, we can achieve different pulse-shaped signals by adjusting the distance between Minimal Cells 2 and 3, i.e., r_{23}. The longer the distance is, the longer the Minimal Cell 3 keeps a logic 1 output, which results in a higher peak value of the generated pulse.

[3]Throughout this chapter, the promoter transfer function is defined as the promoter output (the intensity of fluorescent protein reported in a.u.) as a function of the inducer concentration at a steady state.

Table 6.2 The Shea-Ackers parameters of promoters [64, 161].

Cell	Minimal Cells 1 and 2			Minimal Cell 3				Minimal Cells 1 and 3
Promoter	BAD	Tet*	sicA	Tac	Lux	Lux*	Las	CI
K_D	0.1 mmol/L	1.3 ng/mL	N/A	0.003 mmol/L	10 nmol/L	10 nmol/L	0.2 μmol/L	N/A
l	2.2	2.6	N/A	1.6	1.7	1.7	1.4	N/A
K_1	0.014	350	1.4×10^{-7}	53	0.10	0.064	0.002	350
K_2	12	300	3.6	1950	8.3	5.6	100 (K_2C_{TF})	0.0015 a.u.$^{-1}$
K_3	4.4	N/A	N/A	N/A	N/A	N/A	N/A	0.5 a.u.$^{-1}$
K_0	N/A	N/A	N/A	N/A	N/A	N/A	N/A	0.18
$\text{gfp}^{\max}$	0.2	0.17	1.3×10^4	0.2	0.37	0.11	690 a.u.	181 a.u.

6.7 Numerical Results

In this section, we assess the transfer functions of the proposed NOR and AND gates, examine the channel response of AHL, and evaluate the behavior of our proposed pulse generation system in Fig. 6.3. The promoter parameters, including the dissociation constant K_D, the Hill coefficient l, the transcription site coefficients (i.e., K_0, K_1, K_2, and K_3), and the maximum induction fluorescence $\text{gfp}^{\max}$, are summarized in Table 6.2. It is noted that the values of $\text{gfp}^{\max}$ for promoters Las and CI are reported using raw fluorescence data (i.e., a.u.) in [64]. By contrast, in [161], the raw fluorescence data measured by flow cytometer is rescaled to a relative expression unit (REU) by a linear factor (i.e., 2.2×10^5) in order to standardize measurements between different projects and labs, that is:

$$\text{gfp}^{\max}\ (\text{REU}) = \frac{\text{gfp}^{\max}\ (\text{a.u.})}{\text{Linear factor}}. \tag{6.55}$$

Moreover, we highlight that for promoter Las, the second transcription site coefficient is given by K_2C_{TF} instead of K_2, where C_{TF} is the total concentration of TFs. Thus, its activity probability should be modified on the basis of (6.1), and please refer to equation (5) of the supplement of [64]. In addition, unless otherwise stated, the inducers and their concentration ranges for different promoters are listed in Table 6.3, and 1000 logarithmically spaced values of each range are used in simulations.

6.7.1 Behavior of Minimal Cells 1 and 2

Fig. 6.16 plots the transfer functions of the promoters used for the NOR gate in Minimal Cell 1. Figs. 6.17 and 6.18 show the OR gate behavior of the tandem promoters

Table 6.3 The inducers of different promoters and their default concentrations used for simulations.

Promoter	BAD	Tet*	Tac	Lux/Lux*	Las
Inducer	Ara	aTc	IPTG	3OC6	3OC12
Concentration range	$[10^{-4}, 25]$	$[10^{-4}, 50]$	$[10^{-4}, 5]$	$[10^{-4}, 5000]$	$[10^{-5}, 10]$
Concentration unit	mmol/L	ng/mL	mmol/L	nmol/L	μmol/L

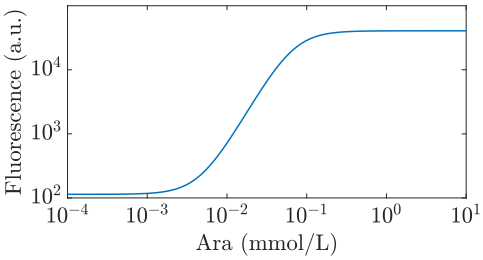

(a) Promoter BAD: Eq. (6.8)

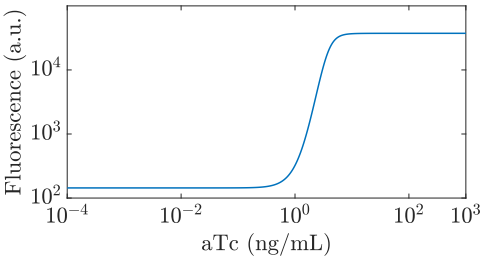

(b) Promoter Tet*: Eq. (6.11)

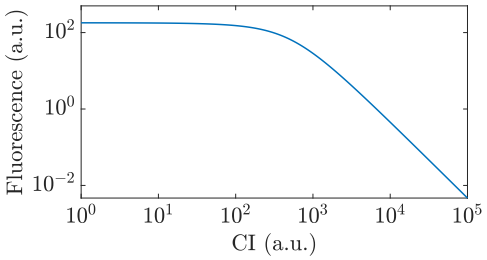

(c) Promoter CI: $\text{gfp}_{\text{CI}}^{\max}\times$Eq. (6.12)

Fig. 6.16 The transfer functions of the promoters BAD, Tet*, and CI of the inducible systems.

using (6.10) and the NOR operation using (6.13), respectively.[4] We set $\zeta_U = \zeta_D = 1$. Moreover, in all of the gate performance figures: the inducer concentration increases from left to right for the horizontal axis, and the inducer concentration increases from bottom to top for the vertical axis. From Figs. 6.16a and b, it is clear that the intensity of red fluorescent protein (RFP), controlled by promoters BAD and Tet, increases with the increase of the inducer concentrations, meaning the binding of inducers to promoters can facilitate the expression of RFP. This characteristic jointly results in the OR gate behavior of the tandem promoters in Fig. 6.17, where the logic 1 output (red and dark red regions) is produced when either or both Ara and aTc are HIGH.

[4] As the binding site coefficients K_2 and K_3 for promoter CI are provided in a.u.$^{-1}$ in Table 6.2, it is unnecessary to convert the outputs of promoters BAD and Tet* from fluorescent intensity to concentration in simulations.

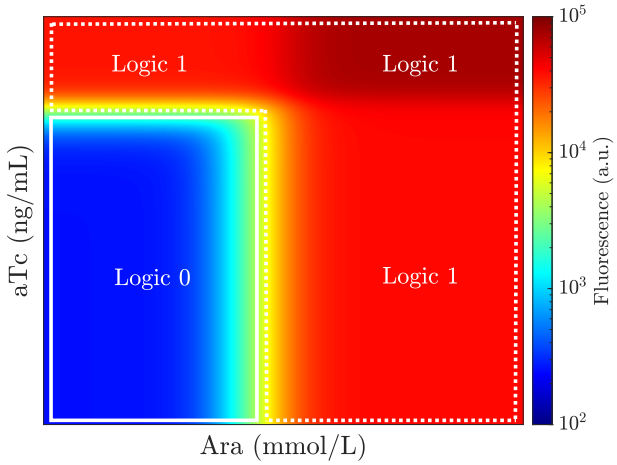

Fig. 6.17 The performance of the OR gate of Minimal Cell 1.

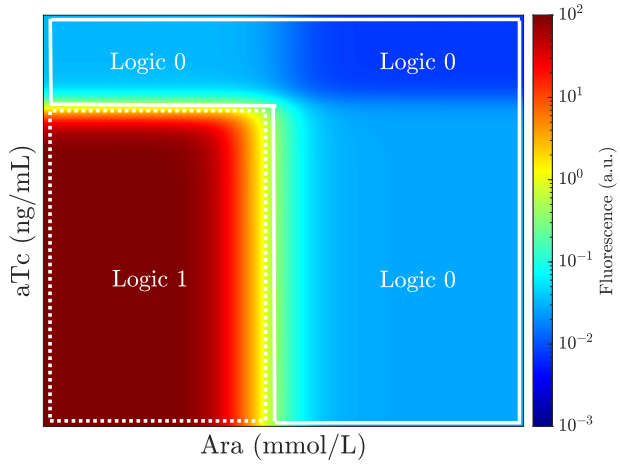

Fig. 6.18 The performance of the NOR gate of Minimal Cell 1.

The transform of the output of tandem promoters (i.e., OR gate output) to the NOR gate output by promoter CI can be observed from Figs. 6.16c, 6.17 and 6.18. Promoter CI can convert the logic 1 (i.e., fluorescent $\geq 10^4$ a.u.) and the logic 0 (i.e., fluorescent $\leq 10^3$ a.u.) outputs of the OR gate in Fig. 6.17 to opposite logic states, yielding the NOR behavior in Fig. 6.18.

In Fig. 6.19, we plot the output fluorescent intensity of Minimal Cell 2 using (6.25) versus the concentration of Ara and aTc.[5] We observe that the heatmap is divided into a yellow-green region (fluorescence $\geq 10^4$ a.u.) and a blue region (fluorescence $\approx$

[5]As the binding site coefficients of promoter sicA are provided in REU in Table 6.2, it is unnecessary to convert the input of promoter sicA (i.e., $I_{\mathrm{AC}_2}^{\mathrm{SS}}$ given in (6.21)) from REU to a.u.

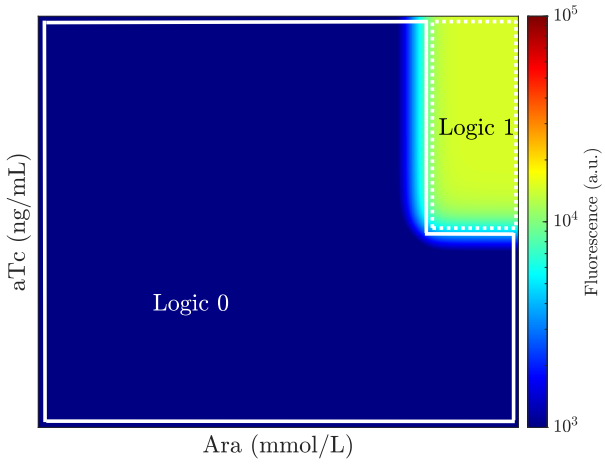

Fig. 6.19 The performance of the AND gate of Minimal Cell 2.

10^3 a.u.), where the distinctive fluorescence difference makes them be interpreted as logic 1 and logic 0, respectively. As the logic 1 output is only produced when both inducers are High, Minimal Cell 2 demonstrates an AND gate response.

6.7.2 Channel Response of AHL

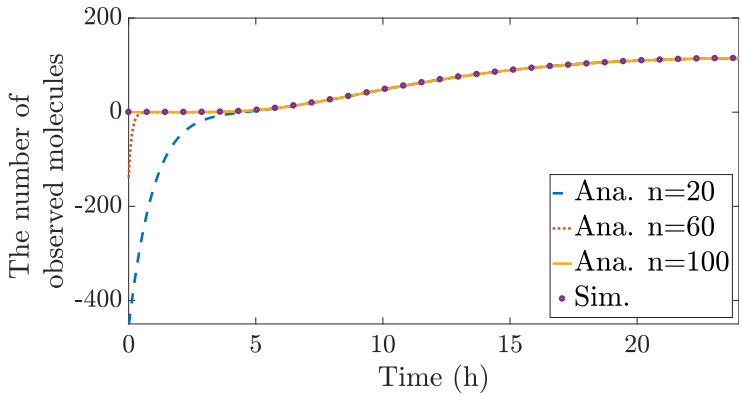

Fig. 6.20 The number of absorbed molecules by time t, where different number of of summation terms n are applied in (6.48).

To verify the expected number of molecules in (6.48), we use the particle-based simulation framework described in [16]. The parameters are set as: $r_1 = 0.8$ cm, $r_2 = 1$ cm, $r_b = 5$ cm, and diffusion coefficient $D = 6 \times 10^{-3}$ cm^2/h. Moreover, the molecule degradation rate $k_d = 0.012$ h^{-1}, and the degradation probability of a molecule during a simulation time step Δt is calculated by $P_{deg} = 1 - \exp(-k_d \Delta t)$.

Table 6.4 The tandem-promoter combinations of Minimal Cell 3.

Tandem promoters	Tac–Lux	Tac–Lux*	Tac–Las	Las–Lux	Las–Lux*
Fluorescence max	0.6098	5.7595	22.6118	0.8110	15.9670
Fluorescence min	0.0035	0.0115	0.0242	0.0087	0.1020
Fold-change	174.2	500.8	934.4	93.2	156.5

We average the expected number of molecules inside the observing region over 1000 independent emissions with $N_{\mathrm{TX}} = 1000$ information molecules.

Fig. 6.20 plots the expected number of molecules with different numbers of summation terms n defined in (6.48). We note that with the increase of n, the analytical curves gradually match the simulation results. When $n = 100$, it shows a precise agreement between the analytical curve and simulation results, which demonstrates the validity of our analysis. In the following simulations, the n is set as 100 to ensure the accuracy of the concentration distribution in (6.29) and to avoid high computational complexity.

6.7.3 Behavior of Minimal Cell 3

Fig. 6.21 plots the performance of the five combinations of the tandem promoters (see Table 6.1) for the NOR gate of Minimal Cell 3. We observe that there is an incorrect output logic for promoters Tac–Las, Las–Lux, Las–Lux*, which are bounded by white dash lines in Figs. 6.21c-e. Thus, the above three combinations fail to realize the NOR operation. The reason is that the outputs of the tandem promoters (i.e., the outputs of the OR gate) do not fall into the dynamic range of promoter CI. Moreover, to measure the dynamic range of a design, we define a fold-change between the lowest and the highest fluorescent intensity as

$$\text{Fold-change} = \frac{\text{Maximum fluorescent intensity}}{\text{Minimum fluorescent intensity}}. \tag{6.56}$$

The fold-change of the five NOR gates is listed in Table 6.4. Compared to Tac-Lux, it is clear that Tac-Lux* has a higher fold-change and a higher maximum fluorescence. Therefore, we finally choose tandem promoters Tac-Lux* to design the NOR gate of Minimal Cell 3.

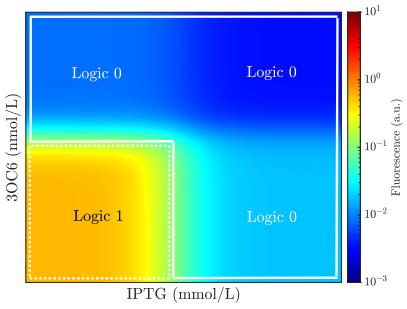

(a) Tandem promoters Tac–Lux

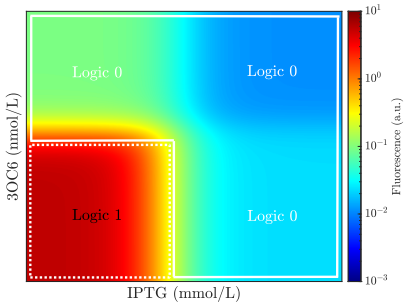

(b) Tandem promoters Tac–Lux*

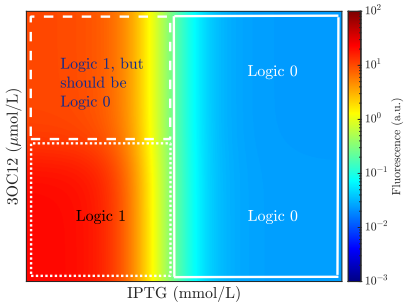

(c) Tandem promoters Tac–Las

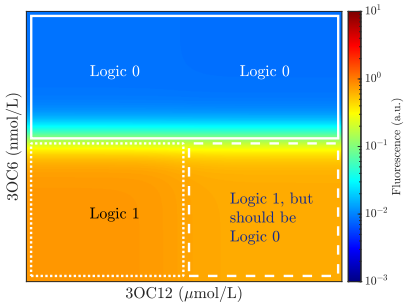

(d) Tandem promoters Las–Lux

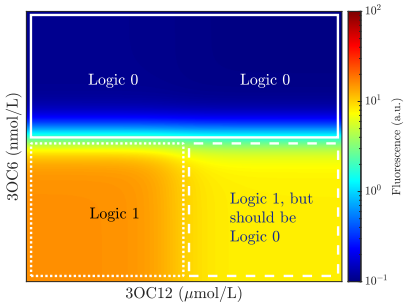

(e) Tandem promoters Las–Lux*

Fig. 6.21 The performance of the NOR gate with five tandem-promoter combinations of Minimal Cell 3.

6.7.4 Pulse Generation

With the desired behavior of all the minimal cells and the verified channel response of AHL, in the following, we evaluate the pulse-shaped signal generated at Minimal Cell 3. Specifically, we assume that 0.5 mmol/L of Ara and 25 ng/mL of aTc are added to the culture plate. From Figs. 6.16a and b, these two concentrations represent logic 1 inputs for promoters BAD and Tet*, and lead to a logic 0 output of Minimal Cell 1

Table 6.5 The property of fluorescent proteins [165].

Fluorescent protein	YFP	RFP
Molar absorptivity ε ($\mathrm{L}\cdot\mathrm{mol}^{-1}\cdot\mathrm{cm}^{-1}$)	$83,400$	$112,000$
Quantum yield Φ (Dimensionless quantity)	0.61	0.35

and a logic 1 output of Minimal Cell 2, where the corresponding output fluorescent intensities can be calculated through (6.13) and (6.25).

To convert the fluorescent intensity to concentration, for simplicity, we assume that the spectrometer is ideal, i.e., $k = 1$ in (6.9), meaning that 100% of the input light successfully enters the spectrometer. Meanwhile, we also set $L = 1$ cm and $I_0 = 1$ W throughout this chapter as they are frequently used values in experiments. It is noted that the above values can be easily generalized to other experimental setups.

For the fluorescence emission in a specific color, a broad range of fluorescent protein genetic variants have been developed. In the simulations, we choose enhanced YFP (EYFP) and mRuby for YFP and RFP, respectively. The corresponding molar absorptivity and quantum yield are listed in Table 6.5. As the fluorescence is reported in arbitrary unit (i.e., a.u.) in [64, 161], in simulations, we assume the units for YFP and RFP are mW and μW, respectively.[6]

The diffusion coefficient and degradation rate for signaling molecules IPTG and 3OC6 are set as: $D_{\mathrm{IPTG}} = 23.4 \times 10^{-3}$ cm^2/h [166], $D_{\mathrm{3OC6}} = 19.8 \times 10^{-3}$ cm^2/h [167], $k_{d_{\mathrm{IPTG}}} = 0.037$ h^{-1} [168], $k_{d_{\mathrm{3OC6}}} = 0.108$ h^{-1} [169]. The distance between Minimal Cells 1 and 3 is fixed as $r_{13} = 0.7$ cm. Other parameters are set as: $b_{\mathrm{YFP}} = 100$ a.u. /(hr·cell) and $\gamma_{\mathrm{YFP}} = 0.289$ hr^{-1}. With the above parameters, we can obtain the maximum concentration of IPTG at Minimal Cell 3 as 1.3×10^{-8} mmol/L. From Fig. 6.15a, this maximum concentration is less than the logic 1 threshold of promoter Tac so that the first input of Minimal Cell 3 is always logic 0. Thus, the distance between Minimal Cells 1 and 3 has no impact on the generated pulse, which corresponds to the discussion in Section 6.2.3 that we only focus on investigating the impact of different distances between Minimal Cell 2 and Minimal Cell 3, i.e., r_{23}, on the generated pulse in this chapter.

[6]We note that the product of I_0 and Φ determines the light intensity absorbed by proteins, and this value becomes 0.61 W and 0.35 W for YFP and RFP, respectively. From Figs. 6.18 and 6.19, the observed maximum fluorescent intensities for the YFP of Minimal Cell 1 with NOR operation and the RFP of Minimal Cell 2 with AND operation are 10^2 a.u. and 10^5 a.u., respectively. By assuming the units for YFP and RFP are mW and μW, we can ensure that the observed fluorescent intensity is always smaller than the light intensity absorbed by proteins.

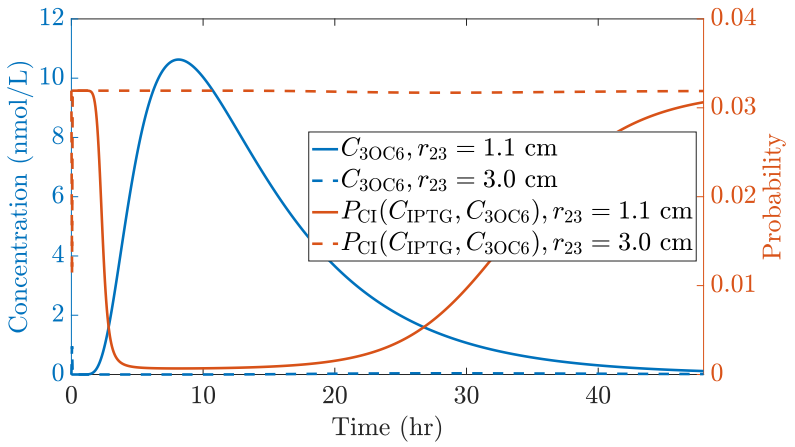

Fig. 6.22 The concentration of 3OC6 and the transcription probability of promoter CI at Minimal Cell 3.

Fig. 6.22 plots the concentration of 3OC6 and the transcription probability of promoter CI at Minimal Cell 3 with different r_{23} (distance between Minimal Cells 2 and 3). With $r_{23} = 1.1$ cm, we observe that the arrived 3OC6 molecules can significantly change the transcription probability for promoter CI, meaning a functional connection between Minimal Cells 2 and 3. While with $r_{23} = 3.0$ cm, the maximum concentration of 3OC6 is roughly 10^{-1} nmol/L, less than the threshold concentration that generates a logic 1 state in Fig. 6.15b, so the transcription probability stays a relatively high value.

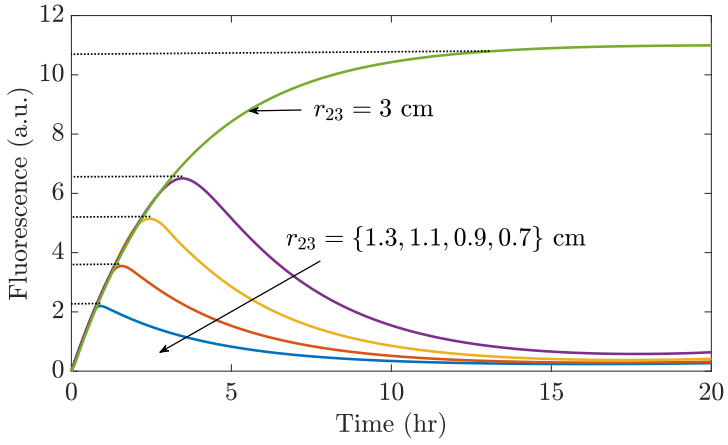

Fig. 6.23 The generated pulse signals with different r_{23}.

In Fig. 6.23, we show the generated pulse with different r_{23}. As can be seen from Fig. 6.23, different pulse-shaped signals can be generated by adjusting r_{23}. With an

increase of r_{23}, Minimal Cell 3 has more time to keep a logic HIGH output, which results in an accumulation of YFP. However, when $r_{23} = 3.0$ cm, the pulse-shaped signal cannot be produced. This is because only a small portion of 3OC6 molecules (produced by Minimal Cell 2) arrives at Minimal Cell 3 and they cannot alter the HIGH output to a LOW output, thus failing to prevent the accumulation of YFP (see Fig. 6.22).

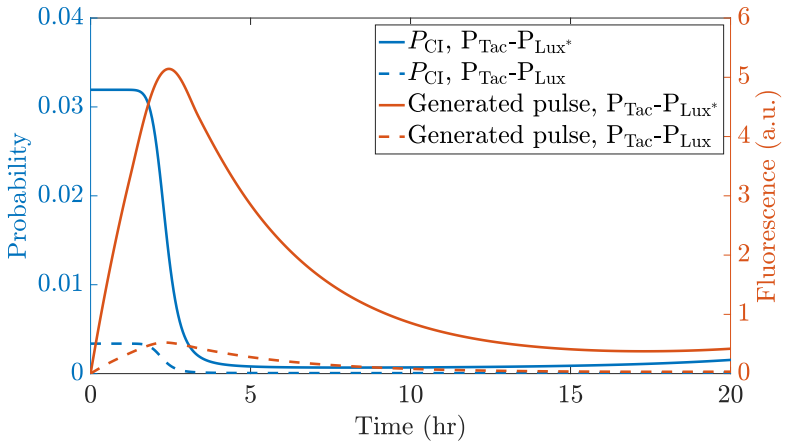

Fig. 6.24 The impact of the input promoters of the NOR gate (Minimal Cell 3) on the generated pulse when $r_{23} = 1.1$ cm.

Fig. 6.24 further investigates the influence of the input promoters of the Minimal Cell 3 NOR gate on the generated pulse. Specifically, we compare the combinations of P_{Tac}-P_{Lux} and P_{Tac}-P_{Lux^*}, where their corresponding performance and the fold-change values can be found in Fig. 6.21 and Table 6.4, respectively. As can be seen from Fig. 6.24, P_{Tac}-P_{Lux^*} demonstrates a larger dynamic range of the transcription probability compared with P_{Tac}-P_{Lux}, due to the larger fold-change and a higher maximum fluorescence. It is also clear that P_{Tac}-P_{Lux^*} is able to produce a pulse with higher peak amplitude, and this reveals the relationship between the gate performance and the generated pulse.

6.8 Conclusion

In this chapter, we designed, analyzed, and simulated a synthetic pulse generation circuit for molecular communication. The proposed synthetic circuit consists of three engineered minimal cells (with AND or NOR logic operation), and the pulse generation is based on the logic state alteration of a NOR gate controlled by the quorum sensing molecules released from another two minimal cells. We used the Shea-Ackers method

to formulate the stochastic behavior of gene expressions incorporating activators and repressors for the engineered minimal cells. We also derived the propagation of signaling molecules that forms the "wires" between different gates. We have demonstrated that by arranging the engineered minimal cells in different spatial configurations, it is possible to control the peak amplitude of the generated pulse, which can be considered as a means to encode information to different peak amplitudes. Moreover, we have also shown that a synthetic digital gate with a larger fold-change and a higher maximum fluorescence can result in a pulse with higher amplitude. This chapter not only provides an improved understanding of the principles and kinetics behind the prevalent pulse generation behavior, but also serves as a basis for the synthetic circuit design for molecular communication. Further work can consider the experimental validation of our proposed system and the design of other signal processing operations.

Chapter 7

Conclusions and Topics for Future Research

7.1 Conclusions

To Unleash the potential of MC for interdisciplinary applications, in this dissertation, we focused on the design and analysis of MC signal processing circuits. In particular, we investigated the signal processing capabilities of chemical-reactions-based microfluidic circuits and genetic circuits. We summarize the contributions and findings of this dissertation in the following.

Fundamentals of Chemical-Reactions-based Microfluidic Circuits: In Chapter 3, the basic characteristics of fluids in microfluidic channels were first analyzed. Thereby, we derived the concentration and velocity changes for microfluidic devices when several flow streams converge to a single flow at a combining connection and a single flow is separated into different flow streams at a bifurcation connection. Moreover, we further investigated the idea of applying and regulating chemical reactions in microfluidic devices to process chemical concentration signals. We compared chemical processing systems with electronic processing systems and proposed a five-level architecture for digital microfluidic circuits. At the same time, the designs of digital AND, NAND, OR, NOR, XOR, and XNOR gates were provided, which show significant advantages in versatility and modularity. The versatility is reflected in that the subtraction-amplification module and the AND-OR gate share the same microfluidic geometry structure but with different reactions and species concentrations. Hence, a microfluidic structure can perform different functions by using different design parameters, which reduces implementation costs and enables the separation of function design from device manufacture. The modularity is embodied in the construction of different logic gates.

The proposed microfluidic logic gates can be constructed via the combination of three microfluidic modules, which is similar to Lego that the construction of vehicles or buildings is built merely via interlocking plastic bricks. With versatility and modularity, microfluidic circuits with more complex MC functions are envisioned to be built through combinations of the proposed logic gates.

Chemical-Reactions-based Microfluidic BCSK Realization: In Chapter 4, a chemical-reactions-based microfluidic BCSK transceiver was proposed. Upon a high digital rectangular input signal, the proposed BCSK transmitter is capable of producing a predefined pulse shape, and the proposed BCSK receiver is able to demodulate the received pulse to a rectangular output signal. Moreover, the spatial-temporal concentration distribution of molecules was also obtained by deriving a 1D advection-diffusion-reaction PDE, which reveals the dependence of transmitted pulses and demodulated signals on design parameters. Based on the theoretical analysis, we developed a microfluidic channel length optimization framework to control the maximum concentration of a transmitted pulse. Furthermore, we studied the time gap between two input bits to ensure a continuous transmission of non-distorted and identical-shaped pulses. We implemented the proposed BCSK transceiver design in COMSOL Multiphysics and the simulation results demonstrated successful pulse generation and signal demodulation. There is an agreement between the theoretical analysis and the simulation results, which validates the theoretical characterizations. In addition, we also connected the transmitter with the receiver to present an end-to-end microfluidic MC system. As the COMSOL Multiphysics simulator can simulate flows in the most accurate way, the successful implementations of the proposed transceiver design in COMSOL provided evidence of the circuits' feasibility in practice.

Chemical-Reactions-based Microfluidic QCSK Realization: In Chapter 5, a chemical-reactions-based microfluidic QCSK transceiver was proposed. The proposed QCSK transmitter is able to represent two digital inputs as four concentration levels of a transmitted signal, while the proposed QCSK receiver can demodulate a received signal to two outputs. We derived the impulse response of a straight advection-diffusion channel. Moreover, we also studied straight advection-diffusion-reaction channels with different forms of reactions. Thereby, we developed a general mathematical framework to characterize the proposed QCSK transceiver. The simulation results obtained from COMSOL Multiphysics not only showed the desired behavior of QCSK modulation and demodulation functions but also confirmed the accuracy of the developed mathematical framework. The QCSK transceiver design is consisted of microfluidic digital logic gates, thus this chapter presented a realization of the five-level architecture of microfluidic

circuits proposed in Chapter 3. Most importantly, the QCSK design can be extended to the general nth order CSK modulation scheme by using a microfluidic $n : 2^n$ decoder constructed from 2^n AND gates. This extension reveals the scalability and extendibility of the proposed microfluidic circuit design. Thus, we believe that this chapter provides not only a design principle and mathematical framework for microfluidic MC circuits, but also a foundation for utilizing simple microfluidic logic gates to produce diverse and complex signal processing functions.

Genetic Circuit with Controllable Pulse Generation: In Chapter 6, we designed, analyzed, and simulated a multicellular circuit with a pulse generation function. We partitioned the pulse generation function into three synthetic minimal cells with digital signal processing abilities and wired these minimal cells by intercellular signaling pathways. For each synthetic minimal cell, we presented the underlying gene regulatory networks and modeled its individual behavior. Moreover, we derived the response of the intercellular signaling propagation channel that supports cell-to-cell communication. In addition, the pulse generation mechanism was also analyzed. Simulation results showed the desired behavior of each synthetic minimal cell and demonstrated that the proposed system is capable of generating a pulse-shaped signal with different peak amplitudes by arranging minimal cells in different spatial configurations. Furthermore, simulation results also revealed that an engineered digital logic gate with a larger response range and a higher maximum output (i.e., fluorescence intensity) can result in a higher peak amplitude of a pulse.

7.2 Future Work

In this section, we provide the possible future research directions for chemical-reactions-based microfluidic circuits and genetic circuits.

7.2.1 Microfluidic Circuits

In general, the engineering of microfluidic circuits with complex signal processing functions can follow the design-test cycle as shown in Fig. 7.1. As the complexity of a signal processing function largely depends on the number of available gates, the first step in the design stage is to expand the logic gate library. Second, logic synthesis should be executed to produce a circuit diagram with available components to perform a specified operation, which provides a basis for the followed gate assignment to choose the correct gates. Then, functional connecting components should be theoretically

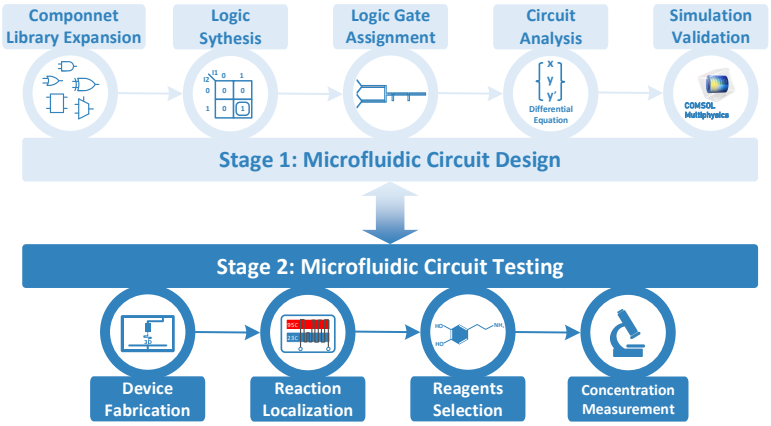

Fig. 7.1 The design-test cycle for the development of microfluidic circuits with complex signal processing functions.

analyzed and verified by simulation results. After verifying a well-defined microfluidic circuit, the next stage is to build a circuit prototype, which includes circuit fabrication, reaction localization, and reagent selection. Moreover, detection techniques should also be selected to visualize the circuit's outputs. In the following, we discuss the future directions of component library expansion, logic gate assignment, circuit analysis, and microfluidic circuit testing.

Component Library Expansion

Compared with the number of electronic logic gates in the literature, the number of microfluidic logic gates is still limited. Thus, a future research direction could be designing more microfluidic logic gates (e.g., multiplexers) and expanding the component library to allow for complex signal processing. As the microfluidic logic gates at Level 4 are built from the microfluidic modules at Level 3 (see Fig. 3.5), one can expand the library by designing or introducing more components at lower levels. This includes but is not limited to introducing serpentine and herringbone-like geometry for Level 1, designing biologically inspired reactions for Level 2, and proposing basic arithmetic operations (e.g., half adder) for Level 3. Moreover, the microfluidic logic gates proposed in this dissertation are all combinational circuits, where circuits' outputs only depend on current input signals. However, the realization of many signal processing functions can be based on sequential logic circuits, where circuits' outputs depend on both current and previous input signals. Thus, the design of sequential circuits is also an important direction for future research.

Logic Gate Assignment

After logic synthesis, the next step is to select available gates from the logic library. We note that even for a *single* gate in a *whole* circuit, it is likely to have different microfluidic designs, which introduces a challenge to identify the optimal gate combination for the whole circuit. A straightforward method is to permute all possible designs for each gate and identify the optimal combination of the whole circuit. However, this approach becomes intractable with the increase in library size and circuit scale. To address this challenge, the design of an assignment algorithm is an interesting problem for future work. Furthermore, quantified metrics should be developed to analyze circuit complexity, such as the total number of species and reactions, and the speed to finish specified signal processing tasks.

Circuit Analysis

An integral part of microfluidic circuit development is how to derive circuits' outputs and theoretically analyze circuit performance, such as the channel noise characterization and channel capacity calculation for a circuit with communication functionalities. By doing so, it would reveal the dependency of circuit performance on design parameters, and provide feedback for the circuit design. We highlight two main directions as follows:

- **Propagation Analysis:** In this dissertation, we directly derived the 1D advection-diffusion-reaction PDE in Chapter 4 and established a mathematical framework to characterize microfluidic circuits by deriving the impulse response of the 1D advection-diffusion PDE in Chapter 5. The above analyses are all based on the assumption that flows fall into the dispersion regime (see Fig. 3.2), which allows us to reduce 3D advection-diffusion-reaction PDE to 1D advection-diffusion-reaction PDE. However, this assumption does not always hold in reality. Hereby, the most challenging aspect of microfluidic channel modeling is the coupling between the axial and cross-sectional particle distributions caused by laminar flows with the parabolic velocity profile. Although the authors of [170] addressed this challenge for a single microfluidic channel, developing a general framework for microfluidic circuits consisting of multiple channels is still a significant topic for future research. Moreover, for the proposed QCSK transceiver, the incorporation of the transmitter-channel interface and channel-receiver interface into the propagation analysis can be an extension of this dissertation.

- **Noise Analysis:** Both the proposed mathematical analysis and the COMSOL Multiphysics simulator are based on deterministic PDEs, which describe a deter-

ministic and average response of the proposed microfluidic circuits. In this sense, proposing a statistical model for microfluidic circuits to capture the noise impacts is an interesting direction for future work, which would be helpful to evaluate the communication performance of a microfluidic system (e.g., transmission rate, bit error rate, and channel capacity) and identify suitable applications. The noise models for MC were studied in [171, 172] and then are widely used in subsequent MC papers. In particular, the authors of [171, 172] proposed the particle sampling noise model for the emission process, the particle counting noise model for the diffusion process, and the particle reception noise model for the reception process. Unfortunately, one significant assumption under these noise models is that the molecule propagation only relies on diffusion, but this assumption will not be valid for the proposed microfluidic systems where the particle movement is induced by the movement of fluid and bounded by closed microfluidic channels. Although a noise model for a single microfluidic channel has been proposed in [125], this noise model has not been validated at all and its accuracy is unknown. Therefore, the noise for microfluidic systems has not been well defined and mathematically formulated in the existing literature. There are various noise sources for microfluidic circuits. For example, the noise can be caused by the mechanical limitations of the solution injection devices (e.g., syringe pump), by the chemical reactions, and by the external observation equipment (e.g., spectrometer or pH meter). In this regard, proposing a statistical model to capture these effects can be a future research direction.

Microfluidic Circuit Testing

Although all the proposed microfluidic circuits have been implemented in COMSOL and show desired behavior, it is worthwhile to build the corresponding microfluidic testbeds to further investigate the accuracy of mathematical models and study the reliability of the proposed microfluidic circuits. One can start by developing a low-cost macroscale prototype for *in vitro* proof-of-concept and then transitioning into the development of a miniaturized microfluidic chip for specific applications. As shown in Fig. 7.1, a key step in the testing stage is to choose appropriate chemical molecules to map to CRNs. For the AND gate design proposed in Fig. 3.7, we can rely on *aniline derivatives*, *sodium nitrite*, *phenyldiazonium derivatives*, *hypophosphorous acid*, *phenol*, and *4-(Phenyldiazenyl)phenol derivatives*, which correspond to species I_1 (or I_2), M, N, ThL, *Amp*, and O, respectively. We note that these candidates are selected as a proof-of-concept for the proposed design, and they should vary with targeted

applications. However, the selected compounds need to meet the following general requirements:

- The selected reagents and reaction products should not be harmful to the human body, disturb existing physiological activities, and be toxic to the environment.
- The interactions among selected reagents, reaction products, and channel materials should be studied so as to prevent any side reactions.
- The outputs of a logic gate are expected to be the inputs of the cascaded gate. By doing so, the interconnection of logic gates can be automated. Otherwise, a converter module that transforms the output species of a previous gate to the input species of the next gate should be included.
- The disposition or recycling of remaining solutions for future use should be taken into account.

With the above requirements, the reagents selection is still an important open problem in this field.

7.2.2 Genetic Circuits

In the following, we outline a number of possible future research directions for genetic circuits.

Genetic Circuit Architecture

From the microfluidic QCSK circuit in Chapter 4, it is clear that the proposed five-level architecture can facilitate microfluidic circuit design. Thus, developing a similar architecture for genetic circuits can be an extension of this dissertation. As multicellular circuits adopt the strategy that distributes a desired function among different cell populations, multicellular circuits share the same idea as the abstraction for electronic and microfluidic processing systems, which conceals the implementation details of lower levels to systematically manage circuit complexity. Therefore, multicellular circuit design will greatly benefit from a genetic circuit architecture.

Genetic Circuit Analysis

There are many interesting problems that can be considered in the modeling of genetic circuits. For example, the point transmitter and 2D propagation assumptions can be

relaxed to incorporate more realistic physical phenomena, including cell shape, cell growth, and 3D propagation movement. A related research direction is how realistic a model needs to be in order for it to be useful in practice, i.e., to make informed predictions or to effectively guide system design. Moreover, noise modeling still remains an issue. In genetic circuits, noises can be caused by intracellular, intercellular, and extracellular stochastic biochemical elements. Although additive white Gaussian noise (AWGN) can represent the noise contribution from genetic circuits [73], it is still unclear what the exact noise level is caused by a specific biological environment.

Genetic Circuit Testing

As stated in Section 7.2.2, the theoretical characterizations of cell behavior and propagation channel are derived from physical principles and under some idealized assumptions. Although such models provide insightful predictions of the proposed genetic circuits, it remains unknown whether the developed models are still effective and accurate in practical setups. Ultimately, a future work is the wet-lab experiments, which are highly interdisciplinary and need diverse scientific knowledge.

References

[1] I. F. Akyildiz, F. Brunetti, and C. Blázquez, "Nanonetworks: A new communication paradigm," *Comput. Netw.*, vol. 52, no. 12, pp. 2260–2279, Aug. 2008.

[2] B. Alberts, A. D. Johnson, J. Lewis, D. Morgan, M. Raff, K. Roberts, and P. Walter, *Molecular Biology of the Cell*, 6th ed. New York, NY, USA: Garland Science, 2015.

[3] T. Nakano, A. W. Eckford, and T. Haraguchi, *Molecular Communication*. Cambridge, U.K.: Cambridge University Press, 2013.

[4] D. Bi, A. Almpanis, A. Noel, Y. Deng, and R. Schober, "A survey of molecular communication in cell biology: Establishing a new hierarchy for interdisciplinary applications," *IEEE Commun. Surv. Tutorials*, pp. 1–1, Mar. 2021.

[5] S. Haykin, *Communication Systems*. Hoboken, NJ, USA: John Wiley & Sons, Inc., 2008.

[6] T. Suda, M. Moore, T. Nakano, R. Egashira, and A. Enomoto, "Exploratory research on molecular communication between nanomachines," in *Proc. ACM GECCO*, Jun. 2005, pp. 1–5.

[7] S. Hiyama, Y. Moritani, T. Suda, R. Egashira, A. Enomoto, M. Moore, and T. Nakano, "Molecular communication," in *Proc. NSTI Nanotechnol. Conf.*, May 2005, pp. 392–395.

[8] S. Hiyama, T. Inoue, T. Shima, Y. Moritani, T. Suda, and K. Sutoh, "Autonomous loading, transport, and unloading of specified cargoes by using DNA hybridization and biological motor-based motility," *Small*, vol. 4, no. 4, pp. 410–415, Apr. 2008.

[9] T. Nakano, M. J. Moore, F. Wei, A. V. Vasilakos, and J. Shuai, "Molecular communication and networking: Opportunities and challenges," *IEEE Trans. Nanobiosci.*, vol. 11, no. 2, pp. 135–148, Jun. 2012.

[10] A. W. Eckford, "Nanoscale communication with Brownian motion," in *Proc. IEEE CISS*, Mar. 2007, pp. 160–165.

[11] A. O. Bicen and I. F. Akyildiz, "System-theoretic analysis and least-squares design of microfluidic channels for flow-induced molecular communication," *IEEE Trans. Signal Process.*, vol. 61, no. 20, pp. 5000–5013, Oct. 2013.

[12] Y. Chahibi, I. F. Akyildiz, and I. Balasingham, "Propagation modeling and analysis of molecular motors in molecular communication," *IEEE Trans. Nanobiosci.*, vol. 15, no. 8, pp. 917–927, Dec. 2016.

[13] T. Suda and T. Nakano, "Modeling the stochastic behavior of kinesin-coated beads," in *Proc. IEEE ICC*, May 2019, pp. 1–7.

[14] A. Noel, K. C. Cheung, and R. Schober, "Improving receiver performance of diffusive molecular communication with enzymes," *IEEE Trans. Nanobiosci.*, vol. 13, no. 1, pp. 31–43, Mar. 2014.

[15] H. B. Yilmaz, A. C. Heren, T. Tugcu, and C.-B. Chae, "Three-dimensional channel characteristics for molecular communications with an absorbing receiver," *IEEE Commun. Lett.*, vol. 18, no. 6, pp. 929–932, Jun. 2014.

[16] Y. Deng, A. Noel, M. Elkashlan, A. Nallanathan, and K. C. Cheung, "Modeling and simulation of molecular communication systems with a reversible adsorption receiver," *IEEE Trans. Mol. Biol. Multi-Scale Commun.*, vol. 1, no. 4, pp. 347–362, Dec. 2015.

[17] A. Ahmadzadeh, H. Arjmandi, A. Burkovski, and R. Schober, "Comprehensive reactive receiver modeling for diffusive molecular communication systems: Reversible binding, molecule degradation, and finite number of receptors," *IEEE Trans. Nanobiosci.*, vol. 15, no. 7, pp. 713–727, Oct. 2016.

[18] M. U. Mahfuz, D. Makrakis, and H. T. Mouftah, "On the characterization of binary concentration-encoded molecular communication in nanonetworks," *Nano Commun. Netw.*, vol. 1, no. 4, pp. 289–300, Dec. 2010.

[19] M. S. Kuran, H. B. Yilmaz, T. Tugcu, and I. F. Akyildiz, "Interference effects on modulation techniques in diffusion based nanonetworks," *Nano Commun. Netw.*, vol. 3, no. 1, pp. 65–73, Mar. 2012.

[20] P.-J. Shih, C.-H. Lee, P.-C. Yeh, and K.-C. Chen, "Channel codes for reliability enhancement in molecular communication," *IEEE J. Sel. Areas Commun.*, vol. 31, no. 12, pp. 857–867, Dec. 2013.

[21] O. B. Akan, H. Ramezani, T. Khan, N. A. Abbasi, and M. Kuscu, "Fundamentals of molecular information and communication science," *Proc. IEEE*, vol. 105, no. 2, pp. 306–318, Feb. 2017.

[22] Y. Chahibi, M. Pierobon, S. O. Song, and I. F. Akyildiz, "A molecular communication system model for particulate drug delivery systems," *IEEE Trans. Biomed. Eng.*, vol. 60, no. 12, pp. 3468–3483, Dec. 2013.

[23] T. Nakano, S. Kobayashi, T. Suda, Y. Okaie, Y. Hiraoka, and T. Haraguchi, "Externally controllable molecular communication," *IEEE J. Sel. Areas Commun.*, vol. 32, no. 12, pp. 2417–2431, Dec. 2014.

[24] T. Nakano, Y. Okaie, S. Kobayashi, T. Hara, Y. Hiraoka, and T. Haraguchi, "Methods and applications of mobile molecular communication," *Proc. IEEE*, vol. 107, no. 7, pp. 1442–1456, Jul. 2019.

[25] N. Farsad, W. Guo, and A. W. Eckford, "Tabletop molecular communication: Text messages through chemical signals," *PLoS One*, vol. 8, no. 12, p. e82935, Dec. 2013.

[26] B.-H. Koo, C. Lee, H. B. Yilmaz, N. Farsad, A. Eckford, and C.-B. Chae, "Molecular MIMO: From Theory to Prototype," *IEEE J. Sel. Areas Commun.*, vol. 34, no. 3, pp. 600–614, March 2016.

[27] N. Farsad, D. Pan, and A. Goldsmith, "A novel experimental platform for in-vessel multi-chemical molecular communications," in *Proc. IEEE GLOBECOM*, Dec. 2017, pp. 1–6.

[28] H. Unterweger, J. Kirchner, W. Wicket, A. Ahmadzadeh, D. Ahmed, V. Jamali, C. Alexiou, G. Fischer, and R. Schober, "Experimental molecular communication testbed based on magnetic nanoparticles in duct flow," in *Proc. IEEE SPAWC*, Jun. 2018, pp. 1–5.

[29] L. Khaloopour, S. V. Rouzegar, A. Azizi, A. Hosseinian, M. Farahnak-Ghazani, N. Bagheri, M. Mirmohseni, H. Arjmandi, R. Mosayebi, and M. Nasiri-Kenari, "An experimental platform for macro-scale fluidic medium molecular communication," *IEEE Trans. Mol. Biol. Multi-Scale Commun.*, vol. 5, no. 3, pp. 163–175, Dec. 2019.

[30] S. Giannoukos, D. T. McGuiness, A. Marshall, J. Smith, and S. Taylor, "A chemical alphabet for macromolecular communications," *Anal. Chem.*, vol. 90, no. 12, pp. 7739–7746, Jun. 2018.

[31] S. Bhattacharjee, M. Damrath, F. Bronner, L. Stratmann, J. P. Drees, F. Dressler, and P. A. Hoeher, "A testbed and simulation framework for air-based molecular communication using fluorescein," in *Proc. ACM NANOCOM*, Sep. 2020, pp. 1–6.

[32] B. Krishnaswamy, C. M. Austin, J. P. Bardill, D. Russakow, G. L. Holst, B. K. Hammer, C. R. Forest, and R. Sivakumar, "Time-elapse communication: Bacterial communication on a microfluidic chip," *IEEE Trans. Commun.*, vol. 61, no. 12, pp. 5139–5151, Dec. 2013.

[33] M. Kuscu, H. Ramezani, E. Dinc, S. Akhavan, and O. B. Akan, "Fabrication and microfluidic analysis of graphene-based molecular communication receiver for Internet of Nano Things (IoNT)," *Sci. Rep.*, vol. 11, no. 1, pp. 1–20, Oct. 2021.

[34] D. P. Martins, M. T. Barros, B. O'Sullivan, I. Seymour, A. O'Riordan, L. Coffey, J. Sweeney, and S. Balasubramaniam, "Microfluidic-based Bacterial Molecular Computing on a Chip," *arXiv:2104.07341*, Apr. 2021.

[35] M. T. Barros, P. Doan, M. Kandhavelu, B. Jennings, and S. Balasubramaniam, "Engineering calcium signaling of astrocytes for neural–molecular computing logic gates," *Sci. Rep.*, vol. 11, no. 1, pp. 1–10, Jan. 2021.

[36] L. Grebenstein, J. Kirchner, R. S. Peixoto, W. Zimmermann, F. Irnstorfer, W. Wicke, A. Ahmadzadeh, V. Jamali, G. Fischer, R. Weigel, A. Burkovski, and R. Schober, "Biological optical-to-chemical signal conversion interface: A small-scale modulator for molecular communications," *IEEE Trans. Nanobiosci.*, vol. 18, no. 1, pp. 31–42, Jan. 2019.

[37] N. A. Abbasi, D. Lafci, and O. B. Akan, "Controlled Information Transfer Through An *In Vivo* Nervous System," *Sci. Rep.*, vol. 8, no. 1, p. 2298, Dec. 2018.

[38] E. De Leo, L. Donvito, L. Galluccio, A. Lombardo, G. Morabito, and L. M. Zanoli, "Communications and switching in microfluidic systems: Pure hydrodynamic control for networking labs-on-a-chip," *IEEE Trans. Commun.*, vol. 61, no. 11, pp. 4663–4677, Nov. 2013.

[39] N. Farsad, H. B. Yilmaz, A. Eckford, C.-B. Chae, and W. Guo, "A comprehensive survey of recent advancements in molecular communication," *IEEE Commun. Surv. Tuts.*, vol. 18, no. 3, pp. 1887–1919, 2016.

[40] V. Jamali, A. Ahmadzadeh, W. Wicke, A. Noel, and R. Schober, "Channel modeling for diffusive molecular communication: A tutorial review," *Proc. IEEE*, vol. 107, no. 7, pp. 1256–1301, Jul. 2019.

[41] K. Darchini and A. S. Alfa, "Molecular communication via microtubules and physical contact in nanonetworks: A survey," *Nano Commun. Netw.*, vol. 4, no. 2, pp. 73–85, Jun. 2013.

[42] M. Kuran, H. B. Yilmaz, I. Demirkol, N. Farsad, and A. Goldsmith, "A survey on modulation techniques in molecular communication via diffusion," *IEEE Commun. Surv. Tutorials*, pp. 1–1, Dec. 2020.

[43] I. F. Akyildiz, M. Pierobon, and S. Balasubramaniam, "An information theoretic framework to analyze molecular communication systems based on statistical mechanics," *Proc. IEEE*, vol. 107, no. 7, pp. 1230–1255, Jul. 2019.

[44] M. Kuscu, E. Dinc, B. A. Bilgin, H. Ramezani, and O. B. Akan, "Transmitter and receiver architectures for molecular communications: A survey on physical design with modulation, coding, and detection techniques," *Proc. IEEE*, vol. 107, no. 7, pp. 1302–1341, Jul. 2019.

[45] C. A. Soldner, E. Socher, V. Jamali, W. Wicke, A. Ahmadzadeh, H.-G. Breitinger, A. Burkovski, K. Castiglione, R. Schober, and H. Sticht, "A survey of biological building blocks for synthetic molecular communication systems," *IEEE Commun. Surv. Tutorials*, pp. 1–1, Jul. 2020.

[46] T. Nguyen, T. S. Jones, P. Fontanarrosa, J. V. Mante, Z. Zundel, D. Densmore, and C. Myers, "Design of asynchronous genetic circuits," *Proc. IEEE*, vol. 107, no. 7, pp. 1356–1368, Jul. 2019.

[47] D. Carmean, L. Ceze, G. Seelig, K. Stewart, K. Strauss, and M. Willsey, "DNA data storage and hybrid molecular–electronic computing," *Proc. IEEE*, vol. 107, no. 1, pp. 63–72, Dec. 2018.

[48] E. Kim, J. Li, M. Kang, D. L. Kelly, S. Chen, A. Napolitano, L. Panzella, X. Shi, K. Yan, S. Wu, J. Shen, W. E. Bentley, and G. F. Payne, "Redox is a global biodevice information processing modality," *Proc. IEEE*, vol. 107, no. 7, pp. 1402–1424, Jul. 2019.

[49] J. M. Jornet, Y. Bae, C. R. Handelmann, B. Decker, A. Balcerak, A. Sangwan, P. Miao, A. Desai, L. Feng, E. K. Stachowiak, and M. K. Stachowiak, "Optogenomic interfaces: Bridging biological networks with the electronic digital world," *Proc. IEEE*, vol. 107, no. 7, pp. 1387–1401, Jul. 2019.

[50] U. A. K. Chude-Okonkwo, R. Malekian, B. T. Maharaj, and A. V. Vasilakos, "Molecular communication and nanonetwork for targeted drug delivery: A survey," *IEEE Commun. Surv. Tutorials*, vol. 19, no. 4, pp. 3046–3096, 2017.

[51] L. Felicetti, M. Femminella, G. Reali, and P. Liò, "Applications of molecular communications to medicine: A survey," *Nano Commun. Netw.*, vol. 7, pp. 27–45, Mar. 2016.

[52] Y. Chahibi, "Molecular communication for drug delivery systems: A survey," *Nano Commun. Netw.*, vol. 11, pp. 90–102, Mar. 2017.

[53] I. F. Akyildiz, M. Pierobon, and S. Balasubramaniam, "Moving forward with molecular communication: from theory to human health applications [point of view]," *Proc. IEEE*, vol. 107, no. 5, pp. 858–865, May 2019.

[54] S. Andreescu and O. A. Sadik, "Trends and Challenges in Biochemical Sensors for Clinical and Environmental Monitoring," *Pure Appl Chem*, vol. 76, no. 4, pp. 861–878, Jan. 2004.

[55] M. Cook, D. Soloveichik, E. Winfree, and J. Bruck, "Programmability of chemical reaction networks," in *Algorithmic Bioprocesses*. Berlin, Heidelberg: Springer Verlag, 2009, pp. 543–584.

[56] R. Weiss, S. Basu, S. Hooshangi, A. Kalmbach, D. Karig, R. Mehreja, and I. Netravali, "Genetic circuit building blocks for cellular computation, communications, and signal processing," *Nat. Comput.*, vol. 2, no. 1, pp. 47–84, Mar. 2003.

[57] R. W. Bradley and B. Wang, "Designer cell signal processing circuits for biotechnology," *N. Biotechnol.*, vol. 32, no. 6, pp. 635–643, Dec. 2015.

[58] R. Sarpeshkar, "Analog synthetic biology," *Philos. Trans. R. Soc. A Math. Phys. Eng. Sci.*, vol. 372, no. 2012, p. 20130110, Mar. 2014.

[59] H. Jiang, M. D. Riedel, and K. K. Parhi, "Digital logic with molecular reactions," in *Proc. IEEE/ACM ICCAD*, Nov. 2013, pp. 721–727.

[60] L. Ge, Z. Zhong, D. Wen, X. You, and C. Zhang, "A formal combinational logic synthesis with chemical reaction networks," *IEEE Trans. Mol. Biol. Multi-Scale Commun.*, vol. 3, no. 1, pp. 33–47, Mar. 2017.

[61] T. Song, S. Garg, R. Mokhtar, H. Bui, and J. Reif, "Analog computation by DNA strand displacement circuits," *ACS Synth. Biol.*, vol. 5, no. 8, pp. 898–912, Aug. 2016.

[62] C. T. Chou, "Chemical reaction networks for computing logarithm," *Synth. Biol.*, vol. 2, no. 1, p. ysx002, Jan. 2017.

[63] L. Cardelli, M. Tribastone, and M. Tschaikowski, "From electric circuits to chemical networks," *Nat. Comput.*, vol. 19, no. 1, pp. 237–248, Mar. 2020.

[64] A. Tamsir, J. J. Tabor, and C. A. Voigt, "Robust multicellular computing using genetically encoded NOR gates and chemical 'wires'," *Nature*, vol. 469, no. 7329, pp. 212–215, Jan. 2011.

[65] B. Wang, R. I. Kitney, N. Joly, and M. Buck, "Engineering modular and orthogonal genetic logic gates for robust digital-like synthetic biology," *Nat. Commun.*, vol. 2, no. 1, p. 508, Sep. 2011.

[66] B. H. Weinberg, N. T. Pham, L. D. Caraballo, T. Lozanoski, A. Engel, S. Bhatia, and W. W. Wong, "Large-scale design of robust genetic circuits with multiple inputs and outputs for mammalian cells," *Nat. Biotechnol.*, vol. 35, no. 5, pp. 453–462, May 2017.

[67] M. N. Win and C. D. Smolke, "Higher-order cellular information processing with synthetic RNA devices," *Science*, vol. 322, no. 5900, pp. 456–460, Oct. 2008.

[68] J. Kim, Y. Zhou, P. D. Carlson, M. Teichmann, S. Chaudhary, F. C. Simmel, P. A. Silver, J. J. Collins, J. B. Lucks, P. Yin, and A. A. Green, "De novo-designed translation-repressing riboregulators for multi-input cellular logic," *Nat. Chem. Biol.*, vol. 15, no. 12, pp. 1173–1182, Dec. 2019.

[69] J. J. Tabor, H. M. Salis, Z. B. Simpson, A. A. Chevalier, A. Levskaya, E. M. Marcotte, C. A. Voigt, and A. D. Ellington, "A synthetic genetic edge detection program." *Cell*, vol. 137, no. 7, pp. 1272–81, Jun. 2009.

[70] R. Daniel, J. R. Rubens, R. Sarpeshkar, and T. K. Lu, "Synthetic analog computation in living cells," *Nature*, vol. 497, no. 7451, pp. 619–623, May 2013.

[71] J. J. Y. Teo, S. S. Woo, and R. Sarpeshkar, "Synthetic biology: A unifying view and review using analog circuits," *IEEE Trans. Biomed. Circuits Syst.*, vol. 9, no. 4, pp. 453–474, Aug. 2015.

[72] J. Ang, E. Harris, B. J. Hussey, R. Kil, and D. R. McMillen, "Tuning response curves for synthetic biology," *ACS Synth. Biol.*, vol. 2, no. 10, pp. 547–567, Oct. 2013.

[73] A. Marcone, M. Pierobon, and M. Magarini, "Parity-check coding based on genetic circuits for engineered molecular communication between biological cells," *IEEE Trans. Commun.*, vol. 66, no. 12, pp. 6221–6236, Dec. 2018.

[74] C. T. Chou, "Molecular circuits for decoding frequency coded signals in nano-communication networks," *Nano Commun. Netw.*, vol. 3, no. 1, pp. 46–56, Mar. 2012.

[75] M. Egan, T. Q. Duong, and M. D. Renzo, "Biological circuits for detection in MoSK-based molecular communication," *IEEE Access*, vol. 7, pp. 21 094–21 102, Feb. 2019.

[76] H. Awan and C. T. Chou, "Impact of receiver molecular circuits on the performance of reaction shift keying," in *Proc. ACM NANOCOM*, Sep. 2015, pp. 1–6.

[77] ——, "Molecular communications with molecular circuit-based transmitters and receivers," *IEEE Trans. Nanobiosci.*, vol. 18, no. 2, pp. 146–155, Apr. 2019.

[78] B. D. Unluturk, A. O. Bicen, and I. F. Akyildiz, "Genetically engineered bacteria-based biotransceivers for molecular communication," *IEEE Trans. Commun.*, vol. 63, no. 4, pp. 1271–1281, Apr. 2015.

[79] C. Zhang, L. Ge, X. Zhang, W. Wei, J. Zhao, Z. Zhang, Z. Wang, and X. You, "A uniform molecular low-density parity check decoder," *ACS Synth. Biol.*, vol. 8, no. 1, pp. 82–90, Jan. 2019.

[80] G. M. Whitesides, "The origins and the future of microfluidics," *Nature*, vol. 442, no. 7101, pp. 368–373, Jul. 2006.

[81] J. W. Putney, "Capacitative calcium entry," *J. Cell Biol.*, vol. 169, no. 3, pp. 381–382, May 2005.

[82] R. Phillips, J. Kondev, J. Theriot, H. G. Garcia, and N. Orme, *Physical Biology of the Cell*, 2nd ed. New York, NY, USA: Garland Science, 2013.

[83] T. F. Martin, "Tuning exocytosis for speed: Fast and slow modes," *Biochim. Biophys. Acta - Mol. Cell Res.*, vol. 1641, no. 2-3, pp. 157–165, Aug. 2003.

[84] C. T. Chou, "A Markovian approach to the optimal demodulation of diffusion-based molecular communication networks," *IEEE Trans. Commun.*, vol. 63, no. 10, pp. 3728–3743, Oct. 2015.

[85] H. Arjmandi, A. Ahmadzadeh, R. Schober, and M. Nasiri Kenari, "Ion channel based bio-synthetic modulator for diffusive molecular communication," *IEEE Trans. Nanobiosci.*, vol. 15, no. 5, pp. 418–432, Jul. 2016.

[86] H. Ramezani and O. B. Akan, "Information capacity of vesicle release in neuro-spike communication," *IEEE Commun. Lett.*, vol. 22, no. 1, pp. 41–44, Jan. 2018.

[87] E. Nasi and D. Tillotson, "The rate of diffusion of Ca^{2+} and Ba^{2+} in a nerve cell body," *Biophys. J.*, vol. 47, no. 5, pp. 735–738, May 1985.

[88] D. B. Dusenbery and T. W. Snell, "A critical body size for use of pheromones in mate location," *J. Chem. Ecol.*, vol. 21, no. 4, pp. 427–438, Dec. 1995.

[89] A. Tempestini, C. Monico, L. Gardini, F. Vanzi, F. S. Pavone, and M. Capitanio, "Sliding of a single lac repressor protein along DNA is tuned by DNA sequence and molecular switching," *Nucleic Acids Res.*, vol. 46, no. 10, pp. 5001–5011, Mar. 2018.

[90] B. Fagrell, A. Fronek, and M. Intaglietta, "A microscope-television system for studying flow velocity in human skin capillaries," *Am. J. Physiol. Circ. Physiol.*, vol. 233, no. 2, pp. H318–H321, Aug. 1977.

[91] T. Gervais and K. F. Jensen, "Mass transport and surface reactions in microfluidic systems," *Chem. Eng. Sci.*, vol. 61, no. 4, pp. 1102–1121, Feb. 2006.

[92] A. Einstein, *Investigations on the Theory of the Brownian Movement*. New York, NY, USA: Dover Publications, 1956.

[93] T. Nakano, T. Suda, M. Moore, R. Egashira, A. Enomoto, and K. Arima, "Molecular communication for nanomachines using intercellular calcium signaling," in *Proc. IEEE Conf. Nanotechnol.*, Jul. 2005, pp. 478–481.

[94] W. H. Bossert and E. O. Wilson, "The analysis of olfactory communication among animals," *J. Theor. Biol.*, vol. 5, no. 3, pp. 443–469, Nov. 1963.

[95] H. C. Berg, *Random Walks in Biology*. Princeton, NJ, USA: Princeton University Press, 1993.

[96] W. Hundsdorfer and J. Verwer, *Numerical Solution of Time-Dependent Advection-Diffusion-Reaction Equations*. Berlin, Heidelberg: Springer, 2003.

[97] B. Kirby, *Micro- and Nanoscale Fluid Mechanics: Transport in Microfluidic Devices*. Cambridge, U.K.: Cambridge University Press, 2010.

[98] H. Bruus, *Theoretical Microfluidics*. London, U.K.: Oxford Univ. Press, 2008.

[99] E. Yariv, G. Ben-Dov, and K. D. Dorfman, "Polymerase chain reaction in natural convection systems: A convection-diffusion-reaction model," *Europhys. Lett.*, vol. 71, no. 6, pp. 1008–1014, Sep. 2005.

[100] T. M. Squires, R. J. Messinger, and S. R. Manalis, "Making it stick: Convection, reaction and diffusion in surface-based biosensors," *Nat. Biotechnol.*, vol. 26, no. 4, pp. 417–426, Apr. 2008.

[101] M. T. van Genuchten and W. J. Alves, *Analytical Solutions of the One-dimensional Convective-dispersive Solute Transport Equation*. Washington, D.C., USA: US Department of Agriculture, Agricultural Research Service, 1982, no. 1661.

[102] L. Birnbaumer, "G proteins in signal transduction," *Annu. Rev. Pharmacol. Toxicol.*, vol. 30, no. 1, pp. 675–705, Apr. 1990.

[103] A. G. Gilman, "G proteins: Transducers of receptor-generated signals," *Annu. Rev. Biochem.*, vol. 56, no. 1, pp. 615–649, Jun. 1987.

[104] V. Syrovatkina, K. O. Alegre, R. Dey, and X. Y. Huang, "Regulation, signaling, and physiological functions of G-proteins," *J. Mol. Biol.*, vol. 428, no. 19, pp. 3850–3868, Sep. 2016.

[105] D. E. Clapham, "Calcium signaling," *Cell*, vol. 131, no. 6, pp. 1047–1058, Dec. 2007.

[106] B. Lindner, "Mechanisms of information filtering in neural systems," *IEEE Trans. Mol. Biol. Multi-Scale Commun.*, vol. 2, no. 1, pp. 5–15, Jun. 2016.

[107] K. H. Srivastava, C. M. Holmes, M. Vellema, A. R. Pack, C. P. H. Elemans, I. Nemenman, and S. J. Sober, "Motor control by precisely timed spike patterns," *Proc. Natl. Acad. Sci.*, vol. 114, no. 5, pp. 1171–1176, Jan. 2017.

[108] F. Dinc, B. C. Akdeniz, A. E. Pusane, and T. Tugcu, "Impulse response of the molecular diffusion channel with a spherical absorbing receiver and a spherical reflective boundary," *IEEE Trans. Mol. Biol. Multi-Scale Commun.*, vol. 4, no. 2, pp. 118–122, Mar. 2019.

[109] Ankit and M. R. Bhatnagar, "Molecular channel characterization for a rectangular container with reflecting and absorbing boundaries," *IEEE Commun. Lett.*, vol. 24, no. 2, pp. 234–238, Feb. 2020.

[110] J. Jaeger and H. Carslaw, *Conduction of Heat in Solids*. London, U.K.: Oxford Univ. Press, 1986.

[111] A. Noel, K. C. Cheung, and R. Schober, "Diffusive molecular communication with disruptive flows," in *Proc. IEEE ICC*, Jun. 2014, pp. 3600–3606.

[112] W. Wicke, T. Schwering, A. Ahmadzadeh, V. Jamali, A. Noel, and R. Schober, "Modeling duct flow for molecular communication," in *Proc. IEEE GLOBECOM*, Dec. 2018, pp. 206–212.

[113] L. Zha, Y. Deng, A. Noel, M. Elkashlan, and A. Nallanathan, "Transceiver observations in asymmetric and symmetric diffusive molecular communication systems," in *Proc. IEEE GLOBECOM*, Dec. 2018, pp. 206–212.

[114] A. Noel, K. C. Cheung, and R. Schober, "A unifying model for external noise sources and ISI in diffusive molecular communication," *IEEE J. Sel. Areas Commun.*, vol. 32, no. 12, pp. 2330–2343, Dec. 2014.

[115] A. Noel, D. Makrakis, and A. Hafid, "Channel impulse responses in diffusive molecular communication with spherical transmitters," in *Proc. Bienn. Symp. Commun.*, Apr. 2016.

[116] C. R. Kahn, "Membrane receptors for hormones and neurotransmitters," *J. Cell Biol.*, vol. 70, no. 2, pp. 261–286, Aug. 1976.

[117] S. S. Andrews, "Accurate particle-based simulation of adsorption, desorption and partial transmission," *Phys. Biol.*, vol. 6, no. 4, p. 046015, Nov. 2009.

[118] D. Bi and Y. Deng, "Digital signal processing for molecular communication via chemical-reaction-based microfluidic circuits," *IEEE Commun. Mag.*, vol. 59, no. 5, pp. 26–32, May 2021.

[119] G. M. Whitesides, "The origins and the future of microfluidics," *Nature*, vol. 442, no. 7101, pp. 368–373, July 2006.

[120] C. S. Kumar, *Microfluidic Devices in Nanotechnology: Fundamental Concepts*. Hoboken, NJ, USA: Wiley, 2010.

[121] L. Back, J. Radbill, Y. Cho, and D. Crawford, "Measurement and prediction of flow through a replica segment of a mildly atherosclerotic coronary artery of man," *J. Biomech.*, vol. 19, no. 1, pp. 1–17, Jan. 1986.

[122] J. A. Jensen, *Lectures Notes on Medical Imaging Systems–Lecture 5: Blood Flow in the Human Body*. Lyngby, Denmark: Technical University of Denmark, 2018.

[123] R. F. Probstein, *Physicochemical Hydrodynamics: An introduction*. Hoboken, NJ, USA: Wiley, 1994.

[124] K. W. Oh, K. Lee, B. Ahn, and E. P. Furlani, "Design of pressure-driven microfluidic networks using electric circuit analogy," *Lab. Chip*, vol. 12, no. 3, pp. 515–545, Nov. 2012.

[125] A. O. Bicen and I. F. Akyildiz, "End-to-End Propagation Noise and Memory Analysis for Molecular Communication over Microfluidic Channels," *IEEE Trans. Commun.*, vol. 62, no. 7, pp. 2432–2443, July 2014.

[126] Y. Xiang, N. Dalchau, and B. Wang, "Scaling Up Genetic Circuit Design for Cellular Computing: Advances and Prospects," *Natural computing*, vol. 17, no. 4, pp. 833–853, Oct. 2018.

[127] D. Harris and S. Harris, *Digital Design and Computer Architecture*. CA, San Mateo: Morgan Kaufmann, 2010.

[128] D. Scalise and R. Schulman, "Designing modular reaction-diffusion programs for complex pattern formation," *Technology*, vol. 2, no. 01, pp. 55–66, March 2014.

[129] Y. Deng, M. Pierobon, and A. Nallanathan, "A Microfluidic Feed Forward Loop Pulse Generator for Molecular Communication," in *Proc. IEEE GLOBECOM*, Dec 2017, pp. 1–7.

[130] D. Bi *et al.*, "Chemical Reactions-Based Microfluidic Transmitter and Receiver Design for Molecular Communication," *IEEE Trans. Commun.*, vol. 68, no. 9, pp. 5590–5605, Sep. 2020.

[131] R. W. Bradley, M. Buck, and B. Wang, "Recognizing and engineering digital-like logic gates and switches in gene regulatory networks," *Curr Opin Microbiol*, vol. 33, pp. 74–82, Oct. 2016.

[132] K. Lee, C. Kim, B. Ahn, R. Panchapakesan, A. R. Full, L. Nordee, J. Y. Kang, and K. W. Oh, "Generalized Serial Dilution Module for Monotonic and Arbitrary Microfluidic Gradient Generators," *Lab. Chip*, vol. 9, no. 5, pp. 709–717, Nov. 2009.

[133] G. Karlebach and R. Shamir, "Modelling and analysis of gene regulatory networks," *Nat. Rev. Mol. Cell Biol.*, vol. 9, no. 10, pp. 770–780, October 2008.

[134] R. Milo, S. Shen-Orr, S. Itzkovitz, N. Kashtan, D. Chklovskii, and U. Alon, "Network motifs: simple building blocks of complex networks," *Science*, vol. 298, no. 5594, pp. 824–827, October 2002.

[135] U. Alon, "Network motifs: theory and experimental approaches," *Nat. Rev. Genet.*, vol. 8, no. 6, pp. 450–461, June 2007.

[136] A. Uri, *An introduction to systems biology: design principles of biological circuits*. London, UK: Chapman & Hall, 2006.

[137] S. Mangan, S. Itzkovitz, A. Zaslaver, and U. Alon, "The incoherent feed-forward loop accelerates the response-time of the gal system of escherichia coli," *J Mol Biol*, vol. 356, no. 5, pp. 1073–1081, March 2006.

[138] A. Grimmer, M. Hamidović, W. Haselmayr, and R. Wille, "Advanced simulation of droplet microfluidics," *ACM J. Emerg. Technol. Comput. Syst.*, vol. 15, no. 3, pp. 1–16, Apr. 2019.

[139] D. Bi and Y. Deng, "Microfluidic AND Gate Design for Molecular Communication," in *Proc. ACM NanoCom*, Sep. 2020, pp. 1–7.

[140] ——, "Microfluidic QCSK Transmitter and Receiver Design for Molecular Communication," *IEEE Trans. Commun.*, vol. 70, no. 9, pp. 5837–5852, Sep. 2022.

[141] D. Verrall and W. Read, "A quasi-analytical approach to the advection–diffusion–reaction problem, using operator splitting," *Appl. Math. Modell.*, vol. 40, no. 2, pp. 1588–1598, Sep. 2016.

[142] R. Chang, *Physical Chemistry for the Biosciences*. Herndon, VA, USA: University Science Books, 2005.

[143] B. K. Yen, A. Günther, M. A. Schmidt, K. F. Jensen, and M. G. Bawendi, "A Microfabricated Gas–Liquid Segmented Flow Reactor for High-Temperature Synthesis: the Case of CdSe Quantum Dots," *Angew. Chem. Int. Ed.*, vol. 44, no. 34, pp. 5447–5451, Aug. 2005.

[144] M. S. Kuran, H. B. Yilmaz, T. Tugcu, and I. F. Akyildiz, "Modulation Techniques for Communication via Diffusion in Nanonetworks," in *Proc. IEEE ICC*, June 2011, pp. 1–5.

[145] P. Du, H. Zhao, H. Zhang, R. Wang, J. Huang, Y. Tian, X. Luo, X. Luo, M. Wang, Y. Xiang *et al.*, "De novo design of an intercellular signaling toolbox for multi-channel cell–cell communication and biological computation," *Nat. Commun.*, vol. 11, no. 1, pp. 1–11, Aug. 2020.

[146] A. S. Khalil and J. J. Collins, "Synthetic biology: applications come of age," *Nat. Rev. Genet.*, vol. 11, no. 5, pp. 367–379, May 2010.

[147] P. E. Purnick and R. Weiss, "The second wave of synthetic biology: from modules to systems," *Nat. Rev. Mol. Cell Biol.*, vol. 10, no. 6, pp. 410–422, Jun. 2009.

[148] J. Macía, F. Posas, and R. V. Solé, "Distributed computation: the new wave of synthetic biology devices," *Trends Biotechnol*, vol. 30, no. 6, pp. 342–349, Jun. 2012.

[149] N. Kylilis, Z. A. Tuza, G.-B. Stan, and K. M. Polizzi, "Tools for engineering coordinated system behaviour in synthetic microbial consortia," *Nat. Commun.*, vol. 9, no. 1, pp. 1–9, Jul. 2018.

[150] S. Mukherjee and B. L. Bassler, "Bacterial quorum sensing in complex and dynamically changing environments," *Nat. Rev. Microbiol.*, vol. 17, no. 6, pp. 371–382, Jun. 2019.

[151] D. Ausländer, S. Ausländer, X. Pierrat, L. Hellmann, L. Rachid, and M. Fussenegger, "Programmable full-adder computations in communicating three-dimensional cell cultures," *Nat. Methods*, vol. 15, no. 1, pp. 57–60, Jan. 2018.

[152] H. H. McAdams and L. Shapiro, "A bacterial cell-cycle regulatory network operating in time and space," *Science*, vol. 301, no. 5641, pp. 1874–1877, Sep. 2003.

[153] S. Basu, R. Mehreja, S. Thiberge, M.-T. Chen, and R. Weiss, "Spatiotemporal control of gene expression with pulse-generating networks," *Proc. Natl. Acad. Sci.*, vol. 101, no. 17, pp. 6355–6360, Apr. 2004.

[154] D. Bi and Y. Deng, "Spatiotemporal control of genetic circuit with pulse generation for molecular communication," in *Proc. IEEE GLOBECOM*, Dec. 2021, pp. 1–6.

[155] ——, "Engineering Controllable Pulse Generation for Molecular Communication via Genetic Circuits," *Accepted by IEEE Trans. Mol. Biol. Multi-Scale Commun.*

[156] G. K. Ackers, A. D. Johnson, and M. A. Shea, "Quantitative model for gene regulation by λ phage repressor," *Proc. Natl. Acad. Sci.*, vol. 79, no. 4, pp. 1129–1133, Nov. 1982.

[157] H. Sauro and S. Yang, "Fundamental Dynamic Units: Feedforward Networks and Adjustable Gates," *arXiv:0907.2005*, Jul. 2009.

[158] T. Gedeon, K. Mischaikow, K. Patterson, and E. Traldi, "When activators repress and repressors activate: A qualitative analysis of the shea–ackers model," *Bull. Math. Biol.*, vol. 70, no. 6, p. 1660, 2008.

[159] L. Bintu, N. E. Buchler, H. G. Garcia, U. Gerland, T. Hwa, J. Kondev, and R. Phillips, "Transcriptional regulation by the numbers: models," *Curr. Opin. Genet. Dev.*, vol. 15, no. 2, pp. 116–124, Mar. 2005.

[160] N. E. Buchler, U. Gerland, and T. Hwa, "On schemes of combinatorial transcription logic," *Proc. Natl. Acad. Sci.*, vol. 100, no. 9, pp. 5136–5141, Mar. 2003.

[161] T. S. Moon, C. Lou, A. Tamsir, B. C. Stanton, and C. A. Voigt, "Genetic programs constructed from layered logic gates in single cells," *Nature*, vol. 491, no. 7423, pp. 249–253, Nov. 2012.

[162] *Fluorescence*, Aug. 2020. [Online]. Available: https://chem.libretexts.org/@go/page/1766

[163] A. Tamsir, J. J. Tabor, and C. A. Voigt, "Robust multicellular computing using genetically encoded nor gates and chemical 'wires'," *Nature*, vol. 469, no. 7329, pp. 212–215, Jan. 2011.

[164] D. G. Zill, *Differential equations with boundary-value problems*. Nelson Education, 2016.

[165] *Introduction to Fluorescent Proteins*. [Online]. Available: https://www.microscopyu.com/techniques/fluorescence/introduction-to-fluorescent-proteins

[166] P. S. Stewart, "Diffusion in biofilms," *J. Bacteriol.*, vol. 185, no. 5, pp. 1485–1491, Mar. 2003.

[167] G. E. Dilanji, J. B. Langebrake, P. De Leenheer, and S. J. Hagen, "Quorum activation at a distance: spatiotemporal patterns of gene regulation from diffusion of an autoinducer signal," *J. Am. Chem. Soc.*, vol. 134, no. 12, pp. 5618–5626, Feb. 2012.

[168] L. Pasotti, S. Zucca, M. Casanova, G. Micoli, M. G. C. De Angelis, P. Magni *et al.*, "Half-life measurements of chemical inducers for recombinant gene expression," *J. Med. Biol. Eng.*, vol. 8, no. 1, pp. 1–10, Feb. 2014.

[169] *Synthesis and degradation rate constant of 3OC6-HSL (3OC6-homo-serine lactone) in the lux system*. [Online]. Available: https://bionumbers.hms.harvard.edu/search.aspx?trm=degradation+rate+\of+3OC6

[170] M. Schäfer, W. Wicke, L. Brand, R. Rabenstein, and R. Schober, "Transfer Function Models for Cylindrical MC Channels With Diffusion and Laminar Flow," *IEEE Trans. Mol. Biol. Multi-Scale Commun.*, vol. 7, no. 4, pp. 271–287, Feb. 2021.

[171] M. Pierobon and I. F. Akyildiz, "Diffusion-based noise analysis for molecular communication in nanonetworks," *IEEE Trans. Signal Process.*, vol. 59, no. 6, pp. 2532–2547, Feb 2011.

[172] ——, "Noise Analysis in Ligand-Binding Reception for Molecular Communication in Nanonetworks," *IEEE Trans. Signal Process.*, vol. 59, no. 9, pp. 4168–4182, June 2011.

[173] J. Wendel, "The non-absolute convergence of Gil-Pelaez'inversion integral," *The Annals of Mathematical Statistics*, vol. 32, no. 1, pp. 338–339, Apr. 1961.

[174] Y. Deng, A. Noel, M. Elkashlan, A. Nallanathan, and K. C. Cheung, "Molecular communication with a reversible adsorption receiver," in *Proc. IEEE ICC*, May 2016, pp. 1–7.

[175] F. Oberhettinger and L. Badii, *Tables of Laplace transforms.* New York, NY, USA: Springer, 1973.

Appendix A

Proofs for Chapter 4

A.1 Proof of Theorem 1

To solve the spatial-temporal concentration distributions of species S_i and S_k, we first define some initial boundary conditions. Species S_i and S_j are injected at the inlet of a straight microfluidic channel $x = 0$, the initial condition is

$$\begin{aligned} \mathrm{IC}_3 : C_{S_i}(0,t) &= \min\left\{C_{S_{i0}}, C_{S_{j0}}\right\} = C_0,\ 0 \le t \le T_{\mathrm{ON}} \\ &= C_0[u(t) - u(t - T_{\mathrm{ON}})]. \end{aligned} \tag{A.1}$$

Here, we must be careful that $C_{S_i}(0,t)$ may not equal its injected concentration. This is because the one-to-one stoichiometric relation between species S_i and S_j in $S_i + S_j \rightarrow S_k$ determines that either the reacting concentration of species S_i or S_j equals the smaller supplied concentration, i.e., $\min\left\{C_{S_{i0}}, C_{S_{j0}}\right\}$. At $t = 0$, the concentration of species S_i in any position is zero, thus a boundary condition being

$$\mathrm{BC}_5 : C_{S_i}(x,0) = 0,\ x \ge 0. \tag{A.2}$$

As the concentration change over locations far away from the source equals zero, another boundary condition is

$$\mathrm{BC}_6 : \frac{\partial C_{S_i}(x,t)}{\partial x}|_{x=\infty} = 0,\ t \ge 0. \tag{A.3}$$

The concentration distribution can be obtained by taking the Laplace transform of (4.8), (A.1), and (A.3) using

$$\widetilde{C_{S_i}}(x,s) = \int_0^\infty e^{-st} C_{S_i}(x,t)\,\mathrm{d}t. \tag{A.4}$$

The Laplace transform of (4.8) satisfying (A.2) is

$$D_{\text{eff}}\frac{\partial^2 \widetilde{C_{S_i}}(x,s)}{\partial x^2} - u_{\text{eff}}\frac{\partial \widetilde{C_{S_i}}(x,s)}{\partial x} = (s + k_f C_0)\,\widetilde{C_{S_i}}(x,s). \tag{A.5}$$

The Laplace transforms of (A.1) and (A.3) can be expressed

$$\widetilde{C_{S_i}}(0,s) = \frac{C_0}{s}(1 - e^{-T_{\text{ON}}s}), \tag{A.6}$$

$$\frac{\partial \widetilde{C_{S_i}}(\infty,s)}{\partial x} = 0. \tag{A.7}$$

Combining (A.5), (A.6), and (A.7), we derive

$$\widetilde{C_{S_i}}(x,s) = \frac{C_0(1 - e^{-T_{\text{ON}}s})}{s}\exp\left[\frac{u_{\text{eff}}x}{2D_{\text{eff}}} - x\sqrt{\frac{u_{\text{eff}}^2}{4D_{\text{eff}}^2} + \frac{s + k_f C_0}{D_{\text{eff}}}}\right]. \tag{A.8}$$

Taking the inverse Laplace transform of (A.8), we arrive at the concentration distribution of S_i in (4.11).

To derive the concentration of species S_k, we combine (4.8) and (4.9) as

$$\frac{\partial C_S(x,t)}{\partial t} = D_{\text{eff}}\frac{\partial^2 C_S(x,t)}{\partial x^2} - u_{\text{eff}}\frac{\partial C_S(x,t)}{\partial x}, \tag{A.9}$$

where $C_S(x,t) = C_{S_i}(x,t) + C_{S_k}(x,t)$. Interestingly, this equation is the advection-diffusion equation for the total concentration distribution of molecule S_i and S_k, and the corresponding initial and boundary conditions are

$$\text{IC}_3 : C_S(0,t) = C_0,\ 0 \le t \le T_{\text{ON}}, \tag{A.10}$$

$$\text{BC}_2 : C_S(\infty,t) = 0,\ t \ge 0, \tag{A.11}$$

$$\text{BC}_5 : C_S(x,0) = 0,\ x \ge 0. \tag{A.12}$$

Following [16, eq. (11)], we can derive the molecular concentration as

$$C_S(x,t) = \begin{cases} h(x,t), & 0 \le t \le T_{\mathrm{ON}} \\ h(x,t) - h(x,t-T_{\mathrm{ON}}), & t > T_{\mathrm{ON}}, \end{cases} \tag{A.13}$$

where $h(x,t)$ is given in (4.12). Taking the deduction of $C_{S_i}(x,t)$ in (4.11) from $C_S(x,t)$, we arrive at the concentration of S_k in (4.12). This completes the proof.

A.2 Proof of Theorem 2

Similar to the Proof of **Theorem 1**, we first define initial boundary conditions. On the condition of $C_{S_{j_0}} < \max\{C_{S_{i0}}(t)\}$ and due to the one-to-one stoichiometric relation between S_i and S_j, the initial condition varies with $C_{S_{j_0}}$, and can be expressed as

$$\mathrm{IC}_5 : C_{S_i}(0,t) = \begin{cases} C_{S_{i_0}}(t), & 0 \le t < t_1 \\ C_{S_{j_0}}, & t_1 \le t < t_2 \\ C_{S_{i_0}}(t), & t_2 \le t, \end{cases} \tag{A.14}$$

where t_1 and t_2 are obtained through solving $C_{S_{i0}}(t) = C_{S_{j_0}}$, and finally $t_1 = \mu - \sqrt{-2\sigma^2 \ln \frac{C_{S_{j_0}}\sqrt{2\pi\sigma^2}}{C_{S_{i0}}}}$ and $t_2 = \mu + \sqrt{-2\sigma^2 \ln \frac{C_{S_{j_0}}\sqrt{2\pi\sigma^2}}{C_{S_{i0}}}}$. The second and third boundary conditions are the same with (A.2) and (A.3), respectively. Next, we introduce two methods to solve (4.8), where we split the fully coupled advection-diffusion-reaction process into two sequential processes: 1) the reaction process (described by a reaction equation), and 2) the advection or advection-diffusion process (described by an advection or advection-diffusion equation). Under the assumption that $S_i + S_j \to S_k$ has been finished as soon as species S_i and S_j enter a straight microfluidic channel, we can use the solution of the reaction equation as an initial condition for the advection or advection-diffusion equation.

A.2.1 The First Method

The first method splits (4.8) into a reaction equation and an advection equation by ignoring the diffusion term. The concentration of residual species S_i is the portion whose concentration is greater than $C_{S_{j_0}}$, and can be expressed as

$$C_{S_{i0}}(t) - C_{S_{j_0}},\ t_1 \le t \le t_2. \tag{A.15}$$

The subsequent transport of species S_i will be only affected by advection. It has shown in [96] that the advection effect is merely a shift of initial specie profiles in time with velocity u_{eff} and without any change of shape, so the outlet concentration of S_i at the reaction channel can be expressed as

$$C_A^{\text{Method1}}(x,t) = \begin{cases} C_{S_{i_0}}(t - \frac{x}{u_{\text{eff}}}) - C_{S_{j_0}}, & t_1 + \frac{x}{u_{\text{eff}}} \leq t \leq t_2 + \frac{x}{u_{\text{eff}}}, \\ 0, & \text{otherwise.} \end{cases} \tag{A.16}$$

A.2.2 The Second Method

Different from the first method, the second one takes the diffusion effect into account. The advection-diffusion equation with the initial condition in (A.15) and other boundary conditions can be constructed as

$$\frac{\partial C_{S_i}^{\text{Method2}}(x,t)}{\partial t} = D_{\text{eff}} \frac{\partial^2 C_{S_i}^{\text{Method2}}(x,t)}{\partial x^2} - u_{\text{eff}} \frac{\partial C_{S_i}^{\text{Method2}}(x,t)}{\partial x}, \tag{A.17}$$

$$\text{IC}_6 : C_{S_i}^{\text{Method2}}(0,t) = C_{S_{i_0}}(t) - C_{S_{j_0}},\ t_1 \leq t \leq t_2, \tag{A.18}$$

$$\text{BC}_5 : C_{S_i}^{\text{Method2}}(x,0) = 0,\ x \geq 0, \tag{A.19}$$

$$\text{BC}_6 : \frac{\partial C_{S_i}^{\text{Method2}}(x,t)}{\partial x} \mid_{x=\infty} = 0,\ t \geq 0. \tag{A.20}$$

We take the Laplace transform of (A.17) with respect to t and obtain

$$D_{\text{eff}} \frac{\partial^2 \widetilde{C_{S_i}^{\text{Method2}}}(x,s)}{\partial x^2} - u_{\text{eff}} \frac{\partial \widetilde{C_{S_i}^{\text{Method2}}}(x,s)}{\partial x} - s\widetilde{C_{S_i}^{\text{Method2}}}(x,s) = 0. \tag{A.21}$$

The solution $\widetilde{C_{S_i}^{\text{Method2}}}(x,s)$ of this second order differential equation satisfying the Laplace transforms of (A.18) and (A.20) is (4.18).

In order to obtain $C_{S_i}^{\text{Method2}}(x,t)$, it is necessary to take the inverse Laplace transform of (4.18). However, due to the complexity of (4.18), we cannot derive the closed-form expression $\mathcal{L}^{-1}\left\{C_{S_i}^{\text{Method2}}(x,s)\right\}$. Hence, we employ the Gil-Pelaez theorem [173, 174]. Considering that the Fourier transform of a probability density function (PDF) is its characteristic function, (4.18) is first converted to Fourier transform $\widetilde{C_{S_i}^{\text{Method2}}}(x,\omega)$ by substituting $j\omega$ for s, and then we regard $\widetilde{C_{S_i}^{\text{Method2}}}(x,\omega)$ as the characteristic function of $\mathcal{L}^{-1}\left\{C_{S_i}^{\text{Method2}}(x,s)\right\}$. The corresponding cumulative distribution function (CDF)

can be given in terms of $\widetilde{C_{S_i}^{\text{Method2}}}(x,\omega)$ as

$$F(t) = \frac{1}{2} - \frac{1}{\pi}\int_0^\infty \frac{e^{-j\omega t}\overline{\widetilde{C_{S_i}^{\text{Method2}}}(x,\omega)} - e^{j\omega t}\widetilde{C_{S_i}^{\text{Method2}}}(x,\omega)}{2j\omega}\mathrm{d}\omega, \tag{A.22}$$

where $\overline{\widetilde{C_{S_i}^{\text{Method2}}}(x,\omega)}$ is the complex conjugate of $\widetilde{C_{S_i}^{\text{Method2}}}(x,\omega)$.

Taking the derivative of $F(t)$, we derive the inverse Laplace transform and obtain the concentration of species S_i given in (4.17). This completes the proof.

Appendix B

Proofs for Chapter 5

B.1 Proof of Theorem 3

To derive the impulse response $H(x,t)$, the initial condition for (4.6) can be written as

$$\text{IC}_7 : C_{S_i}(0,t) = \delta(t), \tag{B.1}$$

where $\delta(\cdot)$ is the Kronecker delta function. The Laplace Transform of (4.6) with respect to t is

$$D_{\text{eff}}\frac{\partial^2 \widetilde{C_{S_i}}(x,s)}{\partial x^2} - u_{\text{eff}}\frac{\partial \widetilde{C_{S_i}}(x,s)}{\partial x} - s\widetilde{C_{S_i}}(x,s) = 0, \tag{B.2}$$

where $\widetilde{C_{S_i}}(x,s)$ is the Laplace Transform of $C_{S_i}(x,t)$. The general solution for (B.2) can be expressed as

$$\widetilde{C_{S_i}}(x,s) = d_1 e^{\frac{u_{\text{eff}}+\sqrt{u_{\text{eff}}^2+4D_{\text{eff}}s}}{2D_{\text{eff}}}x} + d_2 e^{\frac{u_{\text{eff}}-\sqrt{u_{\text{eff}}^2+4D_{\text{eff}}s}}{2D_{\text{eff}}}x}, \tag{B.3}$$

where d_1 and d_2 are two constants and are constrained by BC_5 in (A.2) and BC_6 in (A.3). To determine d_1 and d_2, we also apply Laplace Transform to (A.2) and (A.3), and finally arrive at the particular solution for (B.2) as

$$\widetilde{C_{S_i}}(x,s) = e^{\frac{u_{\text{eff}}-\sqrt{u_{\text{eff}}^2+4D_{\text{eff}}s}}{2D_{\text{eff}}}x}, \tag{B.4}$$

In order to obtain the impulse response, we need to calculate the inverse Laplace Transform of (B.4), i.e., $\mathcal{L}^{-1}\left\{\widetilde{C_{S_i}}(x,s)\right\}$. In the following, we provide two methods to derive $\mathcal{L}^{-1}\left\{\widetilde{C_{S_i}}(x,s)\right\}$. The first method relies on the table provided in [175].

According to [175, eqs. (1.3) and (5.58)], the inverse Laplace Transform[1] can be derived as

$$\mathcal{L}^{-1}\left\{\widetilde{C_{S_i}}(x,s)\right\} = \frac{x}{2\sqrt{\pi D_{\text{eff}} t^3}} e^{\frac{u_{\text{eff}} x}{2D_{\text{eff}}} - \frac{u_{\text{eff}}{}^2 t^2 + x^2}{4D_{\text{eff}} t}}. \tag{B.5}$$

However, when we consider a much more practical scenario, e.g., a time-varying distribution of average velocity due to the imperfectness of syringe pumps, the first method may become infeasible. Therefore, the second method is more general. This method resorts to the Gil-Pelaez theorem. According to the description of Gil-Pelaez theorem in Appendix A, the cumulative distribution function (CDF) $F(x,t)$ for $\mathcal{L}^{-1}\left\{\widetilde{C_{S_i}}(x,s)\right\}$ can be expressed using (A.22). Take the derivative of $F(x,t)$ with respect to t, we can arrive at (5.2). This completes the proof.

B.2 Proof of Lemma 5

Recall that we separate an advection-diffusion-reaction equation into a reaction part and an advection-diffusion part, we consider the remaining concentrations of S_i in (5.11a) and S_j in (5.11b) as inputs to a straight advection-diffusion channel. According to (5.4), we can obtain (5.12a) and (5.12b).

To derive the concentration of product S_k in (5.12c), we combine (4.8) and (4.9) and denote $C_S(x,t) = C_{S_i}(x,t) + C_{S_k}(x,t)$, which yields the advection-diffusion equation in (A.9). As the initial condition of (A.9) is

$$C_S(0,t) = C_{S_{i_0}}(0,t), \tag{B.6}$$

we can write

$$C_S(x,t) = C_{S_{i_0}}(0,t) * H(x,t). \tag{B.7}$$

Combined with (5.11a) and (5.12a), we can arrive at the concentration of product S_k in (5.12c). This completes the proof.

[1] In Matlab, we need to manually set value 0 for (B.5) when $t = 0$ as Matlab returns the scalar "not a number" (NaN).

Appendix C

Proofs for Chapter 6

C.1 Proof of Lemma 8

Let us denote $I^{\mathrm{SS}}_{\mathrm{AC}_2} = y - \frac{I^{\mathrm{SS}}_{\mathrm{A}_0} + I^{\mathrm{SS}}_{\mathrm{Ch}_0}}{3}$, and (6.20) can be reduced to

$$y^3 + py + q = 0, \tag{C.1}$$

where p and q are defined in (6.22) and (6.23), respectively. The property of the roots of (C.1) depends on the sign of the discriminant of the equation, that is

$$\Delta = (q/2)^2 + (p/3)^3. \tag{C.2}$$

When $\Delta > 0$, eq. (C.1) has three distinct roots, where only one of them is a real number and the other two are non-real complex conjugate numbers. As $(q/2)^2$ is positive, in the following we prove $\Delta > 0$ through demonstrating that the numerator of p (i.e., $12K_{AC} - (4I^{\mathrm{SS}}_{\mathrm{A}_0} - 2I^{\mathrm{SS}}_{\mathrm{Ch}_0})^2$) is positive.

Recall $I^{\mathrm{SS}}_{\mathrm{Ch}_0}$ and $I^{\mathrm{SS}}_{\mathrm{A}_0}$ are functions of the activities of promoters BAD and Tet*, i.e., $\mathrm{gfp}^{\max}_{\mathrm{BAD}} \cdot P_{\mathrm{BAD}}$ and $\mathrm{gfp}^{\max}_{\mathrm{Tet}^*} \cdot P_{\mathrm{Tet}^*}$, and can be calculated by (6.14) and (6.15), respectively. Fig. 6.16 plots the promoter activities of BAD and Tet* versus their corresponding inducers. It is clear that $\mathrm{gfp}^{\max}_{\mathrm{BAD}} \cdot P_{\mathrm{BAD}} > 0$ and $\mathrm{gfp}^{\max}_{\mathrm{Tet}^*} \cdot P_{\mathrm{Tet}^*} < 1$. Thus, we can obtain the following relation

$$\Delta = 12K_{AC} - (4I^{\mathrm{SS}}_{\mathrm{A}_0} - 2I^{\mathrm{SS}}_{\mathrm{Ch}_0})^2 > 12K_{AC} - (4\theta_A)^2 = 6.34 \times 10^{-8} > 0. \tag{C.3}$$

According to Cardano's formula, the real root of (C.1) is

$$y=\sqrt[3]{-\frac{q}{2}+\sqrt{(\frac{q}{2}^2)+(\frac{p}{3}^3)}}+\sqrt[3]{-\frac{q}{2}-\sqrt{(\frac{q}{2}^2)+(\frac{p}{3}^3)}}. \tag{C.4}$$

With $I_{\mathrm{AC}_2}^{\mathrm{SS}}=y-\frac{I_{\mathrm{A}_0}^{\mathrm{SS}}+I_{\mathrm{Ch}_0}^{\mathrm{SS}}}{3}$, we can arrive at (6.21). This completes the proof.

C.2 Proof of Lemma 9

To derive the orthogonality of Bessel functions in (6.46) with $\beta_n r_b$ and $\beta_m r_b$ being the two roots of $J_0'(r)$, we let $J_0(\beta_n r)$ and $J_0(\beta_m r)$ with $n\neq m$ be two solutions of the Bessel functions

$$r^2\frac{\mathrm{d}^2J_0(\beta_n r)}{\mathrm{d}r^2}+r\frac{\mathrm{d}J_0(\beta_n r)}{\mathrm{d}r}+\beta_n^2r^2J_0(\beta_n r)=0, \tag{C.5}$$

$$r^2\frac{\mathrm{d}^2J_0(\beta_m r)}{\mathrm{d}r^2}+r\frac{\mathrm{d}J_0(\beta_m r)}{\mathrm{d}r}+\beta_m^2r^2J_0(\beta_m r)=0. \tag{C.6}$$

Multiplying (C.5) by $J_0(\beta_m r)/r$ and (C.6) by $J_0(\beta_n r)/r$, and subtracting, we find that

$$\frac{\mathrm{d}}{\mathrm{d}r}\left\{r\left[J_0(\beta_n r)\frac{\mathrm{d}J_0(\beta_m r)}{\mathrm{d}r}-J_0(\beta_m r)\frac{\mathrm{d}J_0(\beta_n r)}{\mathrm{d}r}\right]\right\}=(\beta_n^2-\beta_m^2)rJ_0(\beta_n r)J_0(\beta_m r). \tag{C.7}$$

When both β_n and β_m are nonzero, we integrate (C.7) from 0 to r_b and omit the integration constant, and this operation yields the so-called Lommel integral as

$$\begin{aligned}
&\int_0^{r_b}rJ_0(\beta_n r)J_0(\beta_m r)\mathrm{d}r\\
=&\frac{1}{\beta_n^2-\beta_m^2}\int_0^{r_b}\frac{\mathrm{d}}{\mathrm{d}r}\left\{r\left[J_0(\beta_n r)\frac{\mathrm{d}J_0(\beta_m r)}{\mathrm{d}r}-J_0(\beta_m r)\frac{\mathrm{d}J_0(\beta_n r)}{\mathrm{d}r}\right]\right\}\mathrm{d}r\\
=&\frac{r}{\beta_n^2-\beta_m^2}\left[J_0(\beta_n r)\frac{\mathrm{d}J_0(\beta_m r)}{\mathrm{d}r}-J_0(\beta_m r)\frac{\mathrm{d}J_0(\beta_n r)}{\mathrm{d}r}\right]\Bigg|_0^{r_b}\\
=&\frac{r_b}{\beta_n^2-\beta_m^2}\Big[J_0(\beta_n r_b)\beta_m J_0'(\beta_m r_b)-J_0(\beta_m r_b)\beta_n J_0'(\beta_n r_b)\Big],
\end{aligned} \tag{C.8}$$

where $J_0'(\beta r_b)$ is defined as

$$J_0'(\beta r_b)=\left.\frac{\mathrm{d}J_0(r)}{\mathrm{d}r}\right|_{r=\beta r_b}. \tag{C.9}$$

If $\beta_n r_b$ and $\beta_m r_b$ are two different roots of $J_0'(r)$, i.e., $J_1(r)$, we have the following orthogonality property

$$\int_0^{r_b} r J_0(\beta_n r) J_0(\beta_m r) \mathrm{d}r = 0, \tag{C.10}$$

meaning the functions $J_0(\beta_n r)$ and $J_0(\beta_m r)$ are orthogonal over the finite interval $0 \leq r \leq r_b$. However, if $\beta_n \to \beta_m$, eq. (C.8) cannot be evaluated as it exhibits an indeterminate form. Therefore, we regard β_n as a variable and based on the L'Hôpital's rule (C.8) becomes

$$\begin{aligned}
&\int_0^{r_b} r J_0(\beta_m r) J_0(\beta_m r) \mathrm{d}r \\
&= \lim_{\beta_n \to \beta_m} \frac{r_b}{\beta_n^2 - \beta_m^2} \Big[J_0(\beta_n r_b)\beta_m J_0'(\beta_m r_b) - J_0(\beta_m r_b)\beta_n J_0'(\beta_n r_b) \Big] \\
&= \lim_{\beta_n \to \beta_m} \frac{r_b}{2\beta_n} \left\{ \frac{\mathrm{d}J_0(\beta_n r_b)}{\mathrm{d}\beta_n} \beta_m J_0'(\beta_m r_b) - J_0(\beta_m r_b) \left[J_0'(\beta_n r_b) + \beta_n \frac{\mathrm{d}J_0'(\beta_n r_b)}{\mathrm{d}\beta_n} \right] \right\} \\
&= -\frac{r_b^2}{2} J_0(\beta_m r_b) J_0''(\beta_m r_b),
\end{aligned} \tag{C.11}$$

where $J_0''(\beta_m r_b)$ is defined as

$$J_0''(\beta r_b) = \left. \frac{\mathrm{d}J_0'(r)}{\mathrm{d}r} \right|_{r=\beta r_b}. \tag{C.12}$$

Remind that $J_0(\beta_m r)$ is the solution of (C.6) so that $J_0''(\beta_m r_b) = -J_0(\beta_m r_b)$. We substitute this relation into (C.11) and obtain

$$\int_0^{r_b} r J_0(\beta_m r) J_0(\beta_m r) \mathrm{d}r = \frac{r_b^2}{2} J_0^2(\beta_m r_b). \tag{C.13}$$

It is noted that the above derivation does not apply to the case where both β_n and β_m are zero. For this scenario, we can calculate the integration directly, which is

$$\int_0^{r_b} r J_0(0r) J_0(0r) \mathrm{d}r = \int_0^{r_b} r \mathrm{d}r = \frac{r_b^2}{2}. \tag{C.14}$$

We observe that $\frac{r_b^2}{2}$ can be rewritten as $\frac{r_b^2}{2} J_0^2(0 \cdot r_b)$, which can be regarded as a special case of (C.13). Thus, we complete the proof.

C.3 Proof of Corollary 1

According to (6.47), the expected number of molecules inside the receiver at time t is

$$\begin{aligned} N_{\mathrm{RX}}(t) &= \frac{N_{\mathrm{TX}}}{\pi r_b^2} \int_{r_1}^{r_2} \int_0^{2\pi} \sum_{n=0}^{\infty} \frac{r J_0(\beta_n r)}{J_0^2(\beta_n r_b)} e^{-(\alpha_n^2+k)t} \mathrm{d}r\mathrm{d}\theta \\ &= \frac{2N_{\mathrm{TX}}}{r_b^2} \sum_{n=0}^{\infty} \frac{e^{-(\alpha_n^2+k)t}}{J_0^2(\beta_n r_b)} \int_{r_1}^{r_2} r J_0(\beta_n r) \mathrm{d}r. \end{aligned} \tag{C.15}$$

For $n = 0$ (i.e., $\beta_0 = 0$), we have

$$\frac{e^{-(\alpha_0^2+k)t}}{J_0^2(\beta_0 r_b)} \int_{r_1}^{r_2} r J_0(\beta_0 r) = \frac{r_2^2 - r_1^2}{2} e^{-kt}. \tag{C.16}$$

For $n > 0$, according to the definition of $J_v(x)$ and the relationship between gamma function and the factorial function [164, Ch. 6.3, eq. (7)], the Maclaurin series of $rJ_0(\beta_n r)$ is

$$r J_0(\beta_n r) = r \sum_{m=0}^{\infty} \frac{(-\beta_n r/2)^{2m}}{(m!)^2}. \tag{C.17}$$

The integral of (C.17) is

$$\begin{aligned} \int r J_0(\beta_n r) &= \sum_{m=0}^{\infty} \frac{1}{m!^2} \int r(-\beta_n r/2)^{2m} \mathrm{d}r \\ &= \frac{r}{\beta_n} \sum_{m=0}^{\infty} \frac{(-\beta_n r/2)^{2m+1}}{m!(m+1)!} \\ &= \frac{r J_1(\beta_n r)}{\beta_n}. \end{aligned} \tag{C.18}$$

Thus, for any $n \geq 0$, we derive

$$\frac{e^{-(\alpha_n^2+k)t}}{J_0^2(\beta_n r_b)} \int_{r_1}^{r_2} r J_0(\beta_n r) \mathrm{d}r = \frac{[r_2 J_1(\beta_n r_2) - r_1 J_1(\beta_n r_1)]}{\beta_n J_0^2(\beta_n r_b)} e^{-(\alpha_n^2+k)t}. \tag{C.19}$$

Combining (C.16) and (C.19), we complete the proof of **Corollary 1**.

Appendix D

Glossary of Biological Terms

Table D.1 Glossary of Biological Terms.

Term	Description
Action potential	Rapid and transient change in electric potential across a membrane
Autoinducers	Diffusible signal molecules produced by cells to monitor local population changes. They can also have additional functions (e.g., act as antibiotics or toxins)
Cytosol	The aqueous part of the cytoplasm
DNA	Deoxyribonucleic acid. Carrier of the hereditary information for the building and maintenance of organisms
Endoplasmic reticulum (ER)	Continuous membrane system connected to the nucleus. Involved in folding, modification, and transport of proteins
Enzyme	A biologically relevant molecule acting as a catalyst, making chemical reactions possible or greatly increasing their rate
Exocytosis	Active transport of material out of the cell via membrane vescicles
Golgi apparatus	Large organelle of eukaryotic cells responsible for modification, packaging, and transportation of proteins
G-protein-coupled receptors	Large group of cell surface receptor proteins

Messenger RNA (mRNA)	Single-stranded RNA molecule, carrying the information for protein production outside the cell nucleus
Neurotransmitters	Chemical messengers that are released into a chemical synapse to convey a message between neurons
Promoter sequence	Small DNA sequence preceding a gene that marks where transcription should start
Protein	Organic compound comprised of one or more macromolecules. Integral to most cellular processes
Ribosomes	Protein-synthesizing factories, comprised of ribosomal RNA and associated helper proteins
RNA	Ribonucleic acid. A single-stranded biopolymer that is essential for protein production by carrying sequence information from DNA to ribosomes
RNA polymerase (RNAP)	Enzyme that can bind and follow a strand of DNA, replicating its sequence
Signaling pathway	A chain of cell components and molecules working in succession to transfer a signal
Transcription factor (TF)	A protein that can bind a specific DNA sequence, controlling the expression of a gene
Transfer RNA (tRNA)	Special RNA molecule involved in protein production within ribosomes. It matches a loose amino acid to mRNA sequence